

DISS. ETH NO. 18934

**2.5D elastic modelling and sensitivity investigations
directed towards
near-surface seismic waveform analysis**

A dissertation submitted to the
ETH ZURICH
for the degree of

Doctor of Sciences (Dr. sc. ETH Zürich)

presented by

SABINE LATZEL

Diplom-Physikerin (Dipl. Phys.)
University of Stuttgart (Germany)
born December 19, 1979
citizen of Germany

accepted on the recommendation of

Prof. Dr. Hansruedi Maurer, examiner
Prof. Dr. Alan G. Green, co-examiner
Prof. Dr. Stewart Greenhalgh, co-examiner
Prof. Dr. Christopher Juhlin, co-examiner

2010

Gewidmet meiner Großmutter, Gertrud Jantschke.

Acknowledgements

Without the constant support of the members of my working group at ETH, my family and friends, writing this thesis would not have been possible.

First of all, I want to thank my direct supervisor Hansruedi Maurer for providing me with this challenging thesis topic. I also have to thank him for his continuing believe in my capabilities despite of all the failures and for his patience towards my stolidity. I thank Alan Green, who always put me back on track and helped me with advise when I had lost the thread of my thesis. Without Stewart Greenhalgh I would have never finished my work. He constantly encouraged me to go on, proofread my technical reports and contributed with his advise to improve the text of my thesis in a major way and with his jokes and stories to keep up my moral.

A special thank to Thomas Bohlen for providing me with his finite difference modelling code; without him the sensitivity analysis would not have been possible as I presented it in my thesis.

A big thank you to André Blanchard for all the technical assistance and for being a good friend and to Elisabeth Läderach, Chrissula Chatzidis, Sabine Räss and Sabine Schulze for their administational help and their kindness.

I also thank all the people working in the AUG group and at the institute of geophysics during my time there. First of all I thank Jaques Ernst, who always offered me advise and interesting discussions. Thanks to Jaques, Klaus Holliger, Tom Spillmann, Rolf Sidler and the staff of the geophysics E-Lab for the interesting early lunches at the physics restaurant. Special thanks go to the O9 inmates, that is Mark Blome, Edgar Manukyan, Stefano Marelli and Giovanni Meles, for keeping me alive during the last part of my thesis. I cannot thank you enough, guys.

I also want to thank my parents, my brother and my grandmother for always believing in me and always keeping their interest in my work, even though I did not really take enough time for calling and visiting them during the last few years.

Last but not least, my biggest thanks go to my partner and centre of my life Matthias Schick. Without him, I would never have survived my studies. He never complained, neither about me leaving him alone to go to Zurich nor about the little time I had for him during the time of my thesis.

Contents

1	Introduction	1
1.1	Seismic methods: main areas of application	1
1.2	Seismic methods: model parameters and data types	2
1.2.1	Subsurface parameters	2
1.2.2	Observables	3
1.3	Seismic methods: technology and information content	3
1.3.1	Seismic reflection	3
1.3.2	Seismic refraction	4
1.3.3	Surface wave analysis	4
1.3.4	Transmission travel time tomography	6
1.3.5	Passive methods	6
1.3.6	Full waveform inversion	6
1.4	Specific problems of surface-based near-surface seismics	9
1.5	State-of-the-art of seismic full waveform inversions	10
1.5.1	Numerical modelling	10
1.5.2	Inversion	12
1.6	Thesis Objectives and Structure	12
2	2D sensitivity and information content analyses of seismic data	14
2.1	Introduction	14
2.1.1	Experimental setup	16
2.1.2	Sensitivity computation	23
2.1.3	Data information	25
2.2	Wave field analysis	27
2.2.1	Acoustic approximation	27
2.2.2	Adding source and receiver directionality	28
2.2.3	The effect of vertical heterogeneity	28
2.3	Waveform sensitivity analysis	34
2.3.1	Acoustic approximation	37
2.3.2	Adding source and receiver directionality	40
2.3.3	The influence of vertical inhomogeneity	40
2.4	Data information	47
2.4.1	Preliminaries	47
2.4.2	Data information analysis	52
2.5	Conclusions	59

3	Theory, implementation and validation of a frequency-domain finite element (FEM) forward solver	61
3.1	Theory and formulae	61
3.1.1	2.5D elemental equations	62
3.1.2	Boundary conditions	69
3.1.3	The source term	77
3.1.4	The global system matrix	78
3.2	Assessment of accuracy and efficiency for the 2D problem	79
3.2.1	FEM Accuracy	80
3.2.2	PML validation	83
3.2.3	FEM Comparability	90
3.2.4	FEM efficiency	95
3.3	Conclusions	97
4	2.5D forward modelling	98
4.1	Introduction	98
4.2	Homogeneous isotropic full space	100
4.2.1	Anatomy of the analytic spectra	100
4.2.2	Efficient sampling strategy	103
4.2.3	FEM results	107
4.3	Homogeneous isotropic half space	109
4.4	Sampling problems for heterogeneous models	109
4.4.1	Sampling strategy for even sampling	112
4.4.2	Grid density dh versus sampling density Δk_y	112
4.4.3	The failure of the PML boundary conditions at the critical wavenumbers	117
4.5	Conclusions	119
5	Conclusions and Outlook	120
5.1	Main results	120
5.1.1	Sensitivities and data information content	120
5.1.2	Elastic modelling	121
5.1.3	Sampling strategies for elastic 2.5D forward modelling	121
5.2	Areas of future research	122
5.2.1	Sensitivities and data information content	122
5.2.2	Elastic modelling	124
5.2.3	Elastic 2.5D forward modelling	124
A	Mathematical details	127
A.1	Fourier transform definition	127
A.2	Elemental matrix entries in the PMLs	128
A.3	2.5D FEM solution symmetries with respect to k_y	132
B	FEM matrix assembly	134
C	Analytic Green's functions	138

D Gauss Newton type iterative local optimisation algorithms	143
E Relation between sensitivities for different sets of parameters	147
F Frequency and spatial sampling strategies	153
Curriculum Vitae	185

Nomenclature

A_x, A_z, B_x, B_z	Coefficients of the coordinate stretching functions, see equation (3.34)
\mathcal{D}	Data space, see equation (2.10)
\mathfrak{d}_o	Data set vector containing the observed data, see equation (2.2)
\mathfrak{d}	Data set vector, see equation (2.10)
d	Distance between source and receiver, page 101
d^{\max}	Maximum distance between source and receiver, see equation (4.6)
$d_{i_s}^{l,(ij)} = d_{i_s}^l$	Data sample for source/receiver pair l and configuration ij with $i, j \in \{x, y, z\}$ for time/frequency index i_s , see equation (2.9)
dh	Finite difference or Finite element grid step
dt	Finite difference time step, see equation (2.4)
$\bar{f}_i, \bar{\bar{f}}_i$	i th component of the source force vector in the ω - x - y - z -domain and the ω - x - k_y - z -domain, see equation (3.1)
$\bar{\mathbf{f}}, \bar{\bar{\mathbf{f}}}$	Source force vector in the ω - x - y - z -domain and the ω - x - k_y - z -domain, see equation (3.1)
$\hat{\mathbf{f}} = [\hat{f}_x, \hat{f}_y, \hat{f}_z]^T$	Unit vector specifying the source force direction, see equation (3.40)
\mathfrak{F}	Global source vector, see equation (3.48)
\mathfrak{F}^e	Elemental source vector, see equation (3.16)
f	Frequency, see equation (3.1)
$F_{Ax}^e, F_{Ay}^e, F_{Az}^e$	Components of the elemental source vector, where $A \in \{I, J, K, L\}$, see equation (3.43)
f_c	Approximate centre frequency of the source wavelet, see equation (2.5)
\mathbf{G}	FEM Green's tensor, see equation (A.13)
$\mathbf{G}(\mathfrak{x}; \mathfrak{x}_s)$	Elastic Green's tensor for a source at \mathfrak{x}_s , see equation (C.4)

$\mathfrak{G}_{\zeta v}$	Component vector of the FEM Green's tensor, where $\zeta, v \in \{x, y, z\}$, see equation (A.13)
$G(\mathfrak{x}; \mathfrak{x}_s)$	Scalar Green's function for a source at \mathfrak{x}_s , see equation (C.1)
G_{ij}^P	Component of the P -wave contribution to the elastic Green's tensor, where $i, j \in \{x, y, z\}$, see equation (C.13)
G_{ij}^S	Component of the S -wave contribution to the elastic Green's tensor, where $i, j \in \{x, y, z\}$, see equation (C.14)
g_x, g_z	Coordinate stretching functions used in the PMLs, see equation (3.30)
$G_{ij}(\mathfrak{x}; \mathfrak{x}_s)$	Component of the elastic Green's tensor for a source at \mathfrak{x}_s , where $i, j \in \{x, y, z\}$, see equation (C.4)
i	Imaginary number, i.e. $\sqrt{-1}$
I, J, K, L	Elemental node indices, see equation (3.10)
\mathbf{J}	Jacobian matrix, matrix of Fréchet derivatives or sensitivities, see equation (2.1)
\mathbf{J}^L	Sensitivity with respect to v_P for data subvector \mathfrak{d}^L , see equation (2.17)
\mathbf{S}^L	Sensitivity with respect to v_S for data subvector \mathfrak{d}^L , see equation (2.17)
$\mathbf{J}^T \hat{\mathbf{W}}_D \mathbf{J} + \lambda \hat{\mathbf{W}}_M$	Approximate Hessian matrix, see equation (2.18)
\mathbf{K}	Global stiffness matrix, see equation (3.45)
\mathbf{K}^e	Elemental stiffness matrix, see equation (3.19)
$K_{AB\zeta v}^e$	Component of the elemental stiffness matrix, see equation (3.21)
k_P	Wave number of a wave travelling with longitudinal wave velocity v_P , see equation (4.1)
k_P	Wave number of a wave travelling with longitudinal wave velocity v_P , see equation (4.2)
k_R	Wave number of a wave travelling with Rayleigh wave velocity v_R , see equation (4.10)
k_y	Component of the wave number in the y -direction, see equation (A.2)
k_y^{\max}	Maximum wavenumber sampled in the case of evenly spaced sampling along the k_y -axis, see equation (4.11)
$KY_{j_{\text{GL}}}$	Gauss-Legendre sampling points, see equation (4.7)

$K_{AB\zeta v}^e$	Component of the elemental stiffness matrix, where $\zeta, v \in \{x, y, z\}$ and $A, B \in \{I, J, K, L\}$, see equation (3.46)
$K_{ij\zeta v}$	Component of the elemental stiffness matrix, where $\zeta, v \in \{x, y, z\}$ and $i, j \in [1, n]$, see equation (B.1)
ℓ_{null}	Fractional size of the effective null space of the approximate Hessian matrix, see equation (2.18)
\mathcal{M}	Model space, see equation (2.8)
\mathbf{M}	Global mass matrix, see equation (3.45)
\mathbf{M}^e	Elemental mass matrix, see equation (3.18)
\mathbf{m}	Vector of model parameters, see equation (2.8)
\mathbf{m}^{est}	Model estimated by the inversion algorithm if the true model is taken as the starting model., see equation (D.6)
\mathbf{m}^{true}	True model, see equation (D.6)
M	Parameter determining the sampling density along the k_y -axis, see equation (4.6)
$M_{AB\zeta v}^e$	Component of the elemental mass matrix, see equation (3.20)
$M_{AB\zeta\zeta}^e$	Component of the elemental mass matrix, where $\zeta \in \{x, y, z\}$ and $A, B \in \{I, J, K, L\}$, see equation (3.46)
$M_{ij\zeta\zeta}$	Component of the elemental mass matrix, where $\zeta \in \{x, y, z\}$ and $i, j \in [1, n]$, see equation (B.1)
N	Gridpoints per minimum wavelength
n	Total number of model nodes, see equation (3.47)
n^e	Total number of model elements, see equation (3.47)
n_x^e, n_z^e	Number of model elements in the horizontal and the vertical directions, see equation (3.47)
n_d	Number of data subsets contained in the complete data vector, i.e. number of different combinations of source/receiver pairs and configurations, see equation (2.9)
$n_D = n_d \cdot n_s$	Total number of data points, see equation (2.9)
N_I, N_J, N_K, N_L	Finite element shape functions, see equation (3.10)
n_M	Number of model parameters, i.e. number of degrees of freedom, see equation (2.8)

N_P	Number of Gauss-Legendre sampling points in the interval $[0 - k_P]$, see equation (4.6)
N_R	Number of Gauss-Legendre sampling points in the interval $[0 - k_R]$, see equation (4.10)
N_S	Number of Gauss-Legendre sampling points in the interval $[0 - k_S]$, see equation (4.6)
n_s	Number of data samples for one source/receiver pair and configuration, see equation (2.9)
n_x, n_y, n_z	Number of model nodes in the horizontal (x, y) and vertical (z) directions, see equation (3.47)
n_{k_y}	Number of sampling points in the case of evenly spaced sampling along the k_y -axis, see equation (4.12)
n_{rs}	Number of source/receiver pairs, see equation (2.9)
\mathbf{R}^M	Model resolution matrix, see equation (D.8)
REA	Relative Eigenvalue Area, see equation (2.22)
RER	Relative Eigenvalue Range, see equation (2.18)
$\bar{s}(\omega)$	Frequency spectrum of the source wavelet, see equation (3.40)
$\mathbf{S} = \mathbf{M} + \mathbf{K}$	Global system matrix, see equation (3.45)
$s(t)$	Source wavelet in the time domain, see equation (2.5)
$S_{AB\zeta v}^e$	Component of the elemental system matrix, where $\zeta, v \in \{x, y, z\}$ and $A, B \in \{I, J, K, L\}$, see equation (3.46)
$S_{ij\zeta v}$	Component of the elemental system matrix, where $\zeta, v \in \{x, y, z\}$ and $i, j \in [1, n]$, see equation (B.1)
t	Time
$\bar{u}_i, \bar{\bar{u}}_i$	i th component of the displacement field in the ω - x - y - z -domain and the ω - x - k_y - z -domain, see equation (3.1)
$\bar{\mathbf{u}}, \bar{\bar{\mathbf{u}}}$	Displacement field in the ω - x - y - z -domain and the ω - x - k_y - z -domain, see equation (3.1)
\mathcal{U}	Vector space of displacement field solution vectors, see equation (3.3)
\mathcal{U}_N	Finite dimensional subspace of the vector space of displacement field solution vectors, see equation (3.6)
\mathfrak{U}	Galerkin approximation of the continuous solution $\bar{\bar{\mathbf{u}}}$, i.e. global solution vector, see equation (3.6)

\mathbf{u}^e	Elemental displacement vector, see equation (3.17)
$U_{A\zeta}^e$	Value of the elemental solution vector component \bar{u}_ζ at the location of node $A \in \{I, J, K, L\}$, where $\zeta \in \{x, y, z\}$, see equation (3.12)
$U_{i\zeta}$	Value of the global solution vector component \bar{u}_ζ at the location of node $i \in [1, n]$, where $\zeta \in \{x, y, z\}$, see equation (4.3)
$\bar{\mathbf{v}} = [\bar{v}_x, \bar{v}_y, \bar{v}_z]^T$	Frequency domain (ω - x - y - z) representation of vector field \mathbf{v} , see equation (A.1)
$\bar{\bar{\mathbf{v}}} = [\bar{\bar{v}}_x, \bar{\bar{v}}_y, \bar{\bar{v}}_z]^T$	Wave number domain (ω - x - k_y - z) representation of vector field $\bar{\mathbf{v}}$, see equation (A.2)
v_P	Velocity of the P -wave (or longitudinal wave), see equation (E.1)
v_S	Velocity of the S -wave (or shear wave), see equation (E.1)
$\hat{\mathbf{W}}_D$	Data weighting operator, see equation (2.11)
$\hat{\mathbf{W}}_M$	Model weighting operator, see equation (2.12)
$W_{j_{GL}}$	Gauss-Legendre weights, see equation (4.7)
$\tilde{x}, \tilde{y}, \tilde{z}$	Stretched coordinates, see equation (3.27)
$\mathbf{r}_s = [x_s, y_s, z_s]^T$	Source position, see equation (3.40)
x, y, z	Cartesian coordinates, denoting in-line, cross-line and vertical directions, respectively.
x_m, z_m	x - and z -coordinate of the midpoint of one finite element, see Figure 3.1
Δk_y	Sample spacing in the case of evenly spaced sampling along the k_y -axis, see equation (4.12)
$\Delta x, \Delta z$	Width and height of one finite element, see Figure 3.1
$\delta(\mathbf{r})$	Delta function, see equation (3.40)
δ_{ij}	Kronecker delta with $\delta_{ij} = 1$ for $i = j$ and $\delta_{ij} = 0$ for $i \neq j$
η	Vertical coordinates local to one finite element, see Figure 3.1
$\varepsilon_x, \varepsilon_y, \varepsilon_z$	Coordinate stretching parameters, see equation (3.27)
$\gamma_x, \gamma_y, \gamma_z$	Direction cosines, see equation (C.10)
κ	Compressibility or bulk modulus, see equation (E.1)
λ	Lamé's first parameter, see equation (E.1)

$\lambda_i = \tilde{\lambda}_i/\tilde{\lambda}_1$	Normalized eigenvalue of the approximate Hessian matrix, see equation (2.18)
$\tilde{\lambda}_1$	Maximum eigenvalue of the approximate Hessian matrix, see equation (2.18)
$\tilde{\lambda}_i$	Eigenvalue of the approximate Hessian matrix, see equation (2.18)
λ_P	Wavelength of a wave travelling with compressional wave velocity v_P , see equation (4.6)
λ_R	Wavelength of a wave travelling with Rayleigh wave velocity v_R , see equation (4.10)
λ_S	Wavelength of a wave travelling with shear wave velocity v_S , see equation (4.6)
$\bar{U}_x, \bar{U}_y, \bar{U}_z$	Effective wavenumbers, see equation (3.23)
μ	Shear modulus or Lamé's second parameter, see equation (E.1)
ρ	Density, see equation (E.1)
θ	Threshold value below which eigenvalues are taken to be zero, see equation (2.18)
$\omega = 2\pi f$	Angular frequency, see equation (3.1)
ξ	Horizontal coordinates local to one finite element, see Figure 3.1

Abstract

Analysis of surface-based shallow seismic data can be problematic with traditional methods, such as seismic reflection processing, refraction tomography and surface wave analysis. These methods require identification and isolation of single phases, namely reflected body waves, first break direct/refracted arrivals and dispersed surface wave trains. In shallow seismic data these phases are not well separated, but arrive at the receivers in overlapping time windows. Full waveform inversion methods do not require the individual phases to be separated and are thus expected to be a powerful tool for shallow investigations. Ideally, one would devise a waveform inversion algorithm that considers 3D visco-elastic subsurface models and an arbitrary surface topography. Currently, such a comprehensive approach is computationally too expensive, and the prevalent strategy is to employ a 2D acoustic approximation.

The acoustic approximation is expected to be problematic for shallow seismic data, because such data contain significant portions of surface wave energy that is not considered with this type of numerical modelling. Furthermore, it cannot account for the shear waves and mode conversions, which are prevalent in the seismograms. I quantify the inadequacy of the acoustic approximation with an extensive waveform and waveform sensitivity analysis in both the time domain and the frequency domain, which also highlights the substantial differences between scalar (pressure sources and receivers) and vectorial (directed sources and multi-component receivers) seismic data.

An information content analysis that is based on the eigenvalue spectrum of the approximate Hessian matrix revealed that the combination of vertically oriented sources and horizontally oriented receivers is most favourable. It outperforms the commonly employed combination of vertically directed sources and vertical component receivers. The information content analysis also highlights that there would be little benefit in acquiring full tensorial data, including all possible source/receiver component configurations. If complete seismograms are analysed, there is no difference in information content between time and frequency domain waveform inversions. However, restricting the data space to selected time windows results in a significant loss of information. In contrast, selecting only a few carefully chosen frequencies causes only minor degradations of the information content.

Because of the inadequacy of the acoustic approximation I have implemented a frequency-domain elastic modelling code that is based on the finite element technique. My implementation considers a 2D grid of regular square elements and perfectly matched layer boundary conditions. The resulting matrix equation is evaluated with a state-of-the-art direct matrix solver. Comparisons with analytic 2D solutions indicate that the accuracy depends on the source receiver directivity combination. For example, the accuracy for horizontal and collinear sources and receivers (both at the surface) is about

four times better compared with configurations, where source and receiver directions are perpendicular to each other. Tests with different widths of the perfectly matched boundary layers showed that in most cases a width of 10 grid points is sufficient and that a width of 30 grid points covers all troublesome cases.

A comparison of my frequency-domain finite element modelling results with those from a well established finite difference time domain programme showed a very good match. These comparisons also offered an excellent opportunity to investigate the general efficiency of frequency and time-domain modelling. If the response for several source positions is required, which is a typical scenario during waveform inversions, the frequency-domain approach outperforms the time-domain code approach in terms of computing time. This advantage comes at the expense of a substantially higher memory consumption of the frequency-domain algorithm.

2D waveform modelling does not properly account for the 3D spreading of a point source. This can be partially corrected with 3D to 2D transformation or filtering methods, but these amplitude and phase corrections are not expected to work satisfactorily for shallow seismic data. To strike a balance between the impractical full 3D elastic approach and the problematic 2D approximation, I have implemented a 2.5D modelling algorithm. Here, a Fourier transformation of the 3D differential equations is performed with respect to the coordinate perpendicular to the model plane (y -direction). The resulting 2D differential equations include the resulting wavenumber k_y as a parameter. Choosing an appropriate suite of k_y wavenumbers, with which the inverse transformation to the space domain can be carried out accurately, is a non-trivial problem because the spectra show abrupt disruptions (even pole-like behaviour) at certain critical wavenumbers. For homogeneous and mildly heterogeneous models I propose an uneven sampling strategy based on Gauss-Legendre integration points in which the critical wavenumbers are avoided or skipped. For strongly heterogeneous models this approach is not applicable and an even sampling strategy must be employed because the critical wavenumbers are not known in advance, at least for the surface waves and Stoneley waves. Unfortunately, such an even sampling strategy proved to be numerically unstable, because some k_y wavenumbers may fall on or lie too close to the singularities in the k_y spectrum. The solution to this problem will require more research, perhaps by considering a complex frequency approach or using complex elastic moduli that introduce slight attenuation in the model, thus moving the singularities off the real wavenumber axis along which the inverse transform is applied.

Zusammenfassung

Die Auswertung an der Oberfläche aufgezeichneter flachseismischer Daten mittels herkömmlicher seismischer Methoden wie Reflektionsseismik, Refraktionstomographie und Verfahren zur Oberflächenwellenanalyse ist mit Problemen behaftet. Diese Methoden setzen die Identifizierung bestimmter Anteile des Wellenfeldes voraus, nämlich der Einsätze der reflektierten Raumwellen, der Einsätze der direkten und refraktierten Raumwellen beziehungsweise der Wellenzüge der dispergierten Oberflächenwellen. In flachseismischen Datensätzen treten diese Wellenfeldanteile nicht getrennt auf, sondern werden in sich überlappenden Zeitfenstern aufgezeichnet. Die Methode der Inversion vollständiger Wellenfelder kommt ohne die Identifizierung der einzelnen Anteile des Wellenfeldes aus und ist daher voraussichtlich optimal zur Analyse flachseismischer Daten. Der Idealfall wäre eine Wellenfeldinversion unter Annahme viskoelastischer seismischer Parameter dreidimensionaler heterogener Erdmodelle mit beliebiger Topographie. Ein solcher Ansatz ist gegenwärtig mit zu hohem numerischen Aufwand verbunden. Am weitesten verbreitet sind daher zur Zeit Ansätze, die auf einer akustischen Näherung und zweidimensionalen Modellen basieren.

Es ist abzusehen, daß die akustische Näherung im Fall flachseismischer Datensätze problematisch ist, da diese wesentliche Anteile von Oberflächenwellenenergie enthalten, welche mit einem akustischen Ansatz nicht modelliert werden können. Außerdem läßt die akustische Näherung die Scherwellenanteile und Modenkonversionen außer acht, die häufig in den Seismogrammen zu beobachten sind. Ich quantifiziere das Ausmaß der Unzulänglichkeit der akustischen Näherung mit Hilfe einer umfangreichen Analyse von Wellenfeldern und Wellenfeldsensitivitäten, sowohl im Zeit- als auch im Frequenzbereich, die auch die grundlegenden Unterschiede zwischen skalaren (Beschränkung auf Druckwellen) und vektoriellen (Einsatz gerichteter Quellen und Aufzeichnung sämtlicher Wellenfeldkomponenten) seismischen Daten vor Augen führt.

Die Untersuchung des Informationsgehalts flachseismischer Datensätze mittels der Eigenwertspektren der Hessischen Matrizen offenbart, daß die Kombination vertikal gerichteter Einzelkraftquellen mit der Aufzeichnung der Horizontalkomponente des Wellenfeldes den größten Vorteil bietet. Diese Wahl übertrifft die herkömmlich eingesetzte Kombination vertikaler Einzelkraftquellen mit der Aufzeichnung der Vertikalkomponente des Wellenfeldes in Bezug auf den Informationsgehalt. Die Studie des Informationsgehaltes zeigt auch, daß die Aufzeichnung des gesamten tensoriellen Wellenfeldes für sämtliche Kombinationen von Quell- und Empfängerrichtung wenig weiteren Informationsgewinn bringen würde. Für die Analyse vollständiger Seismogramme besteht kein Unterschied im Informationsgehalt von Wellenforminversionen im Zeit- oder Frequenzbereich. Soll der Datenraum der Inversion jedoch auf einzelne Zeitfenster beschränkt werden führt dies zu einem beträchtlichen Informationsverlust. Demgegenüber ist die Auswahl einiger

mit Bedacht ausgesuchter Frequenzen mit einem relativ geringen Verlust an Information verbunden.

Aufgrund der Unzulänglichkeit der akustischen Näherung habe ich ein Programm zur Modellierung elastischer Wellenausbreitung geschrieben, welches auf der Methode der finiten Elemente beruht. Das Programm basiert auf einem regulären Gitter rechteckiger Elemente und der Anwendung der Methode der „Perfectly Matched Layers“ (PMLs). Das sich aus diesem Ansatz ergebende Gleichungssystem wird unter Verwendung einer dem neuesten Stand der Technik entsprechenden Programmbibliothek gelöst. Vergleiche mit analytischen Lösungen in 2D weisen darauf hin, daß die Genauigkeit der Simulation von der Wahl der Kombination von Quell- und Empfängerrichtung abhängt. So ist beispielsweise die Berechnung der Horizontalkomponente in Quellrichtung für horizontal gerichtete Quellen (Quell- und Empfängerposition an der Oberfläche) etwa viermal genauer als die für Konfigurationen, bei denen Quelle und Empfänger senkrecht zueinander ausgerichtet sind. Versuche mit unterschiedlicher Breite der PMLs ergaben, daß in den meisten Fällen eine Breite von 10 Elementen ausreicht und eine Breite von 30 Elementen auch problematischere Fälle abdeckt.

Ein Vergleich meiner 2D Modellierungsergebnisse im Zeitbereich mit denen eines gängigen Finite-Differenzen Programms demonstrierte eine sehr gute Übereinstimmung. Diese Vergleichsrechnungen boten außerdem eine hervorragende Gelegenheit, die Effizienz von Modellierungen im Frequenz- und Zeitbereich zu ermitteln. Wenn Daten für mehrere Quellpositionen berechnet werden sollen, was im Zuge einer Wellenfeldinversion der Normalfall ist, ist die benötigte Rechenzeit für die Modellierung im Frequenzbereich geringer. Dieser Vorteil wird durch einen wesentlich größeren Speicherplatzbedarf des Frequenzbereichsalgorithmus erkauft.

Die Modellierung von Wellenfeldern in 2D trägt der dreidimensionalen (3D) Wellenausbreitung, ausgehend von einer Punktquelle, nicht ausreichend Rechnung. Mit Hilfe von Filtermethoden zur Transformation eines 2D in ein 3D Wellenfeld kann dies Näherungsweise korrigiert werden, im Fall von flachseismischen Datensätzen ist jedoch ein befriedigendes Ergebnis dieser Amplituden- und Phasenkorrekturen nicht zu erwarten. Als Mittelweg zwischen einer bisher nicht realisierbaren dreidimensionalen elastische Modellierung und dem problematischen zweidimensionalen Ansatz habe ich mich für einen Algorithmus in 2.5D entschieden. Dabei werden die elastischen Bewegungsgleichungen in 3D nach der Raumkoordinate senkrecht zur Modellierungsebene Fouriertransformiert, also in y -Richtung. Die sich ergebenden 2D Gleichungen enthalten die zugehörige Wellenzahl k_y als Parameter. Die geeignete Wahl einer Reihe von Werten für die Wellenzahl k_y , die eine fehlerfreie Rücktransformation in den Ortsbereich ermöglicht, ist keine einfache Aufgabe, da die Wellenzahlspektren für bestimmte kritische Wellenzahlen Unstetigkeitsstellen oder sogar Pole aufweisen. Für homogene oder nur leicht heterogene Erdmodelle schlage ich eine nicht gleichmäßige Auswahl von Wellenzahlen unter Auslassung der kritischen Wellenzahlen vor, die auf den Stützstellen der Gauß-Legendre-Quadratur beruht. Bei stark heterogenen Erdmodellen kann diese Auswahlmethode nicht angewandt werden, da die Lage der kritischen Wellenzahlen, zumindest für die Oberflächenwellen und Stoneleywellen, in diesem Fall nicht bekannt ist. Stattdessen muß auf eine äquidistante Wahl der Wellenzahlen zurückgegriffen werden. Unglücklicherweise ist der Algorithmus für äquidistante Stützstellen numerisch nicht mehr stabil, da einige Wellenzahlen auf oder zu nahe bei den Singularitäten des Wellenzahlspektrums zu liegen kommen können.

Die Lösung dieses Problems ist Gegenstand weiterführender Untersuchungen. Denkbar wären die Anwendung der Methode der komplexen Frequenzen oder die Einführung komplexer elastischer Parameter die zu einer leichten Dämpfung der Wellen führen würde, damit die Singularitäten der Wellenfeldspektren nicht mehr auf der Achse der reellen Wellenzahlen zu liegen kommen, entlang derer die Rücktransformation in den Ortsbereich ausgeführt wird.

Chapter 1

Introduction

1.1 Seismic methods: main areas of application

Seismic methods find wide application in many areas of earth and engineering science. The resolution and fidelity with which structure can be inferred from these methods exceeds that of most alternative geophysical techniques. In the present context 'structure' refers to the vertical and lateral distribution of elastic properties in the subsurface, although it is understood that seismic properties generally reflect geologic properties. Seismic methods can be employed on a variety of length/depth scales from the sub-metre range to thousands of kilometres. Some fields of application and the associated range of target sizes are given in Figure 1.1.

At the upper end of the scale, seismic waves are used for investigating the structure of the earth as a whole (e.g. Kennett and Bunge, 2008) and have yielded fundamental information on the constitution of the deep interior, such as the existence of a liquid outer core and a solid inner core of the earth. Also, the crustal and upper mantle structure of the earth can be effectively explored by means of seismic methods (e.g. Shearer, 2009). This has enabled seismologists to deduce models on local, regional and global scales that allow a better location of earthquakes and seismic risk assessment.

In the field of hydrocarbon exploration and development, the seismic technique is the main tool used to image the subsurface, delineate reservoirs and characterise their properties. (e.g. Claerbout, 1985; Sheriff and Geldart, 1985). The technique also finds important application in coal seam mapping (e.g. Buchanan and Jackson, 1986), mineral exploration (e.g. Eaton et al., 2003), natural hazard assessment (e.g. Butler, 2005; Knödel et al., 2007), hydro-geophysical delineation of aquifer geometry (e.g. Rubin and Hubbard, 2006; Kirsch, 2008), civil engineering site investigations for dams, tunnels and bridges (e.g. Stokoe, 2007) and materials testing (e.g. Appendix A of Rose, 2004). At the very low end of the distance scale, seismic/ultrasonic techniques provide a useful non-invasive means of finding cracks and other defects in structures like bridge decks and buildings.

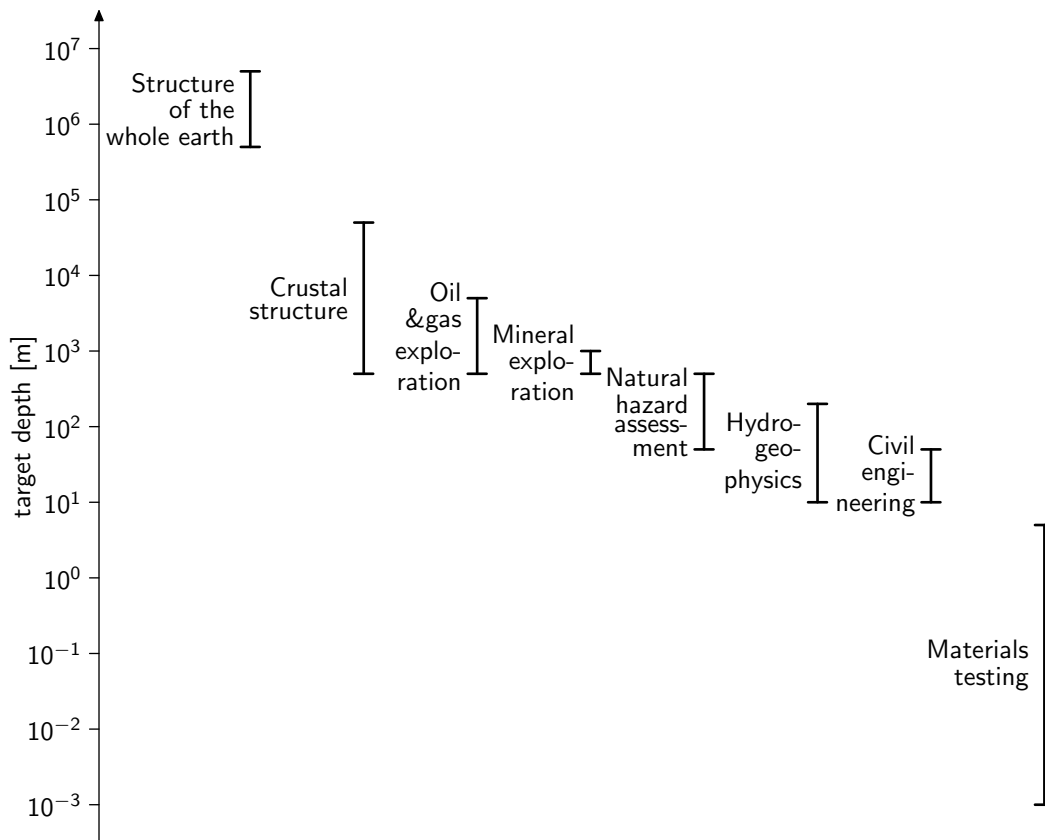


Figure 1.1: Length scales of targets in seismic exploration.

1.2 Seismic methods: model parameters and data types

1.2.1 Subsurface parameters

The subsurface model parameters that can be imaged by seismic methods are mostly linked to the propagation velocities of elastic waves. In the most general case, these propagation velocities are directionally dependent. Such an anisotropic elastic medium can be uniquely described by at most 21 elastic moduli at each spatial point, but for almost all practical applications a higher degree of symmetry is assumed. For transversely anisotropic media, for example, the number of independent elastic moduli reduces to five (see Thomsen, 1986). If the subsurface is isotropic, then the seismic velocities do not change with propagation direction and only three independent parameters have to be considered.

There are several possibilities to choose a set of elastic parameters. Either the wave velocities themselves, that is the compressional (or longitudinal) wave velocity v_P and the shear wave velocity v_S , together with the density ρ can be used, or the Lamé parameters λ and μ in combination with the density can be chosen. Alternatively, one may choose the shear modulus μ , the compressibility modulus κ and the density for describing the subsurface. The relations between these different parameter sets are given in Appendix E. Further possible parameter sets can be found, for example, in Smidt (2009).

Intrinsic attenuation (or seismic Q) is a further material property that may have to be taken into account. This can be achieved by replacing the real parameters, discussed above, by complex quantities. The resulting visco-elastic media properties (anisotropic or isotropic) are frequency dependent (Forbriger and Friederich, 2005).

To simplify the algorithms, an acoustic approximation can be employed. Here, the medium is treated like a fluid and only the compressional wave velocity v_p and the density ρ are used as parameters; the shear wave propagation velocity is assumed to be zero.

1.2.2 Observables

Geophones are routinely used to record land-seismic data on the earth's surface. They measure the ground particle velocity at the points where they are attached. For earthquake monitoring and structural testing sometimes accelerometers are used. They record ground acceleration instead of ground velocity. Compared with geophones, accelerometers typically record a broader range of frequencies, but their amplitude sensitivity is smaller. Therefore, they are most suitable for monitoring strong ground motions. Both geophones and accelerometers measure ground motion (velocity or acceleration, respectively) in a specific direction. When three linearly independent directions are recorded at an observation point, the 3D particle motion can be reconstructed.

In marine and borehole applications hydrophones are often employed to capture the pressure wave field. In contrast to the vectorial measurements with geophones and accelerometers, they record a scalar property. This can create difficulties in identifying shear waves.

Like the forward solver introduced later in my thesis, numerical modelling programmes often compute displacement fields. They can be easily converted to ground velocities and accelerations by computing single or double time derivatives in the time domain or by multiplications with $i2\pi f$ (or $-4\pi^2 f^2$) in the frequency domain, where f is the temporal frequency and i is the imaginary number.

1.3 Seismic methods: technology and information content

Seismic methods:
technology and information content

1.3.1 Seismic reflection

Seismic reflection surveying is the main geophysical imaging tool used in oil and gas exploration, but it is also employed in investigations of the structure of the Earth's crust as well as in mineral exploration (e.g. Yilmaz, 2000).

This method is based on the information contained in the reflected phases, visible in the seismograms. It offers good structural information about impedance contrasts in the subsurface, that is the locations of reflection horizons, but only very limited information on the elastic parameters of the individual units. Reflection seismology is routinely applied to elucidate structure in one, two and three dimensions. 3D high resolution seismics offers

the best results, but it entails an areal distribution of sources and sensors. Near-surface seismic imaging can be problematic since here the important reflected phases are often concealed by other phases, such as ground roll or guided waves (see section 1.4).

1.3.2 Seismic refraction

The seismic refraction method is a useful tool to map structures on a broad variety of scales, from tens of kilometres in the case of crustal studies (e.g. Guterch et al., 2003), to tens of metres in the case of environmental, groundwater and civil engineering investigations (e.g. Lanz et al., 1998), right down to the centimetre scale in the case of materials testing (e.g. Abraham and Dérobert, 2003).

Here, mostly the first arrival travel time data are extracted from the seismogram; the remaining information is neglected. The method offers limited information on the elastic parameters of the subsurface, mainly on the P -wave velocity v_P . If arrivals of the direct or refracted S -waves are visible in the data, also information about the shear wave velocity can be retrieved. This method is routinely applied for 1D and 2D problems and in a few cases also 3D investigations have been performed (e.g. Heincke et al., 2006).

The refraction method requires that the wave speed increases with depth in order to generate the critically refracted arrivals (head waves). Low velocity layers do not generate head waves and so they cannot be directly detected and imaged. Normally, only a few marker horizons can be delineated. Compared with the seismic reflection method, refraction analyses provide more information on gross velocity structure, but reflection technology outperforms refraction methods for imaging discontinuities, both in number and detail. Furthermore, the depth penetration of the refraction method is limited by the largest source/receiver offsets. This is illustrated in Figure 1.2, where results from a combined reflection/refraction experiment are shown.

1.3.3 Surface wave analysis

The surface wave method is used for global and regional scale problems to image the structure of the crust and mantle down to depths of about 1000 km. It is also applied to engineering scale problems for determining subsurface layering to depths of tens of metres (e.g. Socco and Strobbia, 2004). The method mainly exploits the dispersion characteristics of surface waves (Rayleigh and Love type), but full particle motion records are also sometimes used. Dispersion curves are extracted from the surface wave portion of the seismograms.

Surface waves are predominantly sensitive to variations of the shear wave velocities and, to a limited extent, to density variations. In contrast to the seismic reflection method, there is no requirement for abrupt changes of the seismic properties in the subsurface. Furthermore, low velocity zones can be resolved unlike with the refraction seismic method. The theory, on which the method is based, assumes a layered subsurface or continuous variation of velocity with depth and it is therefore inherently a 1D method. Pronounced 2D or 3D effects can thus severely distort the results. Pseudo 2D and 3D approaches are possible by inverting for 1D structures at different locations and correlating them among each other (Socco et al., 2009).

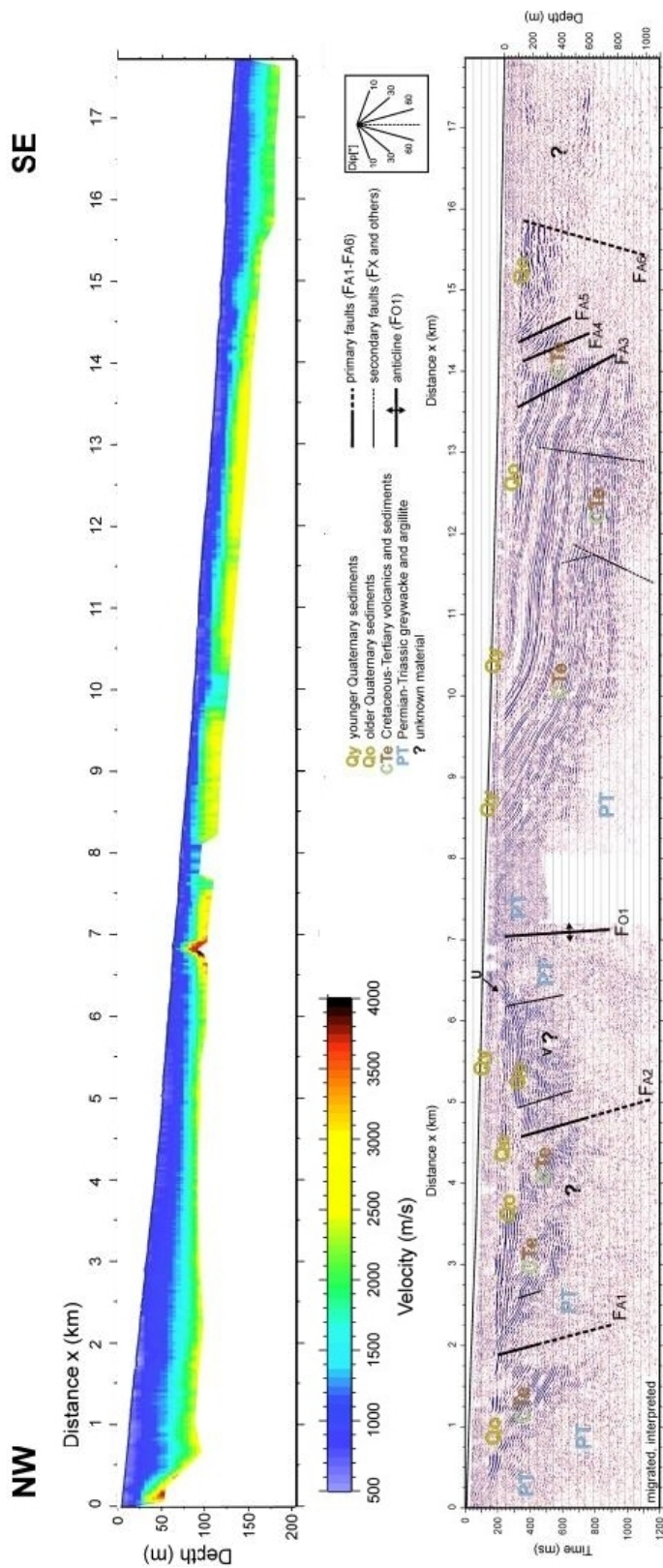


Figure 1.2: Comparison of refraction tomogram (top) and reflection section (bottom) based on the same seismic data set collected over active fault structures in New Zealand (modified after Dorn et al. (2009)). Note that the depth range of the reflection section is five times the depth range of the refraction tomogram. Only the well-resolved parts of the tomogram are shown.

1.3.4 Transmission travel time tomography

Seismic travel time tomography has been used for generating models of the velocity distribution in the earth's crust, mantle and core (see review in Romanowicz, 2003). The ray-based method has been improved by adding finite frequency information along wave paths (Marquering et al., 1999). On a smaller scale, it is also used in exploration geophysics (e.g. Lehmann, 2007, and references therein) and materials testing (e.g. Liu and Guo, 2005), often involving cross-well recording configurations.

The method is based on kinematic information and the data include the picked travel times of the direct body waves. Most studies only yield the distribution of the P -wave velocity v_P in a 2D approach, but also some information about the S -wave velocity can be extracted and extensions to 3D applications are possible. The smallest structures that can be resolved are of the size of the first Fresnel zone along the wave paths under consideration (Williamson and Worthington, 1993).

1.3.5 Passive methods

In recent years, passive seismic methods (also called seismic interferometry), which exploit ambient 'noise' sources, have been developed as a new means of probing the subsurface. The method is based on the reciprocity principle and involves the cross correlation of noise measurements observed at multiple stations for determining the Green's functions (or impulse responses) of the subsurface. A review of the method and its applications is given in Wapenaar et al. (2008). Limited information about the distribution of v_S can be retrieved and only gross structures can be resolved. Figure 1.3 shows example results for array measurements of ambient noise in valley structures in the Wallis area in Switzerland.

1.3.6 Full waveform inversion

Seismic full waveform inversion is a powerful technique that attempts to extract the 'complete' information of the recorded seismogram, both kinematic (travel times or phase) and dynamic (amplitudes or magnitude spectra). This makes it possible (at least theoretically) to resolve sub-wavelength features. An example of the improvements of acoustic waveform inversion compared with travel time transmission tomography is shown in Figure 1.4.

The migration method of seismic reflection processing (e.g. Claerbout, 1985) is related to full waveform inversions, but it stops short of an actual inversion. It is only capable of recovering the short wavelength variations in the velocity field, such as reflector positions and shape. Full waveform inversion seeks to recover, in addition, the long wavelength variations in the wave-speed distributions. In this way it retrieves information about the various seismic parameters throughout the subsurface. Due to the high computational costs and the significant non-linearity of the problem, most applications to date have been restricted to 1D and 2D models. Since developments related with full waveform inversions are a primary objective of my thesis, I will further discuss the current state-of-the-art of this method in section 1.5.

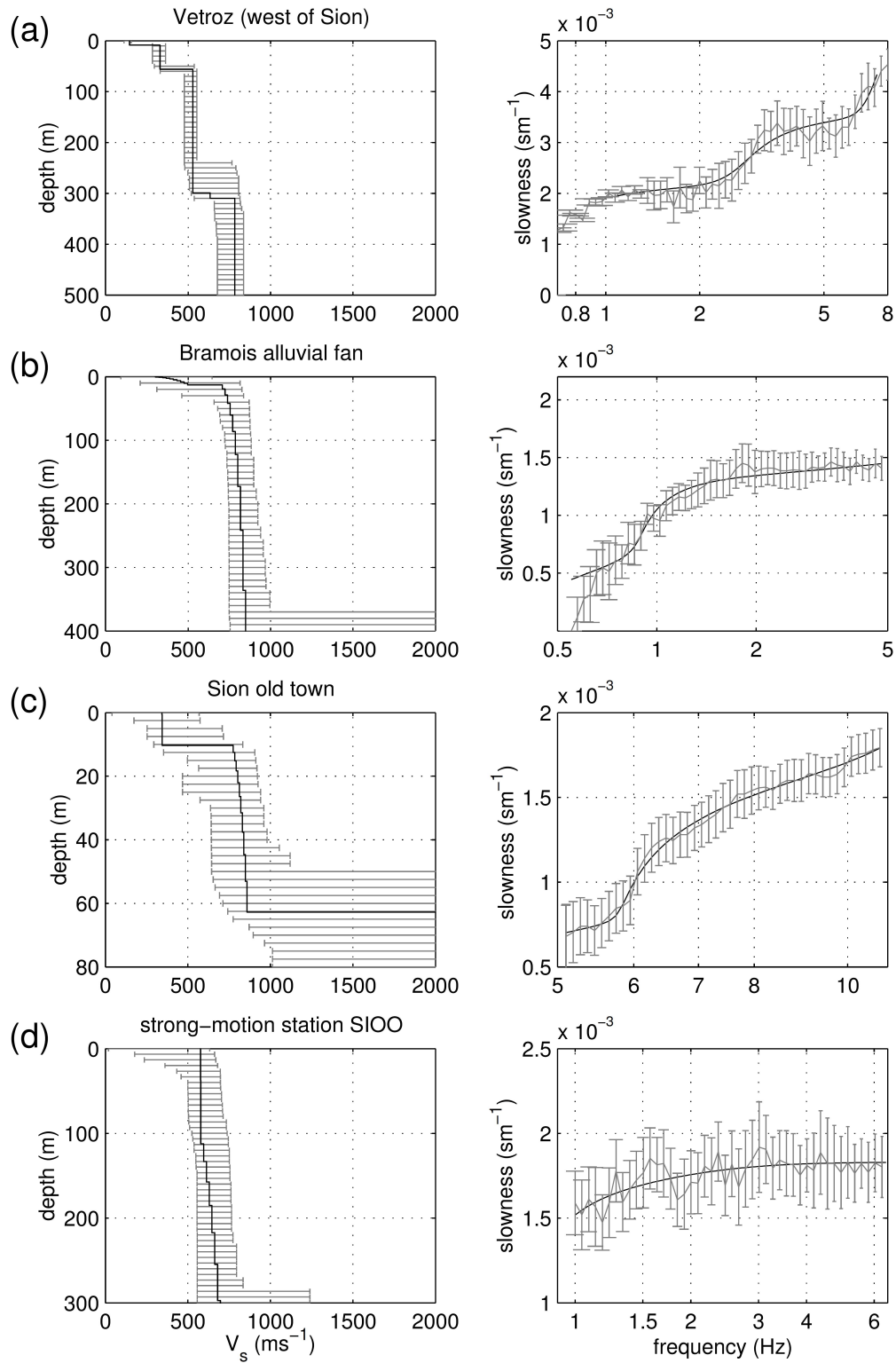


Figure 1.3: Inversion results obtained from array measurements of ambient noise in the Sion region. Right: measured dispersion curves with standard deviations (grey) and dispersion curves for the best-fitting velocity model (black). Left: Shear-wave velocities obtained from inversion. Error bars are showing the velocity range contained in models with acceptable misfit. Taken from Roten (2007).

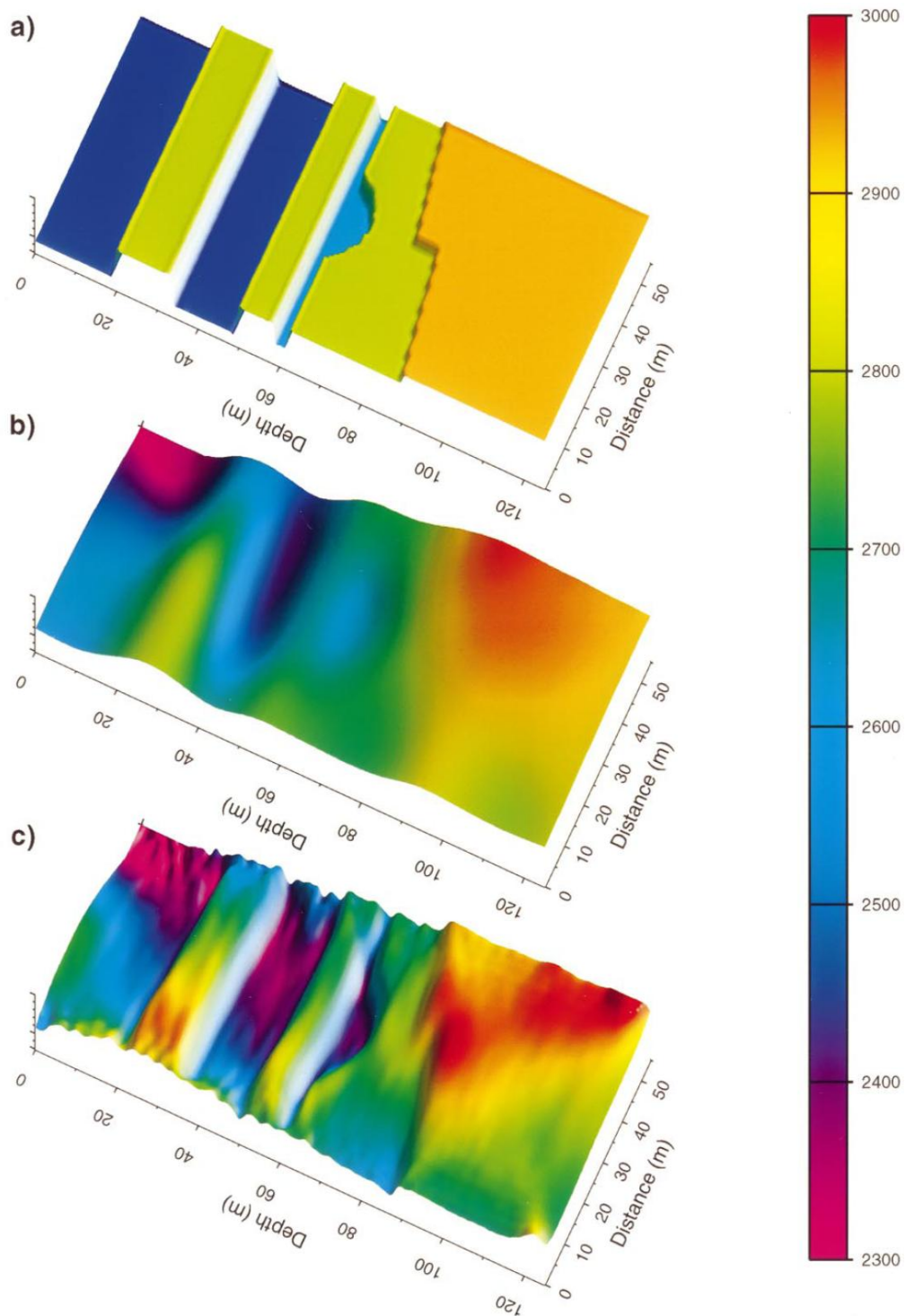


Figure 1.4: Comparison of travel time tomography and waveform inversion results for a scale model experiment simulating a borehole configuration using 51 evenly spaced sources in the left and 51 equally spaced receivers in the right borehole. (a) shows the true velocity model, (b) the travel time tomography result and (c) the waveform inversion result. Taken from Pratt (1999).

1.4 Specific problems of surface-based near-surface seismics

Shallow targets within the near-surface depth range (uppermost 50 to 100 metres) impose several difficulties for most seismic methods. The problem is illustrated in Figure 1.5, which shows observed and synthetic data related with a near-surface experiment. The individual methods, discussed in section 1.3, require the individual phases to be well separated. With the exception of the first breaks, employed for refraction seismics, the individual phases (reflections and surface waves) lie almost on top of each other (see the left and middle panels in Figure 1.5). The situation may be exacerbated by high amplitude guided waves, which may occur from reverberations associated with the weathering layer or the groundwater table (e.g. Roth and Holliger, 1999).

The synthetic data, shown in the right panel of Figure 1.5, were computed with an acoustic finite difference code and should mimic the observed shot gathers in Figure 1.5. The model parameters were estimated from crosshole seismic surveys (Liberty et al., 1999). Since the acoustically modelled data do not include surface waves and no shear waves and guided phases contaminate the shot gather, subtle reflection hyperbolas are visible. However, it is obvious that it will be virtually impossible to recover such low-amplitude reflections in the observed data, no matter what type of reflection processing is applied.

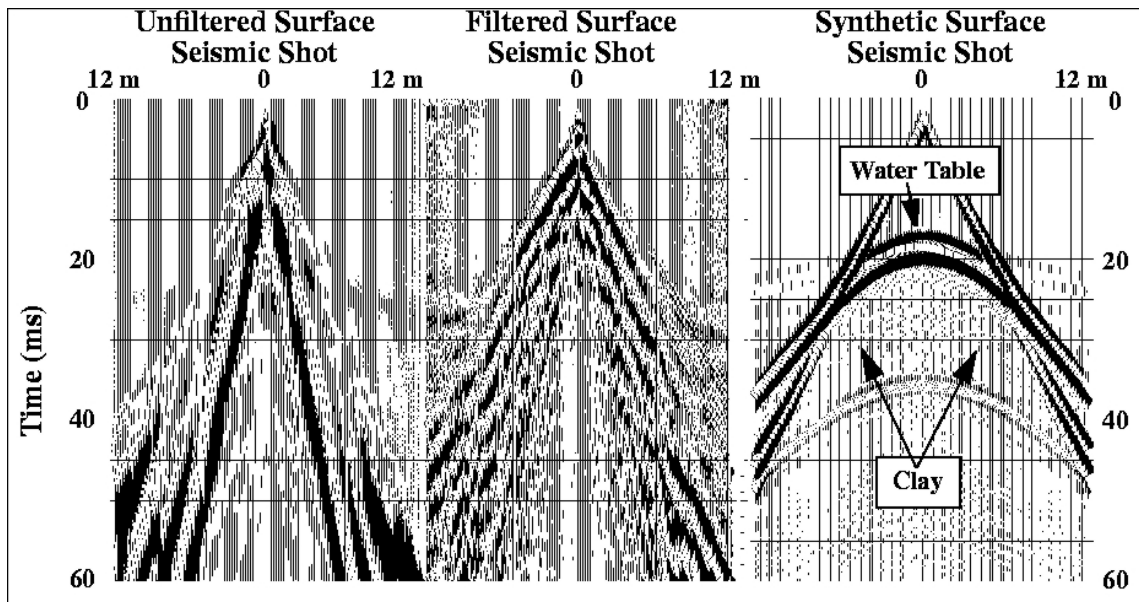


Figure 1.5: Data example from the Boise test site (Liberty et al., 1999) showing an unfiltered surface seismic shot (left), the same shot bandpass filtered (200-800 Hz) (middle) and an acoustic finite difference modelling result for velocities derived from cross-well, VSP and surface seismic surveys. Station spacing is 0.2 m, sample rate is 0.25 ms. 10 Hz geophones and a sledge hammer were used. Note the water table reflection at 17 ms and multiple at 34 ms (on the synthetic record). Also note the relatively low amplitude from the clay reflection that appears on the synthetic record and may also appear at offset in the filtered shot record.

The interference of the individual phases at near shot-receiver offsets would also affect a surface wave analysis, because the reflected phases may contaminate the dispersion curves. Consequently, only the refraction method is expected to provide reliable results. However, the information content provided by this method can be limited (see section 1.3.2).

Considering all these problems, it seems obvious that a full waveform inversion would be particularly useful for near-surface applications. Instead of separating first breaks, reflected phases and surface waves (i.e. throwing away information), full waveform inversions seek a subsurface structure that explains the entire wave field or at least significant parts thereof. A comparison of the synthetic shot gather and the actual data in Figure 1.5 also indicates that an acoustic approximation is likely to be inadequate.

1.5 State-of-the-art of seismic full waveform inversions

Seismic full waveform inversion is a subject currently attracting wide interest amongst the geophysical community, as evidenced by two recently published special issues on this topic in leading international journals viz. the November 2006 issue of *Geophysical Prospecting* and a supplement to the December 2009 issue of *Geophysics* (Plessix, 2008; Buske et al., 2009). The review paper by Virieux and Operto (2009) provides a concise overview of the progress made since the pioneering efforts of researchers like Albert Tarantola and Peter Mora, back in the mid 1980s (Tarantola, 1984; Mora, 1987), and the current state of the art in seismic full waveform inversion.

The first full waveform inversion algorithms were one-parameter inversions in the sense that only the P -wave velocity was inverted for using an acoustic approximation (Tarantola, 1984). Such types of inversions are still the most popular option. Interestingly, elastic inversions were already proposed in the 80's (Mora, 1987), but only recently have several researchers focused on this much more challenging problem (Gélis et al., 2007; Brossier et al., 2009).

The early waveform inversion attempts were performed in the time domain. Later, it was recognised that frequency domain inversions offer several benefits (Pratt, 1999; Zhou and Greenhalgh, 2003; Plessix, 2009; Brossier et al., 2009). The advantages are primarily in the computational efficiency. Today, both time- and frequency domain inversions are practised. They have undergone further development and there is quite some debate as to which of the two approaches is most advantageous (Virieux et al., 2009).

The two main ingredients of any full waveform inversion algorithm include a forward solver (numerical modelling) that predicts seismic data using a given subsurface model, and an inverse operator that estimates subsurface parameters using observed data. In the following, I will briefly outline the current state-of-the-art of numerical modelling and inversion of seismic data.

1.5.1 Numerical modelling

The simplest form of seismic modelling considers a homogeneous full space, for which analytic solutions exist (see Appendix C). In the presence of a free surface, there exist

semi-analytic solutions (Lamb, 1904; Johnson, 1974; Wang, 1999). For horizontally stratified media there also exist semi-analytical solutions that properly account for the 3D radiation characteristics of seismic waves (Takeuchi and Saito, 1972; Müller, 1985; Wang, 1999).

In forward solvers for laterally varying media several popular modelling approaches are employed, namely finite differences, pseudospectral methods, finite elements and spectral elements (Virieux, 1986; Danecek and Seriani, 2008; Marfurt, 1984; Min et al., 2003; Komatitsch and Tromp, 1999). Other options that are less often employed include boundary elements (e.g. Banerjee et al., 1986), integral equations (Kennett, 1985) and others (see Virieux and Operto, 2009, for examples). All of these methods have inherent advantages and disadvantages and are (at least conceptually) applicable in both the time and the frequency domain.

Finite difference techniques are easy to implement and computationally quite efficient. They are predominantly employed for time-domain modelling (Virieux, 1986; Robertsson et al., 1994; Bohlen, 2002), but there also finite difference frequency-domain codes suggested in the literature (e.g. Pratt, 1990; Operto et al., 2007). There exist 2D and 3D finite difference algorithms, some of which also consider anisotropy and anelastic effects (e.g. Robertsson et al., 1994; Igel et al., 1995). The main disadvantages of the finite difference method include the requirement of even spatial sampling and some difficulties in implementing a free surface, although this has been done successfully (e.g. Robertsson et al., 1996), albeit not for arbitrary topography.

Pseudospectral methods can be considered as a variant of finite differences, where the spatial derivatives are evaluated with Fourier transformation methods (Fornberg, 1998). Compared with finite differences, they require a less dense spatial sampling of the subsurface, which makes pseudospectral codes computationally more efficient.

Finite elements offer a more flexible and also a more physical approximation to wave propagation phenomena (e.g. Brenner and Scott, 2008; Zienkiewicz et al., 2005). Unstructured grids can be employed and it is very simple to include an arbitrary free surface topography. Compared with finite differences, implementation of finite element algorithms is generally more complicated. Time-domain finite element codes were presented by Zhang and Verschuur (2002) and frequency-domain algorithms were proposed, for example, by Min et al. (2003).

Spectral element methods have recently received a lot of attention in the seismological community (Komatitsch and Tromp, 2002a,b). They can be considered as a finite element variant, combined with the spectral method, where the elements can be larger and high order interpolants are used to represent the wave field such that numerical integration within the elements is carried out in a more sophisticated manner. This is expected to improve the accuracy of the results.

All of the methods discussed above have been implemented in two and three dimensions, but only the 2D versions are currently computationally tractable in the framework of full waveform inversions, where the forward problem needs to be solved many times. 3D acoustic inversions have started to emerge (e.g. Ben-Hadj-Ali et al., 2008), but 3D elastic inversions still exceed the capabilities of modern HPC computer clusters. Since many seismic data sets are collected along single profiles, 2D inversions seem to be a possible option. However, 2D modelling codes consider line sources that are infinitely extended perpendicular to the modelling domain, which does not mimic properly the 3D

radiation characteristics of actual seismic (point) sources. Therefore, so-called 2.5D-modelling attempts have been made, where a 3D source radiation and a 2D modelling domain are considered (e.g. Bleistein, 1986; Liner, 1991, 1995; Williamson and Pratt, 1995). Most of these attempts include very crude approximations. In particular, the elastic 2.5D frequency domain modelling problem has not yet been properly addressed. There are issues associated with wavenumber sampling and critical points in the wavenumber spectra (e.g. Zhou and Greenhalgh, 2006).

1.5.2 Inversion

Seismic waveform inversion is a highly non-linear problem that has to be solved either with iterative linearised methods or truly non-linear algorithms, such as global optimisers (Sen and Stoffa, 1995; Tarantola, 2005). Employing global optimisers such as genetic algorithms or simulated annealing (e.g. Sen and Stoffa, 1995) can aid in avoiding that the inversion gets ‘trapped’ in a local minimum of the objective function (instead of finding the true solution at the global minimum). Unfortunately, these global optimisers require a very large number of forward modelling computations to be carried out. This is currently prohibitive for realistic waveform inversion problems.

Most algorithms described in the literature consider a non-linear conjugate gradient approach, also referred as the back-propagated residual method. This is computationally quite efficient, but the convergence of the iterative procedure is somewhat slow. Therefore, Gauss-Newton or full Newton methods are occasionally considered. They have better convergence behaviour, but require more computer memory. More details on the different options are described in Pratt et al. (1998).

Conjugate gradients and Gauss-Newton or full Newton methods are so called directed search methods. They may find the solution in the model space quite efficiently, but there is a considerable likelihood that the iterative inversion procedure gets ‘trapped’ in a local minimum. Such local minima are a consequence of the non-linearity of the seismic waveform inversion problem.

Key elements of directed search methods are the so-called sensitivities or Fréchet derivatives. These are the partial derivatives of the individual data points with respect to the unknown subsurface model parameters. They are computed explicitly for Gauss-Newton and full Newton methods and considered implicitly in the conjugate gradient algorithms. Sensitivities are not only an integral part of directed search inversion algorithms, but they also provide very useful diagnostics for experimental design (Curtis, 2004). They are fully determined by the source/receiver geometry and the subsurface model, and do not depend on the actual observed data. Therefore, they can be employed prior to a seismic survey for identifying suitable experimental setups.

1.6 Thesis Objectives and Structure

In the preceding text I have outlined that (i) seismic full waveform inversions are a very powerful tool for imaging the subsurface, (ii) such an approach is particularly relevant and important for exploring the shallow subsurface and (iii) that remarkable progress has been made during the past years, but there exist still a number critical problems that need to be overcome. In this thesis I seek to answer two important questions, namely

- What is the information content of seismic waveform data and which portions of the seismic wave fields include the most significant subsurface information and
- how can appropriate elastic waveform data be modelled in an efficient manner?

In Chapter 2 I will address the first question by an extensive sensitivity analysis, in both the time domain and the frequency domain. In particular, I will examine and discuss the information content offered by the different source/receiver directionality configurations for a range of models.

An important conclusion of Chapter 2 is that the acoustic approximation is unsuitable for analysing surface-based shallow seismic data. Therefore, an efficient elastic forward solver needs to be determined. Based on arguments given in the section 1.5, I have chosen to implement an elastic frequency-domain finite element algorithm. In the first part of Chapter 3, I give an extensive description of the basic equations and some implementation details, such as the perfectly matched layer (PML) boundary conditions. The second part of Chapter 3 is devoted to a variety of tests, in which capabilities and limitations of my algorithm are evaluated. This part concludes with a comparison with a well established time domain finite difference code, which provides interesting insights with regard to general differences in efficiency between time-domain and frequency-domain modelling.

In Chapter 4, I will tackle the challenging 2.5D issue for elastic waves. I present wavenumber sampling strategies that are amenable for homogeneous and mildly heterogeneous full and half spaces. Then, I discuss a series of tests, where I investigate the influence of spatial sampling with the finite element mesh and the wavenumber sampling required to address the 2.5D problem.

The main results of my thesis are summarised and critically reviewed in Chapter 5. Furthermore, I will give a brief overview of research topics related to my thesis that are, in my view, particularly important and deserving of further investigation.

Chapter 2

2D sensitivity and information content analyses of seismic data

2.1 Introduction

Seismic waveform data include a wealth of information about the subsurface, far more than is contained in just the first arrival times or peak pulse amplitudes. This information can be exploited with appropriate inversion schemes. Such techniques were proposed more than 20 years ago (e.g. Tarantola, 1984; Mora, 1987), but only with the availability of powerful computer clusters in recent times have waveform inversions become feasible for realistic data sets. Remarkable progress has been made in the algorithmic developments (e.g. Plessix, 2008), but it has not yet been systematically studied which parts of the seismic waveforms are particularly useful and which combinations of source direction and receiver components should be used. In this chapter, I will make a first attempt to shed light on this issue, by systematically investigating waveform characteristics and associated measures that are involved in waveform inversion schemes.

Seismic waveform inversions typically involve very large data sets and many unknown model parameters. This makes the use of global inversion schemes such as genetic algorithms (e.g. Sen and Stoffa, 1995) impractical. Consequently, local minimisation search inversion algorithms need to be considered (e.g. Menke, 1989). There exist several options to formulate iterative schemes for such linearised inversion problems. Greenhalgh et al. (2006) give a good overview of these different algorithms and their interrelations.

In all of these algorithms, there is the need to define the partial derivative of the data with respect to the model parameters. If the forward algorithm is represented by the generally non-linear relation $\mathfrak{d} = \mathfrak{d}(\mathfrak{m})$, where $\mathfrak{d} \in \mathcal{D}$ is any data set contained in the selected data space and $\mathfrak{m} \in \mathcal{M}$ is a particular model within the model space, then the set of Fréchet derivatives \mathbf{J} can be defined such that

$$\mathfrak{d}(\mathfrak{m} + \delta\mathfrak{m}) = \mathfrak{d}(\mathfrak{m}) + \mathbf{J}\delta\mathfrak{m} + \mathcal{O}(\delta\mathfrak{m}^2) \quad (2.1)$$

is an acceptable approximation for small perturbations $\delta\mathfrak{m}$ to the model \mathfrak{m} . \mathbf{J} is also called the Jacobian matrix or sensitivity matrix and it is important to note that it depends on the location in the model space, \mathfrak{m} , around which the expansion (2.1) is performed. Equation (2.1) acknowledges the non-linear relationship between the data and the model

and merely implies that changes in the data caused by a perturbation $\delta \mathbf{m}$ are, in the close vicinity of \mathbf{m} , proportional to the sensitivities contained in \mathbf{J} .

A Gauss-Newton type inversion scheme without any data weighting and no additional constraints on the model parameters can be written as

$$\mathbf{m}^{k+1} = \left[\mathbf{J}^{kT} \mathbf{J}^k \right]^{-1} \mathbf{J}^{kT} [\mathbf{d}_0 - \mathbf{d}(\mathbf{m}^k) + \mathbf{J}^k \mathbf{m}^k], \quad (2.2)$$

where k is the iteration index, $\mathbf{J}^k = \frac{\partial \mathbf{d}}{\partial \mathbf{m}}|_{\mathbf{m}^k}$ is the sensitivity computed for the current model \mathbf{m}^k and the vector \mathbf{d}_0 contains the observed data. Usually, the so-called *approximate Hessian* matrix $\mathbf{J}^T \mathbf{J}$ (see Pratt et al., 1998, for the reason for this term) is singular or close to singular and thus not invertible, such that (2.2) cannot be used. To overcome this problem, regularisation in the form of constraints has to be added. The simplest option is a damped inversion (Levenberg, 1944; Marquardt, 1963), where $\left[\mathbf{J}^{kT} \mathbf{J}^k \right]^{-1}$ is replaced by $\left[\mathbf{J}^{kT} \mathbf{J}^k + \lambda \mathbf{I} \right]^{-1}$. Here, λ is called the *damping parameter* and \mathbf{I} is the identity (unit) matrix. More general constraints (for example a combination of damping and smoothing) can be applied via a model weighting operator $\hat{\mathbf{W}}_M$, replacing $\mathbf{J}^{kT} \mathbf{J}^k$ by $\left[\mathbf{J}^{kT} \mathbf{J}^k + \lambda \hat{\mathbf{W}}_M \right]^{-1}$.

A further modification of equation (2.2) is necessary if one wants to weight the individual data points in accordance with their reliability or importance. For example, one might want to enhance the influence of the body wave arrivals with respect to the surface wave portion of the data. Otherwise the latter would have a much higher influence on the solution due to their larger relative amplitudes. For that purpose a *data weighting operator* $\hat{\mathbf{W}}_D$ is introduced and $\mathbf{J}^{kT} \mathbf{J}^k$ is replaced by $\left[\mathbf{J}^{kT} \hat{\mathbf{W}}_D \mathbf{J}^k + \lambda \hat{\mathbf{W}}_M \right]^{-1}$ in equation (2.2). This leads to the update equation

$$\mathbf{m}^{k+1} = \left[\mathbf{J}^{kT} \hat{\mathbf{W}}_D \mathbf{J}^k + \lambda \hat{\mathbf{W}}_M \right]^{-1} \mathbf{J}^{kT} \hat{\mathbf{W}}_D [\mathbf{d}_0 - \mathbf{d}(\mathbf{m}^k) + \mathbf{J}^k \mathbf{m}^k], \quad (2.3)$$

which is derived and discussed in more detail in Appendix D and repeated there as equation (D.5b).

Equation (2.3) indicates that the quantities influencing the inversion process are the data residuals, $(\mathbf{d}_0 - \mathbf{d}(\mathbf{m}))$, the sensitivities contained in \mathbf{J} , the data weighting matrix $\hat{\mathbf{W}}_D$, and the regularisation constraints supplied by the parameters $\hat{\mathbf{W}}_M$ and λ .

In this chapter, I will focus on the data-related constraints in equation 2.3. Initially, I will investigate the model response $\mathbf{d}(\mathbf{m})$ for a number of possible scenarios (i) in the light of the acoustic and elastic approximations of the wave equation, and/or (ii) in the absence and presence of a traction-free surface, (iii) as a function of different source and receiver type and directionality and (iv) in the presence of model inhomogeneities. The increasing complexity of the wave fields when moving from (i) to (iv) will be illustrated in both the time domain and the frequency domain.

As the next step, I will show the ramifications of factors (i) to (iv) on the waveform sensitivities contained in the Jacobian matrix \mathbf{J} . Finally, the data information content offered by different experimental setups will be investigated by means of an eigenvalue analysis of the approximate Hessian matrix $\mathbf{J}^T \mathbf{J}$.

All simulations are only performed in 2D for reasons of simplicity and computational tractability. Nevertheless, it allows me to study some of the most important effects. At some future point it would be highly desirable to extend the investigation into 2.5D or even full 3D models.

2.1.1 Experimental setup

Subsurface models

In this chapter I consider four very simple two-dimensional models. Table 2.1 introduces abbreviated names, elastic parameters and other important quantities used for these models. My goal is to approximate realistic scenarios, as observed in many near-surface investigations (e.g. Knödel et al., 2007).

FH is a homogeneous full space model with elastic parameters typical for clay material.

HH is a homogeneous half space model, which has the same elastic parameters as *FH*.

HG is a model exhibiting a slight vertical gradient in all the elastic parameters. It may represent a layer of sand compressed under its own weight.

HL is a model comprising a layer of the same elastic parameters as *FH* and *HH*, overlying a high-velocity half space (e.g. resembling limestone).

	homogeneous models		gradient model	layer over half space
	<i>FH</i>	<i>HH</i>	<i>HG</i>	<i>HL</i>
$\min(v_S)[\text{m/s}]$	1000	1000	600	1000
$\max(v_P)[\text{m/s}]$	2000	2000	2500	3000
$f_c[\text{Hz}]$	500	500	500	500
$dh[\text{m}]$	0.1	0.1	0.05	0.1
N	10	10	12	10
$dt[\mu\text{s}]$	25	25	10	10
$n_x \times n_z$	600×480	600×250	1200×520	600×300
$d_x \times d_z[\text{m}]$	60×48	60×25	60×26	60×30
	acoustic modelling using FEM elastic modelling using FDTD		only elastic FDTD modelling	

Table 2.1: Model parameters of the four models considered in this study, where v_P and v_S are the seismic velocities, f_c is the approximate centre frequency of the source wavelet, $N = \frac{\min(v_S)}{f_{\max} \cdot dh}$ is the number of grid points per minimum wavelength. The quantity dh is the grid step for forward calculations, dt is the time step used, n_x and n_z denote the numbers of grid points in the horizontal and vertical directions and d_x and d_z are the vertical and horizontal model size (including the absorbing boundaries).

The model parameters, seismic velocities v_S and v_P as well as density ρ , are only a function of depth; their values are depicted in Figure 2.1 for the models having a free surface.

Forward modelling

Time-domain finite difference modelling For most of the modelling described in this chapter, a 2D elastic version of the code presented by Bohlen (2002) is used. This is a finite difference time domain (FDTD) algorithm using a second-order centred difference scheme in time and a fourth-order centred difference scheme (on a standard staggered grid) in the spatial domain. The layout of the 2D standard staggered grid employed can be found in Bohlen and Saenger (2006, Figure 1a).

To avoid numeric (grid) dispersion in the presence of a free surface, the grid spacing dh must be chosen such that an appropriate number of grid points per minimum wavelength, $N = \frac{\min(v_S)}{f_{\max} \cdot dh}$, is guaranteed. Here, the quantity v_S represents the shear wave velocity and f_{\max} is the highest frequency for which significant signal energy is present. Bohlen and Saenger (2006) suggest appropriate values for N . For $f_c = 500$ Hz and a receiver at a distance of 60 m from the source, or 40 times the Rayleigh wavelength away from the source, they get reasonable accuracy by using a value of $N = 9$ in combination with an explicit boundary condition at the free surface (image method). For a rotated staggered grid, Levander (1988) claims $N = 5$ to be sufficient.

The largest source-to-receiver distance that I model is 8 m; this is at most seven times the dominant Rayleigh wavelength. Hence no significant numeric dispersion is expected when using values of $N \geq 10$, as given in Table 2.1.

An appropriate choice of the time stepping interval dt is even more critical for the type of study I present here than the choice of the spatial sampling dh . The 2D version of the dimensionality-dependent stability criterion suggested by Bohlen (2002) is

$$dt \leq \frac{6}{7} \frac{dh}{\sqrt{2} \cdot \max(v_P)}. \quad (2.4)$$

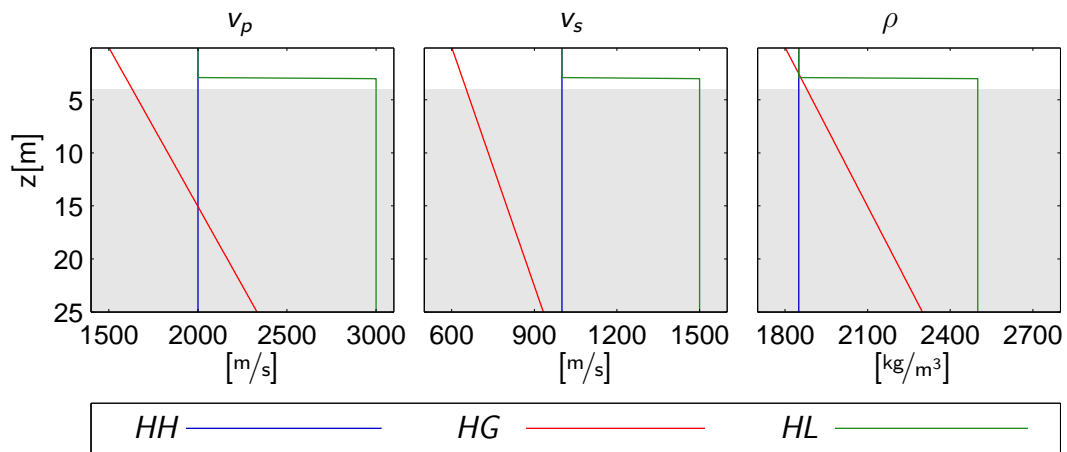


Figure 2.1: Model parameters used for HH , HG and HL . The parameters for FH assume the same constant values as those for HH . The grey area denotes the depth range not considered in the sensitivity computations.

As can be seen in Table 2.1, even smaller time steps dt are chosen, because numerical stability is very important for the brute force perturbation approach used for computing sensitivities (see section 2.1.2).

At the left, right and bottom edges of the models, absorbing zones of width 20 m are applied (see Figure 2.3); for the model *FH*, representing an unbounded domain (full space), an additional absorbing zone is placed at the top edge. The widths of the absorbing boundary zones used are ten to twenty times larger than suggested by Cerjan et al. (1985), where the absorbing frame used in this code is described. Tests showed that such very thick boundary layers are necessary to suppress to a sufficient level the spurious reflections from the computational boundaries.

Finite element modelling in the frequency domain To judge the validity of the acoustic approximation for modelling elastic wave propagation, an acoustic finite element (FEM) code (modified after Zhou and Greenhalgh, 1998a,c) was employed. It operates in the frequency domain. The governing Helmholtz equation is solved on a structured grid with linear elements of quadratic shape (a similar FEM code to solve the elastic wave equation will be described in more detail in Chapters 3 and 4).

Element size and model parameters were chosen to be identical to the ones given in Table 2.1 for the FDTD simulations. However, the width of the absorbing boundary zones could be reduced to ten metres, because a perfectly matched layer (PML) approach (Heikkola et al., 2003) rather than simple absorbing zones was used in this case to suppress boundary reflections.

To analyse differences between acoustic and elastic simulations, frequency responses across the entire bandwidth of the source wavelet need to be computed. To compare the displacements generated by the acoustic code with the particle velocities produced by the elastic FDTD code, a multiplication of the acoustic results in the frequency domain by $i\omega = i2\pi f$ is necessary. This is the frequency-domain equivalent of differentiation. After a further multiplication with the source spectrum, an inverse Fourier transform is applied, which allows a direct comparison of the acoustic and elastic wave fields in the time domain. Vice versa, a Fourier transform of the FDTD results allows a direct comparison in the frequency domain, again after multiplying the FEM solution by both $i\omega$ and the source spectrum.

Source characteristics and recording geometry

Source wavelet The stability criterion introduced in equation (2.4) dictates the need for a very fine grid in the case that the source wavelet includes significant energy at high frequencies. Therefore, a source wavelet with a rather narrow frequency bandwidth is employed to keep the number of grid points needed to a reasonable limit.

One possible wavelet with a frequency spectrum decaying rapidly for higher frequencies is

$$s(\tau) = (1 - 4\tau^2) e^{-2\tau^2} \quad \text{with} \quad \tau = \frac{2f_c\pi}{3} \left(t - \frac{3}{2f_c} \right), \quad (2.5)$$

where f_c is the approximate centre frequency. Using a rule of thumb, the maximal frequency is $f_{\max} \approx 2f_c$. The function $s(t)$ in (2.5) is similar to the *Ricker wavelet* (Hosken, 1988) and is implemented as a standard source time function in the FDTD

forward solver that is used. The signal is shifted in time to ensure $s(t) \equiv 0$ for $t \leq 0$. A plot of (2.5) and the corresponding amplitude spectrum are shown in Figure 2.2.

Source types and wave field components An overview of the source types and recorded wave field components considered in this study is given in Table 2.2, along with the abbreviations that are used in the rest of this chapter and the symbols representing the source and receiver locations in the wave-field and waveform-sensitivity snapshot plots that will be shown in sections 2.2 and 2.3.

The combination of an omni-directional explosive source and recording of the scalar pressure field — called *ep* after Table 2.2 — allows a comparison of the elastic wave fields and the elastic sensitivities with respect to v_P to their corresponding acoustic equivalents.

Employing an explosion type or a vertically-directed single force source and using vertical component geophones — *ez* respective *zz* — is what is mostly used in actual

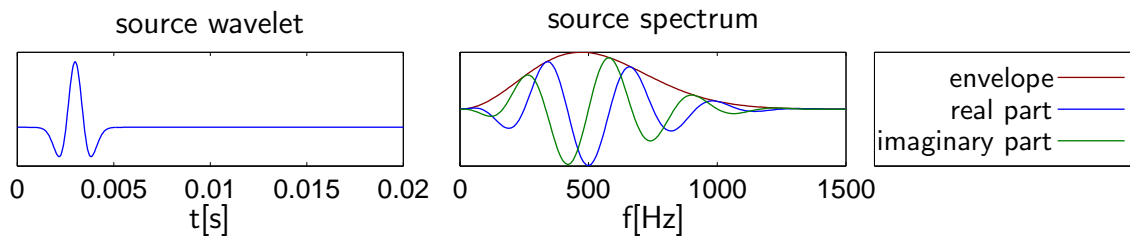


Figure 2.2: The left panel shows the source wavelet, given in equation (2.5), with an approximate centre frequency of $f_c = 500$ Hz that was used for all time-domain simulations, while the right panel depicts the envelope, real and imaginary parts of its spectrum; all frequency-domain simulation results are multiplied by this spectrum.

source types			recorded field components		
	<i>e</i>	explosive source		<i>p</i>	pressure field
	<i>x</i>	single force in x-direction		<i>x</i>	x-component of particle velocity field
	<i>z</i>	single force in z-direction		<i>z</i>	z-component of particle velocity field

Table 2.2: Overview of source types and recorded wave field components considered as well as abbreviations and plotting symbols used for them throughout the chapter. In figures showing source/receiver geometry (e.g. Figure 2.3), sources are shown as red stars and receivers as blue triangles.

surface land seismic field surveying.

The remaining combinations of source type and recorded components involve the traditional sources (explosives and vertically directed) — ex and zx —, and a shear wave source (horizontally directed) — xz and xx ; the combinations with receivers recording the horizontal wave field component are simulated to get the 2D (bi-axial) equivalent of using multi-component (tri-axial) geophones. Typically, in actual field surveys a y -directed source would be employed and the y -component of the wave field recorded (SH case). Due to the 2D approach I instead consider an x -directed source.

Experimental setup The placement of the sources and receivers for the different models is shown in Figure 2.3.

Model FH is only used for comparing elastic and acoustic wave propagation and the corresponding sensitivities. Therefore, only data for one receiver placed at a distance of 8 m from the source are computed.

To be able to perform a meaningful data information content analysis for the models incorporating a free surface, namely HH , HG and HL , several shot positions and source/receiver distances are required. I employ one source, located in the middle of an array of 16 receivers, placed at evenly spaced horizontal distances of one to eight metres from the source. Since the model parameters only vary with depth, this enables me to simulate a data set involving nine different source positions with eight receivers each (see section 2.4.1).

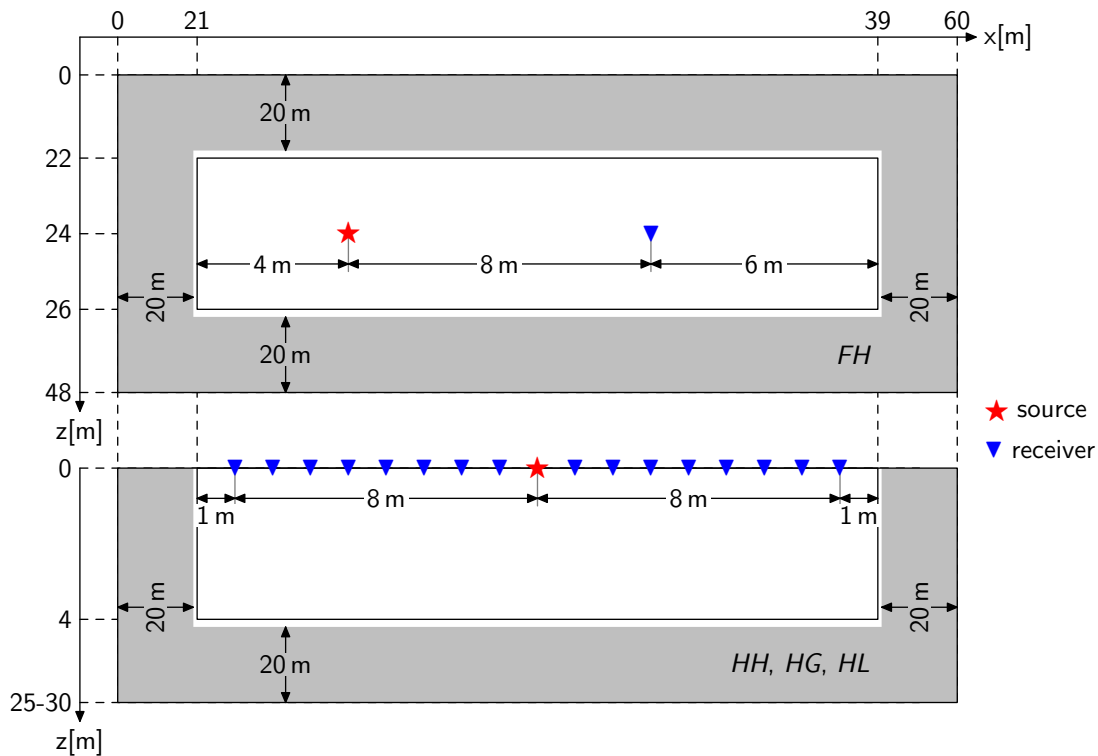


Figure 2.3: Sketch of the source and receiver positions used for (a) model FH and (b) the half-space models HH , HG and HL . The absorbing boundaries are shaded in grey. Note that they are displayed at a smaller scale.

Data space and model space

The sensitivity matrix \mathbf{J} introduced in equation (2.1) is a linear operator mapping a model space \mathcal{M} to a data space \mathcal{D} . So far, they have been considered as general normed linear spaces, but for the numerical analyses, they need to be properly defined. The following definitions are somewhat technical and lengthy but the notation that is introduced here will be used throughout the rest of this chapter.

Model space The model vectors $\mathbf{m} \in \mathcal{M}$ are column vectors containing the parameter values of the model, discretised for inversion. The area of interest is divided into 1800 *inversion cells* of 20 cm edge length numbered in row major order. The location of these 18 m \times 4 m sub-volumes in the forward grid can be seen in Figure 2.3, outlined by the black frames, and a sketch of the inversion cells is provided in Figure 2.4. No anelastic damping is introduced and the density is kept fixed.

In the acoustic case, I define

$$\begin{aligned} \mathbf{m} &= \mathbf{m}^P \\ &= [m_1^P, m_2^P, \dots, m_{n_c}^P]^T, \end{aligned} \quad (2.6)$$

where \mathbf{m}^P is the parameter vector containing only the P -wave velocities and $m_{i_c}^P = v_P(\mathbf{r}_{i_c})$ is the P -wave velocity at point $\mathbf{r}_{i_c} = (x_{i_c}, z_{i_c})$, the midpoint of the inversion cell with index i_c , running from one to the total number of inversion cells, $n_c = 1800$.

In the elastic case, also shear wave velocities are taken into account and I define

$$\begin{aligned} \mathbf{m} &= \begin{bmatrix} \mathbf{m}^P \\ \mathbf{m}^S \end{bmatrix} \\ &= \begin{bmatrix} [m_1^P, m_2^P, \dots, m_{n_c}^P]^T \\ [m_1^S, m_2^S, \dots, m_{n_c}^S]^T \end{bmatrix}, \end{aligned} \quad (2.7)$$

where \mathbf{m}^S , the parameter vector containing only the S -wave velocities, was added and $m_{i_c}^S = v_S(\mathbf{r}_{i_c})$ is the S -wave velocity, again taken at the midpoint of each inversion cell i_c .

In more general form, the model vector \mathbf{m} can be written as

$$\mathbf{m} = [m_1, m_2, \dots, m_{n_M}]^T, \quad (2.8)$$

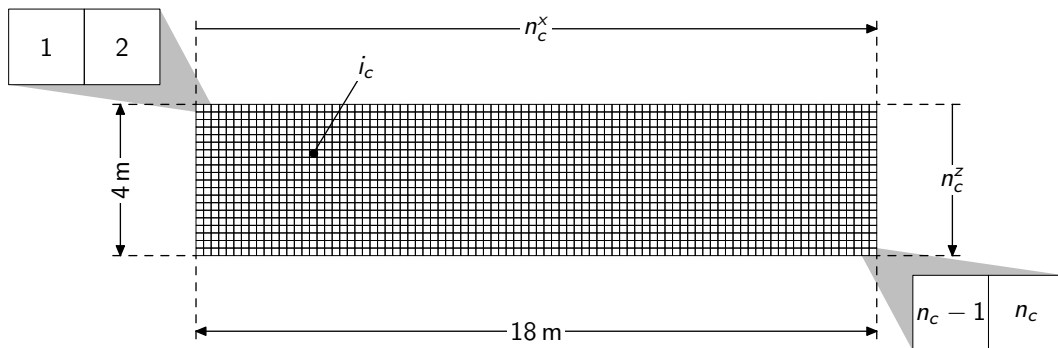


Figure 2.4: Sketch of the model parameter indexing scheme in row major order.

where $n_M = n_p \cdot n_c$ is the total number of model parameters and n_p is the number of parameter sets, that is $n_p = 1$ in the acoustic and $n_p = 2$ in the elastic case.

Data space The data vectors $\mathfrak{d} \in \mathcal{D}$ are divided into sub-vectors containing all time samples (or frequency samples) of the wave field for one specific source/receiver pair l , one source type $i \in \{e, x, z\}$ and one recorded component $j \in \{p, x, z\}$ (See Table 2.2 for an overview of the shorthand notation for sources and receivers). The index $l \in [1, n_{rs}]$ specifies source location \mathfrak{x}_l^s and receiver location \mathfrak{x}_l^r of source/receiver pair l ; n_{rs} is the total number of pairs. Like this, one sub-vector reads

$$\mathfrak{d}^{l,(ij)} = [d^{l,(ij)}(t_1), \dots, d^{l,(ij)}(t_{i_s}), \dots, d^{l,(ij)}(t_{n_s})]^T \quad \text{in the time domain}$$

and

$$\mathfrak{d}^{l,(ij)} = [d^{l,(ij)}(f_1), \dots, d^{l,(ij)}(f_{i_s}), \dots, d^{l,(ij)}(f_{n_s})]^T \quad \text{in the frequency domain,}$$

where t_{i_s} and f_{i_s} are the times and frequencies of the data samples, respectively, and n_s is the total number of samples in the partial data set for pair l and configuration (ij) . To simplify the notation, one can write

$$\begin{aligned} \mathfrak{d}^{l,(ij)} &=: \mathfrak{d}^L \\ &= [d_1^L, \dots, d_{i_s}^L, \dots, d_{n_s}^L]^T \end{aligned} \quad (2.9)$$

abstractly for both domains and introduce super index $L = l, (ij)$ combining the indices for source/receiver pair l and configuration (ij) . Then, the complete data vector is of the form

$$\mathfrak{d} = \begin{bmatrix} \mathfrak{d}^1 \\ \vdots \\ \mathfrak{d}^L \\ \vdots \\ \mathfrak{d}^{n_d} \end{bmatrix} = \begin{bmatrix} [d_1^1, \dots, d_{i_s}^1, \dots, d_{n_s}^1]^T \\ \vdots \\ [d_1^L, \dots, d_{i_s}^L, \dots, d_{n_s}^L]^T \\ \vdots \\ [d_1^{n_d}, \dots, d_{i_s}^{n_d}, \dots, d_{n_s}^{n_d}]^T \end{bmatrix}, \quad (2.10)$$

which contains in total $n_d = \sum_{l=1}^{n_{rs}} n^l$ sub-vectors, if n^l is the number of different combinations of source type and field component recorded for pair l .

This means that the model space is of dimension $n_M = 1800$ in the acoustic case and $n_M = 3600$ in the elastic case, the data space is of dimension $n_D = n_d \cdot n_s$ and the operator \mathbf{J} , defined in (2.1), is a matrix of size $n_D \times n_M$.

Norms To be able to establish an objective function (or cost function) to be minimised for an inversion, it is necessary to measure the distance $\mathfrak{d}_0 - \mathfrak{d}(\mathfrak{m})$ between an observed data set and a synthetic data set computed from model \mathfrak{m} . In other words, a norm in the data space \mathcal{D} has to be defined. To retain all flexibility of choosing subsets of data sets and samples, the definition

$$\|\mathfrak{d}\|_D := \mathfrak{d}^T \underbrace{\mathbf{W}_D^T \mathbf{W}_D}_{\hat{\mathbf{W}}_D} \mathfrak{d} \quad (2.11)$$

is used. \mathbf{W}_D and $\hat{\mathbf{W}}_D$ are $n_D \times n_D$ sized matrices for data weighting and selection; I will only use them for data selection. That is, the diagonal elements of \mathbf{W}_D are either 1 or 0.

Similarly, if the inversion is to be regularised by constraining the solution to a preferred model with certain properties, it is necessary to define a norm in model space \mathcal{M} ,

$$\|\mathbf{m}\|_M := \mathbf{m}^T \underbrace{\mathbf{W}_M^T \mathbf{W}_M}_{\hat{\mathbf{W}}_M} \mathbf{m}, \quad (2.12)$$

by choosing $\mathbf{W}_M \in \mathbb{R}^{n_M \times n_M}$ such that $\|\mathbf{m}\|_M$ is the smaller, the more that \mathbf{m} exhibits the desired properties. Since this study is principally aimed at the à priori question of optimal experimental design independent of any particular model, I use $\hat{\mathbf{W}}_M \equiv \mathbf{I}$.

Based upon these choices of norms, the update equation 2.3 can be derived — see appendix D.

2.1.2 Sensitivity computation

Brute force approach

As introduced in equation (2.1), the sensitivities are partial derivatives of the data with respect to the model parameters around a given model \mathbf{m}^k ,

$$\mathbf{J}^k = \left. \frac{\partial \mathbf{d}}{\partial \mathbf{m}} \right|_{\mathbf{m}^k}. \quad (2.13)$$

A simple option to approximate these partial derivatives numerically is to write them as a differential quotient. Using index notation, one obtains

$$\begin{aligned} J_{ij}^k &= \left. \frac{\partial d_i}{\partial m_j} \right|_{\mathbf{m}^k} \\ &= \lim_{h \rightarrow 0} \frac{d_i(\mathbf{m}^k + h \hat{\mathbf{m}}_j) - d_i(\mathbf{m}^k)}{h}, \end{aligned} \quad (2.14)$$

where $\hat{\mathbf{m}}_j$ is a unit vector in model space, i.e. $(\hat{\mathbf{m}}_j)_i = \delta_{ij}$.

Approximating this by a difference quotient leads to

$$J_{ij}^k \approx \frac{d_i(\mathbf{m}^k + h \hat{\mathbf{m}}_j) - d_i(\mathbf{m}^k)}{h} \quad (2.15)$$

for small h . Reformulating this to

$$J_{ij}^k \approx \frac{d_i((1 + h \hat{\mathbf{m}}_j) \mathbf{m}^k) - d_i(\mathbf{m}^k)}{h |m_j^k|}, \quad (2.16)$$

allows any forward solver to be used for computing sensitivities. For this, we need one forward calculation providing the seismograms $\mathbf{d}^L(\mathbf{m}^k)$ for the unperturbed background model and n_M additional forward calculations to compute the perturbation seismograms $\mathbf{d}^L((1 + h \hat{\mathbf{m}}_j) \mathbf{m}^k)$ for each of the sub-vectors introduced in equation (2.9); the super index L denotes the source/receiver pair l and the source/receiver type ij with $i \in$

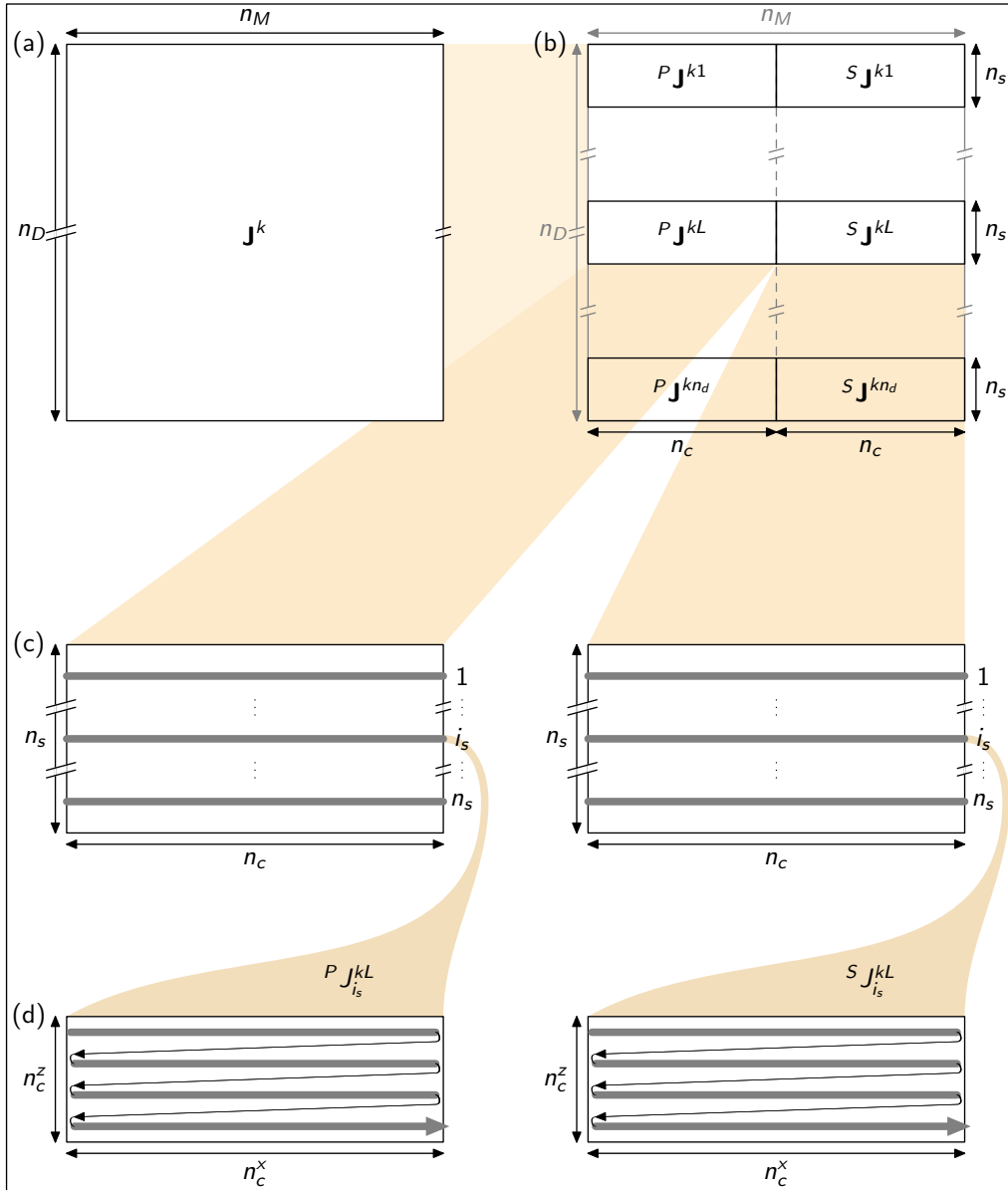


Figure 2.5: Structure of \mathbf{J}^k and extraction of the model cross sections for P- and S-wave sensitivities for the time/frequency sample i_s . (a) depicts the complete Jacobian, (b) how it decomposes into the parts for the different parameters and data sets, (c) how these parts themselves are made up of rows, each containing the sensitivities for one particular time or frequency sample i_s and (d) how these rows form the cross sections for this sample.

$\{e, x, z\}$ and $j \in \{p, x, z\}$ (see Table 2.2 for the abbreviations). For the elastic case this results in 3601 forward calculations for each source type. In Figure 2.5 a schematic of the model for a forward run to get the perturbation seismograms for cell i_c , marked in black, is shown.

Using the general notation introduced before, $(n_M + 1) \cdot n_d$ forward simulations have to be performed for computing the full Jacobian matrix

$$\mathbf{J} = \begin{bmatrix} \mathbf{J}^1 \\ \vdots \\ \mathbf{J}^L \\ \vdots \\ \mathbf{J}^{n_d} \end{bmatrix} = \underbrace{\begin{bmatrix} {}^P\mathbf{J}^1 \\ \vdots \\ {}^P\mathbf{J}^L \\ \vdots \\ {}^P\mathbf{J}^{n_d} \end{bmatrix}}_{\text{acoustic}} = \underbrace{\begin{bmatrix} {}^P\mathbf{J}^1 & {}^S\mathbf{J}^1 \\ \vdots & \vdots \\ {}^P\mathbf{J}^L & {}^S\mathbf{J}^L \\ \vdots & \vdots \\ {}^P\mathbf{J}^{n_d} & {}^S\mathbf{J}^{n_d} \end{bmatrix}}_{\text{elastic}}, \quad (2.17)$$

omitting the iteration index k from now on to simplify the notation.

The sensitivities can be visualised by plotting the values corresponding to the individual cells at their location in the grid shown in Figure 2.4. This results in one cross section showing the sensitivities with respect to either v_P or v_S for each time sample, or, after a FFT, for the real and imaginary parts of the frequency-domain representation at each frequency. The location of the data displayed in these cross sections inside the complete \mathbf{J} is shown in Figure 2.5.

To identify a suitable value for the size of the perturbation h , defined in equation (2.16), test calculations using values of 0.1%, 0.5%, 1%, 5% and 10%, both positive and negative, were performed. They did not show any strong dependence of the resulting sensitivities on h , neither in the amount of variation, nor in the direction of variation. A value of 1% was therefore finally selected for all computations.

Sensitivity calculation in the acoustic case

For computing acoustic sensitivities, I use the explicit expressions given by Zhou and Greenhalgh (1999). Compared with the brute force approach required for the elastic sensitivities, this is not only much faster, but also results in a significantly higher accuracy. Formulation of explicit expressions for the elastic case is currently under development. Unfortunately they were not available for my thesis project.

For an unbounded homogeneous medium (represented by model *FH*), an explosive source and pressure field recording, the explicit acoustic expressions can be compared to the results of the brute force perturbation approach. The similarity of the results serves as a verification of the validity of the brute force approximation.

2.1.3 Data information

The update equation (2.3) indicates that the stability of the inversion is strongly dependent on the degree of regularity of the matrix $\mathbf{J}^T \hat{\mathbf{W}}_D \mathbf{J} + \lambda \hat{\mathbf{W}}_M$. The second part of this matrix, $\lambda \hat{\mathbf{W}}_M$, represents the additional a priori constraints on the model vector \mathbf{m} and is independent of the experimental setup. To maximise the contribution of the data and optimise their information content for the model parameters of choice, one has to concentrate on the first part of the matrix, which is the approximate Hessian $\mathbf{J}^T \hat{\mathbf{W}}_D \mathbf{J}$.

This matrix is usually singular or nearly singular and therefore ill-conditioned. Since the regularity of the problem is not related to the absolute size of the eigenvalues, but to the condition number of the matrix, which is the ratio of its largest to its smallest eigenvalue (see, e.g. Trefethen and Bau, 1997), the normalised eigenvalue spectrum of $\mathbf{J}^T \hat{\mathbf{W}}_D \mathbf{J}$ will now be considered. If $\tilde{\Lambda} := \{\tilde{\lambda}_1, \dots, \tilde{\lambda}_i, \dots, \tilde{\lambda}_{n_M}\}$ is the set of eigenvalues of $\mathbf{J}^T \hat{\mathbf{W}}_D \mathbf{J}$, sorted in descending order, the normalised eigenvalue spectrum is $\Lambda := \{\dots, \lambda_i = \tilde{\lambda}_i / \tilde{\lambda}_1, \dots\}$ with $\lambda_1 \equiv 1$.

When computing the eigenvalue spectrum, finite numerical precision leads to nonzero results for eigenvalues which should in theory be zero. This requires the introduction of a threshold value θ , below which normalised eigenvalues are insignificant and thus belong to the null space of the Hessian matrix (see Figure 2.6). The choice of the value of θ is governed by the amount of damping necessary to render $\mathbf{J}^T \hat{\mathbf{W}}_D \mathbf{J} + \lambda \hat{\mathbf{W}}_M$ regular, which is in turn determined by the amount of noise present in the data, or, in my case, by the numerical precision available.

To compare the data information for model vectors of different length n_M , I look at the fractional size of the effective null space ℓ_{null} , which is determined by choosing θ , counting the number of normalised eigenvalues smaller than θ ($|\{\lambda_i \in \Lambda | \lambda_i < \theta\}|$) and then normalising this number by the total number of eigenvalues $|\Lambda| = n_M$, i.e. $\ell_{\text{null}} = \frac{|\{\lambda_i \in \Lambda | \lambda_i < \theta\}|}{n_M}$. Then,

$$1 - \ell_{\text{null}} = \frac{|\{\lambda_i \in \Lambda | \lambda_i \geq \theta\}|}{n_M} \quad (2.18)$$

is the measure of choice for the information content of the data set used for computing $\mathbf{J}^T \hat{\mathbf{W}}_D \mathbf{J}$. The quantity (2.18) will be subsequently referred to as the *Relative Eigenvalue Range* (RER), first introduced by Maurer et al. (2009). It varies between 0 (no information) and 1 (all parameters resolved). A qualitative sketch of a typical eigenvalue spectrum, a chosen threshold θ and the resulting RER and ℓ_{null} are shown in Figure 2.6.

The RER value does not require any actually observed data, but depends only on the geometry of the measurement setup, that is, on the location and type/orientation

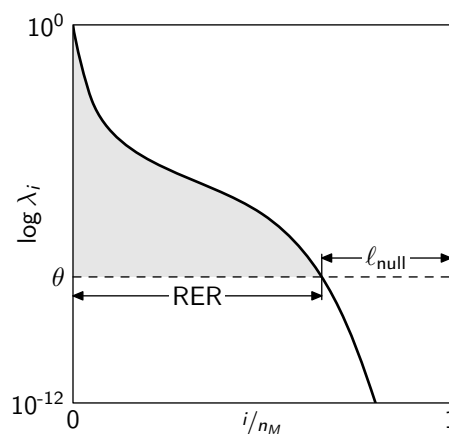


Figure 2.6: Descriptive sketch of a normalised eigenvalue spectrum of an approximate Hessian matrix with threshold θ and quantities RER and ℓ_{null} as introduced in the text.

of sources and receivers, and to a much lesser extent on the subsurface parameters. Therefore, the RER is a useful tool for experimental design.

2.2 Wave field analysis

A primary goal of this chapter is to quantify the information content of seismic data as a function of the various parameters introduced in the previous section. The determination of information content, here expressed with the RER value introduced in equation (2.18), is based on waveform sensitivities, which are themselves based on the actual Green's functions. Therefore, I first investigate waveform characteristics for a variety of scenarios.

Results from the different simulations are shown in Figures 2.8 to 2.13, which have a common layout. From top to bottom they show wave field snapshots taken at five different times or frequencies, labelled A, B, C, D and E (see Table 2.3). Source and receiver locations and types are indicated using the symbols introduced in Table 2.2. For Figures 2.8, 2.9, 2.10 and 2.11, the seismograms and their frequency-domain representations corresponding to the depicted snapshots are shown at the bottom of the two panels, the seismograms corresponding to Figure 2.12 are shown in Figure 2.13, the frequency domain representations corresponding to Figure 2.14 are shown in Figure 2.15. All data are shown using a constant scale. Only the results from acoustic simulations (Figures 2.8 and 2.9) were multiplied by a constant factor to account for amplitude differences due to the different forward solver used. For all wave-field plots a common colour scale, shown in Figure 2.7a, is used. The seismogram traces are normalised to the maximum value of all traces shown in the same panel, but in Figures 2.8 and 2.9 they are shown trace normalised; the same scaling approach is used for the seismogram spectra. If two traces or spectra are shown in the same panel, one of the lines is shifted vertically for display purposes.

2.2.1 Validity of the acoustic approximation and effects of a free surface

As can be seen from Figure 2.8, the elastic and acoustic modelling results are identical in homogeneous unbounded media (such as model *FH*), provided that an explosive source is used and the motion is sensed only as excess pressure. The reason is that only radially

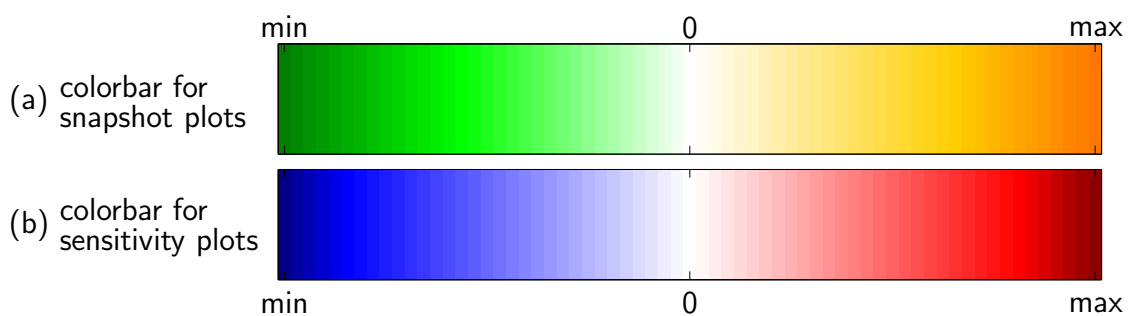


Figure 2.7: Colour bars for the colour plots showing (a) wave field snapshots and (b) sensitivities.

model	A	B	C	D	E	
<i>FH</i>	5.7	7.0	9.0	11.6	18.0	<i>t</i> [ms]
<i>HH</i>	5.7	7.0	9.0	11.6	18.0	
<i>HG</i>	6.6	9.0	12.3	17.0	25.0	
<i>HL</i>	5.7	7.0	9.0	11.6	18.0	
all	100	300	500	700	900	<i>f</i> [Hz]

Table 2.3: Overview of the times and frequencies for which wave field snapshots and sensitivity cross sections are shown in Figures 2.8 to 2.13 and Figures 2.16 to 2.25, respectively.

symmetric wave fields are excited by such an omni-directional source and the detector is also omni-directional; that is, it responds only to (radial) pressure.

In the presence of a free surface (model *HH*), the elastic wave field loses its radial symmetry due to the emanating surface waves. This is demonstrated in the left panels of Figure 2.9. By contrast, the acoustic approximation (right panels in Figure 2.9) is simply the full-space solution (Figure 2.8) cut in half. The radial symmetry is retained and the surface waves are absent. This clearly demonstrates the inadequacy of the acoustic approximation in the presence of a free surface or any internal boundary surface along which significant interface waves (Scholte, Stoneley or tunnel waves) could propagate.

2.2.2 Adding source and receiver directionality

In surface-based seismic measurements, the scalar pressure field (*ep*, see Table 2.2 for short notations of source and receiver types) is routinely recorded in marine exploration but rarely in on-shore surveying. Instead, single component (typically the vertical) or several components of the vector wave field of the particle velocity are sensed with geophones or seismometers (*ex*, *ez*). Besides explosion sources on land, it is also common practise to employ directed sources (*zx*, *zz*, *xx*, *xz*), such as a weight drop, sledge hammer, or vibrator. Figure 2.10 shows the simulation results for the source/receiver combinations *ex* and *ez*. Compared with the results from the *ep* combination, shown in Figure 2.9, there are quite substantial changes in all quantities displayed. These strong differences indicate that directionality may have an important influence on the waveform sensitivities and data information content, which are discussed later in this chapter. Results for the directed source and receiver combinations *zz* and *zx* are shown in Figure 2.11. Qualitatively, they are comparable to the results from *ez* and *ex* shown in Figure 2.10.

2.2.3 The effect of vertical heterogeneity

The effect of subsurface properties which vary as a function of depth (constant, piecewise increase or continuous increase) is illustrated in Figures 2.12 to 2.15. The time-domain snapshots for the homogeneous half space *HH* (Figure 2.12a) and the gradient model *HG* (Figure 2.12b) are quite similar, but a horizontal discontinuity, as in the layer model *HL* (Figure 2.12c), affects the wave fields in a major way. Similar observations are made for

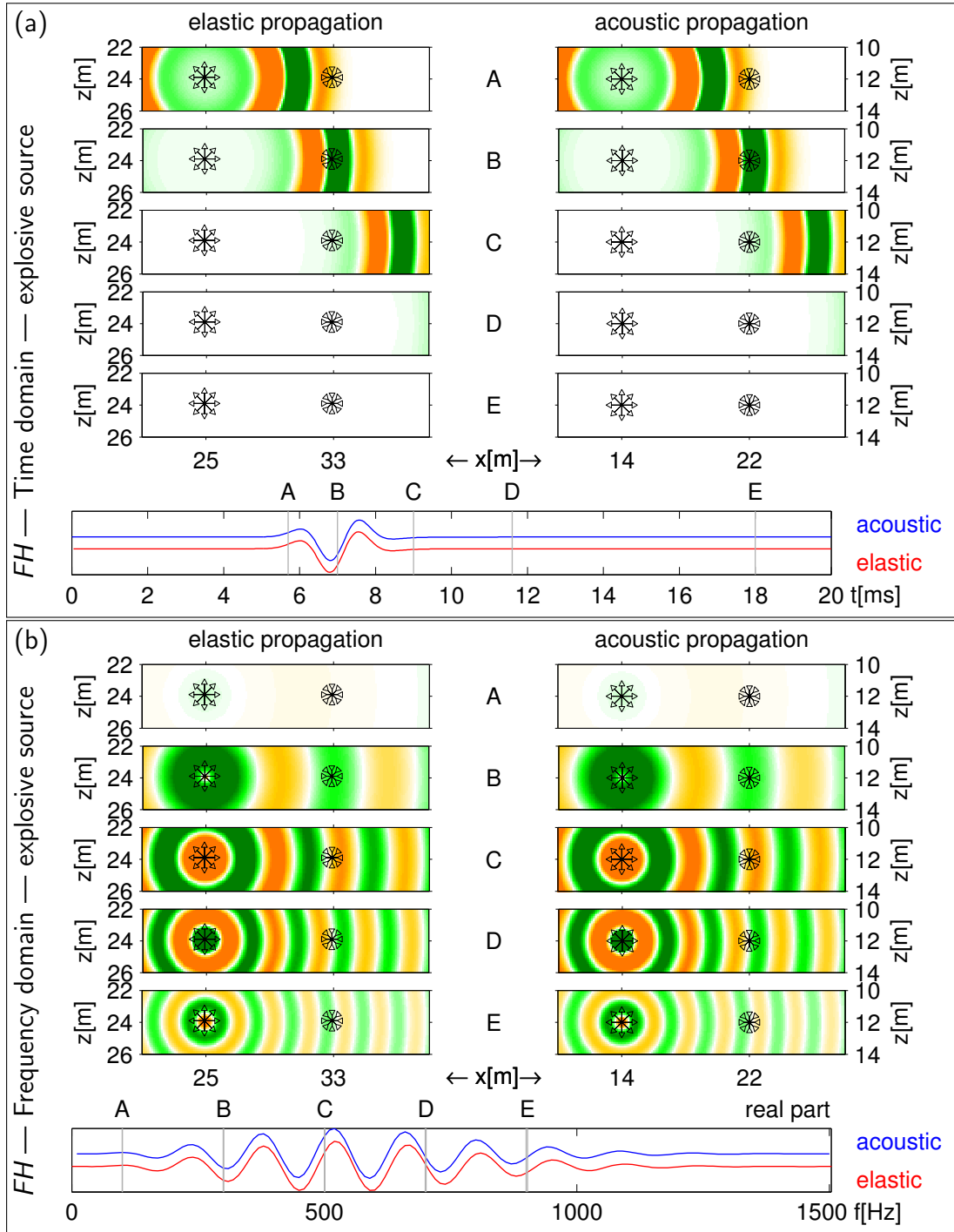


Figure 2.8: Comparison of elastic (left panels) to the corresponding acoustic (right panels) wave propagation through model *FH*. (a) shows time-domain solutions for times A to E (see Table 2.3), also marked on the seismograms, for a receiver at the position denoted in the wave field plots. (b) displays the real part of the frequency-domain representations of (a) for frequencies A to E (see Table 2.3). At the bottom, the real parts of the frequency spectra of the seismograms shown in (a) are included. All data are scaled to a common value, with a constant factor between acoustic and elastic results; see Figure 2.7a for the colour scale and Table 2.2 for the source and receiver symbols. For display purposes the traces and spectra at the bottom of the panels are drawn with a vertical offset.

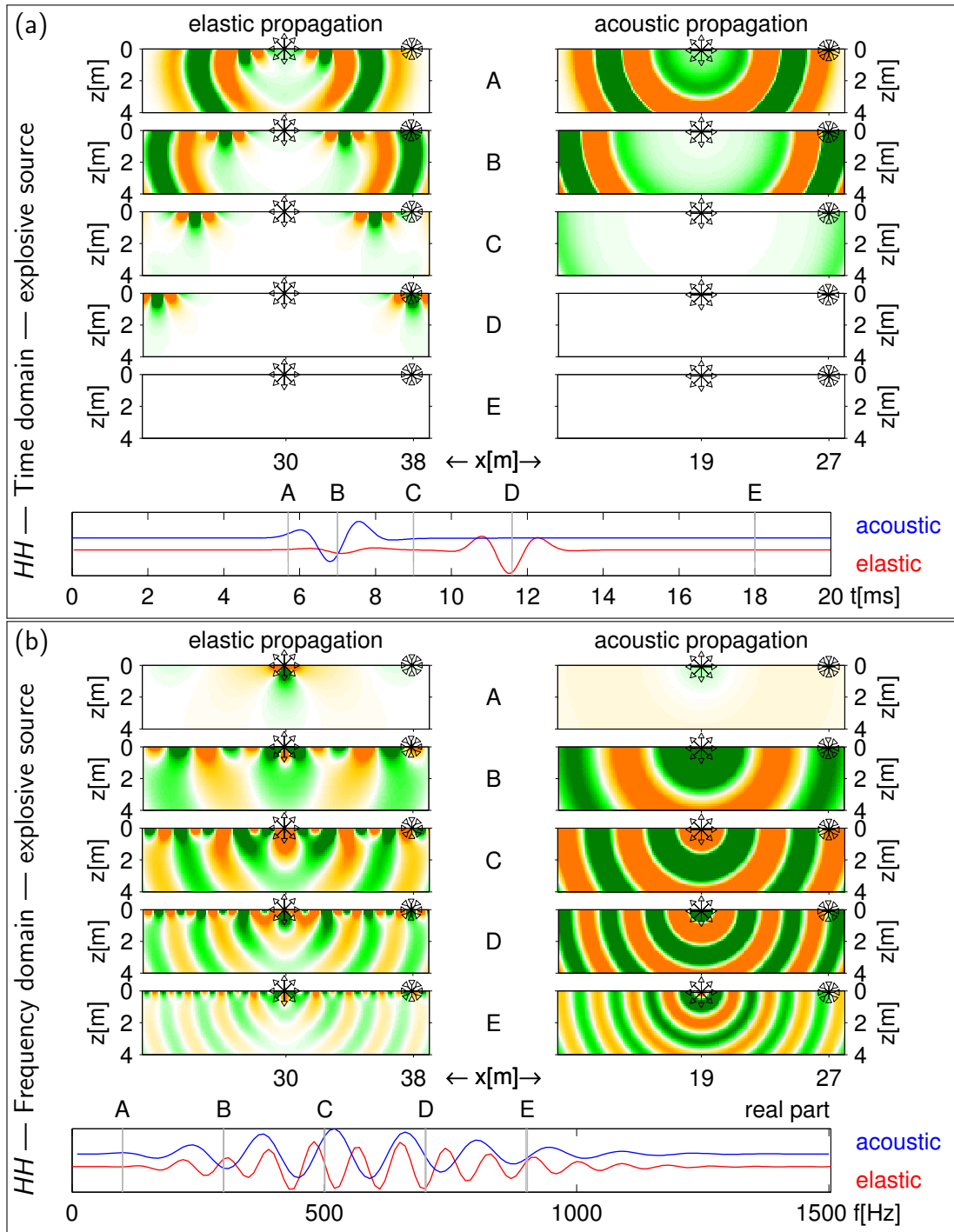


Figure 2.9: As for Figure 2.8, but for wave propagation through model *HH*. The free surface causes the formation of surface waves in the elastic solution (left panels), whereas the solution for the acoustic approximation (right panels) remains unchanged with respect to the full-space solution shown in Figure 2.8. For display purposes the traces and spectra at the bottom of the panels are drawn with a vertical offset.

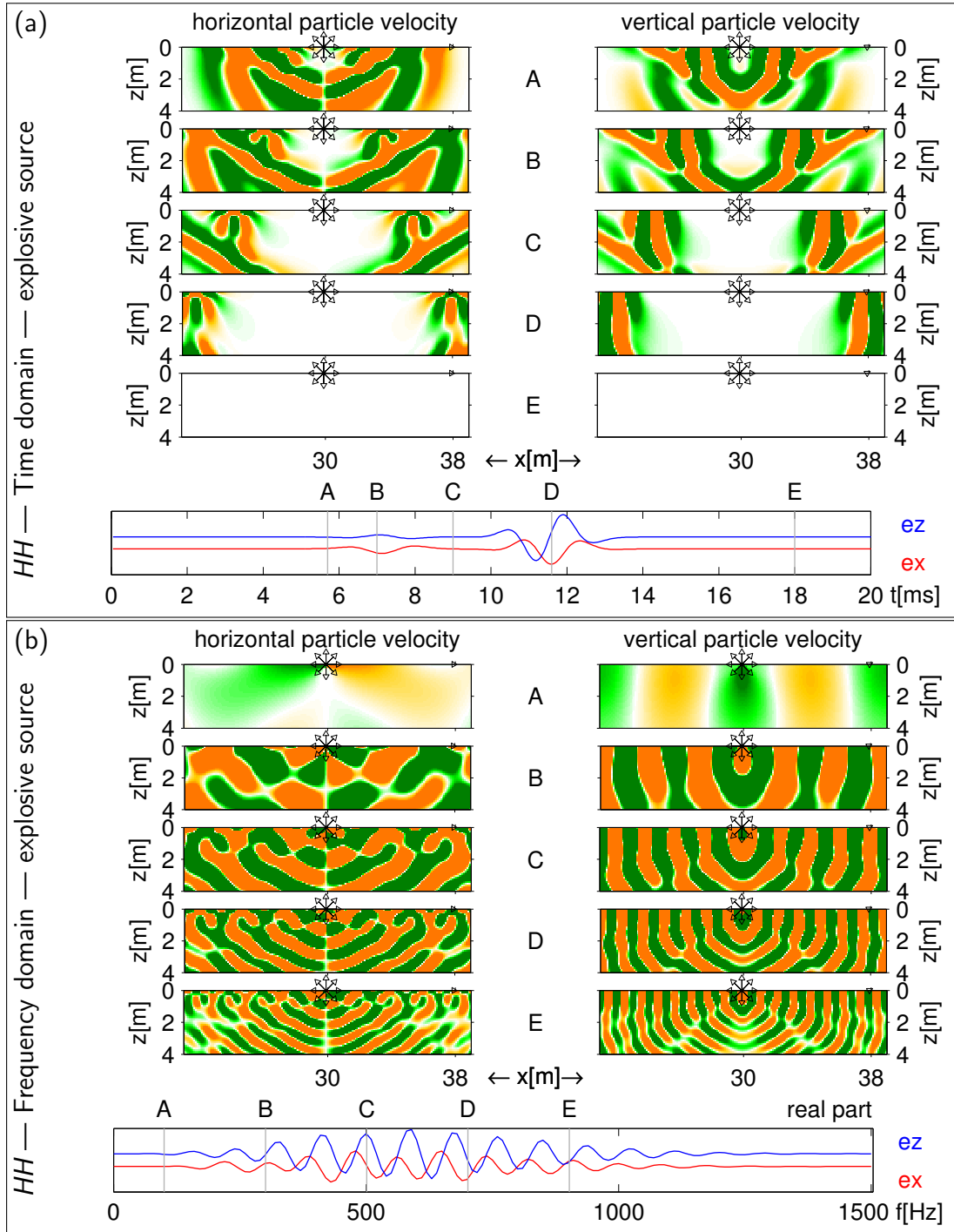


Figure 2.10: Horizontal (left panels) and vertical (right panels) particle velocities for a wave excited by an explosive source, propagated through model *HH*. (a) shows time-domain solutions for times A to E (see Table 2.3), also marked on the seismograms, for a receiver at the position denoted in the wave field plots. (b) displays the real part of the frequency-domain representations of (a) for frequencies A to E (see Table 2.3). At the bottom, the real parts of the frequency spectra of the seismograms shown in (a) are included. All data are scaled to a common value, frequency-domain results are scaled up by a factor of two; see Figure 2.7a for the colour scale and Table 2.2 for the source and receiver symbols. For display purposes the traces and spectra at the bottom of the panels are drawn with a vertical offset.

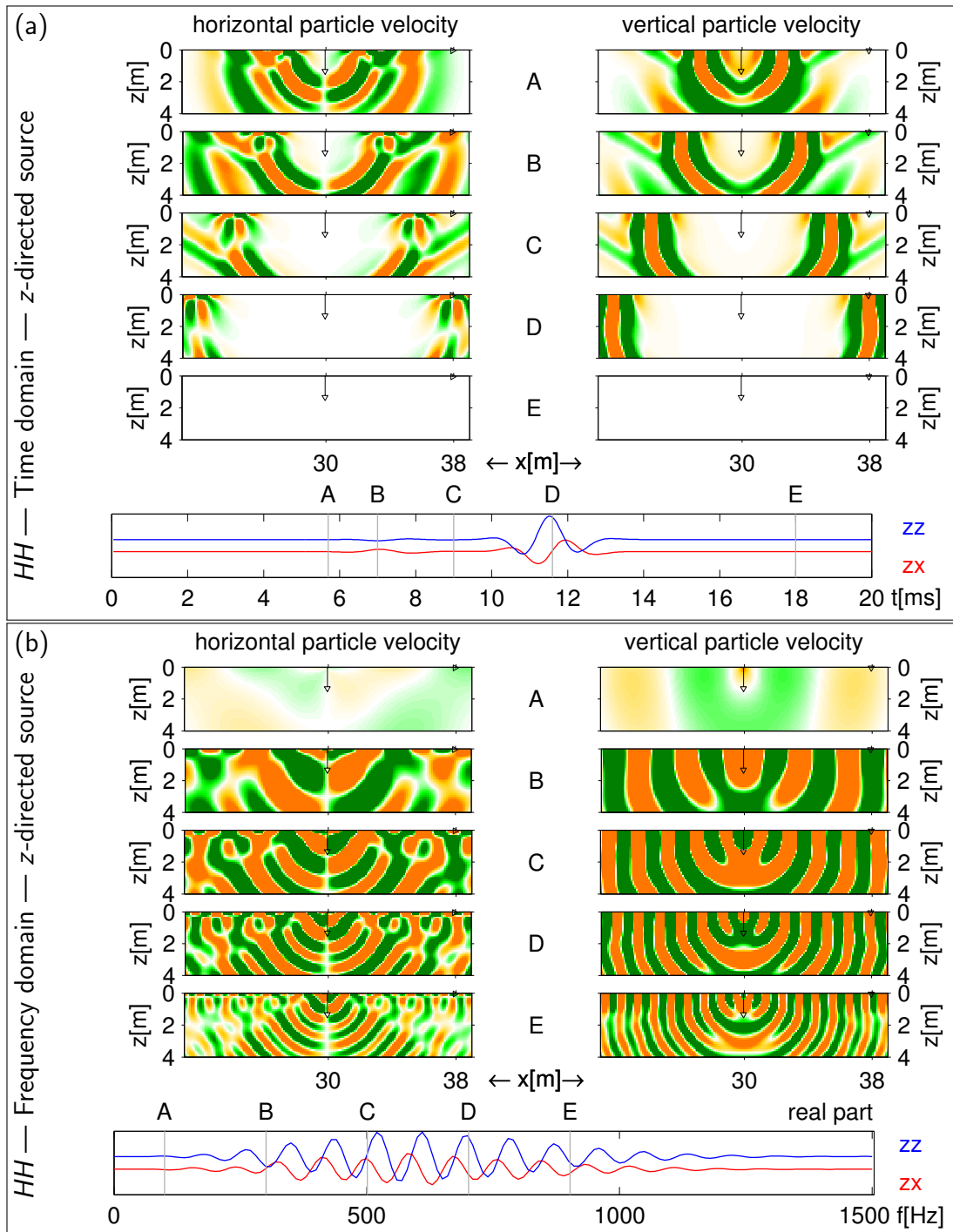


Figure 2.11: As for Figure 2.10, but for a single force source in the vertical direction.

the frequency-domain results shown in Figure 2.14. The reference seismograms extracted at a source-receiver distance of 8 m are shown in Figure 2.13 and the real parts of the corresponding seismogram frequency spectra in 2.15.

The reason for the qualitatively similar results for models *HH* and *HG* as opposed to the wave fields propagated through model *HL* is the appearance of new phases in the wave field, caused by the discontinuity at three metres depth in model *HL*. The wave field propagating through models *HH* and *HG* only consists of direct and diving body waves and the surface waves of Rayleigh type. The wave field propagating through model *HL*, on the other hand, additionally includes body wave phases due to reflections, mode conversions and multiple reverberations at the discontinuity, as well as refracted

Time domain — *z*-directed source

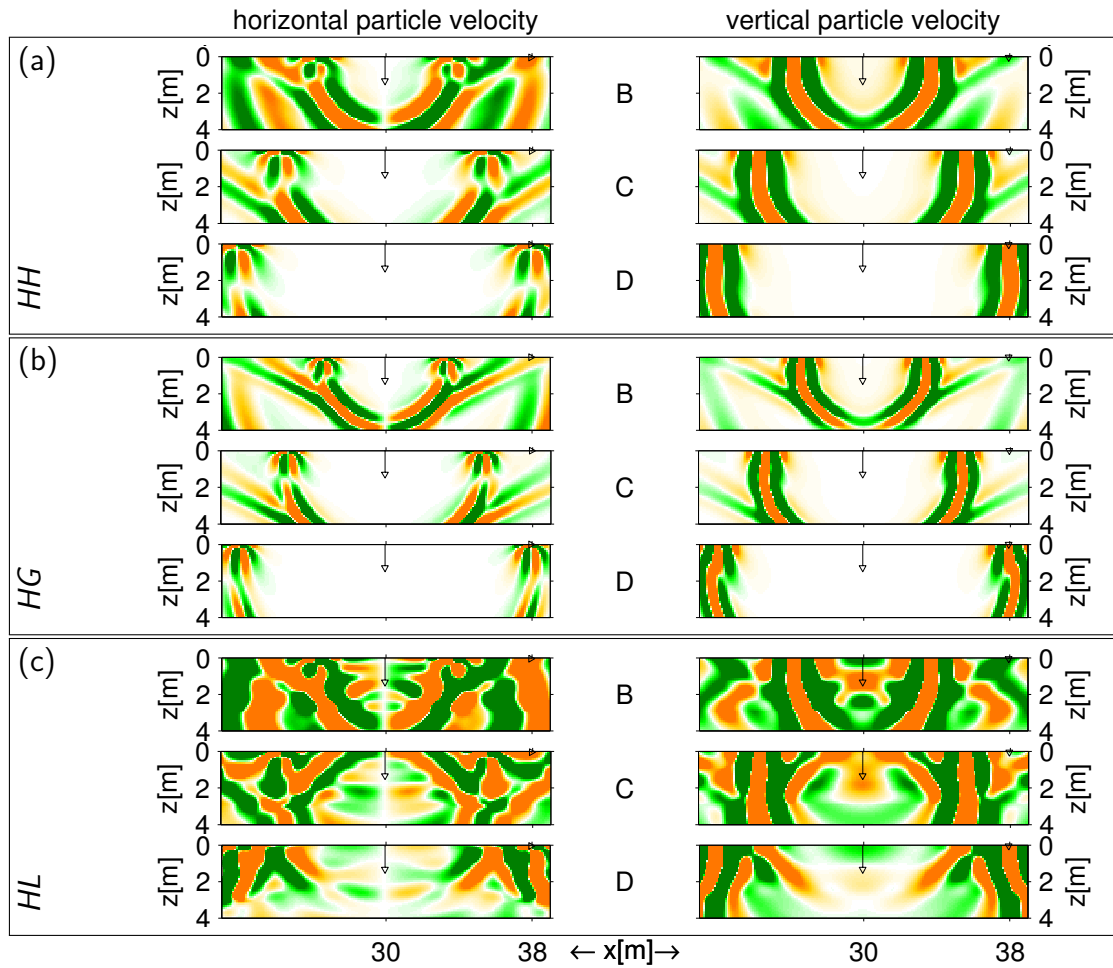


Figure 2.12: Comparison of time-domain representations of horizontal (left panels) and vertical (right panels) particle velocities for a wave excited by a single force source in the vertical direction, propagated through (a) model *HH*, (b) model *HG* and (c) model *HL*. Figure 2.13 shows seismogram traces for a receiver at the position denoted in the wave field plots with times B to D (see Table 2.3) marked. All data are scaled to a common value; see Figure 2.7a for the colour scale and Table 2.2 for the source and receiver symbols.

Seismogram traces — z-directed source

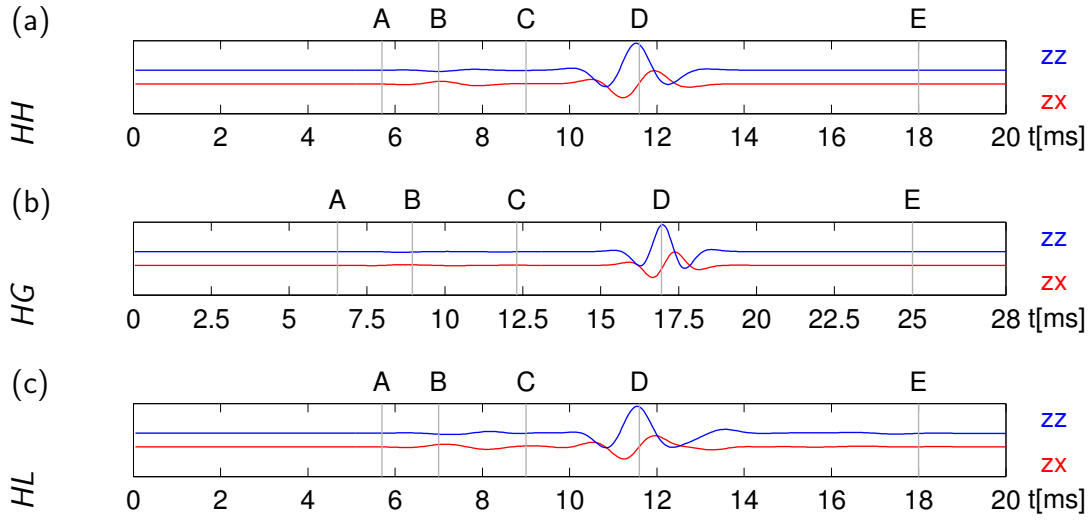


Figure 2.13: Seismogram traces corresponding to the wave field plots shown in Figure 2.12. There the receiver position is marked (see Table 2.2 for the source and receiver symbols) and snapshots of the particle velocity field at times B to D (see Table 2.3) are displayed. (a) shows traces for propagation through model HH , (b) for propagation through model HG and (c) for propagation through model HL . For display purposes the traces are drawn with a vertical offset.

phases and a substantial portion of guided wave energy contained in the surface waves, due to the layering. The effect of these additional phases is the presence of persistent wave energy near to the source at later times; this can be seen in Figure 2.12c.

2.3 Waveform sensitivity analysis

In keeping with the treatment of the waveform characteristics in the previous section, I next analyse the waveform sensitivities for the different scenarios of acoustic/elastic media, the absence/presence of a free surface, the source and receiver directionality and the heterogeneity of the subsurface model. In the elastic case, one needs to distinguish between the sensitivities with respect to the P- and S-wave velocities.

The sensitivities with respect to density were also computed but for the sake of brevity are not presented here. Using the relations given in appendix E, I also computed sensitivities with respect to other choices of parameter sets, i.e the Lamé parameters λ and μ and the compressibility κ and μ . Since the sensitivities with respect to μ were qualitatively equivalent to those with respect to v_S and the λ - and the κ -sensitivities strongly resembled those for v_P , I kept with the parameters v_S and v_P , thus avoiding additional numerical inaccuracies introduced by transformation of the sensitivities into those for a different parameter set than that employed in the FDTD code.

Using the same notation as in equation (2.17), the sensitivities are denoted by $^P \mathbf{J}^{ij}$ or $^S \mathbf{J}^{ij}$ in the following, where the left superscript indicates sensitivities with respect to v_P or v_S . The super index L used as the right superscript in equation (2.17) and introduced in equation (2.9) was reduced to its part denoting the source/receiver type

Frequency domain — z -directed source

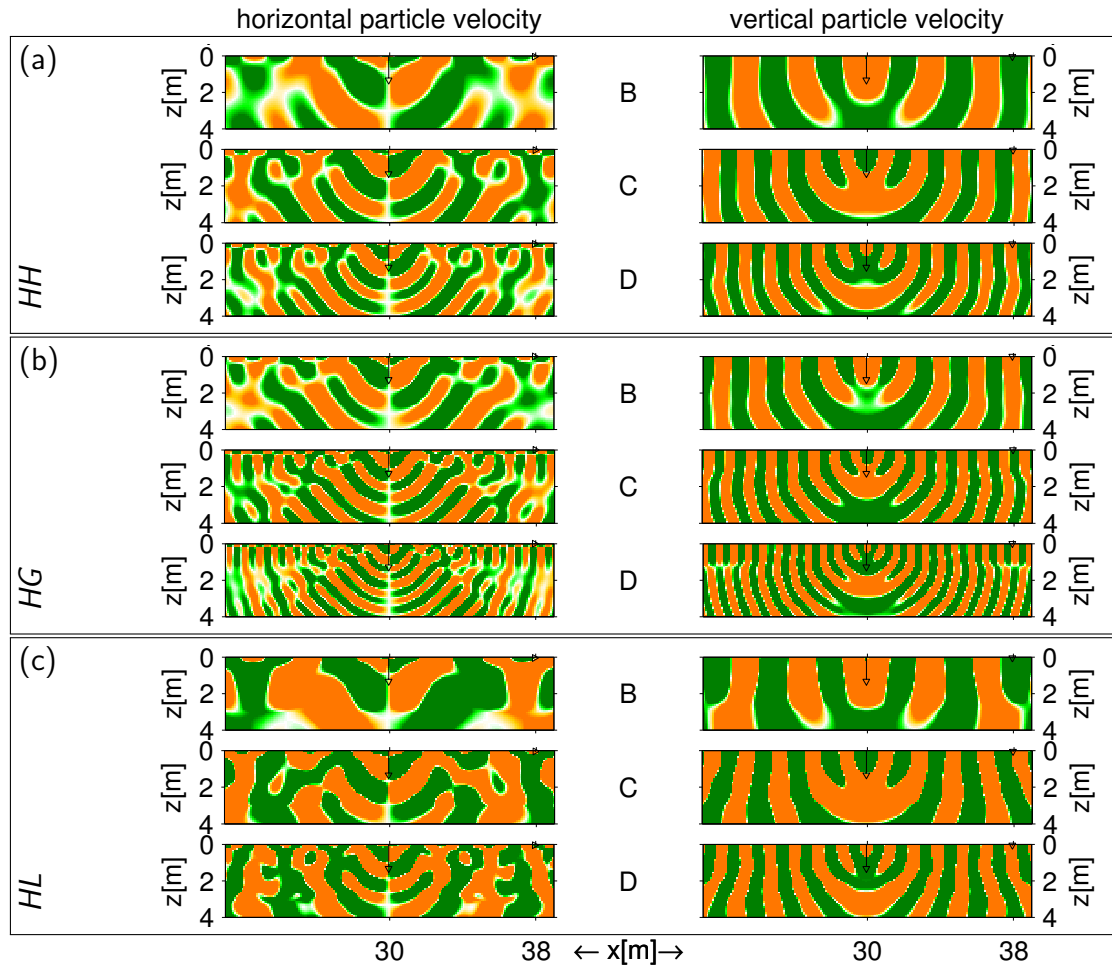


Figure 2.14: Comparison of real parts of the frequency-domain representations of horizontal (left panels) and vertical (right panels) particle velocities for a wave excited by a single force source in the vertical direction, propagated through (a) model HH , (b) model HG and (c) model HL . Figure 2.15 shows the real parts of the frequency spectra of the seismograms for a receiver at the position denoted in the wave field plots, with the frequencies B to D (see Table 2.3) marked. All data are scaled to a common value; see Figure 2.7a for the colour scale and Table 2.2 for the source and receiver symbols.

Seismogram spectra — z-directed source

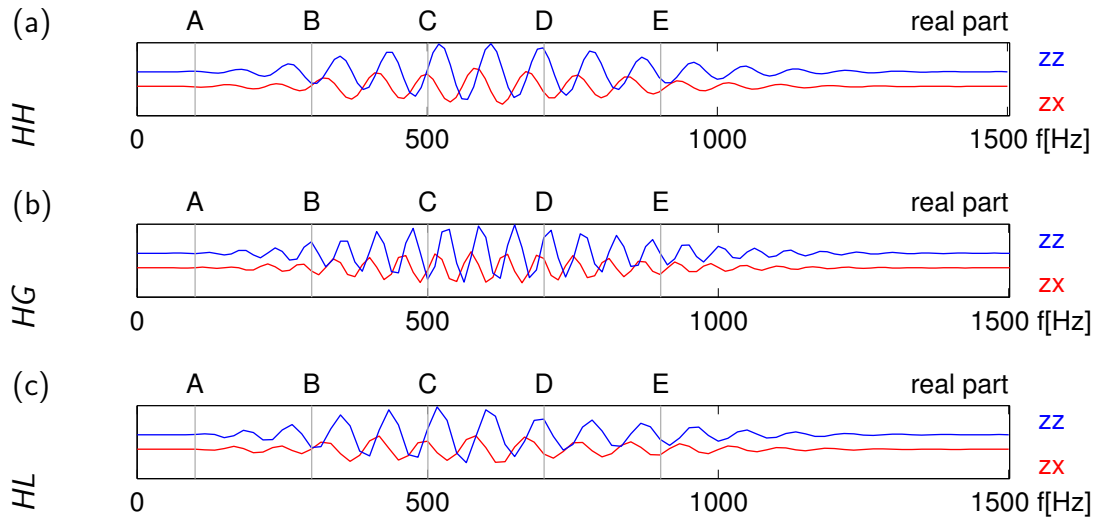


Figure 2.15: Real parts of the frequency spectra of the seismogram traces corresponding to the wave field plots shown in Figure 2.14. There, the receiver position is marked (see Table 2.2 for the source and receiver symbols) and snapshots of the real parts of the frequency-domain representation of the particle velocity field at frequencies B to D (see Table 2.3) are displayed. (a) shows traces for propagation through model *HH*, (b) for propagation through model *HG* and (c) for propagation through model *HL*. For display purposes the spectra are drawn with a vertical offset.

ij with $i \in \{e, x, z\}$ and $j \in \{p, x, z\}$ (see Table 2.2), since only sensitivities for the source/receiver pair with the receiver placed 8 m to the right of the source (see Figure 2.3b) are considered.

Results for the different sensitivity types are shown in Figures 2.16 to 2.25, which have a common layout resembling that of the wave field plots shown in Figures 2.8 to 2.13. From top to bottom they show sensitivity cross sections (see section 2.1.2 and Figure 2.5), taken at five different times or frequencies, labelled A, B, C, D and E (see Table 2.3). Source and receiver locations and types are indicated using the symbols introduced in Table 2.2. The seismograms for the corresponding source/receiver type and model and their frequency domain representations are shown at the bottom of the panels. All data are shown using a constant scale. Only the results from the acoustic simulations (Figures 2.16 and 2.18) were multiplied by the same constant factor as used to account for amplitude differences between the elastic and acoustic forward solver in the case of the wave field plots. For all sensitivity plots a common colour scale, which is shown in Figure 2.7b, is used. The seismogram traces are normalised to the maximum value of all traces shown in the same panel, only in Figures 2.16 and 2.18 they are shown trace normalised; the same scaling approach is used for the seismogram spectra. If two traces (or spectra) are shown in the same panel, one of the lines is shifted vertically for display purposes.

2.3.1 Validity of the acoustic approximation and effects of a free surface

Homogeneous full-space model FH

Acoustic and elastic full-space sensitivities ${}^P\mathbf{J}^{ep}$ for model *FH* are shown in Figure 2.16. Their shapes are almost identical. Only the overall amplitudes are somewhat reduced for the elastic sensitivities. This is likely to be an effect of the brute force sensitivity computations employed in the elastic case.

The early time sensitivities (times A and B) only have significant amplitudes in the spatial region directly between the source and the receiver. At later times, the high amplitude sensitivities form ellipses with focal points at the source and receiver positions. It may seem somewhat counterintuitive that (i) nonzero sensitivities exist at times where the corresponding seismogram amplitudes are virtually zero (times C, D and E) and (ii) that significant sensitivities exist outside the region delimited by the source and the receiver.

These observations can be explained by means of a simple physical interpretation of the meaning of sensitivities. They express the expected effects on the seismogram caused by a small perturbation in a particular region (i.e. inversion cell) of the model. If a model cell would be perturbed (effectively done for the elastic sensitivity computations and conceptually assumed in the explicit expressions for the acoustic case), then it represents a diffracting heterogeneity, which produces a scattered wave; the elliptical isochron pattern is precisely what one would see from a diffractor and hence this explains the sensitivity patterns in Figure 2.16a.

A comparison of the elastic P- and S-wave sensitivities ${}^P\mathbf{J}^{ep}$ and ${}^S\mathbf{J}^{ep}$ for model *FH* is shown in Figure 2.17. One might think that the sensitivities with respect to v_S should be zero, because no S-waves are observed in the seismograms, but a look at the interrelations between sensitivities with respect to different equivalent sets of elastic parameters, given in Appendix E, shows the reason for ${}^S\mathbf{J}^{ep}$ being nonzero.

A less mathematical and more physical explanation of the observations related to the equations in Appendix E can be obtained by looking at the definition of the seismic P- and S-wave velocities v_P and v_S :

$$v_P := \sqrt{\frac{\kappa + 4/3\mu}{\rho}} \quad \text{and} \quad v_S := \sqrt{\frac{\mu}{\rho}}. \quad (2.19)$$

Here κ is the bulk modulus, μ is the shear modulus and ρ denotes density (see also Appendix E). For computing the shear-wave sensitivity, v_S needs to be slightly perturbed (effectively or formally), while keeping v_P constant. This is only possible, by increasing μ and decreasing κ accordingly (or vice versa). The decrease of κ affects the behaviour of the radiating P-waves, which results in the patterns for ${}^S\mathbf{J}^{ep}$ shown in the right panels of Figure 2.17.

Computing P-wave sensitivities requires perturbing κ , while μ must remain fixed. This implies that computations of the sensitivities with respect to v_S and v_P require perturbations of κ with opposite signs. Interestingly, the corresponding P- and S-wave panels in Figure 2.17 exhibit similar patterns, but they have reversed signs. This may indicate that κ is the dominant parameter for both ${}^P\mathbf{J}^{ep}$ and ${}^S\mathbf{J}^{ep}$.

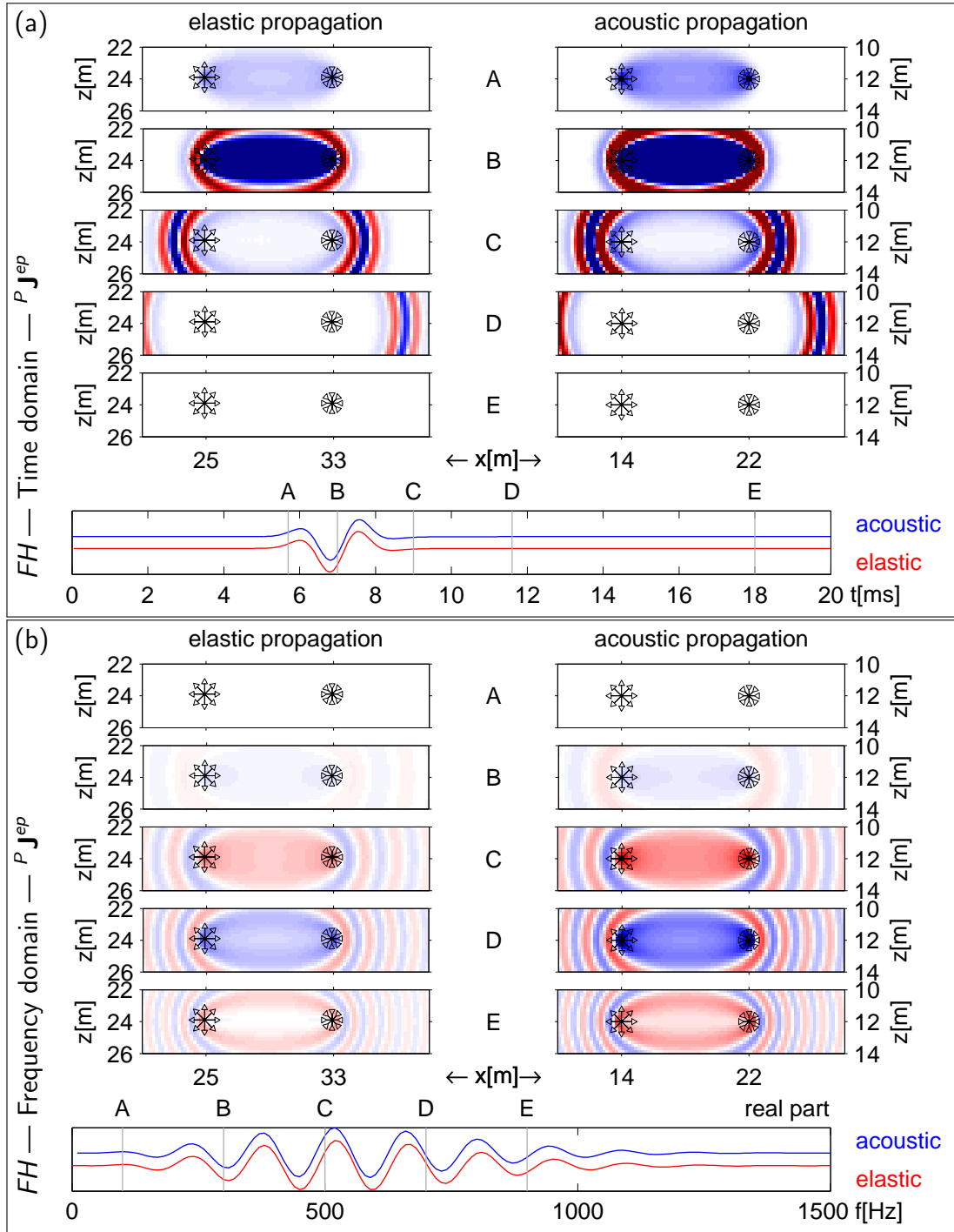


Figure 2.16: Comparison of acoustic and elastic sensitivities in the full space model FH with the elastic version of $^P\mathbf{J}^{ep}$ given in the left panels and its acoustic approximation in the right panels. (a) shows time-domain results for times A to E (see Table 2.3), also marked on the seismograms, for a receiver at the position denoted in the colour plots. (b) displays the real part of the frequency-domain representations of (a) for frequencies A to E (see Table 2.3). At the bottom, the real parts of the frequency spectra of the seismograms shown in (a) are included. All data are scaled to a common value, with a constant factor between acoustic and elastic results; see Figure 2.7b for the colour scale and Table 2.2 for the source and receiver symbols.

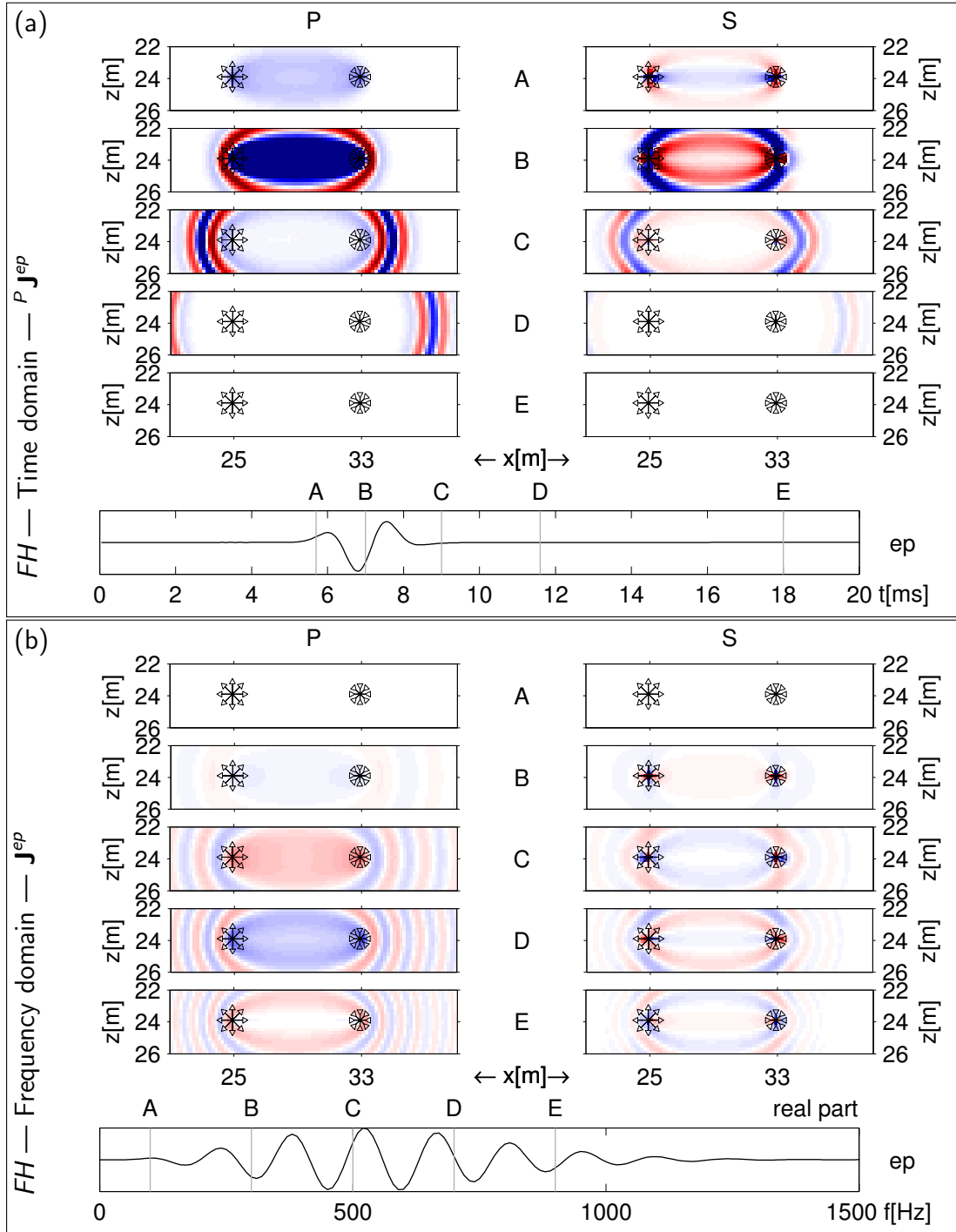


Figure 2.17: Sensitivities $P J^{ep}$ (left panels) and $S J^{ep}$ (right panels) in the full space model FH . (a) shows time-domain results for times A to E (see Table 2.3), also marked on the seismograms, for a receiver at the position denoted in the colour plots. (b) displays the real part of the frequency-domain representations of (a) for frequencies A to E (see Table 2.3). At the bottom, the real parts of the frequency spectra of the seismograms shown in (a) are included. All data are scaled to a common value; see Figure 2.7b for the colour scale and Table 2.2 for the source and receiver symbols.

Frequency-domain results, shown in Figures 2.16b and 2.17b, are more difficult to interpret in physical terms. They show oscillating patterns across the entire model, in which the spatial frequency of the oscillations scales with the temporal frequencies under consideration. As for the time-domain results, ${}^P\mathbf{J}^{ep}$ and ${}^S\mathbf{J}^{ep}$ have similar shapes but exhibit reversed signs.

Homogeneous half-space model HH

Comparisons of the acoustic and elastic sensitivities ${}^P\mathbf{J}^{ep}$ for the homogeneous half space *HH* are shown in Figure 2.18. Considering the wave field comparisons in Figure 2.9, it is not surprising that the sensitivities are also very different. The acoustic sensitivities are basically identical to the full-space results (with regard to the shape), but the elastic sensitivities are dominated by the effects of the surface wave. Both time- and frequency-domain sensitivities show high amplitudes near the surface. This suggests that P-wave information is predominantly carried by the surface wave and the contribution of the body waves is very small.

Figure 2.19 compares the elastic sensitivities with respect to ν_P and ν_S for half space *HH*. ${}^P\mathbf{J}^{ep}$ is repeated from Figure 2.18. Both the time- and frequency-domain representations of ${}^S\mathbf{J}^{ep}$ cover a much larger depth range compared with ${}^P\mathbf{J}^{ep}$.

2.3.2 Adding source and receiver directionality

As for the waveform analysis, the complexity is now increased by considering source and receiver directionality. Figure 2.20 shows the elastic sensitivities for the commonly employed combination *ez* (explosion source, vertical component geophone), and Figure 2.21 shows the less commonly considered combination *ex* (explosion source, horizontal component geophone). Both combinations exhibit quite complicated time- and frequency-domain sensitivity patterns. As already observed for the *ep* case, also the remaining ${}^P\mathbf{J}^{ej}$ ($j \in \{x, z\}$) seem to be dominated by the surface waves. The P-type body waves ought to manifest themselves in the time-domain sensitivity plots in the form of expanding ellipses, as observed for the acoustic case in Figure 2.18. There are only hints of such ellipses, having very small amplitudes.

Interestingly, the P-type body wave contribution seems to be more significant, when a vertically-directed source is employed. The corresponding plots for the *zz* and *zx* cases are shown in Figures 2.22 and 2.23. Here, both P-type body wave and surface wave contributions are observed.

For a horizontally-directed source and a horizontal component receiver (configuration *xx*, not shown) the sensitivity plots are very similar to those for the *ex* case shown in Figure 2.21. The *xz* sensitivities (also not shown) are identical to those for *zx* in Figure 2.23, but with reversed signs, as was to be expected regarding the symmetry of the problem.

2.3.3 The influence of vertical inhomogeneity

As one would anticipate after looking at the wave field analysis (see Figures 2.12 and 2.14), the sensitivities for model *HG* are very similar to those for model *HH*. Thus, for

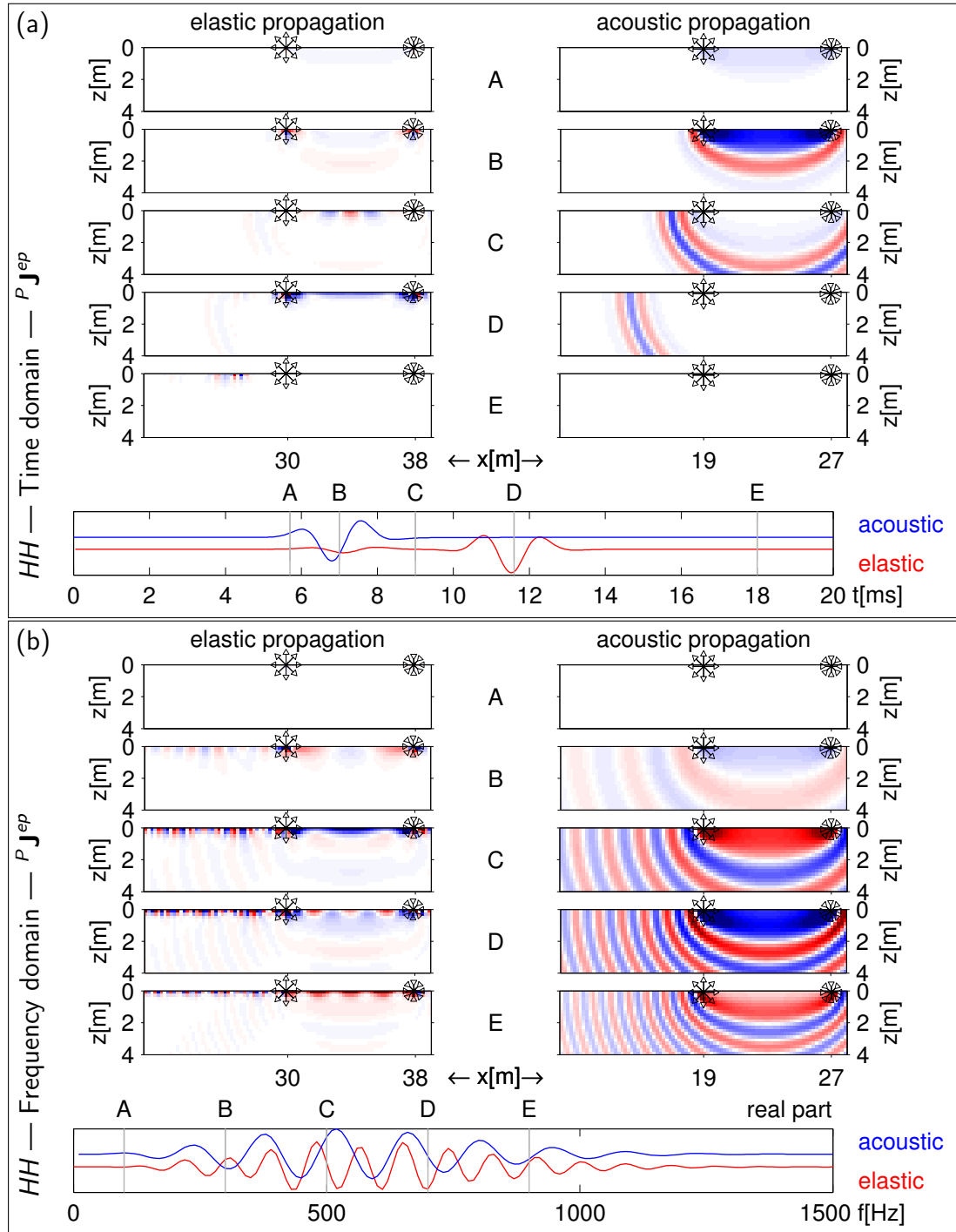


Figure 2.18: As for Figure 2.16, but for model HH . In the elastic case (left panels), the emanating surface waves lead to a concentration of the sensitivities close to the surface, whereas their acoustic approximation (right panels) remain unchanged with respect to Figure 2.16. For display purposes the spectra are drawn with a vertical offset.

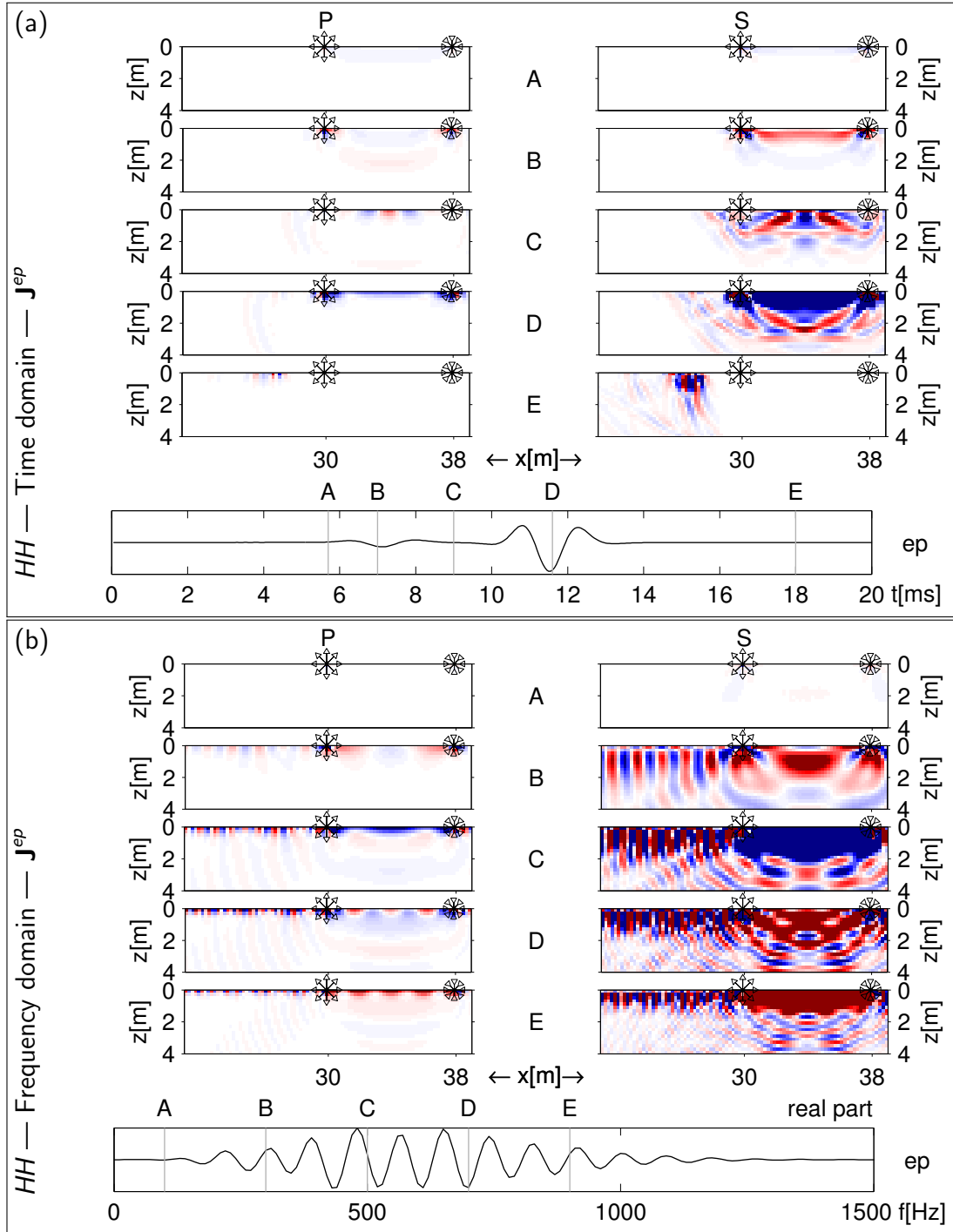


Figure 2.19: Sensitivities $^P J^{ep}$ (left panels) and $^S J^{ep}$ (right panels) in the homogeneous half space model HH . (a) shows time-domain results for times A to E (see Table 2.3), also marked on the seismograms, for a receiver at the position denoted in the colour plots. (b) displays the real part of the frequency-domain representations of (a) for frequencies A to E (see Table 2.3). At the bottom, the real parts of the frequency spectra of the seismograms shown in (a) are included. All data are scaled to a common value; see Figure 2.7b for the colour scale and Table 2.2 for the source and receiver symbols.

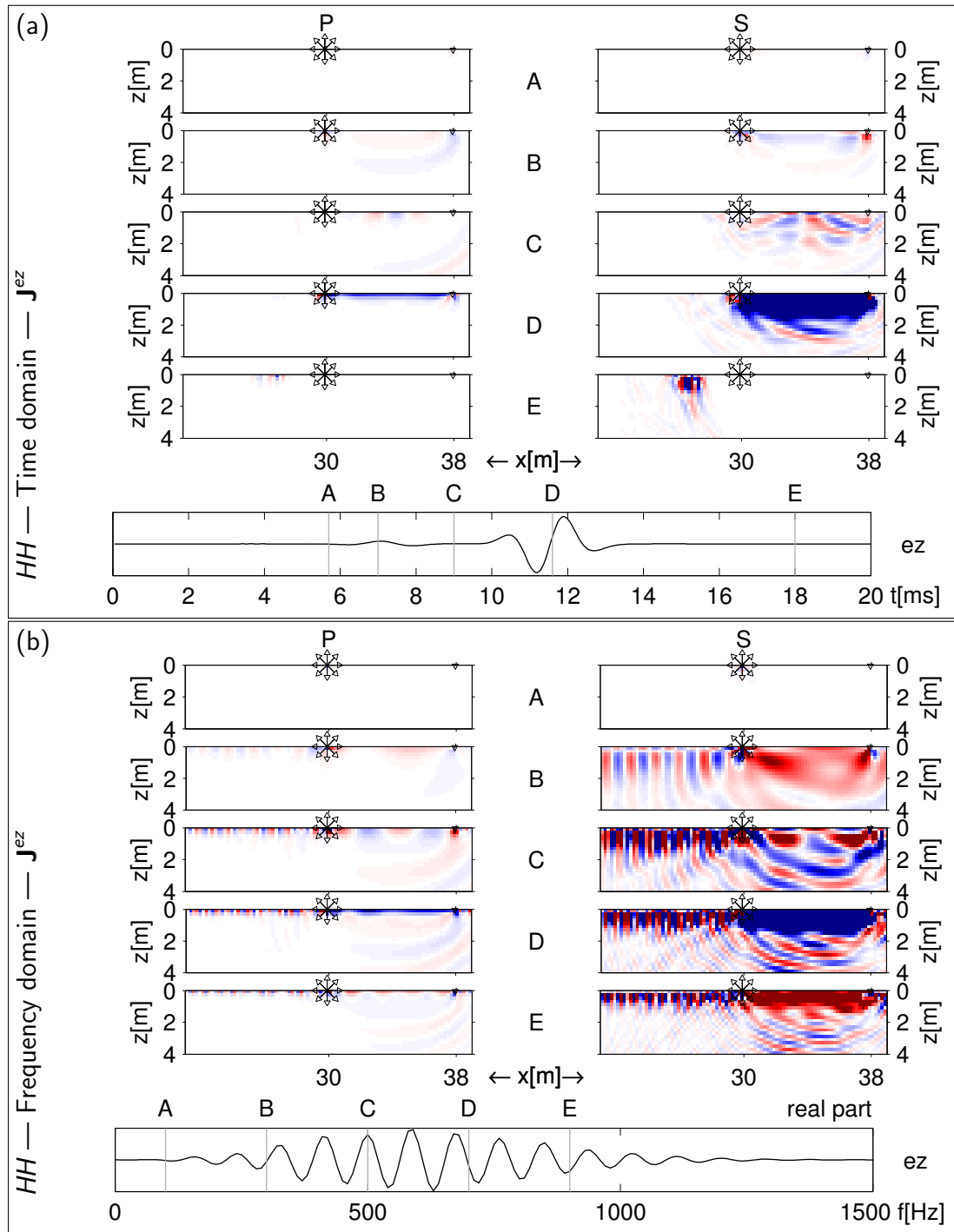


Figure 2.20: Sensitivities $P J^{ez}$ (left panels) and $S J^{ez}$ (right panels) in the homogeneous half space model HH . (a) shows time-domain results for times A to E (see Table 2.3), also marked on the seismograms, for a receiver at the position denoted in the colour plots. (b) displays the real part of the frequency-domain representations of (a) for frequencies A to E (see Table 2.3). At the bottom, the real parts of the frequency spectra of the seismograms shown in (a) are included. All data are scaled to a common value; see Figure 2.7b for the colour scale and Table 2.2 for the source and receiver symbols.

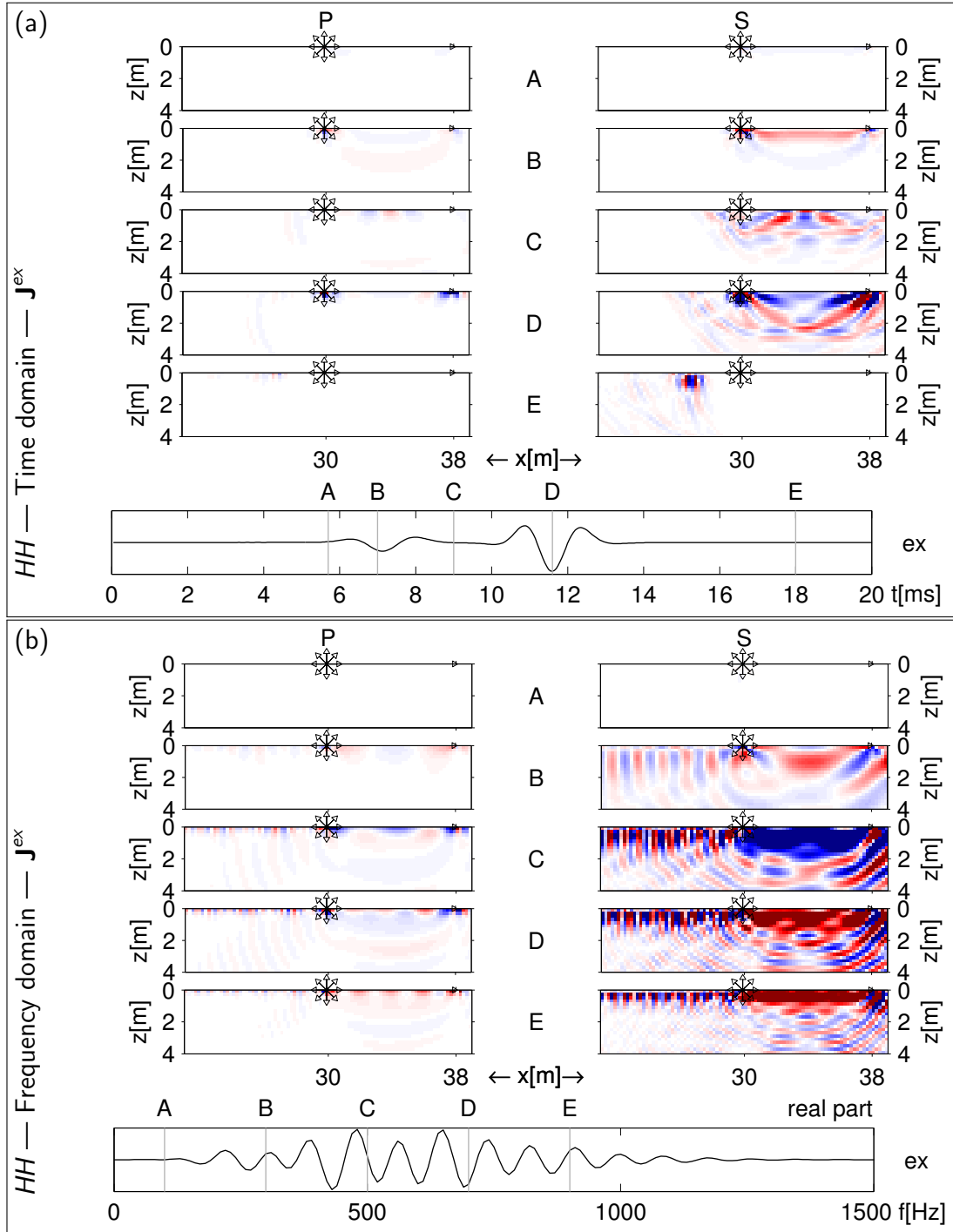


Figure 2.21: Sensitivities $^P \mathbf{J}^{ex}$ (left panels) and $^S \mathbf{J}^{ex}$ (right panels) in the homogeneous half space model HH . (a) shows time-domain results for times A to E (see Table 2.3), also marked on the seismograms, for a receiver at the position denoted in the colour plots. (b) displays the real part of the frequency-domain representations of (a) for frequencies A to E (see Table 2.3). At the bottom, the real parts of the frequency spectra of the seismograms shown in (a) are included. All data are scaled to a common value; see Figure 2.7b for the colour scale and Table 2.2 for the source and receiver symbols.

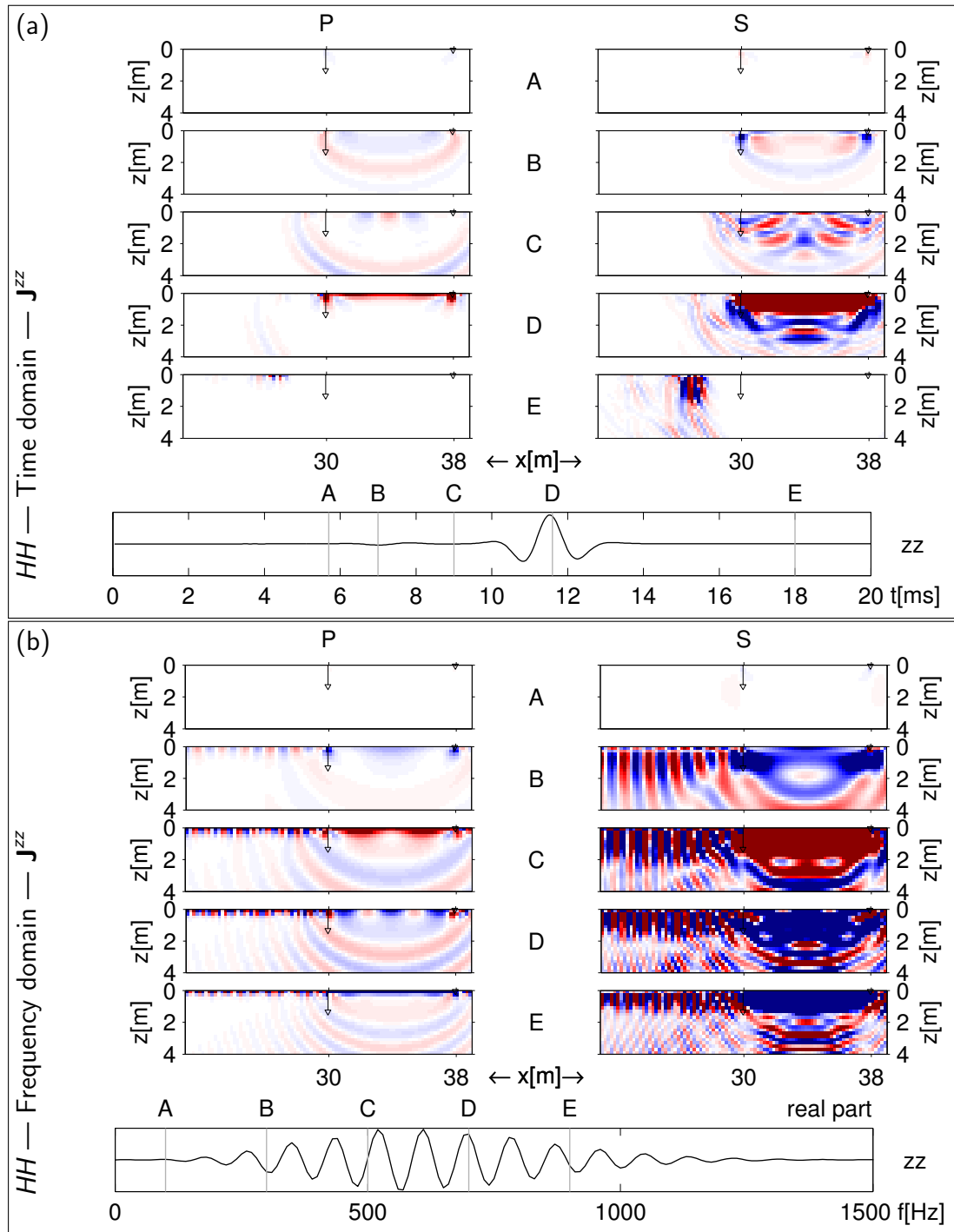


Figure 2.22: Sensitivities $^P J^{zz}$ (left panels) and $^S J^{zz}$ (right panels) in the homogeneous half space model HH . (a) shows time-domain results for times A to E (see Table 2.3), also marked on the seismograms, for a receiver at the position denoted in the colour plots. (b) displays the real part of the frequency-domain representations of (a) for frequencies A to E (see Table 2.3). At the bottom, the real parts of the frequency spectra of the seismograms shown in (a) are included. All data are scaled to a common value; see Figure 2.7b for the colour scale and Table 2.2 for the source and receiver symbols.

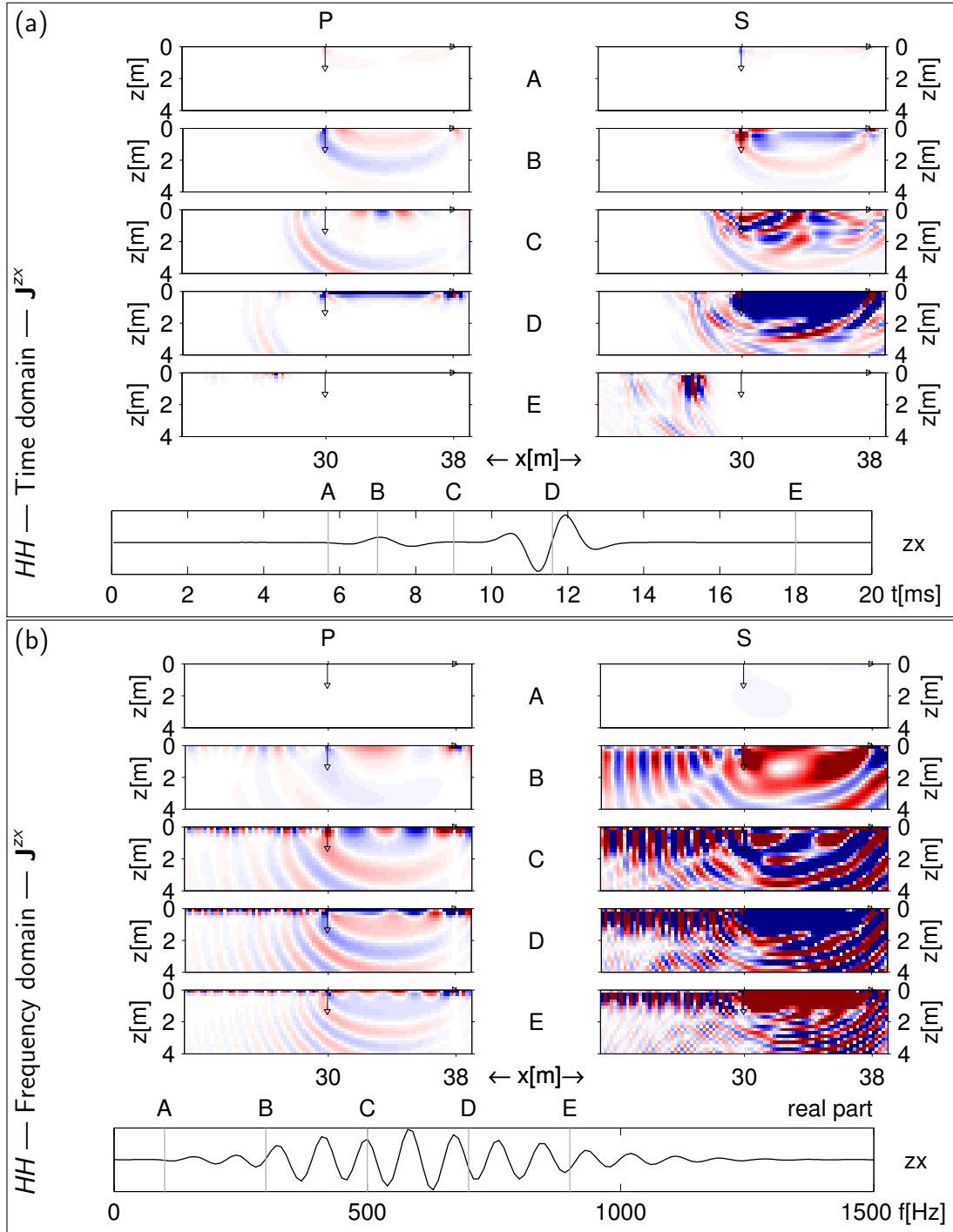


Figure 2.23: Sensitivities $^P J^{zx}$ (left panels) and $^S J^{zx}$ (right panels) in the homogeneous half space model HH . (a) shows time-domain results for times A to E (see Table 2.3), also marked on the seismograms, for a receiver at the position denoted in the colour plots. (b) displays the real part of the frequency-domain representations of (a) for frequencies A to E (see Table 2.3). At the bottom, the real parts of the frequency spectra of the seismograms shown in (a) are included. All data are scaled to a common value; see Figure 2.7b for the colour scale and Table 2.2 for the source and receiver symbols.

reasons of space economy, here I will only present results for the model *HL* and directed sources. Time-domain results are shown in Figure 2.24 and their frequency-domain counterparts are displayed in Figure 2.25. As already observed in the waveform plots, the additional phases, that is, reflections and mode conversions at the layer interface, the associated multiple reflections and the head wave propagating along the layer bottom, play a dominant role. This results in increased sensitivities associated with the P-type body waves within the entire upper layer with respect to those for the models without a discontinuity (see left sides of Figures 2.22 and 2.23). Of the sensitivities with respect to v_P , only $^P J^{zz}$ has significant amplitude below the layer boundary, especially at later times (see left side of Figure 2.24a), whereas the sensitivities with respect to v_S , especially $^S J^{xx}$ (see right side of Figure 2.24c), all stretch out into the half space and their amplitude in this region rather increases with time. This behaviour is also reflected in the frequency-domain representations, where significant amplitude in the half space can only be observed for $^P J^{zz}$ (see left side of Figure 2.25a) and the $^S J^{ij}$ shown on the right side of Figure 2.25.

2.4 Data information

After studying waveform characteristics and waveform sensitivities in the previous sections, the information content of an entire data set will now be analysed by studying properties of the approximate Hessian matrix. After some preliminary remarks, results for different experimental setups and subsurface models will be presented.

2.4.1 Preliminaries

A virtual data set

Computing sensitivities with the brute force perturbation approach for a suite of shot positions would be computationally very demanding. Since all subsurface models considered in this study are laterally invariant, it is possible to simulate data sets and their corresponding sensitivities by lateral shifting. I have computed sensitivities for a virtual data set involving nine shot positions, whereby each shot is recorded at eight receiver positions evenly spaced at one metre.

The resulting sensitivities cover an area to a depth of four meters and a width of ten meters. For this area, a coordinate system with the origin in the middle of the free surface of the model is chosen. It spans x-coordinates from -5 m to 5 m and z-coordinates from 0 m to 4 m, as it is shown in Figure 2.26.

This figure also illustrates how the original data needs to be ‘manipulated’. The sketch at the top represents the simulation layout and the model parametrisation already shown in Figures 2.3 and 2.4. Below, it is indicated how the data sets are shifted to obtain virtual sensitivities for different spatial source/receiver configurations. For example, to get sensitivities for a shot at position $x = 4$ m in the new coordinate system, I cut a subset out of the perturbed volume that starts one metre to the left of the leftmost receiver and ends one metre to the right of the source. Then, I shift this subset such that the middle of the region that was cut lies at the origin of the new coordinate system.

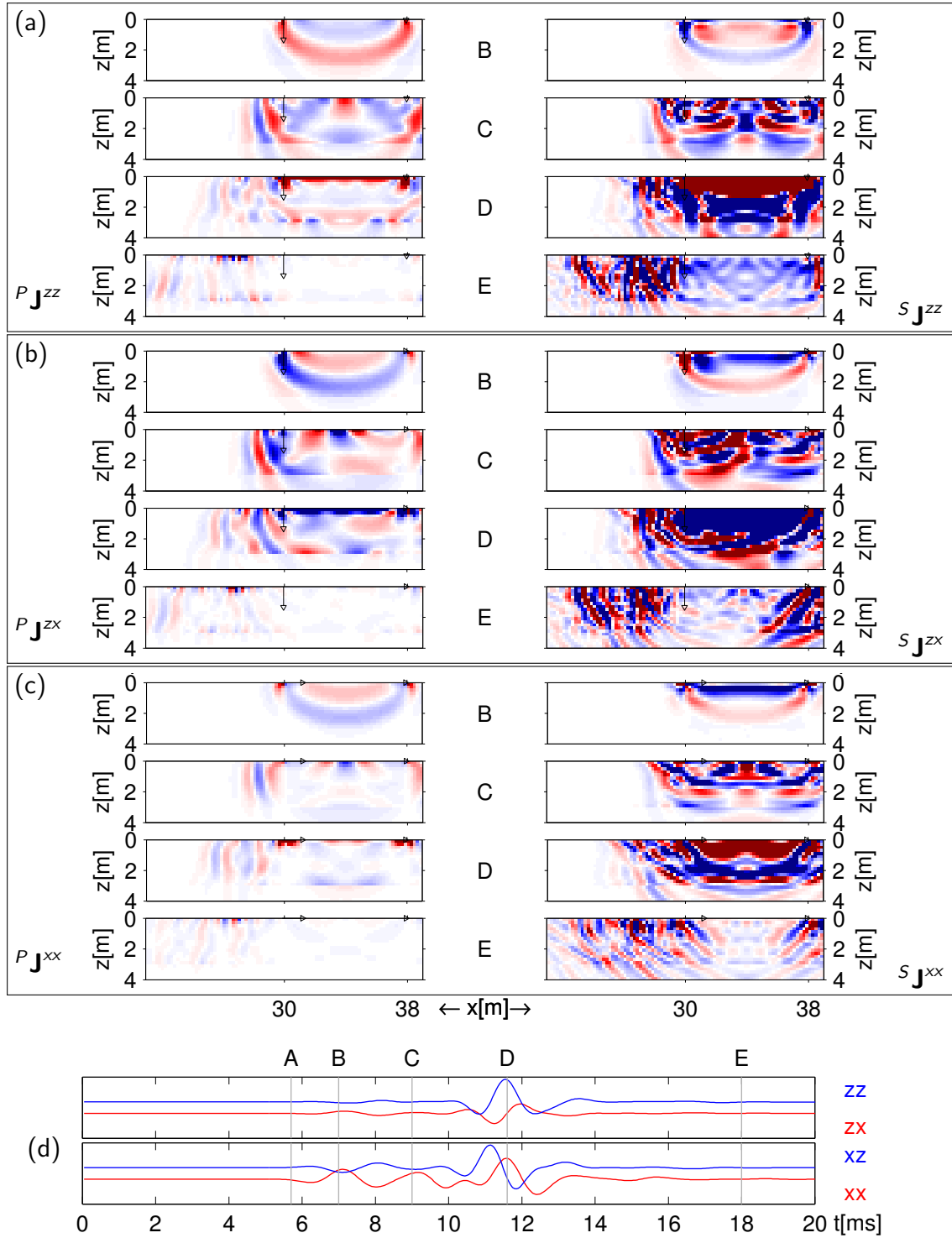
Time domain — *HL*

Figure 2.24: Time-domain representation of sensitivities $P_{J^{ij}}$ (left panels) and $S_{J^{ij}}$ (right panels) in layer model *HL*. (a) shows J^{zz} , (b) J^{zx} and (c) J^{xx} for times B to E (see Table 2.3), also marked on the seismograms shown in (d) for a receiver at the position denoted in the colour plots. All data are scaled to a common value; see Figure 2.7b for the colour scale and Table 2.2 for the source and receiver symbols.

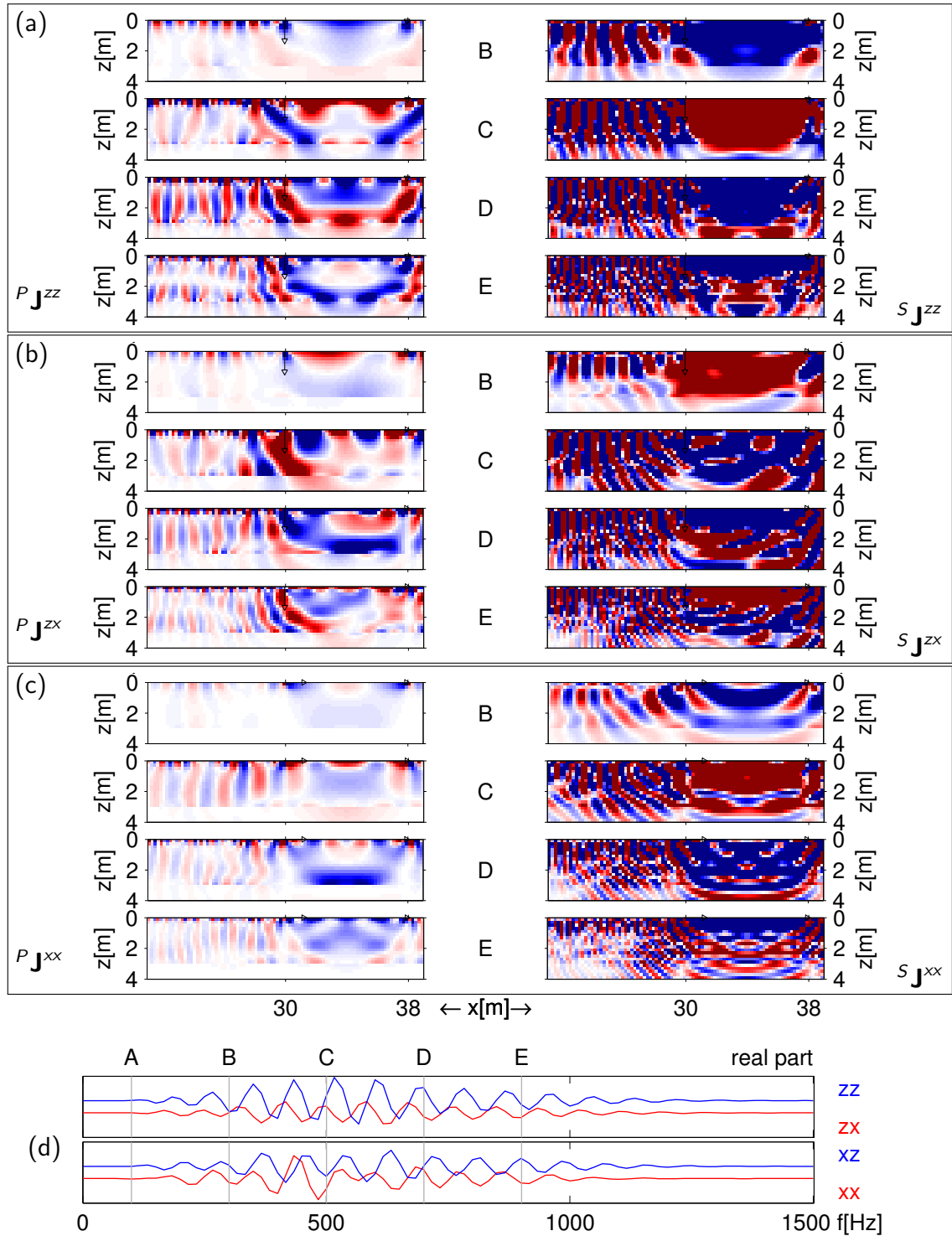
Frequency domain — *HL*

Figure 2.25: Real parts of the frequency-domain representation of $P \mathbf{J}^{ij}$ (left panels) and $S \mathbf{J}^{ij}$ (right panels) in *HL*. (a) shows \mathbf{J}^{zz} , (b) \mathbf{J}^{zx} and (c) \mathbf{J}^{xx} for frequencies B to E (see Table 2.3), also marked on the real parts of the seismogram frequency spectra shown in (d). All data are scaled to a common value; see Figure 2.7b for the colour scale and Table 2.2 for the source and receiver symbols.

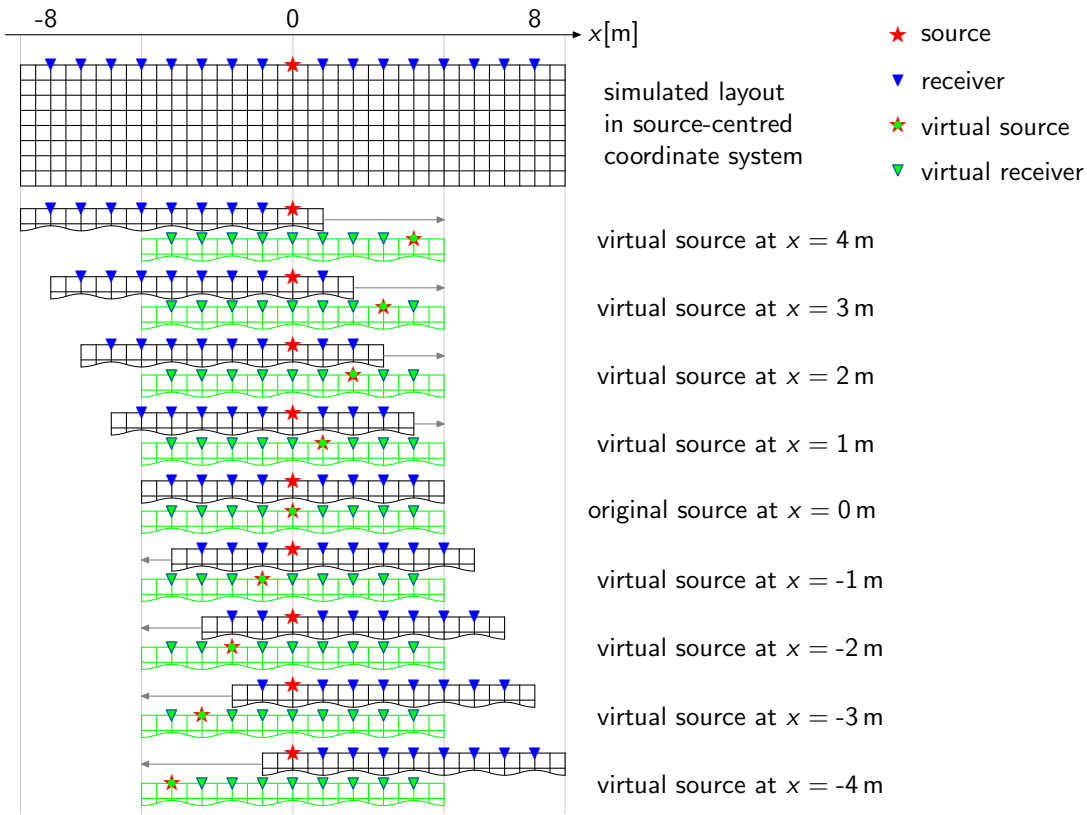


Figure 2.26: Computation scheme for creating \mathbf{J} for a virtual data set involving several source positions using the sensitivities calculated for only one source position and exploiting the lateral invariance of the subsurface models.

The complete data set and data selection

The complete data set for the data information analysis comprises data from nine sources, each recorded at eight receiver positions as shown in Figure 2.26. Referring to the terminology introduced in equations (2.9) to (2.11) of section 2.1.1, we have a total number of $n_{rs} = 72$ source/receiver pairs. For each pair, up to six different configurations are possible (zz, ez, zx, ex, xz and xx; pressure sensors are not considered, because they are rarely used in surface land-seismic applications; also note that xz is redundant to zx for such a symmetric model). The complete data vector \mathbf{d} , introduced in equation (2.10), therefore consists of $n_d = 9 \times 8 \times 6 = 432$ sub-vectors.

In the time domain, each of these sub-vectors includes all time samples of the seismogram for the source/receiver configuration to which the sub-vector belongs; in the frequency domain each comprises the real and imaginary parts of the frequency spectrum of this seismogram, for frequencies up to the maximum frequency for which the source wavelet contains significant energy, $f_{\max} = 1500$ Hz (see Figure 2.2).

In the following, I analyse the data information content offered by the six different combinations of source/receiver type. Additionally, I consider data sets including multiple combinations. For this, the additional pair of source type and receiver component 'a' is introduced, as a shorthand way for denoting the use of both types x and z. Thus, ea includes ez and ex, za stands for zx and zz, az for xz and zz and aa consists of the four

configurations xx , xz , zx and zz .

Choosing model parameter sets

Inversion of a real data set usually requires consideration of both the P- and the S-wave velocities. To gain further insights into the information content of seismic data sets, I have additionally considered model parameter sets that either include only v_P (v_S assumed to be known) or only v_S (v_P assumed to be known).

RER threshold determination and RER validity

Figure 2.27 shows an example for the semi-logarithmic normalised eigenvalue curves used to evaluate the information content of the approximate Hessian matrix. These curves are based on data sets computed for model HH for different choices of data selection. I have plotted results for the source/receiver configurations xz and zx . Data sets including all time samples in the time domain and real and imaginary parts of the spectrum for all frequencies in the frequency domain have been considered and eigenvalue curves are shown for all three possible selections of model parameters, that is for ' v_P only', ' v_S only' and ' v_P and v_S '.

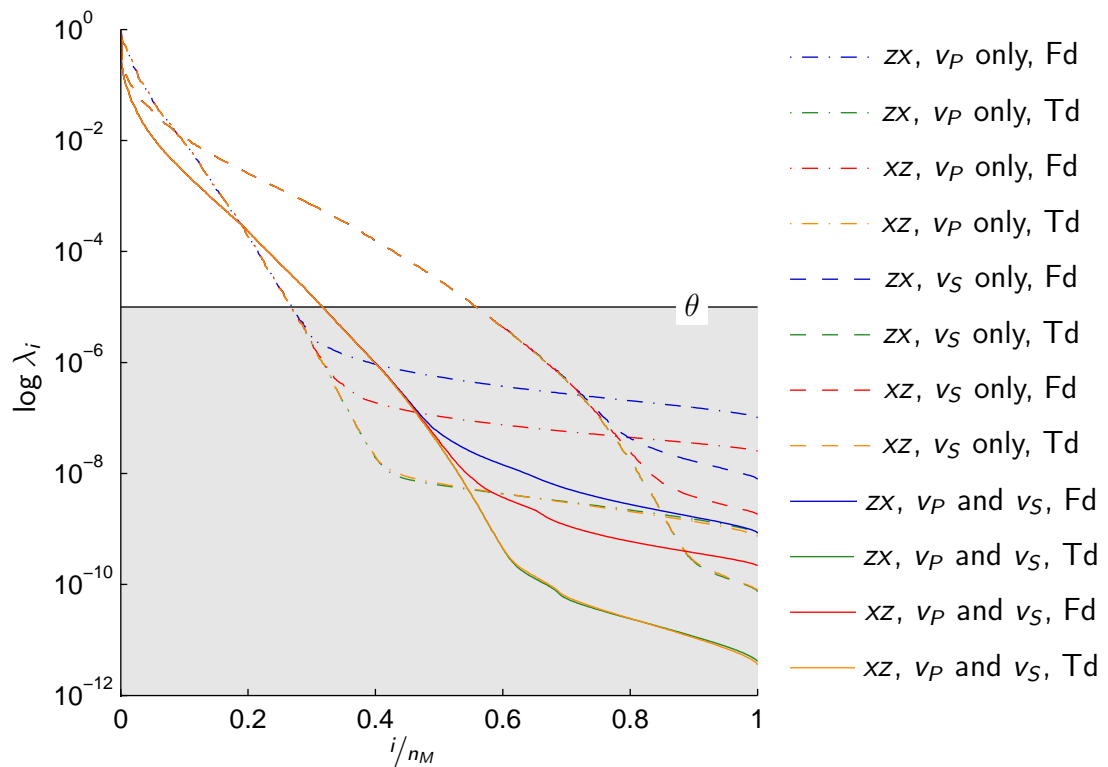


Figure 2.27: Semi-logarithmic plot of the normalised eigenvalues λ_i of the approximate Hessian matrix computed for the virtual data set for model HH . Complete data sets in both the time domain (Td) and the frequency domain (Fd), involving the equivalent configurations zx and xz , are compared.

Theoretically, all normalised eigenvalue curves included in Figure 2.27 for one particular parameter set should be identical. However, the lines for equivalent data sets are only identical for larger eigenvalues and start splitting up for eigenvalues $\lambda_i < 10^{-5}$. Below this threshold, the curves also do not exhibit the shape one would expect for an undamped problem, i.e. they are expected to drop off rapidly as shown in Maurer et al. (2009). Instead, the curves in Figure 2.27 flatten out and seem to reach a plateau value. I attribute this observation to numerical inaccuracies associated with the brute force perturbation approach for sensitivity computation, acting like an inherent damping. This effect is less severe for time-domain data. The FFT of the time-domain results (see section 2.1.1) may have introduced further inaccuracies.

On the basis of the observations made in Figure 2.27, I have chosen the threshold value $\theta = 10^{-5}$ for computing the RER values. By choosing such a relatively high value for θ , effects of numerical inaccuracies can be suppressed, but minor artifacts may persist. Therefore, subtle differences between RER values for different experimental setups should not be overinterpreted.

2.4.2 Data information analysis

Information offered by complete data sets

Examples of eigenvalue curves are shown in Figure 2.28. They are computed from approximate Hessian matrices that include both v_P and v_S velocity parameters and the

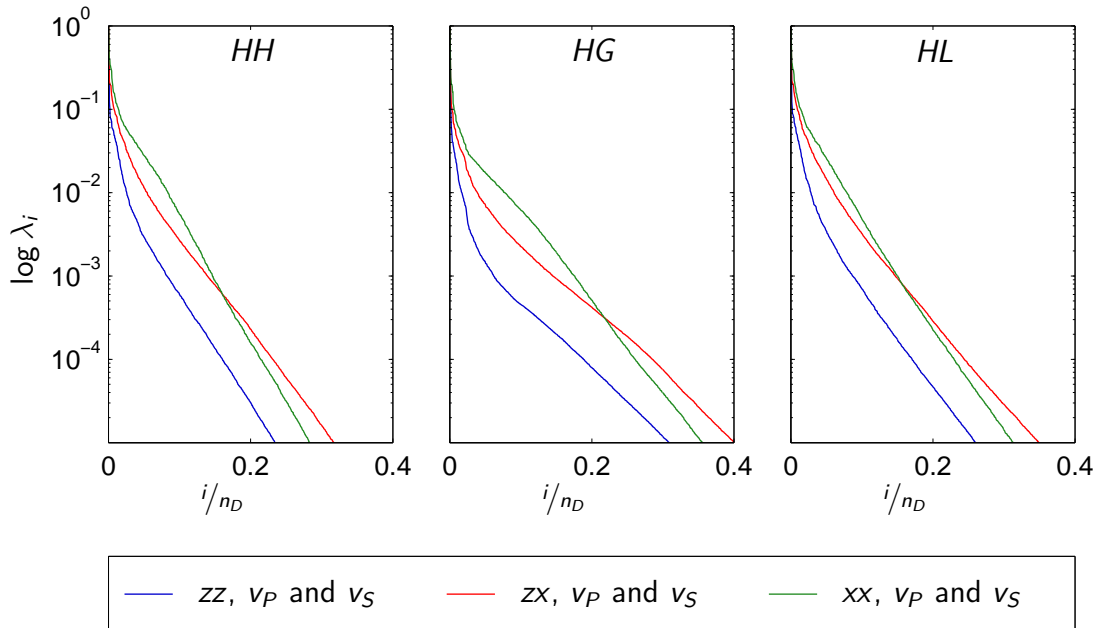


Figure 2.28: Eigenvalue curves for the approximate Hessian matrix based on complete data sets and including both v_P and v_S , from left to right for the three models *HH*, *HG* and *HL*. Only the parts for $\lambda_i > \theta$ are shown, such that the RER value of the respective source/receiver configurations is equivalent to the abscissa value of the corresponding curve.

complete seismograms. The curves are plotted such that the RER value corresponds to the intersections of the curves with the horizontal axes.

For all three models the source/receiver combination *zx* yields the highest RER values. The next best option appears to be *xx*, whereas *zz* shows the lowest RER values. For the gradient model *HG*, the RER values are generally the highest. This is caused by the low velocities near the surface (see Figure 2.1), which result in shorter wavelengths compared with the other models. For a fixed model parametrisation, as employed in this study, the generally shorter wavelengths lead to better constrained model parameters.

Figure 2.28 also illustrates a limitation of the RER criterion. The RER value considers only the intersection of the eigenvalue curves with a horizontal threshold line, but it ignores the actual shapes of the curves. It is noteworthy that the curves for combination *xx* lie above those for *zx* at larger eigenvalues, but the *xx* curves drop off more rapidly towards smaller eigenvalues. Possible other options for measuring the information content of a certain data set are offered by Curtis (2004). One alternative to account for the shape of the spectra is using the determinant of the Hessian matrix

$$\det(\mathbf{J}^T \mathbf{J}) = \prod_{i=1}^{n_M} \tilde{\lambda}_i, \quad (2.20)$$

as a measure (corresponds to Θ_3 in Curtis, 2004, equation (7)), where the $\tilde{\lambda}_i$ are the non-normalised eigenvalues (see 2.1.3) and n_M is the number of model parameters considered in $\mathbf{J}^T \mathbf{J}$, i.e. the number of its eigenvalues. Rewriting equation (2.20) for normalised eigenvalues results in

$$\det(\mathbf{J}^T \mathbf{J}) = \tilde{\lambda}_1^{n_M} 10^{\sum_{i=1}^{n_M} \log \lambda_i}, \quad (2.21)$$

where $\tilde{\lambda}_1$ is the maximal eigenvalue, the $\lambda_i = \tilde{\lambda}_i / \tilde{\lambda}_1$ are the normalised eigenvalues and \log denotes the base 10 logarithm. To focus on the numerical stability, that is on the relation between the highest and the smallest eigenvalue, the factor $\tilde{\lambda}_1^{n_M}$ should be omitted, and to get rid of the part of the eigenvalue curves affected by numerical inaccuracies, the sum should be restricted to the eigenvalues $\lambda_i > \theta$ above the threshold chosen for the RER criterion. Thus, a possible new criterion adapted to my study would be

$$\text{REA} := \frac{1}{n_M} \sum_{\lambda_i \geq \theta} \log \lambda_i, \quad (2.22)$$

which is the area delineated by the normalised eigenvalue curve, the vertical axis and the horizontal line $\lambda_i \equiv \theta$ in a semi-logarithmic plot, shaded grey in Figure 2.6; REA ranges between 0 and $\text{RER}(1 - \theta)$.

Such a determinant-related measure would return approximately the same value for curves like those found for the *xx* combinations as for those found for the *xz* combinations in Figure 2.28. It is a topic of future research to investigate in more detail whether the RER or a determinant-related measure is more useful. The RER is a direct measure of the size of the null space, whereas the determinant is just an indicator of the numerical stability of the inversion of the approximate Hessian matrix. Therefore, the RER is judged to be more relevant for present purposes, but the discussion above may indicate that the RER probably overestimates the difference between the *xx* and *zx* curves.

Figure 2.29 gives an overview of the RER values computed for all three half-space models and using complete data sets for different source/receiver configurations. The

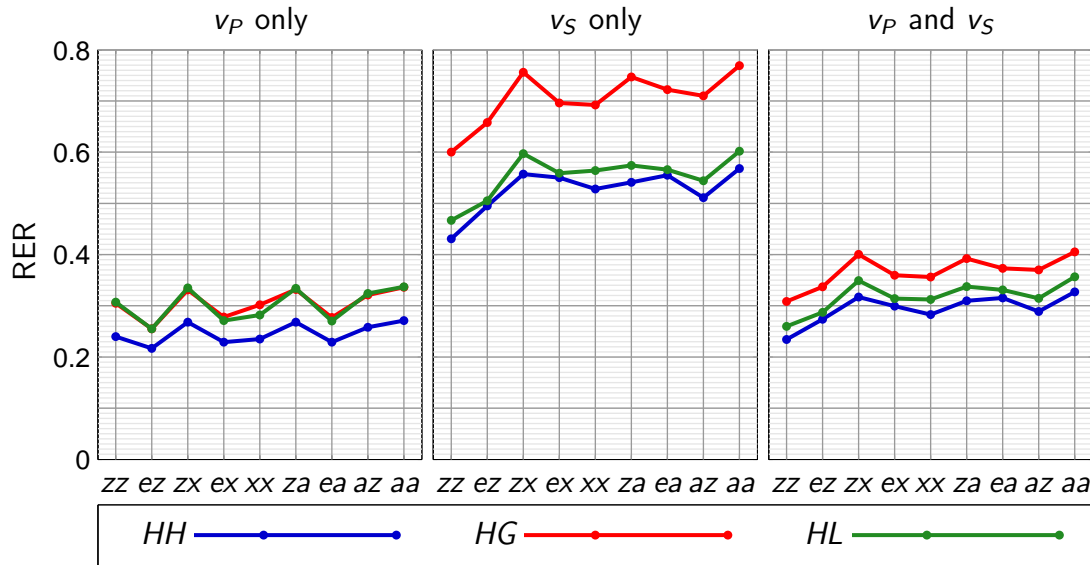


Figure 2.29: RER values for complete seismograms or all frequencies for different configuration selection and different models.

term ‘complete’ here denotes the usage of all available time samples, or, equivalently, all frequencies. The three panels show the RER for approximate Hessian matrices involving ‘ v_P only’ (left), ‘ v_S only’ (middle) and ‘ v_P and v_S ’ (right). From a practical point of view, the scenario ‘ v_P and v_S ’ is most important, because both velocities are usually unknown. Within each panel, the different source/receiver configurations are sorted by increasing experimental effort, starting with the combination of a vertically-directed source and a vertical component geophone (zz) and ending with the combination including horizontally-directed and vertically-directed sources as well as horizontal and vertical component geophones (aa).

Comparison of the ‘ v_P only’ and ‘ v_S only’ scenarios reveals that the data information content of the latter is significantly higher. This is the combined effect of the lower velocities (shorter wavelengths) and the dominance of the surface waves that are more sensitive to changes in v_S than changes in v_P (see section 2.3). Since the RER value is governed primarily by the least resolved model parameters, the values for the ‘ v_P and v_S ’ scenario are comparable to the ‘ v_P only’ case, while the shapes of the curves resemble those of the ‘ v_S only’ case.

The RER values for the different components and a particular subsurface model lie within a relatively narrow range. Considering the numerical accuracy problems and the approximate nature of the RER value discussed earlier in this section, small variations in Figure 2.29 should be interpreted with care, but it seems that the zz combinations are always inferior compared to all other source/receiver combinations. By contrast, the zx combinations seem to be a particularly good choice.

It should be mentioned, though, that in actual field surveys the implementation of a horizontally-directed source and/or geophones recording the horizontal component of the wave field is more problematic than the conventional vertically-directed source in combination with vertical-component geophones. Additional effort is required to ensure good ground coupling.

Using source forces at an angle of 45° to the surface in opposite directions (e.g. by hitting the opposite sides of a well positioned metal triangular cylinder with a sledge hammer), followed by the subtraction of the resulting data sets, is an effective way to produce an ‘equivalent’ horizontally-directed force. Adding the data resulting from the two source forces at 45° inclination results in data for an ‘equivalent’ vertically-directed force. When selecting geophones for recording the horizontal component of motion, great care has to be taken to ensure good sensor quality and ground coupling; simply using sensors built for recording the vertical component and mounting them horizontally is not advisable, unless the elements have a very high natural frequency.

It is also worth mentioning that the general shapes of the curves within one panel of Figure 2.29 are very similar. This implies that the results are not strongly model-dependent and can be generalised (at least for laterally invariant subsurface models).

Data selection in the time domain

In order to study the influence of the different wave types on the data information content, three different time windows were applied to the seismograms. They are determined by a window of the same length as the support of the source wavelet (i.e. the length of its nonzero part) shown in Figure 2.2, starting at 3 ms and ending at 5 ms. This window is ‘propagated’ with three different velocities over the seismogram sections (see Figure 2.30). The first window ‘propagates’ with velocity v_P and isolates the P -wave arrival out of the seismograms (window P). The second window (S) is propagated with

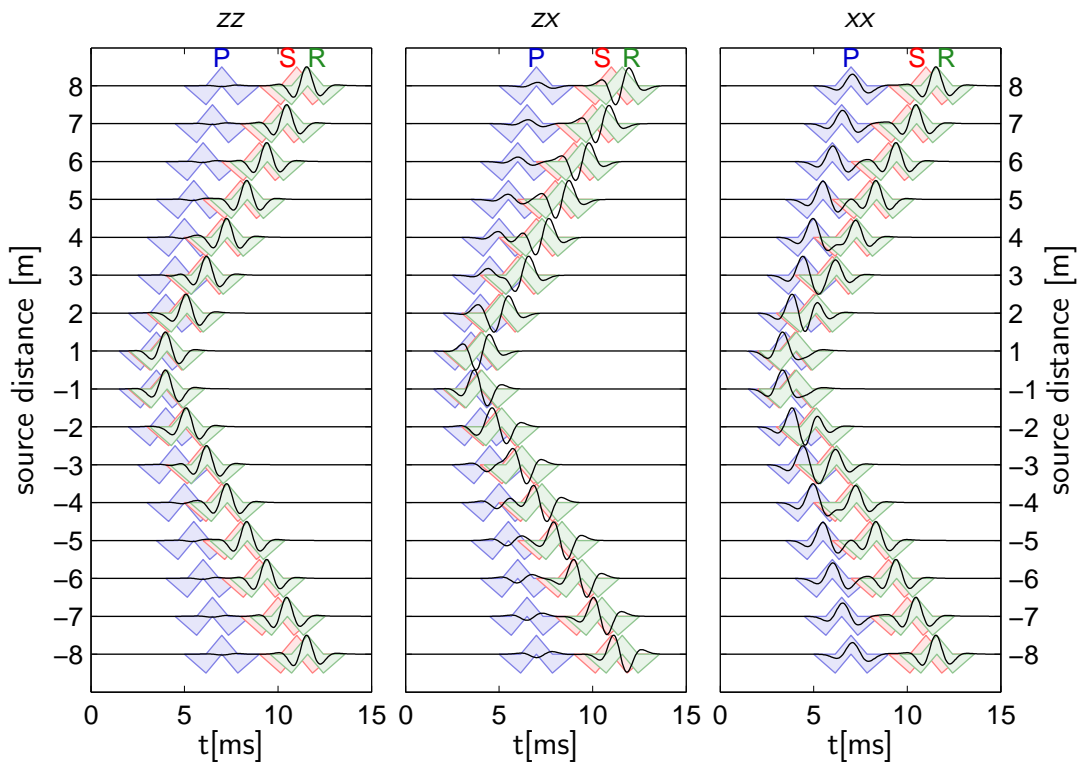


Figure 2.30: Time window selection on seismogram traces for the example of model *HH*. The locations of the source and the receivers is shown in Figure 2.3.

v_S to provide the S -wave contribution and the third window (R) is propagated with the Rayleigh velocity to match the surface wave train. As shown in Figure 2.30 these windows may overlap. For the homogeneous half space HH , the Rayleigh velocity can be computed analytically (Nkemzi, 2008), and for the other two models, HG and HL , the seismic velocities at the model surface are used for computing the Rayleigh velocity and propagating the time windows.

This approach captures the direct body waves and the Rayleigh wave, but neglects the refracted waves, the reflected waves and their multiples and the Love waves in the case of the layered model HL . Not taking into account these additional phases reflects the *a priori* nature of this study and illustrates a problem inherent in choosing data windows in the time domain, that is, the selected windows are strongly connected to the elastic parameters of the model under consideration, which are unknown.

Figure 2.31 shows the RER values for the same source/receiver configurations and models as Figure 2.29, but only time samples from a particular time window are considered for computing the approximate Hessian matrices. The curves for the complete data sets (all time samples) are repeated from Figure 2.29 as a reference.

Again, there is not too much difference between the respective models. The surface wave window R seems to provide the most information, closely followed by the shear wave window S. The least information can be expected from the P window.

The most important observation in Figure 2.31 is the significant reduction of information content described by the RER values obtained with the windowed seismograms. This was to be expected, for the reasons given in section 2.3.1 regarding the high sensitivities observed outside the region located between source and receiver at later times, i.e. the coda is the part of the seismogram that would change due to changes of model parameters in these regions, such that information about these parameters is lost by using only the time windows suggested above. If the quality of observed seismograms is sufficiently good, it is therefore advisable to consider the complete seismograms for an elastic waveform inversion.

Data selection in the frequency domain

Selection of individual frequencies is less model-dependent than windowing the seismograms. The frequency selection can be further constrained when the spectrum of the seismic source is known approximately.

Figure 2.32 is similar to of Figure 2.31 for frequency-domain data and the different frequency selections listed in Table 2.4. As a minimal data set, I use just the centre frequency of the source wavelet, $f_c = 500$ Hz (subset f_1). The second subset (f_2) includes the frequencies 100 Hz, 500 Hz and 900 Hz, and f_3 is further augmented by adding 300 Hz and 700 Hz. The subsets f_4 and f_5 include all frequencies up to 500 Hz and 900 Hz, respectively. As a reference, the results for all frequencies (f_0) are repeated from Figure 2.29.

As expected, using only a single frequency provides the least information. But, as already discussed in Maurer et al. (2009) for the acoustic case, selection of only a few well chosen frequencies can be highly beneficial. This is demonstrated with the results from subset f_2 , which contains only three frequencies. The RER values are comparable or even better than those from f_4 , which includes 50 frequencies. Subset f_3 provides an

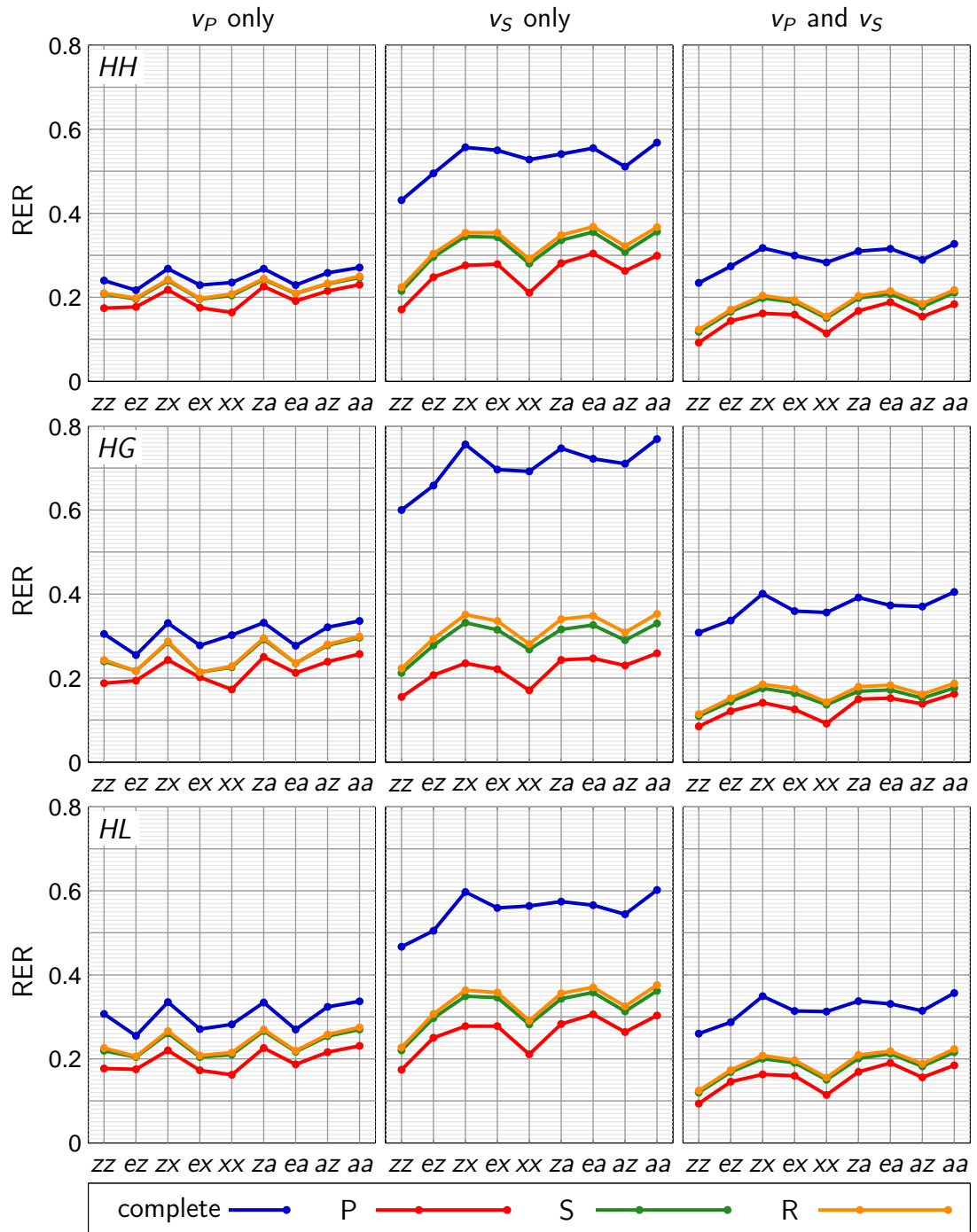


Figure 2.31: RER values for different source/receiver configurations and different time windows.

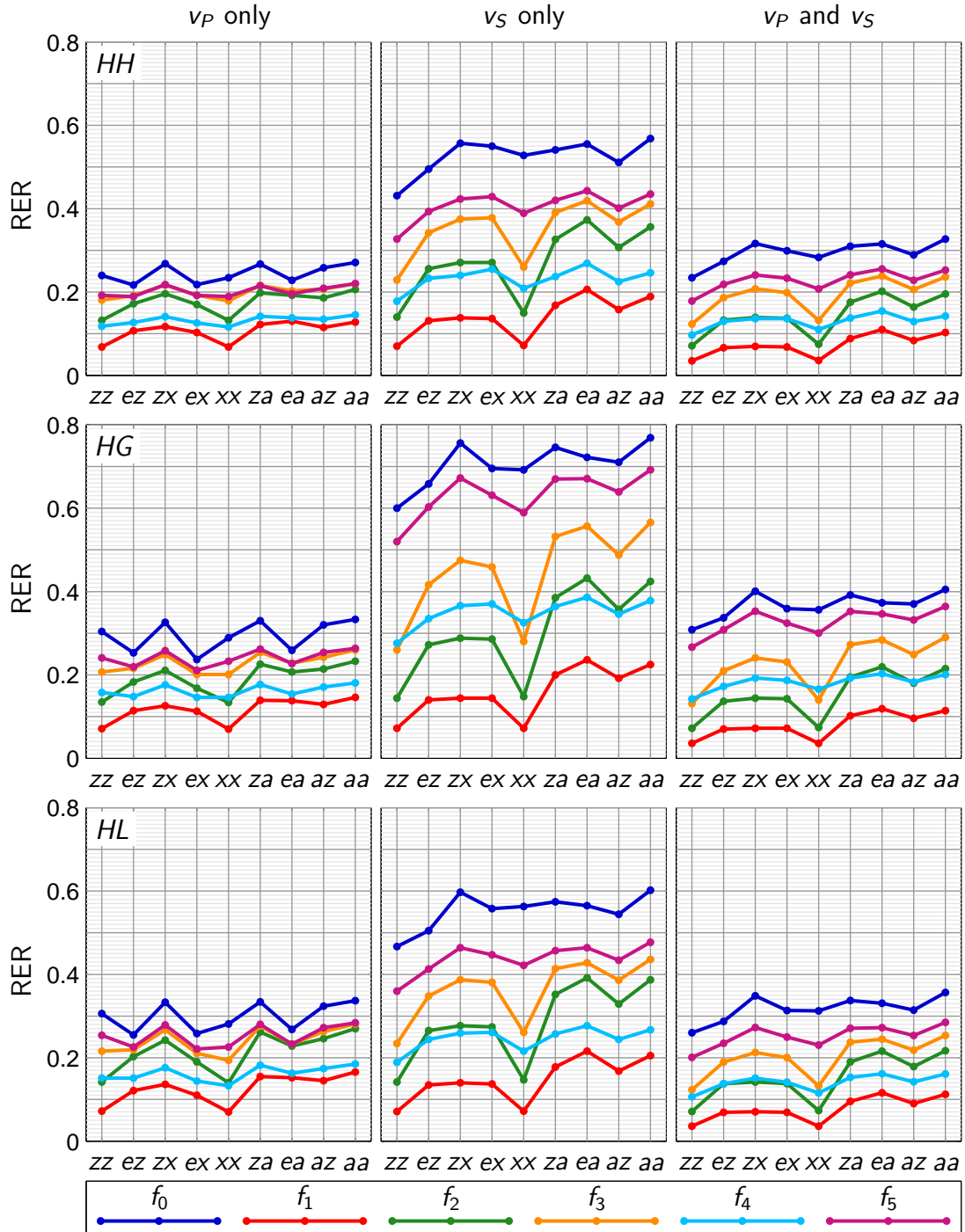


Figure 2.32: RER values for different source/receiver configurations and different frequency selection (see Table 2.4 for the abbreviations f_i).

subset	frequency selection [Hz]	n_f
f_0	0-1500	151
f_1	500	1
f_2	100,500,900	3
f_3	100,300,500,700,900	5
f_4	0-500	50
f_5	0-900	90

Table 2.4: Frequency subsets used for computing the RER values shown in Figure 2.32. n_f is the number of frequencies contained in the respective subsets and f_0 is the complete set.

excellent benefit-cost-ratio. With only five frequencies, relatively high RER values can be achieved. If computational costs are not an issue, subset f_5 , consisting of 90 frequencies, may be a useful option. Of course, the complete data set f_0 provides the highest RER values, but the very high frequencies, included in f_0 and omitted in f_5 , will have small amplitudes and may therefore be strongly contaminated by noise.

Results shown in Figure 2.32 indicate that, with a judicious selection of a few frequencies, large parts of the data information content offered by the complete seismograms can be exploited. This seems to be much more difficult in the time domain, where subsets are generated by data windowing (Figure 2.31).

2.5 Conclusions

In this chapter, I have analysed some properties of elastic waveform data using a few very simple 1D models and various recording configurations and source/receiver types and directivity configurations. Despite the simplicity of the experimental layouts, the study revealed a number of important results that may influence (i) how seismic data sets, amenable for characterising the shallow subsurface, should be collected, and (ii) how waveform inversions should be performed.

1. Wave field and waveform sensitivity analyses have clearly indicated the inappropriateness of the acoustic approximation. The acoustic approximation would require the data to be windowed around the first arriving P-wave, but for small offsets such a time window may still be contaminated by S-wave and surface wave arrivals. Furthermore, it was shown in Figure 2.31 that large parts of the information content of the seismograms is lost, when the data are windowed around specific arrivals.
2. Comparisons of different source/receiver directivity configurations revealed that there are surprisingly small differences between the different combinations. Generally, seismic waves excited by a vertical force (e.g. a weight drop or sledge hammer) and recorded with vertical-component geophones provide the least information, whereas the combination of a vertical force and a horizontal-component receiver seems to be most favourable, if one is prepared to make the additional

effort for implementing this uncommon recording configuration in an actual field survey.

3. My investigations are not entirely conclusive as to whether time- or frequency-domain inversions are more effective. The sensitivity patterns in the two domains are very different. If the complete seismograms and all frequencies are considered, the results are identical, but the picture changes when selected time windows or only a few frequencies are analysed. Information content decreases quite considerably for time-windowed seismograms, but judicious selection of a few key frequencies can maintain similar information content as would be offered by using all frequencies. This at least suggests higher efficiency of frequency-domain inversions, as has been reported by others (e.g. Sirgue and Pratt, 2004).
4. The above findings are not strongly model-dependent. Results for all the subsurface models considered in this study led to similar conclusions, keeping in mind the fact that lateral model variations were not taken into account.

Chapter 3

Theory, implementation and validation of a frequency-domain finite element (FEM) forward solver

In this chapter I describe a frequency-domain finite element (FEM) forward solver for 2.5D elastic problems that I developed as part of my thesis. I start with the theoretical and technical aspects, describing my implementation of the FEM coding with perfectly matched layers (PMLs). The second part of the chapter addresses the accuracy and efficiency of the algorithm. Here, I will restrict myself to the pure 2D problem, which is a special case (line source or $k_y \equiv 0$) of the 2.5D problem (point source). This is required for making comparisons with the time-domain FDTD code already considered in chapter 2. Appraising the accuracy of the full 2.5D solution is more complicated. Therefore, I have devoted a separate chapter to this issue (chapter 4).

3.1 Theory and formulae

After giving the elastic equations of motion, I present my implementation of the finite element method. My approach is similar to that described in Min et al. (2003), but some modifications were required to facilitate 2.5D computations. Next, I give a short motivation for using Perfectly Matched Layers (PMLs) and show how they are implemented in the code. After that, the problem of source implementation is addressed and finally the procedure to assemble the complete system matrix out of the sub-matrices for the single elements is explained.

3.1.1 2.5D elemental equations

The equations of motion

In the frequency domain, the 3D equations of motion for an elastic, isotropic medium can be written as (e.g. Aki and Richards, 2009)

$$\begin{aligned}
 0 = & \rho\omega^2 \bar{u}_x + \partial_x [(\lambda + 2\mu)\partial_x \bar{u}_x + \lambda(\partial_y \bar{u}_y + \partial_z \bar{u}_z)] \\
 & + \partial_y [\mu(\partial_y \bar{u}_x + \partial_x \bar{u}_y)] \\
 & + \partial_z [\mu(\partial_z \bar{u}_x + \partial_x \bar{u}_z)] \\
 & + \bar{f}_x
 \end{aligned} \tag{3.1a}$$

$$\begin{aligned}
 0 = & \rho\omega^2 \bar{u}_y + \partial_x [\mu(\partial_y \bar{u}_x + \partial_x \bar{u}_y)] \\
 & + \partial_y [(\lambda + 2\mu)\partial_y \bar{u}_y + \lambda(\partial_x \bar{u}_x + \partial_z \bar{u}_z)] \\
 & + \partial_z [\mu(\partial_z \bar{u}_y + \partial_y \bar{u}_z)] \\
 & + \bar{f}_y
 \end{aligned} \tag{3.1b}$$

$$\begin{aligned}
 0 = & \rho\omega^2 \bar{u}_z + \partial_x [\mu(\partial_z \bar{u}_x + \partial_x \bar{u}_z)] \\
 & + \partial_y [\mu(\partial_z \bar{u}_y + \partial_y \bar{u}_z)] \\
 & + \partial_z [(\lambda + 2\mu)\partial_z \bar{u}_z + \lambda(\partial_x \bar{u}_x + \partial_y \bar{u}_y)] \\
 & + \bar{f}_z,
 \end{aligned} \tag{3.1c}$$

where the \bar{u}_i are the components of the vector field of spectral displacement $\bar{\mathbf{u}}$, ρ is the density, λ and μ are the Lamé parameters, $\omega = 2\pi f$ is the angular frequency and the \bar{f}_i , $i \in \{x, y, z\}$ are the components of the source force. The definition of the Fourier transform that I use is given in Appendix A.1. Note, that the bar above the displacement and force terms indicates Fourier transformation with respect to time.

For obtaining the corresponding 2.5D solution, equations (3.1) are Fourier transformed with respect to the cross line coordinate y , using (A.2). This leads to the 2.5D frequency domain elastic equations

$$\begin{aligned}
 0 = & \rho\omega^2 \bar{\bar{u}}_x + \partial_x [(\lambda + 2\mu)\partial_x \bar{\bar{u}}_x + \lambda(ik_y \bar{\bar{u}}_y + \partial_z \bar{\bar{u}}_z)] \\
 & + ik_y [\mu(ik_y \bar{\bar{u}}_x + \partial_x \bar{\bar{u}}_y)] \\
 & + \partial_z [\mu(\partial_z \bar{\bar{u}}_x + \partial_x \bar{\bar{u}}_z)] \\
 & + \bar{\bar{f}}_x
 \end{aligned} \tag{3.2a}$$

$$\begin{aligned}
 0 = & \rho\omega^2 \bar{\bar{u}}_y + \partial_x [\mu(ik_y \bar{\bar{u}}_x + \partial_x \bar{\bar{u}}_y)] \\
 & + ik_y [(\lambda + 2\mu)ik_y \bar{\bar{u}}_y + \lambda(\partial_x \bar{\bar{u}}_x + \partial_z \bar{\bar{u}}_z)] \\
 & + \partial_z [\mu(\partial_z \bar{\bar{u}}_y + ik_y \bar{\bar{u}}_z)] \\
 & + \bar{\bar{f}}_y
 \end{aligned} \tag{3.2b}$$

$$\begin{aligned}
 0 = & \rho\omega^2 \bar{\bar{u}}_z + \partial_x [\mu(\partial_z \bar{\bar{u}}_x + \partial_x \bar{\bar{u}}_z)] \\
 & + ik_y [\mu(\partial_z \bar{\bar{u}}_y + ik_y \bar{\bar{u}}_z)] \\
 & + \partial_z [(\lambda + 2\mu)\partial_z \bar{\bar{u}}_z + \lambda(\partial_x \bar{\bar{u}}_x + ik_y \bar{\bar{u}}_y)] \\
 & + \bar{\bar{f}}_z,
 \end{aligned} \tag{3.2c}$$

where k_y is the wavenumber corresponding to the y -direction and the double bar indicates double Fourier transformation (with respect to time and y -coordinate). Here, I

made use of the differentiation property of Fourier transformation pairs, $\frac{\partial}{\partial y} \bar{\bar{u}} = ik_y \bar{\bar{u}}$. In contrast to equation (3.1), this is a differential equation in only two variables, x and z , with k_y appearing as a parameter.

The Galerkin method

An important concept of a finite element (FEM) algorithm is the so called *weak formulation* of the underlying equations of motion (3.2) (e.g. Brenner and Scott, 2008). Assuming the components of the solution vector $\bar{\bar{u}}$ to lie within a certain vector space — $\bar{\bar{u}}_i \in \mathcal{U}$ —, I compute the inner product of the equations (3.2) with an arbitrary test function $w_A \in \mathcal{U}$, defined as an integration over the computational domain. Performing $\int_{\Omega} w_A \{ (3.2a) \} d\Omega$, for example for the x -component results in

$$\begin{aligned}
 0 = & \int_{\Omega} \{ w_A \rho \omega^2 \bar{\bar{u}}_x + w_A \bar{\bar{f}}_x \} d\Omega \\
 & + \int_{\Omega} \{ -\partial_x w_A [(\lambda + 2\mu) \partial_x \bar{\bar{u}}_x + \lambda (ik_y \bar{\bar{u}}_y + \partial_z \bar{\bar{u}}_z)] \\
 & \quad + ik_y w_A [\mu (ik_y \bar{\bar{u}}_x + \partial_x \bar{\bar{u}}_y)] \\
 & \quad - \partial_z w_A [\mu (\partial_z \bar{\bar{u}}_x + \partial_x \bar{\bar{u}}_z)] \} d\Omega \\
 & + \oint_{\partial\Omega=\Gamma} \{ w_A [(\lambda + 2\mu) \partial_x \bar{\bar{u}}_x + \lambda (ik_y \bar{\bar{u}}_y + \partial_z \bar{\bar{u}}_z)] n_x \\
 & \quad + w_A [\mu (\partial_z \bar{\bar{u}}_x + \partial_x \bar{\bar{u}}_z)] n_z \} d\Gamma,
 \end{aligned} \tag{3.3}$$

where I have carried out an integration by parts, giving rise to the line integral over the boundary Γ of the computational domain Ω . Requiring that

$$0 \equiv \oint_{\partial\Omega=\Gamma} \{ w_A [(\lambda + 2\mu) \partial_x \bar{\bar{u}}_x + \lambda (ik_y \bar{\bar{u}}_y + \partial_z \bar{\bar{u}}_z)] n_x + w_A [\mu (\partial_z \bar{\bar{u}}_x + \partial_x \bar{\bar{u}}_z)] n_z \} d\Gamma \tag{3.4}$$

imposes natural Neumann boundary conditions on the solution, that is, $\bar{\bar{u}}$ is the solution for a free surface all around the computational domain. Some algebraic reformulations of condition (3.4) lead to

$$\begin{aligned}
 0 = & \int_{\Omega} \{ w_A (\rho \omega^2 - \mu k_y^2) \bar{\bar{u}}_x + w_A \bar{\bar{f}}_x + ik_y w_A \mu \partial_x \bar{\bar{u}}_y \\
 & - \partial_x w_A [(\lambda + 2\mu) \partial_x \bar{\bar{u}}_x + \lambda (ik_y \bar{\bar{u}}_y + \partial_z \bar{\bar{u}}_z)] - \partial_z w_A [\mu (\partial_z \bar{\bar{u}}_x + \partial_x \bar{\bar{u}}_z)] \} d\Omega,
 \end{aligned} \tag{3.5}$$

which is still equivalent to equation 3.2a.

Now, the actual approximation step is carried out, which makes the numerical treatment of the equation possible. Instead of aiming for the exact solution $\bar{\mathbf{u}}$, I compute its projection $\mathfrak{U} = \mathbf{P}_N \bar{\mathbf{u}}$ onto a finite dimensional subspace $\mathcal{U}_N \subset \mathcal{U}$, spanned by the piecewise linear shape functions N_A . The projection of component \bar{u}_ζ onto \mathcal{U} can be written as

$$\mathbf{P}_N \bar{u}_\zeta = \sum_i U_{A\zeta} N_i, \quad \zeta \in \{x, y, z\}. \quad (3.6)$$

Following the Galerkin formalism (see for example Brenner and Scott, 2008) the arbitrary test functions in (3.5) are chosen to coincide with the shape functions, that is $w_A = N_A$, resulting in

$$\begin{aligned} 0 = & \int_{\Omega} N_i \bar{f}_x d\Omega + \sum_B U_x^B \int_{\Omega} \{ N_i (\rho\omega^2 - \mu k_y^2) N_j \} d\Omega \\ & + \sum_B U_x^B \int_{\Omega} \{ -\partial_x N_i (\lambda + 2\mu) \partial_x N_j - \partial_z N_i \mu \partial_z N_j \} d\Omega \\ & + \sum_B U_y^B \int_{\Omega} \{ -\partial_x N_i \lambda i k_y N_j + i k_y N_i \mu \partial_x N_j \} d\Omega \\ & + \sum_B U_z^B \int_{\Omega} \{ -\partial_x N_i \lambda \partial_z N_j + \partial_z N_i \mu \partial_x N_j \} d\Omega. \end{aligned} \quad (3.7)$$

By means of such an approach, the equations of motion (3.2) can be turned into a matrix equation, as demonstrated in the following section.

Matrix formulation

To complete the discretisation, the computational domain is divided into the eponymous finite elements. I use simple rectangular elements with corner nodes I, J, K , and L as depicted in Figure 3.1.

For now, the derivation is restricted to equations for one finite element $\Omega_e \subset \Omega$. This is possible, since the integration over the complete computational domain can simply be split into a sum of integrations over the single elements. This will be described in more detail in section 3.1.4. One of the addends constituting equation (3.5) then reads

$$\begin{aligned} 0 = & \int_{\Omega_e} \{ w_A (\rho\omega^2 - \mu k_y^2) \bar{u}_x + w_A \bar{f}_x + i k_y w_A \mu \partial_x \bar{u}_y \\ & - \partial_x w_A [(\lambda + 2\mu) \partial_x \bar{u}_x + \lambda (i k_y \bar{u}_y + \partial_z \bar{u}_z)] - \partial_z w_A [\mu (\partial_z \bar{u}_x + \partial_x \bar{u}_z)] \} d\Omega. \end{aligned} \quad (3.8)$$

$\Omega_e = [x_1, x_2] \times [z_1, z_2] \subset \mathbb{R}^2$ is the area of one element in the FEM-mesh and for convenience I introduce a local coordinate system as shown in Figure 3.1 (compare with Min et al., 2003, Figure A1, which has reversed z -direction). Denoting the element's upper left corner with (x_1, z_1) and its lower right corner with (x_2, z_2) , the relations between the global and local coordinates for this element can be written as

$$\xi = \frac{2}{\Delta x} (x - x_m), \quad \eta = \frac{2}{\Delta z} (z - z_m), \quad (3.9a)$$

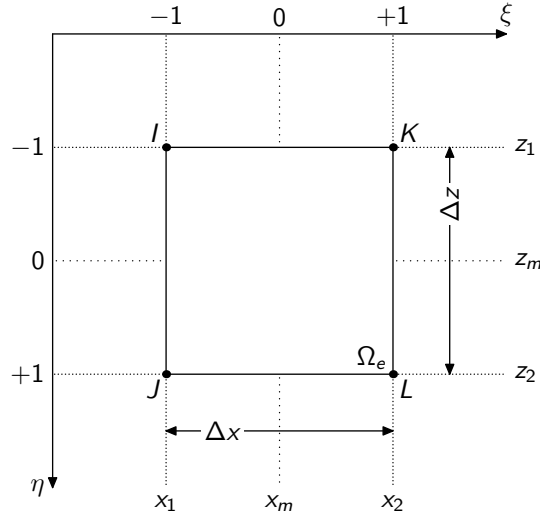


Figure 3.1: One element of the FEM grid with local (ξ, η) and global (x, z) coordinate systems indicated.

where

$$x_m = \frac{1}{2}(x_1 + x_2) \quad \text{and} \quad z_m = \frac{1}{2}(z_1 + z_2) \quad (3.9b)$$

are its midpoint coordinates and

$$\Delta x = x_2 - x_1 \quad \text{and} \quad \Delta z = z_2 - z_1 \quad (3.9c)$$

denote its width and height. With these relations, the derivatives and the volume element can be rewritten as

$$\partial_x = \frac{2}{\Delta x} \partial_\xi, \quad \partial_z = \frac{2}{\Delta z} \partial_\eta \quad \text{and} \quad d\Omega = dx dz = \frac{\Delta x \Delta z}{4} d\xi d\eta \quad (3.10)$$

(c.f. Min et al., 2003, equations (A9) to (A12)).

The linear shape functions N_A , $A \in \{I, J, K, L\}$ are chosen to be of tetrahedral shape, assuming a value of one at the location of their respective nodes and zero at every other node, that is,

$$\begin{aligned} N_I &= \frac{1}{4}(1 - \xi)(1 - \eta) & N_J &= \frac{1}{4}(1 - \xi)(1 + \eta) \\ N_K &= \frac{1}{4}(1 + \xi)(1 - \eta) & N_L &= \frac{1}{4}(1 + \xi)(1 + \eta) \end{aligned} \quad (3.11)$$

(compare with Min et al., 2003, equation (A8)). With these definitions, the projection (3.6) onto \mathcal{U}_N can be written as

$$U_\zeta^e = \sum_A U_{A\zeta}^e N_A, \quad U_{A\zeta}^e := \bar{\bar{u}}_\zeta(x_A, z_A), \quad \zeta \in \{x, y, z\}, \quad (3.12)$$

where I defined $U_{A\zeta}^e$ as the value of the solution vector component $\bar{\bar{u}}_\zeta$ at the location of node A .

The Galerkin step, that is choosing $w_A = N_A$, then leads to

$$\begin{aligned}
 0 = & \int_{\Omega_e} N_A \bar{\bar{f}}_x d\Omega + \sum_B U_{Bx}^e \int_{\Omega_e} \{ N_A (\rho\omega^2 - \mu k_y^2) N_B \} d\Omega \\
 & + \sum_B U_{Bx}^e \int_{\Omega_e} \{ -\partial_x N_A (\lambda + 2\mu) \partial_x N_B - \partial_z N_A \mu \partial_z N_B \} d\Omega \\
 & + \sum_B U_{By}^e \int_{\Omega_e} \{ -\partial_x N_A \lambda i k_y N_B + i k_y N_A \mu \partial_x N_B \} d\Omega \\
 & + \sum_B U_{Bz}^e \int_{\Omega_e} \{ -\partial_x N_A \lambda \partial_z N_B + \partial_z N_A \mu \partial_x N_B \} d\Omega.
 \end{aligned} \tag{3.13}$$

This can be abbreviated to

$$0 = F_{Ax}^e + \sum_B \{ M_{ABxx}^e U_{Bx}^e + K_{ABxx}^e U_{Bx}^e + K_{ABxy}^e U_{By}^e + K_{ABxz}^e U_{Bz}^e \}; \tag{3.14}$$

which is the elemental version of (3.7). Explicit expressions for M_{ABii}^e and K_{ABij}^e with $i, j \in \{x, y, z\}$ are given in equations (3.20) and (3.21)—see later.

The steps that led from equation (3.2a) to (3.13) can be repeated for equations (3.2b) and (3.2c), thus transforming the equations of motion (3.2) into the matrix equation (modified after Min et al., 2003, equation (A2))

$$\mathbf{M}^e \mathfrak{U}^e + \mathbf{K}^e \mathfrak{U}^e + \mathfrak{F}^e = \mathbf{0}, \tag{3.15}$$

where we combined the scalar values $F_{A\zeta}$, $U_{B\zeta}$, $M_{AB\zeta v}$ and $K_{AB\zeta v}$ into the source vector

$$\mathfrak{F}^e = \begin{bmatrix} \mathfrak{F}_x^e \\ \mathfrak{F}_y^e \\ \mathfrak{F}_z^e \end{bmatrix} \quad \text{with} \quad \mathfrak{F}_\zeta^e = \begin{bmatrix} F_{I\zeta}^e \\ F_{J\zeta}^e \\ F_{K\zeta}^e \\ F_{L\zeta}^e \end{bmatrix}, \quad \zeta \in \{x, y, z\}, \tag{3.16}$$

the elemental displacement vector,

$$\mathfrak{U}^e = \begin{bmatrix} \mathfrak{U}_x^e \\ \mathfrak{U}_y^e \\ \mathfrak{U}_z^e \end{bmatrix} \quad \text{with} \quad \mathfrak{U}_\zeta^e = \begin{bmatrix} U_{I\zeta}^e \\ U_{J\zeta}^e \\ U_{K\zeta}^e \\ U_{L\zeta}^e \end{bmatrix}, \quad \zeta \in \{x, y, z\}, \tag{3.17}$$

the elemental mass matrix

$$\mathbf{M}^e = \begin{bmatrix} \mathbf{M}_{xx}^e & 0 & 0 \\ 0 & \mathbf{M}_{zz}^e & 0 \\ 0 & 0 & \mathbf{M}_{yy}^e \end{bmatrix} \quad \text{with} \tag{3.18a}$$

$$\mathbf{M}_{\zeta\zeta}^e = \begin{bmatrix} M_{II\zeta\zeta}^e & M_{IJ\zeta\zeta}^e & M_{IK\zeta\zeta}^e & M_{IL\zeta\zeta}^e \\ M_{JI\zeta\zeta}^e & M_{JJ\zeta\zeta}^e & M_{JK\zeta\zeta}^e & M_{JL\zeta\zeta}^e \\ M_{KI\zeta\zeta}^e & M_{KJ\zeta\zeta}^e & M_{KK\zeta\zeta}^e & M_{KL\zeta\zeta}^e \\ M_{LI\zeta\zeta}^e & M_{LJ\zeta\zeta}^e & M_{LK\zeta\zeta}^e & M_{LL\zeta\zeta}^e \end{bmatrix}, \quad \zeta \in \{x, y, z\} \tag{3.18b}$$

and the elemental stiffness matrices

$$\mathbf{K}^e = \begin{bmatrix} \mathbf{K}_{xx}^e & \mathbf{K}_{xz}^e & \mathbf{K}_{xy}^e \\ \mathbf{K}_{zx}^e & \mathbf{K}_{zz}^e & \mathbf{K}_{zy}^e \\ \mathbf{K}_{yx}^e & \mathbf{K}_{yz}^e & \mathbf{K}_{yy}^e \end{bmatrix} \quad \text{with} \quad (3.19a)$$

$$\mathbf{K}_{\zeta v}^e = \begin{bmatrix} K_{II\zeta v}^e & K_{IJ\zeta v}^e & K_{IK\zeta v}^e & K_{IL\zeta v}^e \\ K_{JI\zeta v}^e & K_{JJ\zeta v}^e & K_{JK\zeta v}^e & K_{JL\zeta v}^e \\ K_{KI\zeta v}^e & K_{KJ\zeta v}^e & K_{KK\zeta v}^e & K_{KL\zeta v}^e \\ K_{LI\zeta v}^e & K_{LJ\zeta v}^e & K_{LK\zeta v}^e & K_{LL\zeta v}^e \end{bmatrix}, \quad \zeta, v \in \{x, y, z\}. \quad (3.19b)$$

The components of the mass and the stiffness matrix are defined as specified in equation 3.13, that is,

$$\begin{aligned} M_{ABxx}^e &= \int_{\Omega_e} N_A (\omega^2 \rho - k_y^2 \mu) N_B d\Omega \\ M_{AByy}^e &= \int_{\Omega_e} N_A (\omega^2 \rho - k_y^2 (\lambda + 2\mu)) N_B d\Omega \\ M_{ABzz}^e &= M_{ABxx}^e, \end{aligned} \quad (3.20)$$

and

$$K_{ABxx}^e = - \int_{\Omega_e} \{ (\partial_x N_A) (\lambda + 2\mu) (\partial_x N_B) + (\partial_z N_A) \mu (\partial_z N_B) \} d\Omega \quad (3.21a)$$

$$K_{AByy}^e = - \int_{\Omega_e} \{ (\partial_x N_A) \mu (\partial_x N_B) + (\partial_z N_A) \mu (\partial_z N_B) \} d\Omega \quad (3.21b)$$

$$K_{ABzz}^e = - \int_{\Omega_e} \{ (\partial_z N_A) (\lambda + 2\mu) (\partial_z N_B) + (\partial_x N_A) \mu (\partial_x N_B) \} d\Omega \quad (3.21c)$$

$$K_{ABxy}^e = - \int_{\Omega_e} \{ (\partial_x N_A) \lambda (ik_y N_B) - (ik_y N_A) \mu (\partial_x N_B) \} d\Omega \quad (3.21d)$$

$$K_{AByx}^e = - \int_{\Omega_e} \{ - (ik_y N_A) \lambda (\partial_x N_B) + (\partial_x N_A) \mu (ik_y N_B) \} d\Omega \quad (3.21e)$$

$$K_{ABxz}^e = - \int_{\Omega_e} \{ (\partial_x N_A) \lambda (\partial_z N_B) + (\partial_z N_A) \mu (\partial_x N_B) \} d\Omega \quad (3.21f)$$

$$K_{ABzx}^e = - \int_{\Omega_e} \{ (\partial_z N_A) \lambda (\partial_x N_B) + (\partial_x N_A) \mu (\partial_z N_B) \} d\Omega \quad (3.21g)$$

$$K_{AByz}^e = - \int_{\Omega_e} \{ - (ik_y N_A) \lambda (\partial_z N_B) + (\partial_z N_A) \mu (ik_y N_B) \} d\Omega \quad (3.21h)$$

$$K_{ABzy}^e = - \int_{\Omega_e} \{ (\partial_z N_A) \lambda (ik_y N_B) - (ik_y N_A) \mu (\partial_z N_B) \} d\Omega. \quad (3.21i)$$

The values of the model parameters λ , μ and ρ are constant within each element, such that these quantities can be taken outside the integrals in (3.20) and (3.21), which leaves only the basic integrals

$$\mathcal{I}^{AB} := \int_{\Omega_e} N_A N_B d\Omega = \begin{bmatrix} 4 & 2 & 2 & 1 \\ 2 & 4 & 1 & 2 \\ 2 & 1 & 4 & 2 \\ 1 & 2 & 2 & 4 \end{bmatrix} \frac{\Delta x \Delta z}{36} \quad (3.22a)$$

$$\mathcal{I}_{xy}^{AB} := \int_{\Omega_e} \partial_x N_A N_B d\Omega = \begin{bmatrix} -2 & -1 & -2 & -1 \\ -1 & -2 & -1 & -2 \\ +2 & +1 & +2 & +1 \\ +1 & +2 & +1 & +2 \end{bmatrix} \frac{\Delta z}{12} \quad (3.22b)$$

$$\mathcal{I}_{yx}^{AB} := \int_{\Omega_e} N_A \partial_x N_B d\Omega = \begin{bmatrix} -2 & -1 & +2 & +1 \\ -1 & -2 & +1 & +2 \\ -2 & -1 & +2 & +1 \\ -1 & -2 & +1 & +2 \end{bmatrix} \frac{\Delta z}{12} \quad (3.22c)$$

$$\mathcal{I}_{zy}^{AB} := \int_{\Omega_e} \partial_z N_A N_B d\Omega = \begin{bmatrix} -2 & -2 & -1 & -1 \\ +2 & +2 & +1 & +1 \\ -1 & -1 & -2 & -2 \\ +1 & +1 & +2 & +2 \end{bmatrix} \frac{\Delta x}{12} \quad (3.22d)$$

$$\mathcal{I}_{yz}^{AB} := \int_{\Omega_e} N_A \partial_z N_B d\Omega = \begin{bmatrix} -2 & +2 & -1 & +1 \\ -2 & +2 & -1 & +1 \\ -1 & +1 & -2 & +2 \\ -1 & +1 & -2 & +2 \end{bmatrix} \frac{\Delta x}{12} \quad (3.22e)$$

$$\mathcal{I}_{xx}^{AB} := \int_{\Omega_e} \partial_x N_A \partial_x N_B d\Omega = \begin{bmatrix} +2 & +1 & -2 & -1 \\ +1 & +2 & -1 & -2 \\ -2 & -1 & +2 & +1 \\ -1 & -2 & +1 & +2 \end{bmatrix} \frac{\Delta z}{6\Delta x} \quad (3.22f)$$

$$\mathcal{I}_{zz}^{AB} := \int_{\Omega_e} \partial_z N_A \partial_z N_B d\Omega = \begin{bmatrix} +2 & -2 & +1 & -1 \\ -2 & +2 & -1 & +1 \\ +1 & -1 & +2 & -2 \\ -1 & +1 & -2 & +2 \end{bmatrix} \frac{\Delta x}{6\Delta z} \quad (3.22g)$$

$$\mathcal{I}_{xz}^{AB} := \int_{\Omega_e} \partial_x N_A \partial_z N_B d\Omega = \begin{bmatrix} +1 & -1 & +1 & -1 \\ +1 & -1 & +1 & -1 \\ -1 & +1 & -1 & +1 \\ -1 & +1 & -1 & +1 \end{bmatrix} \frac{1}{4} \quad (3.22h)$$

$$\mathcal{I}_{zx}^{AB} := \int_{\Omega_e} \partial_z N_A \partial_x N_B d\Omega = \begin{bmatrix} +1 & +1 & -1 & -1 \\ -1 & -1 & +1 & +1 \\ +1 & +1 & -1 & -1 \\ -1 & -1 & +1 & +1 \end{bmatrix} \frac{1}{4} \quad (3.22i)$$

to be computed. I use the abbreviation $A, B \in \{I, J, K, L\}$ and the coefficients for the different combinations of node indices given in the small matrices are ordered following the pattern $\begin{bmatrix} II & IJ & IK & IL \\ JI & JJ & JK & JL \\ KI & KJ & KK & KL \\ LI & LJ & LK & LL \end{bmatrix}$.

With this, the components of \mathbf{M} can be rewritten as

$$M_{AB\zeta\zeta}^e = \mathcal{U}_\zeta \mathcal{I}^{AB}, \quad \zeta \in \{x, y, z\} \quad \text{with} \quad \begin{aligned} \mathcal{U}_x &:= \omega^2 \rho - k_y^2 \mu \\ \mathcal{U}_y &:= \omega^2 \rho - k_y^2 (\lambda + 2\mu) \\ \mathcal{U}_z &:= \omega^2 \rho - k_y^2 \mu, \end{aligned} \quad (3.23)$$

and those of \mathbf{K} take the form

$$\begin{aligned}
 K_{ABxx}^e &= -[(\lambda + 2\mu)\mathcal{I}_{xx}^{AB} + \mu\mathcal{I}_{zz}^{AB}] \\
 K_{AByy}^e &= -\mu[\mathcal{I}_{xx}^{AB} + \mathcal{I}_{zz}^{AB}] \\
 K_{ABzz}^e &= -[(\lambda + 2\mu)\mathcal{I}_{zz}^{AB} + \mu\mathcal{I}_{xx}^{AB}] \\
 K_{ABxy}^e &= -ik_y[\lambda\mathcal{I}_{xy}^{AB} - \mu\mathcal{I}_{yx}^{AB}] \\
 K_{AByx}^e &= -ik_y[-\lambda\mathcal{I}_{yx}^{AB} + \mu\mathcal{I}_{xy}^{AB}] \\
 K_{AByz}^e &= -ik_y[-\lambda\mathcal{I}_{yz}^{AB} + \mu\mathcal{I}_{zy}^{AB}] \\
 K_{ABzy}^e &= -ik_y[\lambda\mathcal{I}_{zy}^{AB} - \mu\mathcal{I}_{yz}^{AB}] \\
 K_{ABxz}^e &= -[\lambda\mathcal{I}_{xz}^{AB} + \mu\mathcal{I}_{zx}^{AB}] \\
 K_{ABzx}^e &= -[\lambda\mathcal{I}_{zx}^{AB} + \mu\mathcal{I}_{xz}^{AB}]
 \end{aligned} \tag{3.24}$$

3.1.2 Boundary conditions

Equations (3.23) and (3.24) could now be immediately implemented in a FEM forward solver. This would be correct for all interior nodes, but at the boundaries this would result in so-called natural or Neumann boundary conditions with stresses being equal to zero (see also section 3.1.1), which imply a traction free surface. However, at least at the ground boundaries (i.e. the left and right sides and the bottom of the model), the solution for an unbounded medium is required.

One possibility to address the problem of truncating an infinite modelling domain would be to employ non-reflecting boundary conditions (NRBCs) of either local or non-local nature (e.g. Givoli, 1991). Such boundary conditions are efficient in the sense that no additional cells need to be added, but they work properly only for particular shapes of the modelling domain, and certain polarisations and propagation directions of the seismic waves.

An alternative option is to implement sponge-like boundary layers, in which gradual damping of the wave fields towards the artificial boundaries is enforced (e.g. Cerjan et al., 1985). A drawback of these sponge-layers is that spurious reflections may occur in the absorbing layer (Sarma et al., 1998).

Perfectly matched layers (PMLs)

Berenger (1994) proposed the concept of perfectly matched layers (PMLs) to overcome this problem. He proposed them in the context of electromagnetic wave modelling, but his ideas have been modified and adapted to a wide range of other wave propagation modelling problems (de Hoop et al., 2007).

The basic idea of the PML approach is to put an additional layer around the computational domain that matches the latter perfectly in the sense that waves passing the boundary between the normal medium and the layer are not reflected since they do not 'see' any change of the material properties. The original idea of Berenger (1994) was to devise an unphysical artificial material exhibiting different model parameters for wave field components tangential and normal to the boundary (split field approach) In this way, the reflection coefficient at the boundary can be forced to be zero, but the waves are nonetheless damped in the direction perpendicular (normal) to the boundary. At

the outermost boundaries, the amplitudes should be very small. Due to the Neumann condition at the outermost boundaries, the waves are totally reflected back into the PML layer. Here, they are further attenuated, such that the amplitudes should be negligible, when they reach the physical medium.

As an alternative to the split field approach one can employ a complex coordinate transformation within the PMLs. This is referred as *coordinate stretching*. I have implemented this technique by following Zheng and Huang (2002) and Basu and Chopra (2003).

For the complex coordinate variables \tilde{x} , \tilde{y} and \tilde{z} , Zheng and Huang (2002, equation (9)) use

$$\tilde{\zeta} = \zeta^0 + \int_{\zeta^0}^{\zeta} \tilde{\varepsilon}_{\zeta}(\zeta') d\zeta' \quad (\zeta \in \{x, y, z\}), \quad (3.25)$$

whereas Basu and Chopra (2003, equation (6)) employ

$$\tilde{\zeta} = \int_0^{\zeta} \varepsilon_{\zeta}(\zeta') d\zeta' \quad (\zeta \in \{x, y, z\}). \quad (3.26)$$

Note that the variables in Equations (3.25) and (3.26) were changed from the original papers to assure notational consistency within my thesis. Both formulations are equivalent when choosing

$$\varepsilon_{\zeta}(\zeta') = \begin{cases} 1 & \text{if } \zeta' \leq \zeta^0 \\ \tilde{\varepsilon}_{\zeta}(\zeta') & \text{if } \zeta' > \zeta^0 \end{cases} \quad (\zeta \in \{x, y, z\}). \quad (3.27)$$

Modified equations of motion

Replacing the coordinates $\{x, y, z\}$ in the 3D equations of motion (3.1) by their stretched counterparts $\{\tilde{x}, \tilde{y}, \tilde{z}\}$ defined in (3.26) and expressing the result again in $\{x, y, z\}$, yields the new PML equations (Zheng and Huang, 2002, equations (22-30))

$$\begin{aligned} 0 = & \rho\omega^2 \varepsilon_x \varepsilon_y \varepsilon_z \bar{u}_x + \partial_x \left[(\lambda + 2\mu) \frac{\varepsilon_y \varepsilon_z}{\varepsilon_x} \partial_x \bar{u}_x + \lambda (\varepsilon_z \partial_y \bar{u}_y + \varepsilon_y \partial_z \bar{u}_z) \right] \\ & + \partial_y \left[\mu (\varepsilon_z \partial_x \bar{u}_y + \frac{\varepsilon_z \varepsilon_x}{\varepsilon_y} \partial_y \bar{u}_x) \right] \\ & + \partial_z \left[\mu (\varepsilon_y \partial_x \bar{u}_z + \frac{\varepsilon_x \varepsilon_y}{\varepsilon_z} \partial_z \bar{u}_x) \right] \\ & + \bar{f}_x \end{aligned} \quad (3.28a)$$

$$\begin{aligned}
0 = \rho\omega^2\varepsilon_x\varepsilon_y\varepsilon_z\bar{u}_y + \partial_x \left[\mu(\varepsilon_z\partial_y\bar{u}_x + \frac{\varepsilon_y\varepsilon_z}{\varepsilon_x}\partial_x\bar{u}_y) \right] \\
+ \partial_y \left[(\lambda + 2\mu)\frac{\varepsilon_z\varepsilon_x}{\varepsilon_y}\partial_y\bar{u}_y + \lambda(\varepsilon_z\partial_x\bar{u}_x + \varepsilon_x\partial_z\bar{u}_z) \right] \\
+ \partial_z \left[\mu(\varepsilon_x\partial_y\bar{u}_z + \frac{\varepsilon_x\varepsilon_y}{\varepsilon_z}\partial_z\bar{u}_y) \right] \\
+ \bar{f}_y
\end{aligned} \tag{3.28b}$$

$$\begin{aligned}
0 = \rho\omega^2\varepsilon_x\varepsilon_y\varepsilon_z\bar{u}_z + \partial_x \left[\mu(\varepsilon_y\partial_z\bar{u}_x + \frac{\varepsilon_y\varepsilon_z}{\varepsilon_x}\partial_x\bar{u}_z) \right] \\
+ \partial_y \left[\mu(\varepsilon_x\partial_z\bar{u}_y + \frac{\varepsilon_z\varepsilon_x}{\varepsilon_y}\partial_y\bar{u}_z) \right] \\
+ \partial_z \left[(\lambda + 2\mu)\frac{\varepsilon_x\varepsilon_y}{\varepsilon_z}\partial_z\bar{u}_z + \lambda(\varepsilon_y\partial_x\bar{u}_x + \varepsilon_x\partial_y\bar{u}_y) \right] \\
+ \bar{f}_z.
\end{aligned} \tag{3.28c}$$

Before transforming the 3D equations (3.28) into a 2.5D formulation (using equation (A.2)), I set $\varepsilon_y \equiv 1$. This is required, because 2.5D computations imply the assumption that the problem is invariant with respect to translations in the cross-line (y -) direction. This choice does not cause any problems, since the transformation to the ω - x - k_y - z -domain allows the model to stretch out infinitely in the y -direction, such that there is no need to truncate it in this direction and thus no spurious reflections are created by an artificial boundary parallel to the x - z -plane.

Bearing these considerations in mind, the 2.5D equations of motion are of the form

$$\begin{aligned}
0 = \rho\omega^2\varepsilon_x\varepsilon_z\bar{\bar{u}}_x + \partial_x \left[(\lambda + 2\mu)\frac{\varepsilon_z}{\varepsilon_x}\partial_x\bar{\bar{u}}_x + \lambda(\varepsilon_z ik_y\bar{\bar{u}}_y + \partial_z\bar{\bar{u}}_z) \right] \\
+ ik_y [\mu(\varepsilon_z\partial_x\bar{\bar{u}}_y + \varepsilon_z\varepsilon_x ik_y\bar{\bar{u}}_x)] \\
+ \partial_z \left[\mu(\partial_x\bar{\bar{u}}_z + \frac{\varepsilon_x}{\varepsilon_z}\partial_z\bar{\bar{u}}_x) \right] \\
+ \bar{\bar{f}}_x
\end{aligned} \tag{3.29a}$$

$$\begin{aligned}
0 = \rho\omega^2\varepsilon_x\varepsilon_z\bar{\bar{u}}_y + \partial_x \left[\mu(\varepsilon_z ik_y\bar{\bar{u}}_x + \frac{\varepsilon_z}{\varepsilon_x}\partial_x\bar{\bar{u}}_y) \right] \\
+ ik_y [(\lambda + 2\mu)\varepsilon_z\varepsilon_x ik_y\bar{\bar{u}}_y + \lambda(\varepsilon_z\partial_x\bar{\bar{u}}_x + \varepsilon_x\partial_z\bar{\bar{u}}_z)] \\
+ \partial_z \left[\mu(\varepsilon_x ik_y\bar{\bar{u}}_z + \frac{\varepsilon_x}{\varepsilon_z}\partial_z\bar{\bar{u}}_y) \right] \\
+ \bar{\bar{f}}_y
\end{aligned} \tag{3.29b}$$

$$\begin{aligned}
0 = \rho\omega^2\varepsilon_x\varepsilon_z\bar{\bar{u}}_z + \partial_x \left[\mu(\partial_z\bar{\bar{u}}_x + \frac{\varepsilon_z}{\varepsilon_x}\partial_x\bar{\bar{u}}_z) \right] \\
+ ik_y [\mu(\varepsilon_x\partial_z\bar{\bar{u}}_y + \varepsilon_z\varepsilon_x ik_y\bar{\bar{u}}_z)] \\
+ \partial_z \left[(\lambda + 2\mu)\frac{\varepsilon_x}{\varepsilon_z}\partial_z\bar{\bar{u}}_z + \lambda(\partial_x\bar{\bar{u}}_x + \varepsilon_x ik_y\bar{\bar{u}}_y) \right] \\
+ \bar{\bar{f}}_z.
\end{aligned} \tag{3.29c}$$

To supply the PMLs with the desired attenuation properties and at the same time keep the model unchanged in the true computational domain, a model zonation as depicted in Figure (3.2) has to be carried out. In each zone the ε_ζ in (3.26) are given by

$$\varepsilon_\zeta = 1 - g_\zeta(\zeta) \quad (\zeta \in \{x, z\}), \quad (3.30)$$

where the *coordinate stretching functions* g_x and g_z run differently in the different zones, as can be seen in Figure 3.3. With the PMLs designed like this, the waves will undergo an attenuation in the margin zones that increases gradually in the outward direction perpendicular to the boundary of the unmodified zone D, such that their amplitudes decay exponentially.

Elemental equations with stretched coordinates

The final step of the PML implementation is to rewrite the component M_{ABij} in (3.23) and K_{ABij} in (3.21) using the modified equations of motion (3.29). The mass matrix

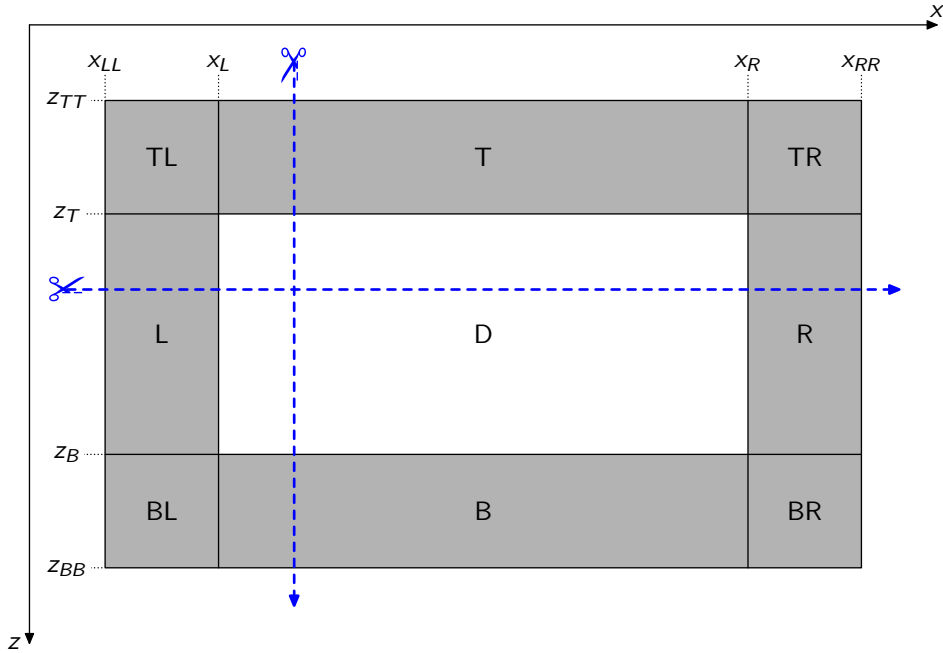


Figure 3.2: Sketch of the different zones of the computational domain. PML parts are shaded grey. L, R, T and B stand for the left, right, top and bottom PML zones, respectively, where always one of the coordinate stretching functions g_x or g_z is different from zero. TL, TR, BL and BR stand for the top right, top left, bottom right and bottom left PML corner zones, where both g_x and g_z are different from zero. D stands for the unmodified medium, where both $g_x \equiv 0$ and $g_z \equiv 0$. The behaviour of g_x and g_z in the respective zones is shown in Figure 3.3; the dashed blue lines indicate the cut directions along which these functions are shown there.

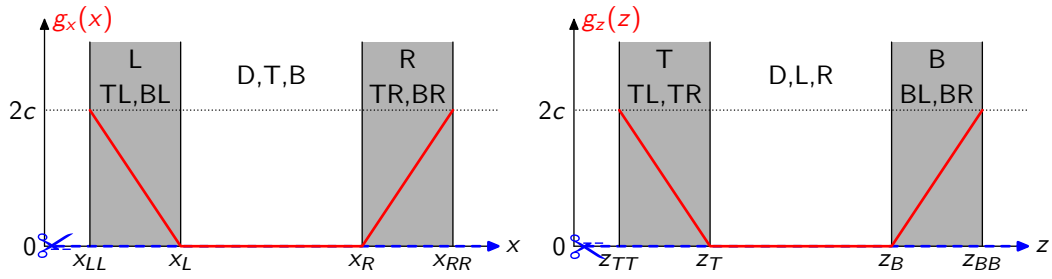


Figure 3.3: Run of the coordinate stretching functions g_x and g_z along the horizontal and vertical lines, as indicated in Figure 3.2, where the different zones of the computational domain are defined.

components are

$$\tilde{M}_{AB\zeta\zeta}^e = \mathcal{U}_\zeta \int_{\Omega_e} \varepsilon_x \varepsilon_z N_A N_B d\Omega, \quad \begin{aligned} \mathcal{U}_x &:= \omega^2 \rho - k_y^2 \mu \\ \mathcal{U}_y &:= \omega^2 \rho - k_y^2 (\lambda + 2\mu) \\ \mathcal{U}_z &:= \omega^2 \rho - k_y^2 \mu, \end{aligned} \quad (3.31)$$

and the stiffness matrix components are

$$\tilde{K}_{ABxx}^e = - [(\lambda + 2\mu) \tilde{\mathcal{I}}_{xx}^{AB} + \mu \tilde{\mathcal{I}}_{zz}^{AB}] \quad (3.32a)$$

$$\tilde{K}_{AByy}^e = -\mu [\tilde{\mathcal{I}}_{xx}^{AB} + \tilde{\mathcal{I}}_{zz}^{AB}] \quad (3.32b)$$

$$\tilde{K}_{ABzz}^e = - [(\lambda + 2\mu) \tilde{\mathcal{I}}_{zz}^{AB} + \mu \tilde{\mathcal{I}}_{xx}^{AB}] \quad (3.32c)$$

$$\tilde{K}_{ABxy}^e = -ik_y [\lambda \tilde{\mathcal{I}}_{xy}^{AB} - \mu \tilde{\mathcal{I}}_{yx}^{AB}] \quad (3.32d)$$

$$\tilde{K}_{AByx}^e = -ik_y [-\lambda \tilde{\mathcal{I}}_{yx}^{AB} + \mu \tilde{\mathcal{I}}_{xy}^{AB}] \quad (3.32e)$$

$$\tilde{K}_{AByz}^e = -ik_y [-\lambda \tilde{\mathcal{I}}_{yz}^{AB} + \mu \tilde{\mathcal{I}}_{zy}^{AB}] \quad (3.32f)$$

$$\tilde{K}_{ABzy}^e = -ik_y [\lambda \tilde{\mathcal{I}}_{zy}^{AB} - \mu \tilde{\mathcal{I}}_{yz}^{AB}] \quad (3.32g)$$

$$\tilde{K}_{ABxz}^e = - [\lambda \tilde{\mathcal{I}}_{xz}^{AB} + \mu \tilde{\mathcal{I}}_{zx}^{AB}] \quad (3.32h)$$

$$\tilde{K}_{ABzx}^e = - [\lambda \tilde{\mathcal{I}}_{zx}^{AB} + \mu \tilde{\mathcal{I}}_{xz}^{AB}], \quad (3.32i)$$

where $\zeta \in \{x, y, z\}$. Note, that \tilde{K}_{ABxz} and \tilde{K}_{ABzx} remain unchanged with respect to equation (3.24). In (3.32) I introduced the modified integral abbreviations

$$\tilde{\mathcal{I}}_{xx}^{AB} := \int_{\Omega_e} \frac{\varepsilon_z}{\varepsilon_x} \partial_x N_A \partial_x N_B d\Omega \quad (3.33a)$$

$$\tilde{\mathcal{I}}_{zz}^{AB} := \int_{\Omega_e} \frac{\varepsilon_x}{\varepsilon_z} \partial_z N_A \partial_z N_B d\Omega \quad (3.33b)$$

$$\tilde{\mathcal{I}}_{xy}^{AB} := \int_{\Omega_e} \varepsilon_z \partial_x N_A \partial_y N_B d\Omega \quad (3.33c)$$

$$\tilde{\mathcal{I}}_{yx}^{AB} := \int_{\Omega_e} \varepsilon_z N_A \partial_x N_B d\Omega \quad (3.33d)$$

$$\tilde{\mathcal{I}}_{zy}^{AB} := \int_{\Omega_e} \varepsilon_x \partial_z N_A N_B d\Omega \quad (3.33e)$$

$$\tilde{\mathcal{I}}_{yz}^{AB} := \int_{\Omega_e} \varepsilon_x N_A \partial_z N_B d\Omega \quad (3.33f)$$

$$\mathcal{I}_{xz}^{AB} := \int_{\Omega_e} \partial_x N_A \partial_z N_B d\Omega \quad (3.33g)$$

$$\mathcal{I}_{zx}^{AB} := \int_{\Omega_e} \partial_z N_A \partial_x N_B d\Omega. \quad (3.33h)$$

To proceed to the elemental version of mass and stiffness matrices, the coordinate stretching functions g_x and g_z , defining the ε_x and ε_z (see equation (3.30)), need to be written down explicitly in local coordinates ξ and η . The linear behaviour shown in Figure 3.3 can be achieved by using

$$g_x := A_x + B_x \xi \quad \text{and} \quad g_z := A_z + B_z \eta \quad (3.34)$$

with coefficients A_ζ and B_ζ ($\zeta \in \{x, z\}$) as given in Table 3.1. Then, (3.34) and (3.30) are inserted in equations (3.31) to (3.33). Again, all integrals are restricted to the area Ω_e of one element and, by means of (3.10), written in local coordinates. As noted in section 3.1.1, the parameters ρ , λ and μ are constant within each element and can be taken outside the integrals. The further steps towards the final elemental mass matrix elements are rather lengthy and the interested reader is referred to the Appendix

	L	R	TL	TR	BL	BR
A_x	$2 \frac{c}{n_L} \frac{x_L - x_m}{\Delta x}$	$2 \frac{c}{n_R} \frac{x_m - x_R}{\Delta x}$	$2 \frac{c}{n_L} \frac{x_L - x_m}{\Delta x}$	$2 \frac{c}{n_R} \frac{x_m - x_R}{\Delta x}$	$2 \frac{c}{n_L} \frac{x_L - x_m}{\Delta x}$	$2 \frac{c}{n_R} \frac{x_m - x_R}{\Delta x}$
B_x	$-\frac{c}{n_L}$	$\frac{c}{n_R}$	$-\frac{c}{n_L}$	$\frac{c}{n_R}$	$-\frac{c}{n_L}$	$\frac{c}{n_R}$
	T	B	TL	TR	BL	BR
A_z	$2 \frac{c}{n_T} \frac{z_T - z_m}{\Delta z}$	$2 \frac{c}{n_B} \frac{z_m - z_B}{\Delta z}$	$2 \frac{c}{n_T} \frac{z_T - z_m}{\Delta z}$	$2 \frac{c}{n_T} \frac{z_T - z_m}{\Delta z}$	$2 \frac{c}{n_B} \frac{z_m - z_B}{\Delta z}$	$2 \frac{c}{n_B} \frac{z_m - z_B}{\Delta z}$
B_z	$-\frac{c}{n_T}$	$\frac{c}{n_B}$	$-\frac{c}{n_T}$	$-\frac{c}{n_T}$	$\frac{c}{n_B}$	$\frac{c}{n_B}$
$n_L := \frac{x_L - x_{LL}}{\Delta x} \quad n_R := \frac{x_{RR} - x_R}{\Delta x} \quad n_T := \frac{z_T - z_{TT}}{\Delta z} \quad n_B := \frac{z_{BB} - z_B}{\Delta z}$						

Table 3.1: Values of the coefficients for the coordinate stretching functions (3.34). n_L , n_R , n_T and n_B are the widths of the respective PMLs given in number of elements, c is a positive constant controlling the rate of attenuation increase relative to the width of the PMLs, the locations of x_{LL} , x_L , x_R , x_{RR} , z_{TT} , z_T , z_B and z_{BB} and the positions of the corresponding PML zones can be seen in Figure 3.2 and x_m , z_m , Δx and Δz are defined in equations (3.9) and Figure 3.1. In zone D, where no coordinate stretching is done, all coefficients are zero, in zones L and R we find $A_z = B_z = 0$ and in zones T and B $A_x = B_x = 0$.

A, section A.2, for the complete derivation. Here, I will only state the result. The elemental mass matrix elements for the medium with PMLs are

$$\begin{aligned} \tilde{M}_{AB\zeta\zeta}^e = \mathcal{V}_\zeta \frac{\Delta x \Delta z}{36} \left\{ 2 [1 - A_x A_z - i(A_x + A_z)] \begin{bmatrix} 4 & 2 & 2 & 1 \\ 2 & 4 & 1 & 2 \\ 2 & 1 & 4 & 2 \\ 1 & 2 & 2 & 4 \end{bmatrix} \right. \\ - iB_x(1 - iA_z) \begin{bmatrix} -2 & -1 & 0 & 0 \\ -1 & -2 & 0 & 0 \\ 0 & 0 & +2 & +1 \\ 0 & 0 & +1 & +2 \end{bmatrix} \\ - iB_z(1 - iA_x) \begin{bmatrix} -2 & 0 & -1 & 0 \\ 0 & +2 & 0 & +1 \\ -1 & 0 & -2 & 0 \\ 0 & +1 & 0 & +2 \end{bmatrix} \\ \left. - B_x B_z \begin{bmatrix} +1 & 0 & 0 & 0 \\ 0 & -1 & 0 & 0 \\ 0 & 0 & -1 & 0 \\ 0 & 0 & 0 & +1 \end{bmatrix} \right\}, \end{aligned} \quad (3.35)$$

with \mathcal{V}_ζ as given in equation (3.31), $\zeta \in \{x, y, z\}$ and coefficient matrices following the same pattern as in equations (3.22). The elements of the stiffness sub-matrices $\mathbf{K}_{\zeta\zeta}$ are found to be

$$\begin{aligned} \tilde{K}_{ABxx}^e = -\frac{1}{12} \left\{ \frac{\Delta z}{\Delta x} (\lambda + 2\mu) \mathcal{G}^x \left((1 - iA_z) \begin{bmatrix} +2 & +1 & -2 & -1 \\ +1 & +2 & -1 & -2 \\ -2 & -1 & +2 & +1 \\ -1 & -2 & +1 & +2 \end{bmatrix} \right. \right. \\ \left. - iB_z \begin{bmatrix} -1 & 0 & +1 & 0 \\ 0 & +1 & 0 & -1 \\ +1 & 0 & -1 & 0 \\ 0 & -1 & 0 & +1 \end{bmatrix} \right) \\ + \frac{\Delta x}{\Delta z} \mu \mathcal{G}^z \left((1 - iA_x) \begin{bmatrix} +2 & -2 & +1 & -1 \\ -2 & +2 & -1 & +1 \\ +1 & -1 & +2 & -2 \\ -1 & +1 & -2 & +2 \end{bmatrix} \right. \\ \left. - iB_x \begin{bmatrix} -1 & +1 & 0 & 0 \\ +1 & -1 & 0 & 0 \\ 0 & 0 & +1 & -1 \\ 0 & 0 & -1 & +1 \end{bmatrix} \right) \left. \right\} \end{aligned} \quad (3.36a)$$

$$\begin{aligned} \tilde{K}_{AByy}^e = -\frac{\mu}{12} \left\{ \frac{\Delta z}{\Delta x} \mathcal{G}^x \left((1 - iA_z) \begin{bmatrix} +2 & +1 & -2 & -1 \\ +1 & +2 & -1 & -2 \\ -2 & -1 & +2 & +1 \\ -1 & -2 & +1 & +2 \end{bmatrix} - iB_z \begin{bmatrix} -1 & 0 & +1 & 0 \\ 0 & +1 & 0 & -1 \\ +1 & 0 & -1 & 0 \\ 0 & -1 & 0 & +1 \end{bmatrix} \right) \right. \\ \left. + \frac{\Delta x}{\Delta z} \mathcal{G}^z \left((1 - iA_x) \begin{bmatrix} +2 & -2 & +1 & -1 \\ -2 & +2 & -1 & +1 \\ +1 & -1 & +2 & -2 \\ -1 & +1 & -2 & +2 \end{bmatrix} - iB_x \begin{bmatrix} -1 & +1 & 0 & 0 \\ +1 & -1 & 0 & 0 \\ 0 & 0 & +1 & -1 \\ 0 & 0 & -1 & +1 \end{bmatrix} \right) \right\} \end{aligned} \quad (3.36b)$$

$$\begin{aligned} \tilde{K}_{ABzz}^e = -\frac{1}{12} \left\{ \frac{\Delta z}{\Delta x} \mu \mathcal{G}^x \left((1 - iA_z) \begin{bmatrix} +2 & +1 & -2 & -1 \\ +1 & +2 & -1 & -2 \\ -2 & -1 & +2 & +1 \\ -1 & -2 & +1 & +2 \end{bmatrix} \right. \right. \\ \left. - iB_z \begin{bmatrix} -1 & 0 & +1 & 0 \\ 0 & +1 & 0 & -1 \\ +1 & 0 & -1 & 0 \\ 0 & -1 & 0 & +1 \end{bmatrix} \right) \\ + \frac{\Delta x}{\Delta z} (\lambda + 2\mu) \mathcal{G}^z \left((1 - iA_x) \begin{bmatrix} +2 & -2 & +1 & -1 \\ -2 & +2 & -1 & +1 \\ +1 & -1 & +2 & -2 \\ -1 & +1 & -2 & +2 \end{bmatrix} \right. \\ \left. - iB_x \begin{bmatrix} -1 & +1 & 0 & 0 \\ +1 & -1 & 0 & 0 \\ 0 & 0 & +1 & -1 \\ 0 & 0 & -1 & +1 \end{bmatrix} \right) \left. \right\}, \end{aligned} \quad (3.36c)$$

with

$$\begin{aligned} \mathcal{G}^x &= \begin{cases} 2 & \text{in T, D and B} \\ \mathcal{G}_1^x + iB_x \mathcal{G}_2^x & \text{else} \end{cases} \\ \mathcal{G}^z &= \begin{cases} 2 & \text{in L, D and R} \\ \mathcal{G}_1^z + iB_z \mathcal{G}_2^z & \text{else} \end{cases} \end{aligned} \quad (3.37)$$

and

$$\begin{aligned} \mathcal{G}_1^\zeta &= \frac{1}{B_\zeta} (\arctan(A_\zeta + B_\zeta) - \arctan(A_\zeta - B_\zeta)) \\ \mathcal{G}_2^\zeta &= \frac{1}{2B_\zeta^2} \ln \left(\frac{(A_\zeta + B_\zeta)^2 + 1}{(A_\zeta - B_\zeta)^2 + 1} \right). \end{aligned} \quad (3.38)$$

The remaining elements are

$$\begin{aligned} \tilde{K}_{ABxy}^e &= -ik_y \frac{\Delta z}{12} \left\{ (1 - iA_z) \begin{bmatrix} -2(\lambda-\mu) & -(\lambda-\mu) & -2(\lambda+\mu) & -(\lambda+\mu) \\ -(\lambda-\mu) & -2(\lambda-\mu) & -(\lambda+\mu) & -2(\lambda+\mu) \\ 2(\lambda+\mu) & \lambda+\mu & 2(\lambda-\mu) & \lambda-\mu \\ \lambda+\mu & 2(\lambda+\mu) & \lambda-\mu & 2(\lambda-\mu) \end{bmatrix} \right. \\ &\quad \left. - iB_z \begin{bmatrix} \lambda-\mu & 0 & \lambda+\mu & 0 \\ 0 & -(\lambda-\mu) & 0 & -(\lambda+\mu) \\ -(\lambda+\mu) & 0 & -(\lambda-\mu) & 0 \\ 0 & \lambda+\mu & 0 & \lambda-\mu \end{bmatrix} \right\} \end{aligned} \quad (3.39a)$$

$$\begin{aligned} \tilde{K}_{AByx}^e &= -ik_y \frac{\Delta z}{12} \left\{ (1 - iA_z) \begin{bmatrix} 2(\lambda-\mu) & \lambda-\mu & -2(\lambda+\mu) & -(\lambda+\mu) \\ \lambda-\mu & 2(\lambda-\mu) & -(\lambda+\mu) & -2(\lambda+\mu) \\ 2(\lambda+\mu) & \lambda+\mu & -2(\lambda-\mu) & -(\lambda-\mu) \\ \lambda+\mu & 2(\lambda+\mu) & -(\lambda-\mu) & -2(\lambda-\mu) \end{bmatrix} \right. \\ &\quad \left. - iB_z \begin{bmatrix} -(\lambda-\mu) & 0 & \lambda+\mu & 0 \\ 0 & \lambda-\mu & 0 & -(\lambda+\mu) \\ -(\lambda+\mu) & 0 & \lambda-\mu & 0 \\ 0 & \lambda+\mu & 0 & -(\lambda-\mu) \end{bmatrix} \right\} \end{aligned} \quad (3.39b)$$

$$\begin{aligned} \tilde{K}_{AByz}^e &= -ik_y \frac{\Delta x}{12} \left\{ (1 - iA_x) \begin{bmatrix} 2(\lambda-\mu) & -2(\lambda+\mu) & (\lambda-\mu) & -(\lambda+\mu) \\ 2(\lambda+\mu) & -2(\lambda-\mu) & (\lambda+\mu) & -(\lambda-\mu) \\ (\lambda-\mu) & -(\lambda+\mu) & 2(\lambda-\mu) & -2(\lambda+\mu) \\ (\lambda+\mu) & -(\lambda-\mu) & 2(\lambda+\mu) & -2(\lambda-\mu) \end{bmatrix} \right. \\ &\quad \left. - iB_x \begin{bmatrix} -(\lambda-\mu) & \lambda+\mu & 0 & 0 \\ -(\lambda+\mu) & \lambda-\mu & 0 & 0 \\ 0 & 0 & \lambda-\mu & -(\lambda+\mu) \\ 0 & 0 & \lambda+\mu & -(\lambda-\mu) \end{bmatrix} \right\} \end{aligned} \quad (3.39c)$$

$$\begin{aligned} \tilde{K}_{ABzy}^e &= -ik_y \frac{\Delta x}{12} \left\{ (1 - iA_x) \begin{bmatrix} -2(\lambda-\mu) & -2(\lambda+\mu) & -(\lambda-\mu) & -(\lambda+\mu) \\ 2(\lambda+\mu) & 2(\lambda-\mu) & \lambda+\mu & \lambda-\mu \\ -(\lambda-\mu) & -(\lambda+\mu) & -2(\lambda-\mu) & -2(\lambda+\mu) \\ \lambda+\mu & \lambda-\mu & 2(\lambda+\mu) & 2(\lambda-\mu) \end{bmatrix} \right. \\ &\quad \left. - iB_x \begin{bmatrix} \lambda-\mu & \lambda+\mu & 0 & 0 \\ -(\lambda+\mu) & -(\lambda-\mu) & 0 & 0 \\ 0 & 0 & -(\lambda-\mu) & -(\lambda+\mu) \\ 0 & 0 & \lambda+\mu & \lambda-\mu \end{bmatrix} \right\} \end{aligned} \quad (3.39d)$$

$$\tilde{K}_{ABxz}^e = -\frac{1}{4} \begin{bmatrix} \lambda+\mu & -(\lambda-\mu) & \lambda-\mu & -(\lambda+\mu) \\ \lambda-\mu & -(\lambda+\mu) & \lambda+\mu & -(\lambda-\mu) \\ -(\lambda-\mu) & \lambda+\mu & -(\lambda+\mu) & \lambda-\mu \\ -(\lambda+\mu) & \lambda-\mu & -(\lambda-\mu) & \lambda+\mu \end{bmatrix} \quad (3.39e)$$

$$\tilde{K}_{ABzx}^e = -\frac{1}{4} \begin{bmatrix} \lambda+\mu & \lambda-\mu & -(\lambda-\mu) & -(\lambda+\mu) \\ -(\lambda-\mu) & -(\lambda+\mu) & \lambda+\mu & \lambda-\mu \\ \lambda-\mu & \lambda+\mu & -(\lambda+\mu) & -(\lambda-\mu) \\ -(\lambda+\mu) & -(\lambda-\mu) & \lambda-\mu & \lambda+\mu \end{bmatrix}. \quad (3.39f)$$

I set $A_x = B_x = A_z = B_z = 0$ in equations (3.35) in zone D, the actual computational domain where no coordinate stretching is applied. This reduces them to the terms given in (3.23) for the model without PMLs. Likewise, equations (3.36) and (3.39) reduce to (3.24).

3.1.3 The source term

For setting up the complete elemental matrix equation (3.15), the source term \mathfrak{F} needs to be suitably rewritten. For a directed single force point source at the location $\mathfrak{x}_s = [x_s, y_s, z_s]^T$ the source terms in equation (3.1) can be written as

$$\begin{aligned}\bar{\mathfrak{f}} &= \bar{s}(\omega) \delta(\mathfrak{x} - \mathfrak{x}_s) \hat{\mathfrak{f}} \\ &= \bar{s}(\omega) \delta(x - x_s) \delta(y - y_s) \delta(z - z_s) \hat{\mathfrak{f}},\end{aligned}\quad (3.40)$$

where $\bar{s}(\omega)$ is the spectrum of the source wavelet, δ is the Dirac-delta function and $\hat{\mathfrak{f}} = [\hat{f}_x, \hat{f}_y, \hat{f}_z]^T$ is a unit vector specifying the force direction. Transforming (3.40) to the ω - x - k_y - z -domain (see equation (A.2)) yields

$$\bar{\mathfrak{f}} = \frac{1}{\sqrt{2\pi}} \bar{s}(\omega) \delta(x - x_s) \delta(z - z_s) e^{-ik_y y_s} \hat{\mathfrak{f}} \quad (3.41)$$

and assuming the source to be located in the x - z -plane, that is $y_s \equiv 0$, results in

$$\bar{\mathfrak{f}} = \frac{1}{\sqrt{2\pi}} \bar{s}(\omega) \delta(x - x_s) \delta(z - z_s) \hat{\mathfrak{f}}. \quad (3.42)$$

The premise $y_s \equiv 0$ is implicit for the 2D case ($k_y \equiv 0$), and for the 2.5D calculations it does not impose a serious problem, since the distance between source and receiver perpendicular to the x - z -plane can be accounted for during the inverse transform of the solution \mathfrak{U} to ω - x - y - z -domain. This will be discussed in more detail in chapter 4.

The final step towards a discretised formulation of \mathfrak{F}^e is to approximate $\bar{\mathfrak{f}}$ using the shape functions given in equation (3.11) as indicated in (3.13):

$$\begin{aligned}F_{A\zeta}^e &:= \int_{\omega_e} N_A \bar{\mathfrak{f}}_\zeta d\Omega \\ &= \frac{1}{\sqrt{2\pi}} \bar{s}(\omega) \hat{\mathfrak{f}}_\zeta \int_{\Omega_e} N_A \delta(x - x_s) \delta(z - z_s) d\Omega \\ &= \frac{1}{\sqrt{2\pi}} \bar{s}(\omega) \hat{\mathfrak{f}}_\zeta \delta_{AS}, \quad A, S \in \{I, J, K, L\}.\end{aligned}\quad (3.43)$$

This restricts possible source locations to the element nodes, implying $\mathfrak{x}_s \in \{\mathfrak{x}_I, \mathfrak{x}_J, \mathfrak{x}_K, \mathfrak{x}_L\}$. For an element containing no source one finds $\mathfrak{F}^e \equiv 0$.

It is important to note that (3.43) is mathematically not exact. What would be desired is a projection of $\bar{\mathfrak{f}}$ in equation (3.42) onto the subspace spanned by the shape functions. Since the product of Delta functions $\delta(x - x_s) \delta(z - z_s)$ that reflects the point source character of $\bar{\mathfrak{f}}$ is not contained in this subspace, (3.43) replaces the Delta shaped source function by a finite element shape function. Thus, replacing (3.40) by

$$\bar{\mathfrak{f}} = \bar{s}(\omega) \delta(y - y_s) N_S(x, z) \hat{\mathfrak{f}}, \quad (3.44)$$

would yield the same result for $F_{A\zeta}^e$. Thus, the resulting source term is not exactly a point source, but the best approximation for a point source that can be achieved using the shape functions (3.11).

3.1.4 The global system matrix

This last section of the technical description of the theory behind the implementation of the finite element solver is concerned with the global system matrix and with its symmetries for certain types of given models. How to assemble a FEM system matrix is well documented in many textbooks (eg. Brenner and Scott, 2008), but since it is, in my opinion, the most complicated part of the implementation, I have described the procedure in more detail in Appendix B.

The global matrix equation

The complete global system matrix \mathbf{S} is the combination of mass matrix and stiffness matrix into

$$\mathbf{S} := \begin{bmatrix} \mathbf{S}_{xx} & \mathbf{S}_{xz} & \mathbf{S}_{xy} \\ \mathbf{S}_{zx} & \mathbf{S}_{zz} & \mathbf{S}_{zy} \\ \mathbf{S}_{yx} & \mathbf{S}_{yz} & \mathbf{S}_{yy} \end{bmatrix} = \begin{bmatrix} \mathbf{M}_{xx} & 0 & 0 \\ 0 & \mathbf{M}_{zz} & 0 \\ 0 & 0 & \mathbf{M}_{yy} \end{bmatrix} + \begin{bmatrix} \mathbf{K}_{xx} & \mathbf{K}_{xz} & \mathbf{K}_{xy} \\ \mathbf{K}_{zx} & \mathbf{K}_{zz} & \mathbf{K}_{zy} \\ \mathbf{K}_{yx} & \mathbf{K}_{yz} & \mathbf{K}_{yy} \end{bmatrix}, \quad (3.45)$$

which implies the definition of corresponding elemental matrices in component notation as

$$\begin{aligned} S_{AB\zeta\zeta}^e &= M_{AB\zeta\zeta}^e + K_{AB\zeta\zeta}^e \\ S_{AB\zeta v}^e &= K_{AB\zeta v}^e \end{aligned} \quad \zeta, v \in \{x, y, z\}. \quad (3.46)$$

The global version of the elemental FEM matrix equation (3.15) can then be written

$$\mathbf{S}\mathfrak{U} + \mathfrak{F} = \mathbf{0}. \quad (3.47)$$

A model consisting of $n^e = n_x^e \cdot n_z^e$ elements, where n_x^e and n_z^e are the number of elements in the horizontal and vertical directions, respectively, contains $n = n_x \cdot n_z$ nodes. Here $n_x = n_x^e + 1$ and $n_z = n_z^e + 1$ are the number of nodes in the horizontal and vertical directions. The system matrix for this model is of size $3n \times 3n$ and can be divided into nine sub-matrices of size $n \times n$, as indicated in equation (3.45). An analogous segmentation can be applied to the global solution vector and the global source vector, viz.

$$\mathfrak{U} = \begin{bmatrix} \mathfrak{U}_x \\ \mathfrak{U}_z \\ \mathfrak{U}_y \end{bmatrix} \quad \text{and} \quad \mathfrak{F} = \begin{bmatrix} \mathfrak{F}_x \\ \mathfrak{F}_z \\ \mathfrak{F}_y \end{bmatrix}, \quad (3.48)$$

introduced in equation 3.47, which are both of length $3n$. The quantities \mathfrak{U}_ζ ($\zeta \in \{x, y, z\}$) are the projections of the exact continuous solution components $\bar{u}_\zeta \in \mathcal{U}$ onto the finite subspace $\mathcal{U}_N \subset \mathcal{U}$ via the projection (3.6). The global shape functions N_i in (3.6) are the same functions as the local ones given in (3.11), but defined in the global coordinate system. The index i runs through all grid nodes in column major order as shown in Figure B.1 for the example of a FEM grid of three by three elements. Thus, the first entry of \mathfrak{U} (U_{1x}) is the x -component of the solution at the upper left corner node of the grid and the last entry (U_{ny}) is the y -component at the lower right corner node.

System matrix symmetries

A close look at the equations for the elemental matrix entries given in (3.35), (3.36) and (3.39) and their relative locations in the global matrix \mathbf{S} reveals that in the most general case this matrix is only of structural symmetry and can be written as a sum of a symmetric and an antisymmetric matrix, as suggested in Figure 3.4.

For solving equation (3.47) I use PARDISO, a state-of-the-art direct linear sparse matrix solver routine (Schenk and Gärtner, 2004, 2006). With a direct solver it is possible to solve for multiple right hand sides, that is, multiple source vectors \mathfrak{F} . PARDISO efficiently exploits the structural symmetry of \mathbf{S} . If $k_y = 0$, then \mathbf{S}_{xy} , \mathbf{S}_{yx} , \mathbf{S}_{zy} and \mathbf{S}_{yz} are zero and the matrix becomes symmetric. Then, only the upper triangular matrix has to be assembled. The solution process becomes faster and more memory efficient compared with a structurally symmetric system matrix.

3.2 Assessment of accuracy and efficiency for the 2D problem

After the technical part on the theory of the FEM forward solver and some of its implementation details in section 3.1, I will now focus on the accuracy and efficiency of the algorithm. First, I will compare results from my FEMFd algorithm with an analytic solution using very conservative settings for the PML boundaries. Then, I investigate to what extent the width of the PML boundary layers can be reduced, such that still acceptable results can be obtained. Finally, I will compare results of my FEMFd algorithm with an FDTD solution. On the basis of this comparison, I will also discuss the general efficiency of frequency- and time-domain modelling.

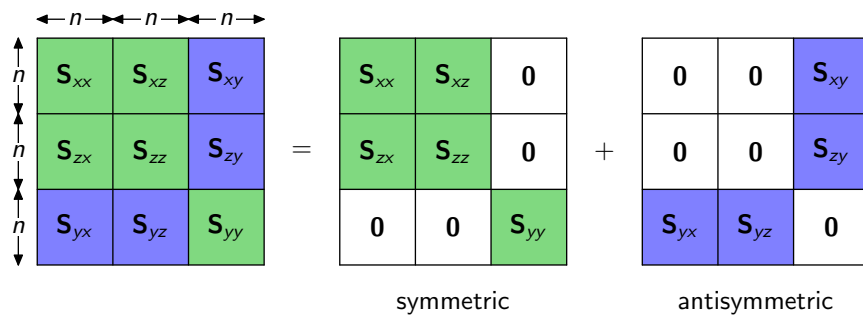


Figure 3.4: Zonation, size and symmetries of the complete system matrix. When n is the total number of nodes in the model, the matrix is of size $3n \times 3n$, containing 9 sub-matrices of size $n \times n$, one for each possible combination of solution vector components x , y and z . The sub-matrices marked green would make up a symmetric matrix when the ones marked in blue would be set to zero. The sub-matrices marked in blue would generate an antisymmetric matrix, when the green parts would be set to zero.

3.2.1 Accuracy: Comparison with an analytic solution

For testing the accuracy of my FEMFd algorithm, I compare my results with an analytic solution for a homogeneous full space model given in Appendix C.2.1. the model is of dimension $40\text{ m} \times 40\text{ m}$ with PML-layers of width $n_{\text{PML}} = 200$ elements, and the medium parameters are the same as for the model *FH* introduced in section 2.1.1 (Table 2.1). As listed in Table 3.2, I have considered three frequencies f and four different grid steps dh . An important quantity for the numerical accuracy is the number of grid steps per minimum wavelength $N = \frac{\lambda_{\min}}{dh}$. The corresponding values are listed in Table 3.2.

Furthermore, the source and receiver directionality need to be taken into account. I have analysed the *xx* configuration (*x*-directed source and *x*-directed receiver) along profiles through the source position (in the centre of the model) that are parallel, perpendicular and at an angle of 45° to the source direction. Due to the symmetry of the problem, corresponding *zz* configurations, rotated by 90° , lead to equivalent results and are not shown. For the *xz* configuration, only profiles at an angle of 45° are analysed (the solution values along profiles parallel and perpendicular to the source direction are equal to zero).

Results for $N = 16$ are displayed in Figure 3.5. The left panels show the relative model sizes, in units of minimum wavelengths λ_S , for the three different frequencies together with the cut directions. In the middle panels, the analytic and numerically computed Green's functions for the three frequencies are displayed. The right panels show the relative errors (normalised by the maximum of the corresponding imaginary part).

The horizontal axis of the wavefield solution and error plots, which represent the distance to the source, are also displayed in minimum wavelengths units. It is interesting to note that, when plotted like this, not only are the analytic solutions equivalent for the different frequencies, but the error curves for all frequencies also lie almost exactly on top of each other. This indicates that only the N value is relevant for the numerical accuracy. The relative errors are quite different for the four cases displayed in Figures 3.5a to 3.5d. The *xx* configuration results for the profile in the direction of the source (Figure 3.5a) have the smallest relative errors (less than 1%), and for the *xz* configuration (Figure 3.5d) errors of up to 13% are observed.

With the exception of the *xx* configuration in Figure 3.5a, all relative errors tend to increase with increasing distance. This is detailed in Figure 3.6, which shows enlarged

f [Hz]	λ_S [m]	$40\text{ m}/\lambda_S$	$N = \lambda_S/dh$				
125	8	5	16	32	64	128	
250	4	10	8	16	32	64	
500	2	20	4	8	16	32	
			0.5	0.25	0.125	0.0625	dh [m]

Table 3.2: Minimum wavelengths λ_S , model edge length (40 m) in units of λ_S , and number of grid steps per minimum wavelength $N = \frac{\lambda_S}{dh}$, for the three frequencies f and four grid steps dh used to test the accuracy of the FEM solution against the analytic solution.

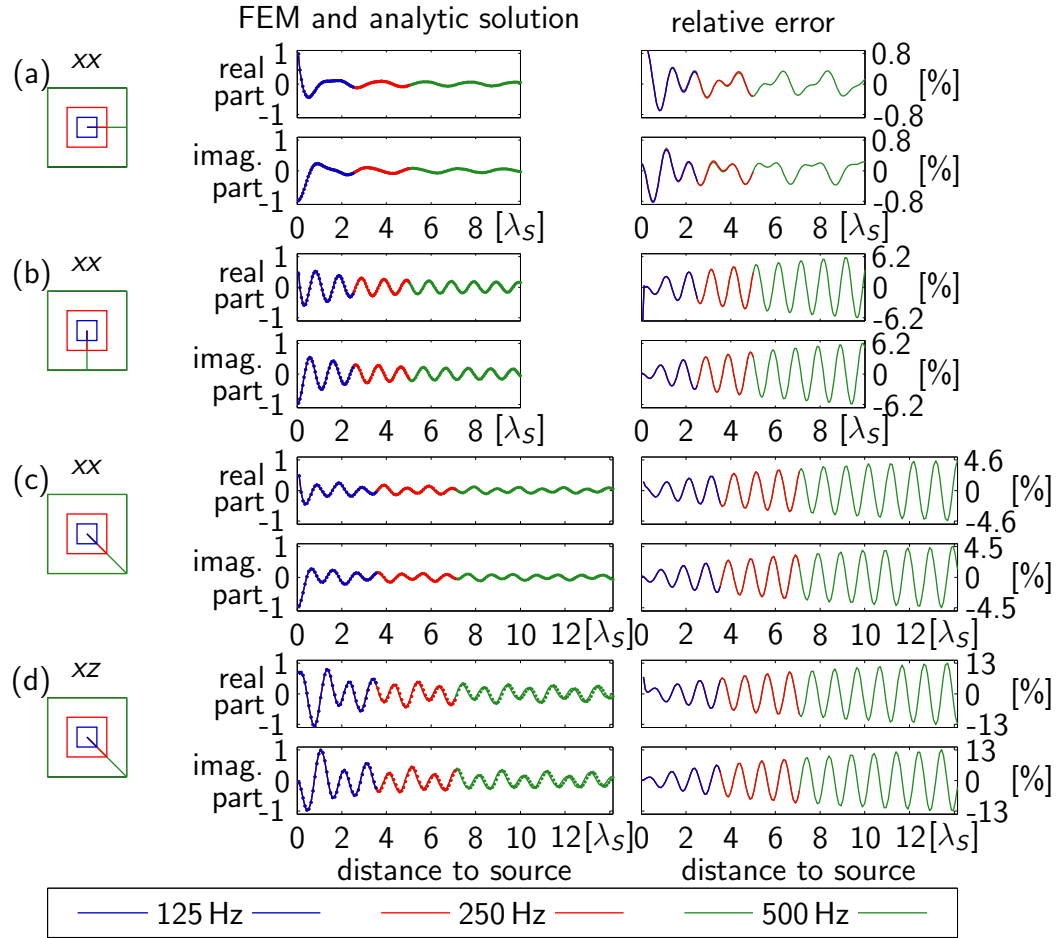


Figure 3.5: Different cuts through the analytic solution given in Appendix section C.2.1. The boxes to the left show sketches of the relative sizes of the solutions for the three different frequencies in units of λ_s , coloured according to the legend, together with the cut, along which the solution is taken for the plot. The middle panels show the FEM solutions as a function distance to the source along the cuts (in units of λ_s) for a value of $N = 16$, plotted (as dots) together with the corresponding analytic solution as solid lines, and in the panels on the right hand side the relative error of the FEM solution is shown. Again the maximum of the imaginary part is taken as a reference. (a) shows real (top) and imaginary (bottom) part of a cut through solution xx in source direction, (b) shows real (top) and imaginary (bottom) part of a cut through solution xx perpendicular to the source direction, (c) shows real (top) and imaginary (bottom) part of a diagonal cut through solution xx and (d) shows real (top) and imaginary (bottom) part of a diagonal cut through solution xz . The amplitude of the FEM solution is correct, but in cases (b) to (d) there is an increasing phase shift with respect to the analytic solution, such that the error values grow with the distance to the source. (See also Figure 3.6).

versions of the middle panels of Figures 3.5a and 3.5d. The error is governed by an increasing stretch of the numerical solution, which can be quantified with a distance dependent lag of the analytic and numerically computed curves (Figure 3.6c). This effect is most pronounced for the xz case and negligible for the xx case along the source direction. The small numerical errors for the xx case along the source direction can be explained by the fact that no S -wave energy is radiated in this direction. Therefore, the minimum wavelength for this configuration rather corresponds to λ_P , which is almost twice as large as λ_S .

The accuracy of the FEMFd solution as a function of N is investigated in Figure 3.7. Here, only the two extreme cases, namely the xx case along a cut in the source direction and the xz case along a cut in the diagonal direction, are displayed. As expected, the errors decrease with increasing N . To achieve an accuracy of 5%, less than 8 grid points per minimum wavelength would be required for the xx case. This corresponds to a commonly employed rule of thumb that about 10 grid points per minimum wavelength are required (e.g. Marfurt, 1984). By contrast, 32 grid points per wavelength would be required to achieve a similar accuracy for the xz case.

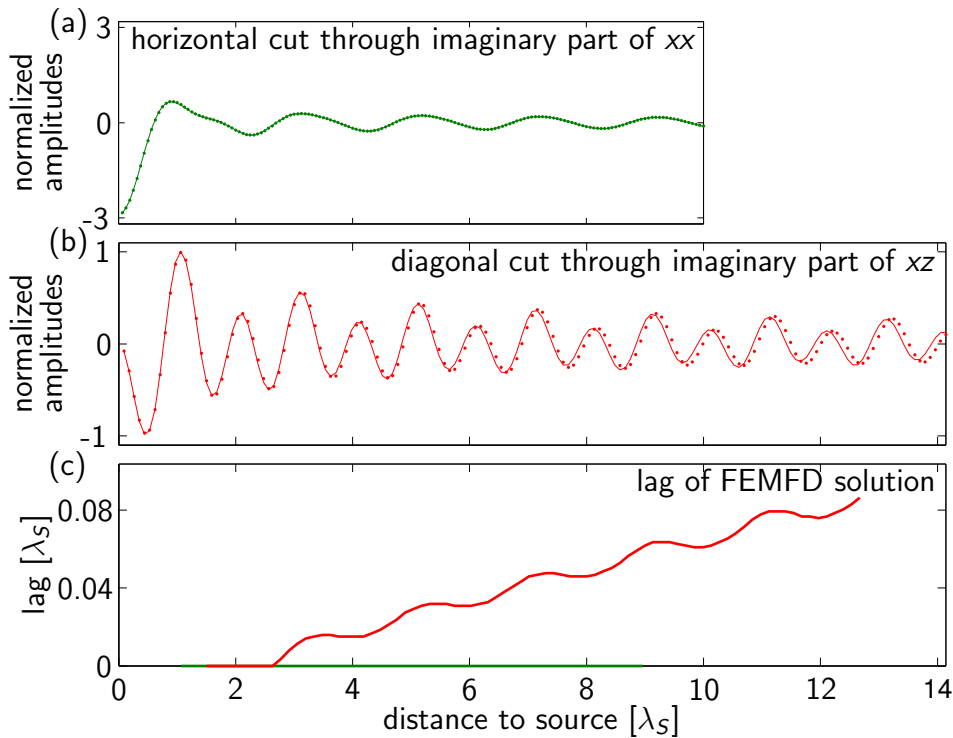


Figure 3.6: Zoom onto the imaginary parts of the solutions for 500 Hz for the cases shown in Figure 3.5 exhibiting the best (xx) and the worst (xz) fit. (a) corresponds to 3.5a and shows the best fit, no phase shift between the analytic and FEM solutions is observed. (b) corresponds to 3.5d and shows the worst fit, due to the phase lag between the analytic and FEM solutions that increases with source distance. (c) shows the phase lag between the analytic and FEM solutions shown in (a) and (b) computed by cross-correlation using a sliding window. It is zero for the ‘well behaved’ case (a) and grows with distance to the source for case (b).

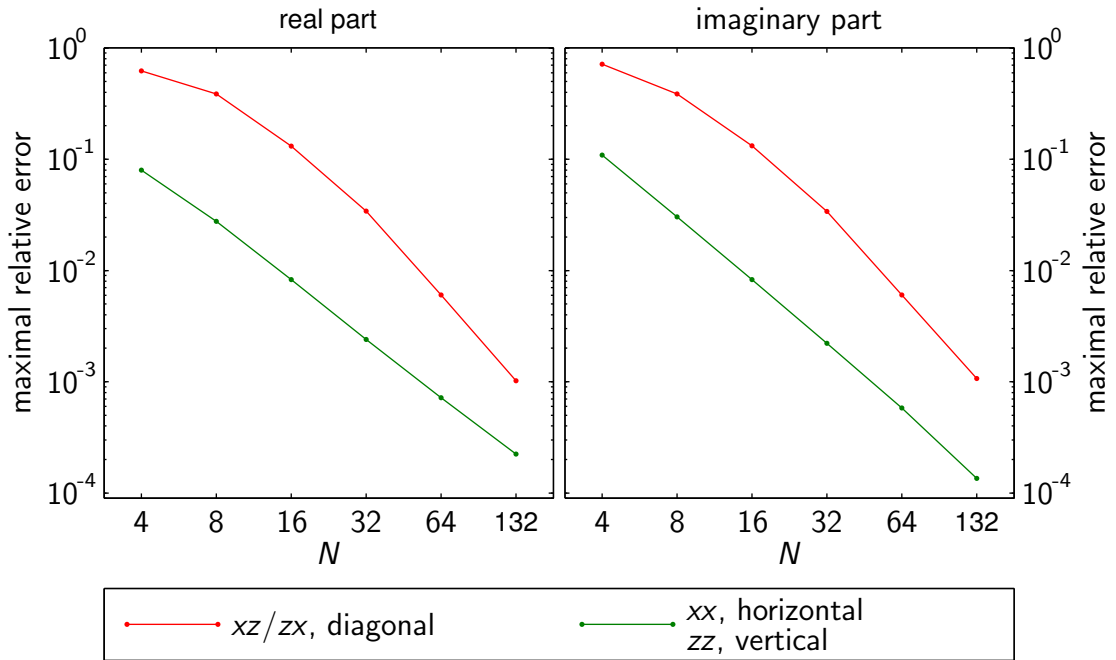


Figure 3.7: Relative errors of the FEM solution with respect to the analytic solution. for different combinations of source type and displacement field component and different parts of the solution. *diagonal* stands for the maximum error along the diagonal, *vertical* for the maximum error along a vertical cut through the source position and *horizontal* for the maximum error along a horizontal cut through the source position. See Table 2.2 for the definition of the abbreviations denoting the different combinations of source type and displacement field component. The errors are relative to the absolute maximum of the imaginary part of the respective analytic solution for the same reason as described in section 3.2.2.

3.2.2 PML validation

For the calculations in the previous subsection, I used a very large number of elements ($n_{\text{PML}} = 200$) to define the PMLs surrounding the model. This high value was chosen to make sure that any difference with the analytic solution is due to grid dispersion and not caused by spurious reflections from the artificial model boundaries. Using such wide PMLs is very inefficient. Therefore, I have investigated by how much n_{PML} can be reduced and still sufficiently suppress the spurious reflections. Simulations for different values of the parameter c , introduced in Table 3.1, showed no strong influence on the PML performance. I have chosen a value of $c = 10$.

To estimate a suitable value of n_{PML} , I perform test calculations for three different elastic isotropic models, using PML widths of $n_{\text{PML}} = 10, 30, 50, 100, 150$ and 200 elements. First, I consider the homogeneous full space model already employed in the previous section (introduced as *FH* in section 2.1.1). Then, to investigate the PML performance in the presence of a free surface, I look at a homogeneous half space model with equivalent elastic parameters (model *HH* defined in section 2.1.1). Finally, I check the performance of the PMLs with a gradient model including a free surface (model *HG* in 2.1.1).

I compute both the horizontal and vertical components of the displacement fields resulting from horizontally and vertically directed single force sources for the three frequencies $f = 125$ Hz, 250 Hz and 500 Hz. For each model, this is performed for two different source locations, one as far away as possible from all the artificial boundaries, the other one placed near to the PMLs (Figure 3.8). This setup allows assessment of whether the distance of the source to the boundary has any influence on PML performance.

PML performance in the absence of a free surface

The FEM model is discretised with finite elements of edge length 10 cm. The resulting values of N , listed in Table 3.3, assure suitable modelling accuracy. The Table also gives the widths of the PMLs (d_{PML}) in metres and in units of wavelengths.

Figures 3.9 and 3.10 show plots of the natural logarithm of the absolute value of the solution amplitudes versus the horizontal coordinate (x , see Figure 3.8a). for the centre source and the source near the boundary. Horizontal profiles through the respective source positions are displayed. The curves start 6 m to the left of the artificial boundary (denoted by x_R , see Figure 3.2) and end 3 m to the right of it. For each configuration and frequency shown, the values are normalised to the amplitude of the solution for $n_{\text{PML}} = 200$ at x_R .

The results for the centre source (Figure 3.9) show, that PML widths of $n_{\text{PML}} > 30$ are sufficient in this case. For the lowest frequency (Figure 3.9a), the least spurious reflections are observed. The amount of noise due to the model truncation increases

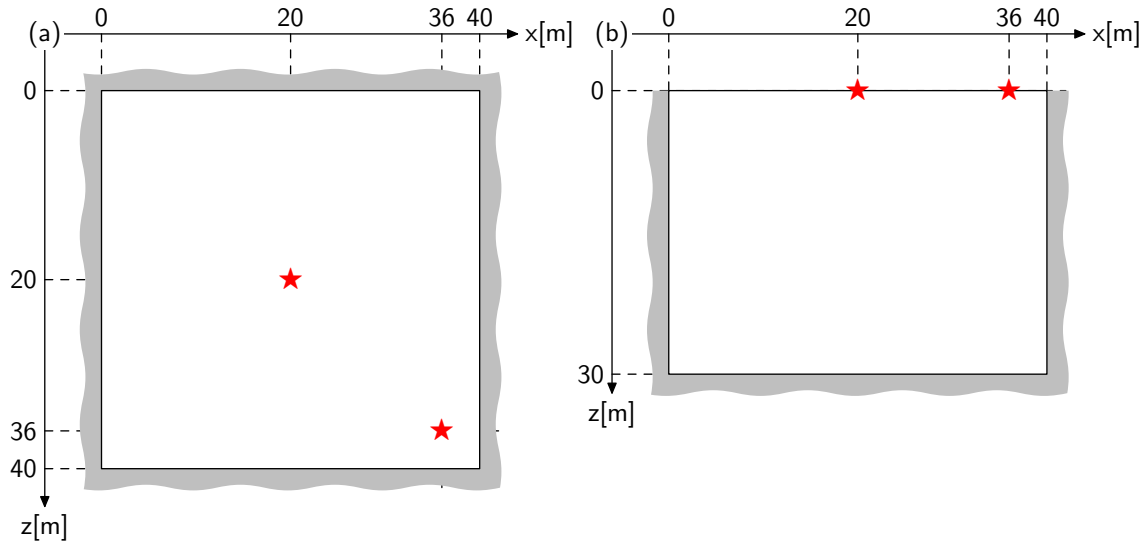


Figure 3.8: Experimental setup for testing the performance of the PMLs. (a) shows a homogeneous model with PMLs as indicated by the areas shaded in grey. The model parameters are identical to model *FH* introduced in section 2.1.1. (b) shows the geometry of a free surface model and PMLs to the left, right and at the bottom of the model. This model geometry is used for a homogeneous half space model with elastic parameters equivalent to that of model *HH* and a gradient model with elastic parameters as those of model *HG*, both introduced in section 2.1.1. The red stars denote source locations.

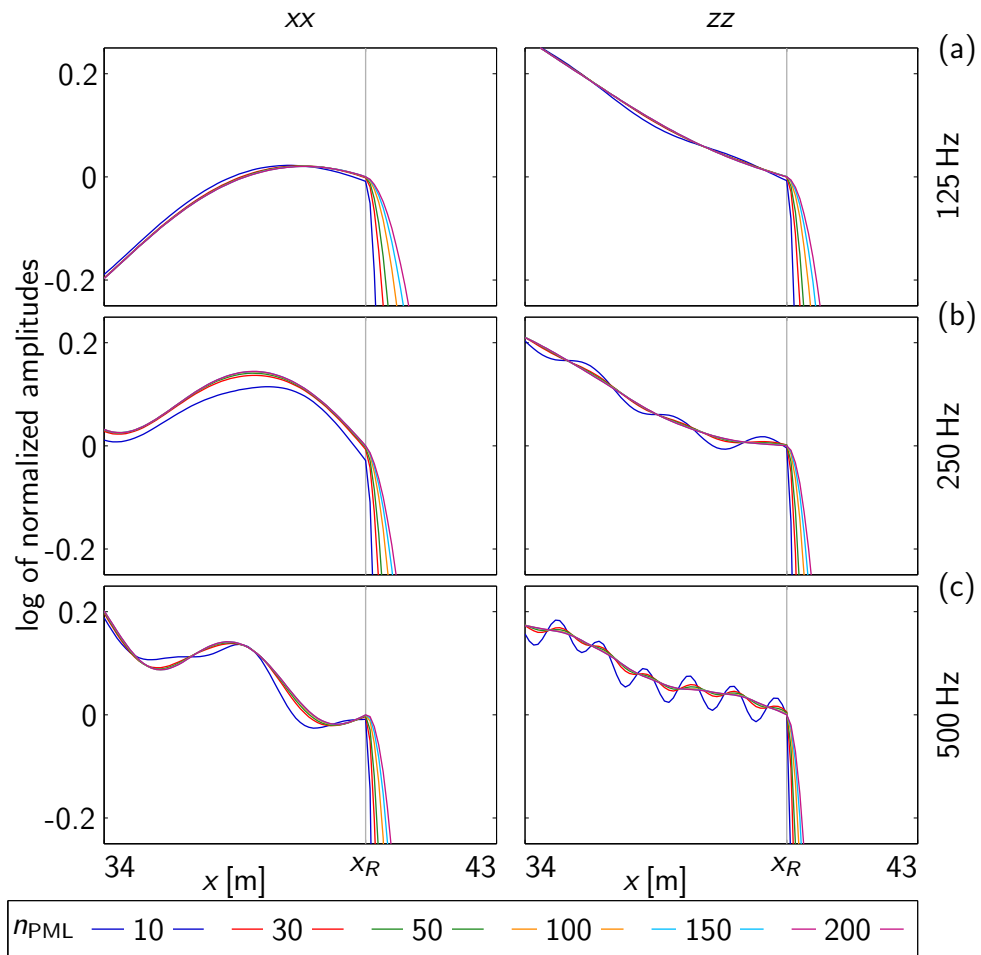


Figure 3.9: PML performance assessment for a source in the centre of a homogeneous full space model (model *FH* in section 2.1.1). FEM solutions for different PML widths and frequencies of (a) 125 Hz, (b) 250 Hz and (c) 500 Hz. Shown is a horizontal profile through the source position for the centre source shown in Figure 3.8a, starting at $x = x_R - 6$ m and ending at $x = x_R + 3$ m, where x_R is the horizontal position of the boundary to the PMLs at the right model edge (see Figure 3.2). Since the solutions for all other combinations of source/receiver components are zero along this profile, I only show configurations *xx* (left) and *zz* (right).

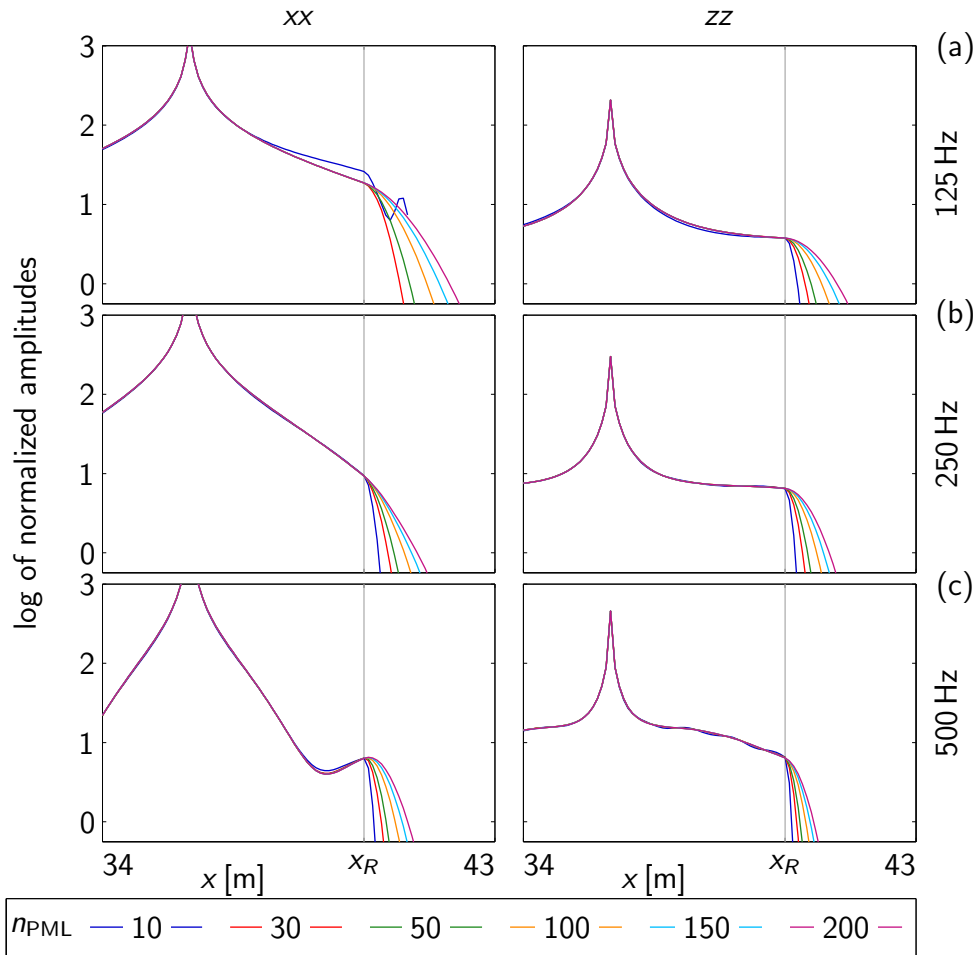


Figure 3.10: PML performance assessment for a source in the lower right corner of a homogeneous full space model (model *FH* in section 2.1.1). FEM solutions for different PML widths and frequencies of (a) 125 Hz, (b) 250 Hz and (c) 500 Hz. Elastic parameters are those of model *FH* in section 2.1.1. Shown is a horizontal profile through the source position for the source in the lower right corner (see Figure 3.8a) starting at $x = x_R - 6$ m and ending at $x = x_R + 3$ m, where x_R is the horizontal position of the boundary to the PMLs at the right model edge (see Figure 3.2). Since all other configurations are zero along this profile, I only show configurations *xx* (left) and *zz* (right).

n_{PML}	10	30	50	100	150	200		
d_{PML} [m]	1	3	5	10	15	20	f [Hz]	N
d_{PML}/λ_S	0.125	0.375	0.625	1.250	1.875	2.500	125	80
	0.250	0.750	1.250	2.500	3.750	5.000	250	40
	0.500	1.500	2.500	5.000	7.500	10.000	500	20
d_{PML}/λ_R	0.134	0.402	0.670	1.340	2.011	2.681	125	75
	0.268	0.804	1.340	2.681	4.021	5.362	250	37
	0.536	1.609	2.681	5.362	8.043	0.724	500	19

Table 3.3: PML widths expressed in terms of number of elements (n_{PML}), metres (d_{PML}) and in minimum propagation wavelengths (corresponding to the shear or Rayleigh wave) for the three different frequencies used for testing the performance of the PMLs in case of a homogeneous unbounded model and a homogeneous half space model with model parameters of models *FH* and *HH* (see section 2.1.1). Also listed are the number of grid steps per minimal wavelength $N = \frac{\lambda_{\min}}{dh}$, where $\lambda_{\min} = \lambda_S$ for the full space and $\lambda_{\min} = \lambda_R$ for the half space.

with increasing frequency. Thus it can be concluded that larger values of n_{PML} have to be chosen for smaller numbers N .

The spurious reflections observed in the solutions for the peripheral source (Figure 3.10) are similar in amplitude and shape. Note the different scale with respect to Figure 3.9. The only remarkable difference from the results for the centre source is the large error for $n_{\text{PML}} = 10$, configuration *xx* and a frequency of 125 Hz. Here, the source is placed only half a wavelength away from the boundary, and it seems that the near-field phases are entering the PMLs, making a larger number of elements to form the PML.

PML performance in the presence of a free surface

To investigate the PML performance in the presence of a free surface, I use two different models, both of size $40 \text{ m} \times 30 \text{ m}$. The two sources are placed on the free surface, the first one horizontally centred and the second one placed near the boundary to the PML on the right side of the model, as shown in Figure 3.8b. For the homogeneous half space I again use a FEM grid step of $dh = 10 \text{ cm}$, and the gradient model is discretised into finite elements of edge length 5 cm. The resulting values of N , given in Table 3.3 for the homogeneous case and in Table 3.4 for the gradient model, guarantee sufficient modelling accuracy.

For the homogeneous model, Figures 3.11 and 3.12 show similar amounts of spurious reflections for the different values of n_{PML} as were already observed for the homogeneous full space in Figures 3.9 and 3.10. But in the case of the simulations for the longest wavelength, the PMLs show a notably worse performance. For the less problematic source position in the centre of the free surface, Figure 3.11a shows a similar failure for the *xx* configuration and $n_{\text{PML}} = 10$, as already observed in Figure 3.10a for the homogeneous full space. Results become even worse when the source is placed near the absorbing boundary. Here (Figure 3.12a) the PMLs fail completely for all configurations in the case $n_{\text{PML}} = 10$. I again attribute this to near-field phases entering the PML

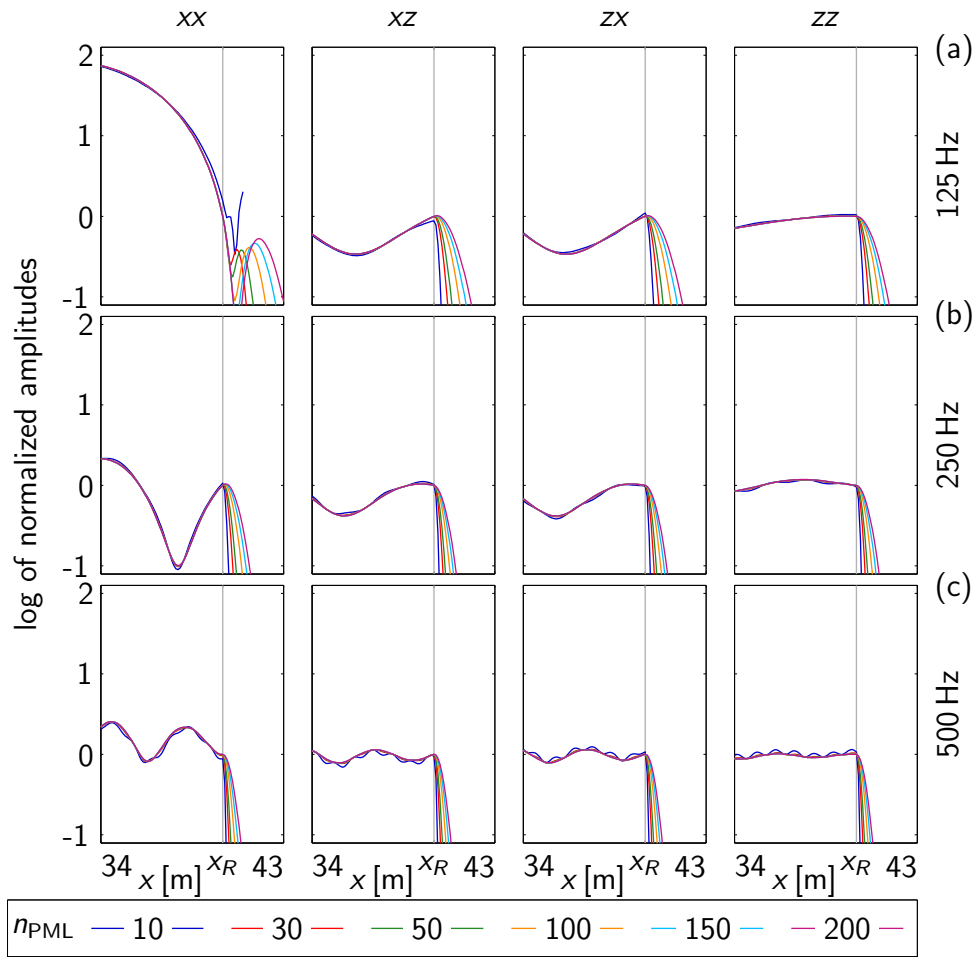


Figure 3.11: PML performance assessment for a source placed in the centre of the free surface of a homogeneous half space (model HH in section 2.1.1). FEM solutions for different PML widths and frequencies of (a) 125 Hz, (b) 250 Hz and (c) 500 Hz. Shown is a horizontal profile along the free surface through the solution for the source at $x = 20$ m (see Figure 3.8b) starting at $x = x_R - 6$ m and ending at $x = x_R + 3$ m, where x_R is the horizontal position of the boundary to the PMLs at the right model edge (see Figure 3.2). Left to right, I show configurations xx , xz , zx and zz .

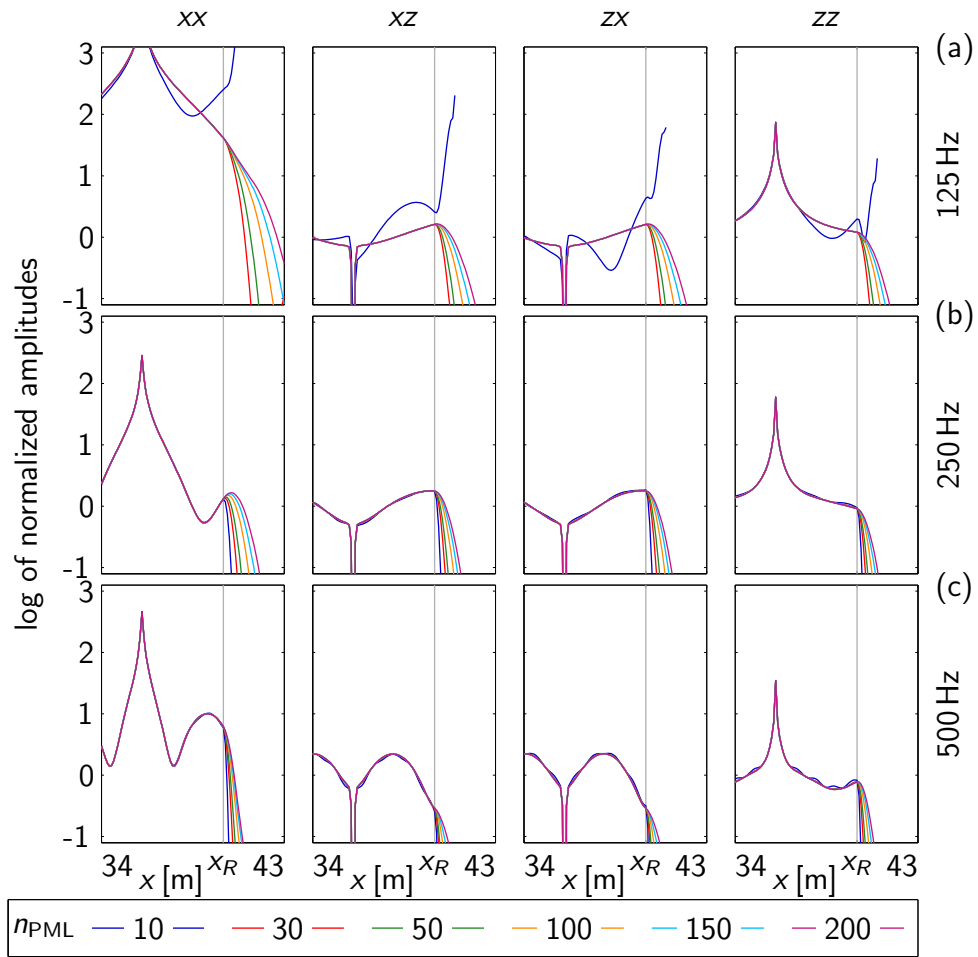


Figure 3.12: PML performance assessment for a source placed near the artificial boundary of the free surface of a homogeneous half space (model HH in section 2.1.1). FEM solutions for different PML widths and frequencies of (a) 125 Hz, (b) 250 Hz and (c) 500 Hz. Shown is a horizontal profile along the free surface through the solution for the source at $x = 36$ m (see Figure 3.8b) starting at $x = x_R - 6$ m and ending at $x = x_R + 3$ m, where x_R is the horizontal position of the boundary to the PMLs at the right model edge (see Figure 3.2). Left to right, I show configurations xx , xz , zx and zz .

n_{PML}	10	30	50	100	150	200		
d_{PML} [m]	0.5	1.5	2.5	5	7.5	10	f [Hz]	N
d_{PML}/λ_R	0.110	0.331	0.552	1.105	1.657	2.210	125	96
	0.221	0.663	1.105	2.210	3.314	4.419	250	48
	0.442	1.326	2.210	4.419	6.629	8.838	500	24

Table 3.4: PML widths expressed in terms of number of elements (n_{PML}), metres (d_{PML}) and in minimum Rayleigh wave wavelengths (approximated by the wavelength computed for the Rayleigh wave velocity of a homogeneous half space with v_P and v_S equivalent to the minimal values in the gradient model) for the three different frequencies used for testing the performance of the PMLs in the case of a gradient model with a free surface and model parameters as model *HG* (see section 2.1.1). Also listed is the number of grid steps per minimum wavelength used.

zone. These evanescent wave types cannot be attenuated properly, as will be discussed in more detail in section 4.4.

As can be seen in Figures 3.13 and 3.14, adding heterogeneity in the form of a vertical gradient to the model does not deteriorate the PML performance. Since the smallest distance of the source to the PMLs is approximately one wavelength (for $f = 125$ Hz), the problem of near-field phases does not appear as pronounced as in the case of the homogeneous model, where the shortest distance was only half a wavelength. Only for configuration *xx* and the source placed near the PML boundary (Figure 3.14a) is this effect observed.

Conclusions on the PML test

The tests in this section have shown that the PMLs as implemented in the FEM code work as expected for 2D forward modelling.

Only if the source is placed at a distance of less than a wavelength away from the boundary to the PMLs and if the width of the PMLs is relatively thin, the performance is unsatisfactory. It is worst if the source direction points towards the near boundary and the field component perpendicular to this boundary is recorded. This effect is more pronounced for models that include a free surface, but it is not observed for PML widths of $n_{\text{PML}} > 30$. Thus I expect PML widths of $n_{\text{PML}} = 30$ to sufficiently attenuate spurious reflections in the 2D case.

3.2.3 Comparison with an established FDTD modelling code

Besides comparing my FEMFd code with an analytic solution, it is equally important to check its reliability under a more realistic scenario, for which no analytic solution exists. Therefore, I have performed a comparison with the well established FDTD code already introduced in chapter 2. Seismograms were computed for the vertical gradient model *HG*, already employed in section 2.1.1.

The setup of the modelling test is shown in Figure 3.15. Note that the source and the topmost row of receivers are not placed directly at the free surface but one FD grid step

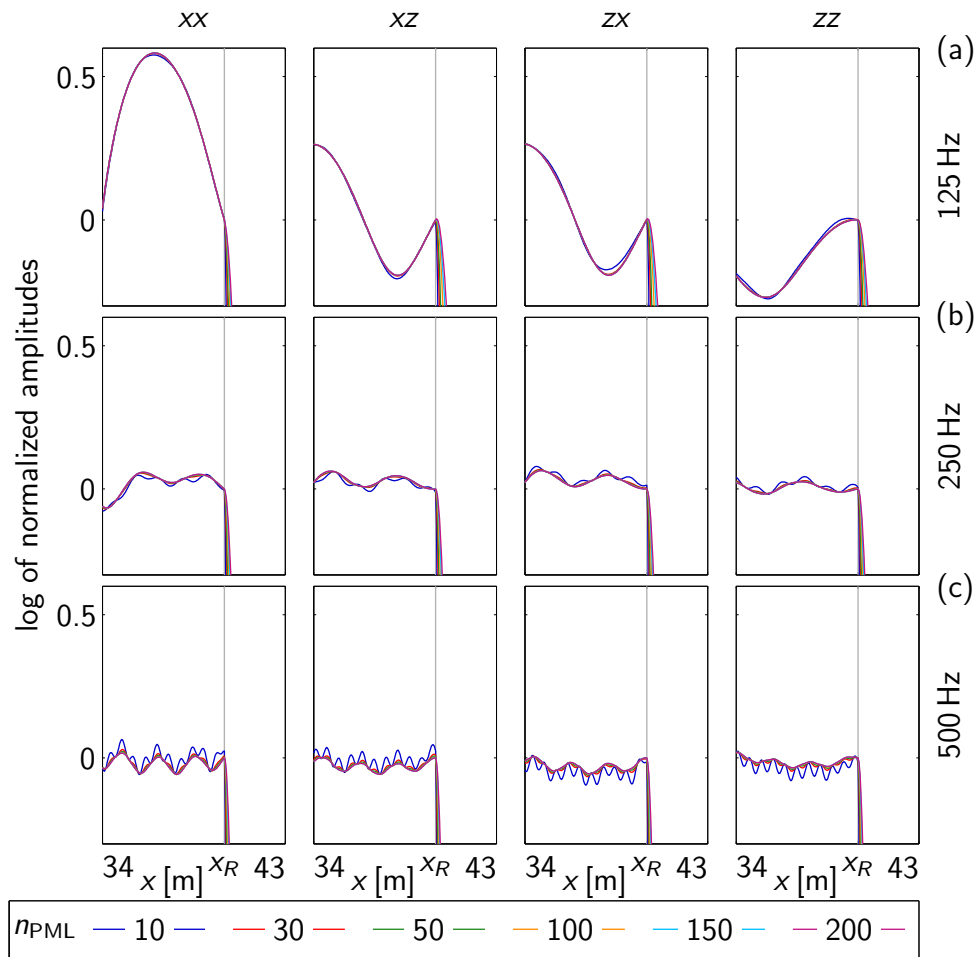


Figure 3.13: PML performance assessment for a source placed in the centre of the free surface of a gradient (model HG in section 2.1.1). FEM solutions for different PML widths and frequencies of (a) 125 Hz, (b) 250 Hz and (c) 500 Hz. Shown is the solution along a horizontal profile along the free surface for the source at $x = 20$ m (see Figure 3.8b) starting at $x = x_R - 6$ m and ending at $x = x_R + 3$ m, where x_R is the horizontal position of the boundary to the PMLs at the right model edge (see Figure 3.2). Left to right, I show configurations xx , xz , zx and zz .

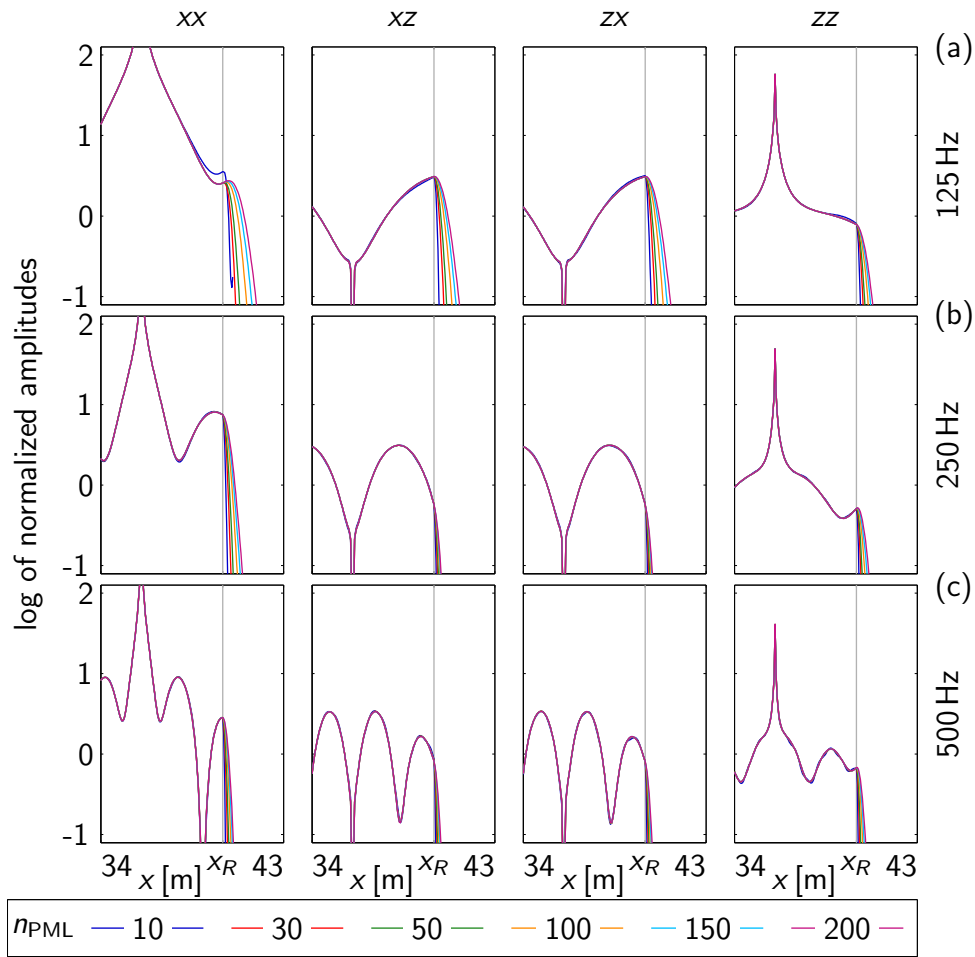


Figure 3.14: PML performance assessment for a source placed near the boundary between physical medium and PMLs at the free surface of a gradient model (model *HG* in section 2.1.1). FEM solutions for different PML widths and frequencies of (a) 125 Hz, (b) 250 Hz and (c) 500 Hz. Shown is the solution along a horizontal profile along the free surface for the source at $x = 36$ m (see Figure 3.8b) starting at $x = x_R - 6$ m and ending at $x = x_R + 3$ m, where x_R is the horizontal position of the boundary to the PMLs at the right model edge (see Figure 3.2). Left to right, I show configurations *xx*, *xz*, *zx* and *zz*.

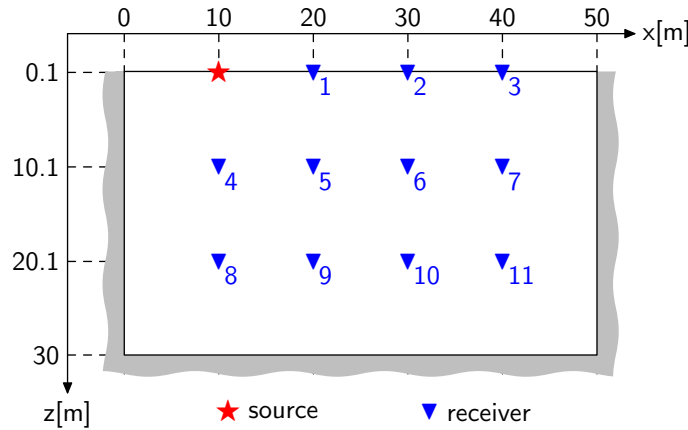


Figure 3.15: Experimental setup for the comparisons of my FEMFd algorithm with the FDTD code introduced in chapter 2. Elastic model parameters are the same as for model *HG* introduced in section 2.1.1.

$d_{FD} = 0.1$ m below it. Since the FD algorithm computes the wave field on a staggered grid (SSG) (see Bohlen and Saenger, 2006, Figure 1a), I have to use half the FD grid step as the size for the finite element computations, that is $d_{FEM} = \frac{d_{FD}}{2} = 0.05$ m, to be able to place the source and receivers at identical positions. In the SSG implementation, the vertically directed force type source force is placed half a grid step to the right and half a grid step below the prescribed source position and the vertical component of the wave field is stored at the same staggered position relative to the receiver coordinates, as it is illustrated in Figure 3.16. The horizontally directed force source and the horizontal component of the wavefield are referred to the actual grid positions as shown.

As a source wavelet I use the Ricker type wavelet, as introduced in section 2.1.1, but here with a centre frequency of 300 Hz. Therefore, only frequencies up to 1000 Hz have

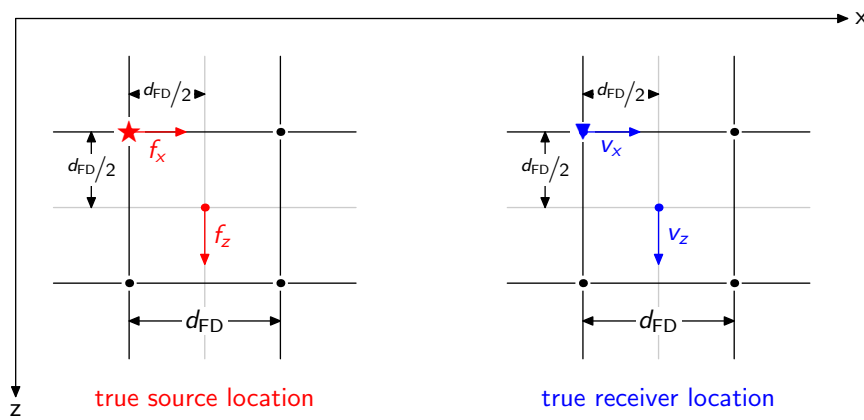


Figure 3.16: Actual positions of the vertical and horizontal source forces and receivers in the SSG implemented in the FD code, shown for a grid step of d_{FD} . The red star marks the source position, the red arrows the actual positions of horizontal single force source f_x and vertical single force source f_z . The blue triangle marks the desired receiver position, the blue arrows denote the points at which horizontal field component v_x and the vertical field component v_z really are computed.

to be computed with my FEM code.

With the FD code I compute seismograms of 0.1 s length, such that I need to sample the frequency space in steps of $df = \frac{1}{0.1} \frac{1}{s} = 10$ Hz, resulting in a total number of 100 FEM forward calculations, i.e. 100 frequencies. Finally, the displacements computed by my FEM code had to be converted to velocities (multiplication by $i2\pi f$) and inversely Fourier transformed for comparing them with the FDTd results.

The resulting traces, plotted together with the FD seismogram traces, are shown in Figure 3.17. The agreement between the two solutions is excellent and confirms the reliability of my code.

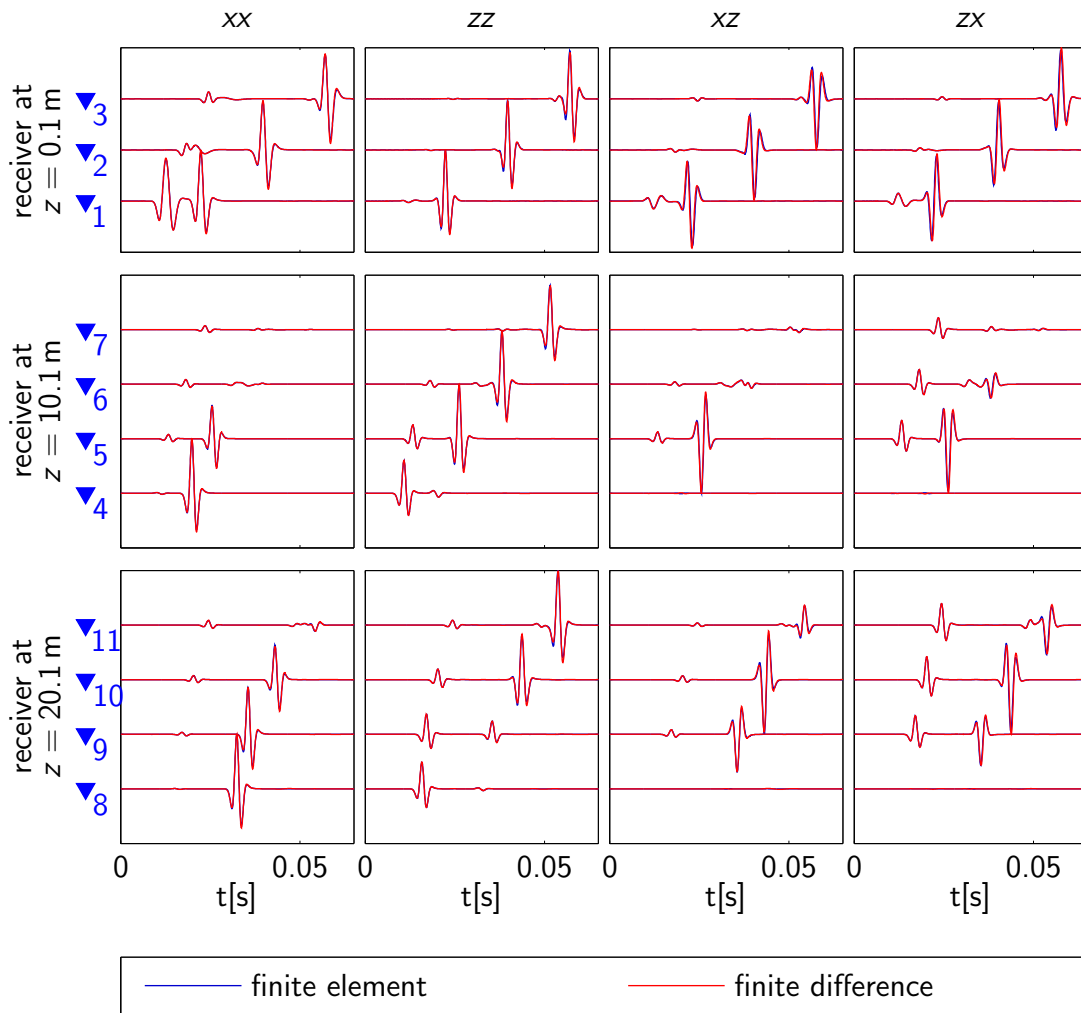


Figure 3.17: Seismograms computed with the FDTd code plotted on top of the solution computed with the FEMFd code. The source location and the receiver positions are shown in Figure 3.15, where the receivers are numbered correspondingly. All FEMFd seismogram traces are multiplied by a constant factor (accounting for the different source amplitudes due to different implementation) to match the amplitudes of the FDTd seismogram traces.

3.2.4 Efficiency: assessment of time-domain and frequency-domain modelling benefits

In the previous section I have demonstrated that seismograms computed with my FEMFd algorithm and the FDTd program of Bohlen (2002) are virtually identical. It is also interesting to compare the computational resources required by the two quite different approaches. In fact, time-domain vs. frequency-domain seismic modelling is an extensively discussed topic, which makes such a comparison even more interesting. I compare the computation times and the memory consumptions of the two codes by means of the modelling task shown in Figure 3.15. As described below, the modelling parameters were slightly changed for a fair comparison of the usage of the computational resources.

Modelling parameters The elastic parameters of the model are discretised for both the FDTd and the FEMFd computations with a grid step of 0.1 m. This dictates a time step for the FDTd computations of $dt \leq \frac{6}{7} \frac{dh}{\sqrt{2} \cdot \max(v_p)} = 24.24 \mu\text{s}$ to fulfil the stability criterion for FDTd modelling (see section 2.1.1). I use $dt = 20 \mu\text{s}$ and compute a total of $n_t = 3250$ time steps to get a seismogram length of 0.065 s (see Figure 3.17).

To compute seismograms of length 0.065 s with the FEMFd code, the frequency space would have to be sampled in steps of $df \leq \frac{1}{0.065} \frac{1}{s} = 15.385 \text{ Hz}$. The source spectrum has significant amplitudes up to roughly 1000 Hz. Therefore, 66 frequencies would be required to compute unaliased seismograms.

Results In the case of the FD code, I have to perform one forward calculation for each source position and source type, leading to a total computation time for n_s sources of $t_{\text{FD}} = n_t \cdot n_s \cdot t_s$, where n_t is the number of time steps and t_s the time required to compute a single time step (approx. 0.06s). The overall computation time t_{FD} is shown with the red line in Figure 3.18a.

Using the direct matrix solver PARDISO (Schenk and Gärtner, 2004, 2006), for the FEMFd computations, it is possible to solve for several source positions at once. Computations for one to fifty sources and one to sixty-six frequencies were carried out. The results are indicated by the green, orange, cyan and blue lines in Figure 3.18a.

The total computation time of the FEMFd code is found to be $t_{\text{FEM}} = A_f + P_f(n_s) + (n_f - 1)(A_o + P_o(n_s))$, where A_f is the time spent for assembling the system matrix when computing for the first frequency, $P_f(n_s)$ is the time PARDISO needs to solve for n_s right hand sides in the case of the first frequency in the program sequence; A_o and $P_o(n_s)$ are the assembly and solving times for every following frequency in the program run. Since the necessary memory is allocated during the computations for the first frequency, A_o and $P_o(n_s)$ are smaller than A_f and $P_f(n_s)$.

The curve for one frequency is given as a reference. Modelling three or five frequencies are possible scenarios for a typical waveform inversion in the frequency domain, as suggested in section 2.4.2 (see Figure 2.32).

Each FDTd forward calculation requires the same amount of memory (14.96 MB). This is indicated by the red line in Figure 3.18b.

The memory consumption of the FEMFd program can be divided into three parts as shown in Figure 3.18b. When solving for one source only, the largest amount of memory is used by the solution process. For the model under consideration roughly one

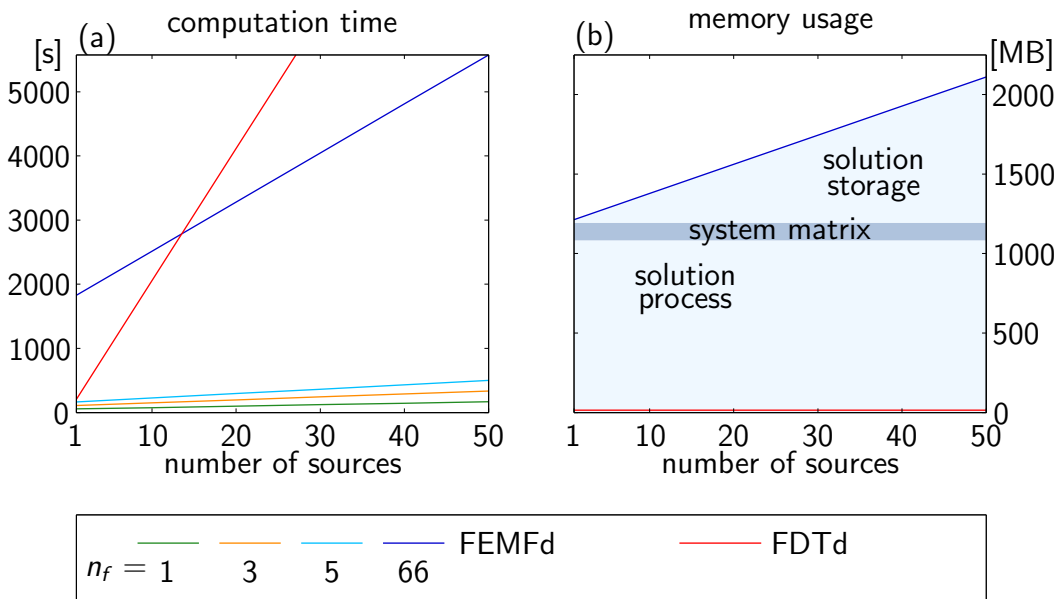


Figure 3.18: Computation times (a) and memory usage (b) of the FEMFd and the FDTd code for computing the response of the model shown in Figure 3.15. The times shown for the FDTd code (red line a) correspond to seismogram lengths of 0.065 s computed with a time step of $dt = 20 \mu\text{s}$. The times shown for the FEMFd code (green, orange, cyan and blue lines in a) correspond to solutions for one, three, five and 66 different frequencies, respectively. 66 frequencies would be necessary to sample the frequency space, such that the inverse Fourier transform results in unaliased seismograms in the time domain. The memory usage for the FEMFd solver (the blue line in b) is independent of the number of frequencies.

GB is needed. Adding more source positions does not change this value significantly. Additionally, some memory is taken up by the system matrix, which is also independent of the number of sources (111 MB). The only part of the memory requirement that grows with the number of sources is the space needed to store the solution vectors. For $n_s = 1$ the solution vector only needs about 18 MB of memory but for $n_s = 50$ this value rises to about 917 MB, as indicated by the wedge-shaped uppermost blue area in 3.18b.

Figure 3.18 shows nicely that FEMFd modelling in the frequency domain offers extremely short computation times for only a few frequencies and a large number of sources. This is a typical scenario in seismic waveform inversions. Interestingly, even for computing complete seismograms the FEMFd algorithm outperforms the FDTd code, when more than $n_s \gtrsim 15$ sources need to be considered!

The drawback of the FEMFd approach, though, is its excessive memory requirement that is already about eighty times higher than that of the FD code in the case of $n_s = 1$ and for $n_s = 50$ it grows to about 140 times that of the FD code. For smaller-scale problems this does not impose a serious problem, but it currently prohibits elastic 3D modelling and inversions to be carried out in the frequency domain.

Large-scale seismic modelling is nowadays performed mostly on computer clusters. FDTd modelling for several sources can be distributed very efficiently on several nodes, since the computations for the different sources are independent of each other. A similarly

efficient distribution can be also achieved for FEMFd simulations. Here, the computations of the individual frequencies are distributed on the cluster.

3.3 Conclusions

In the first part of this chapter, I gave an overview of the implementation details of the frequency-domain finite element (FEMFd) code I wrote and the theory that underlies it, concentrating on a two-dimensional version. The equations and explanations are given with the aim of enabling anyone to retrace the various considerations and reprogramme the code.

In the second part of this chapter, I then showed that the code based on all these theoretical considerations actually works as desired.

The PMLs, used for truncating the infinite models to the actual computational domain, only work properly if their width exceeds 30 elements and the sources are placed more than one dominant wavelength away from the boundary. For certain source/receiver directivity combinations, the PML width can be reduced.

Using the analytic solution for an unbounded elastic isotropic medium, I showed, that to accurately model the amplitudes of the wave fields only about 16 elements per minimum wavelength are needed. However, to match the phase of the analytic solution, within an acceptable error limit of one percent, at a distance of up to 13 wavelengths from the source, one must use an astonishing number of 64 elements per minimum wavelength. I found it especially hard to model combinations of vertically directed source and horizontal component of the displacement field, and similarly the equivalent problem of modelling the vertical component of the displacement field for a horizontally directed source.

I have also shown the equivalence of my FEMFd code to the well established time domain finite difference (FDTD) code I used for the modelling reported in chapter 2, and evaluated their respective areas of use. Based on the modelling comparisons that I conducted, I can state that the benefits of FDTD modelling lie in its efficient use of computer memory, whereas the FEMFd method provides shorter computation times and offers the possibility to solve for several source positions at once, but at the expense of a relatively high memory usage. Thus, FDTD is best used for computing seismogram traces for a few different source locations and types for large models, whereas FEMFd has to be favoured, if one only needs the solution for a few frequencies but for a larger number of sources, as is the case when performing seismic inversion in the frequency domain.

Chapter 4

2.5D forward modelling

4.1 Introduction

Seismic sources in practise can usually be approximated by a point source. Consequently, the data recorded exhibit a 3D geometrical spreading. A 2D forward solver, such as my finite element code, described in section 3.2, computes solutions for an infinite line source perpendicular to the x - z -plane that exhibit a 2D geometrical spreading.

If such 2D forward modelling is employed in an attempt to invert real data, a 3D-to-2D transformation has to be performed (e.g. Amundsen and Reitan, 1994). Using such a transform would restrict the inversion to those parts of the data that are well matched by the transformed 2D synthetics (for each arrival a different 3D-to-2D filter would have to be employed). For near-surface seismic data, such an approach would be not applicable, since the different arrivals typically overlap.

A possible alternative could involve full 3D modelling, perhaps with an elastic FEM algorithm. A simple regular FEM grid would require a system of equations of dimension $(3n_x \cdot n_y \cdot n_z) \times (3n_x \cdot n_y \cdot n_z)$ to be solved, where n_x , n_y and n_z are the number of nodes in the three spatial directions. Even using the best state-of-the-art computer technologies this would be challenging or even impossible. A possible alternative could be to employ 3D FDTD algorithm, but considering that a typical waveform inversion problem includes many source and receiver positions, makes this alternative also impractical.

A compromise between the inappropriate 2D modelling and the prohibitively expensive 3D modelling could be a 2.5D approach, where seismic waves, excited by a (3D) point source propagate through a medium, in which elastic parameters vary only in two spatial directions.

Most treatments in the literature deal only with the 2.5D acoustic case. Only a handful of papers tackle true 2.5D elastic modelling. A time-domain pseudo spectral formulation is given by Furumura and Takenaka (1996). Yang and Hung (2001) gave a hybrid finite element/infinite element solution for viscoelastic media, while Sinclair et al. (2007) solved the 2.5D anisotropic problem in the frequency domain using a spectral element approach. Boundary integral equation 2.5D modelling for elastic isotropic media is described by Takenaka et al. (1996) and (Fujiwara, 1997).

As one of the first considering the 2.5D acoustic case, Bleistein (1986) proposed an operator transforming 2D solutions into 2.5D solutions based on ray tracing. Liner (1991, 1995) heuristically derives 2.5D time domain and frequency domain acoustic

wave equations for constant density by adding additional terms to the 2D acoustic wave equation. Williamson and Pratt (1995) propose an approximate 2.5D acoustic wave equation by integrating an 2.5D-to-2D filter in the acoustic 2D wave equation. The approaches by Bleistein (1986), Liner (1991, 1995) and Williamson and Pratt (1995) are computationally relatively inexpensive, but involve the same problematic approximations as the 3D-to-2D transforms by Amundsen and Reitan (1994) and only provide accurate results for more or less homogeneous media.

A more generally valid acoustic 2.5D wave equation is derived by Song and Williamson (1995) and further developed by Cao and Greenhalgh (1997, 1998) and Zhou and Greenhalgh (1998c). If the elastic properties are assumed to be constant along the y -axis, the 2.5D wave equation can be obtained by Fourier transforming the governing differential equations from the ω - x - y - z -domain to the ω - x - k_y - z -domain, where k_y is the y -coordinate wavenumber. Such a transformation was applied in section 3.1.1 (equation (3.2)).

The Fourier transformation technique results in a 2D problem that requires a much smaller $(3n_x \cdot n_z) \times (3n_x \cdot n_z)$ system of equations to be solved for a suitable selection of k_y values. Finally, the results need to be inversely transformed to the ω - x - y - z -domain.

The acoustic wave equation in the ω - x - k_y - z -domain (see Zhou and Greenhalgh, 2006, equation (1), adapted to the Fourier transform definition (A.2)) is

$$\nabla^2 G(\mathbf{x}; \mathbf{x}_s) + (k_y^2 - k_P^2)G(\mathbf{x}; \mathbf{x}_s) = -\frac{1}{\sqrt{2\pi}}\delta(x - x_s)\delta(z - z_s), \quad (4.1)$$

where $G(\mathbf{x}; \mathbf{x}_s)$ is the Green's function for a source at \mathbf{x}_s , $k_P = \omega/v_P$ is the wavenumber of a wave travelling with longitudinal wave velocity v_P . and $\omega = 2\pi f$ is the angular frequency.

Parts of the solution of equation 4.1 are rapidly varying with respect to k_y and for $k_y \equiv k_P$ the solution of equation 4.1 exhibits a pole with a highly oscillatory behaviour in its surroundings, which may make an even sampling strategy along the k_y axis problematic. Therefore, Zhou and Greenhalgh (2006) introduce an uneven sampling strategy based on the analytic full-space solution of the acoustic 2.5D problem. A similar treatment for the elastic anisotropic 2.5D problem (Zhou and Greenhalgh, 2010b) will be published soon.

The 2.5D wave equations for the elastic case are given in section 3.1.1, equation (3.2). If the elastic parameters are assumed to be constant with respect to x and z (which is the case within a finite element), the 2.5D equations can be rewritten as

$$0 = \mu (k_S^2 - k_y^2)\bar{\bar{u}}_x + [(\lambda + 2\mu)\partial_x^2 + \mu\partial_z^2] \bar{\bar{u}}_x + ik_y(\lambda + \mu)\partial_x\bar{\bar{u}}_y + (\lambda + \mu)\partial_x\partial_z\bar{\bar{u}}_z + \bar{\bar{f}}_x \quad (4.2a)$$

$$0 = (\lambda + 2\mu)(k_P^2 - k_y^2)\bar{\bar{u}}_y + \mu(\partial_x^2 + \partial_z^2)\bar{\bar{u}}_y + ik_y[\mu\partial_x\bar{\bar{u}}_x + (\lambda + 2\mu)\partial_z\bar{\bar{u}}_z] + \bar{\bar{f}}_y \quad (4.2b)$$

$$0 = \mu (k_S^2 - k_y^2)\bar{\bar{u}}_z + [(\lambda + 2\mu)\partial_z^2 + \mu\partial_x^2] \bar{\bar{u}}_z + ik_y(\lambda + \mu)\partial_z\bar{\bar{u}}_y + (\lambda + \mu)\partial_x\partial_z\bar{\bar{u}}_x + \bar{\bar{f}}_z, \quad (4.2c)$$

where $k_P = \frac{\omega}{v_P}$ and $k_S = \frac{\omega}{v_S}$ are the wavenumbers corresponding to the P - and S -waves, respectively. Due to the appearance of the terms $(k_P^2 - k_y^2)$ and $(k_S^2 - k_y^2)$, the solution

of equations 4.2 includes poles at k_P and k_S with the same highly oscillating behaviour as observed in the acoustic 2.5D solutions in ω - x - k_y - z -domain. This requires a similar strategy for the elastic as for the acoustic case.

In section 4.2.1 I introduce such a strategy for elastic isotropic homogeneous full-space models. This sampling scheme is implemented in the FEMFd modelling code introduced in the previous chapter. The proposed sampling strategy can also be adapted to homogeneous, isotropic models with a free surface (see section 4.3), but it fails for strongly inhomogeneous models, since the locations of the poles of the ω - x - k_y - z -domain solutions are unknown in this case. Thus, for inhomogeneous models, the only possibility is to employ an even sampling in k_y followed by an inverse discrete Fourier transform. I show in section 4.4, that the results for an even sampling can be highly contaminated by artifacts due to numerical instabilities in the vicinity of critical wavenumbers.

4.2 Homogeneous isotropic full space

4.2.1 Anatomy of the analytic spectra

The k_y -spectra for acoustic waves in a homogeneous full-space with velocity v_P have a pole at wavenumber $k_y = k_P = \frac{\omega}{v_P} = \frac{2\pi}{\lambda_P}$, where ω is the angular frequency and v_P is the P-wave velocity (Zhou and Greenhalgh, 2006). An example for such spectra is shown in Figure 4.1.

Close to k_P , the spectra oscillate, with the oscillation frequency increasing with increasing source-receiver distance d . Above k_P , the spectra only retain a rapidly decaying real part that represents the evanescent fraction of the wave field. Hence, the sampling density should increase near k_P and the total number of k_y sample points depends on the maximum source-receiver distance d^{\max} .

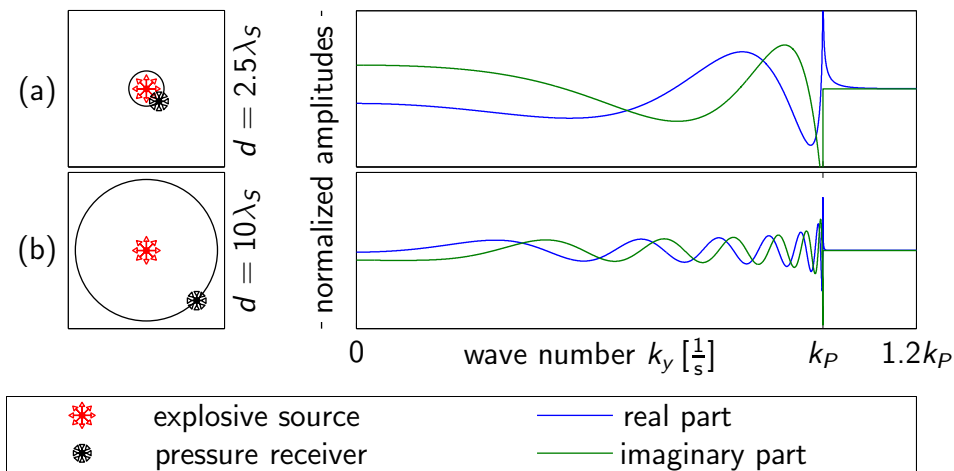


Figure 4.1: Amplitude versus wavenumber k_y plot for a homogeneous full space using the acoustic approximation at source/receiver distances d of (a) $2.5\lambda_s$ and (b) $10\lambda_s$ ($v_P = 1950 \text{ m/s}$). The model is introduced in section 4.2.1. Solutions of the elastic case for the same source/receiver distances d are shown in Figure 4.2.

In the elastic case, the S-wave velocity v_S is generally associated with a second critical wavenumber at $k_y = k_S = \frac{\omega}{v_S} = \frac{2\pi}{\lambda_S}$ and the vectorial nature of the elastic displacement field needs to be considered, such that the scalar acoustic Green's function needs to be replaced by a nine-component Green's tensor that represents the nine possible combinations of source and receiver directions. Analytic equations for the Green's tensor for a homogeneous isotropic elastic unbounded domain are given in Appendix section C.2.2. These analytic solutions can be split up into two parts, where one represents the P -wave portion G_{ij}^P and the other one the S -wave portion G_{ij}^S of the solution (see equations (C.13) and (C.14)). Separated like this, each part of the elastic k_y spectra shows a similar behaviour as the acoustic spectra, with poles or discontinuities only at one wavenumber; at k_P in the case of G_{ij}^P and at k_S in the case of G_{ij}^S .

Due to symmetries, there are only seven independent cases, from which the solutions of all other cases can be derived. Four characteristic cases out of these seven independent ones are shown in Figure 4.2. The left panel of Figure 4.2 shows the four independent source-receiver configurations and the middle and right panels show the corresponding k_y spectra. For each panel, the topmost trace is G_{ij}^P , followed by G_{ij}^S and then the bottommost trace is the complete G_{ij} . The computations are performed for medium parameters $v_P = 1950 \frac{\text{m}}{\text{s}}$, $v_S = 1200 \frac{\text{m}}{\text{s}}$, density $\rho = 1500 \frac{\text{kg}}{\text{m}^3}$ and 300 Hz signal frequency. The source is placed at $(0, 0)$ and the two receivers are located at distances from the source of $d = 2.5 \lambda_S$ and $d = 10 \lambda_S$.

Directivity of the sources results in the k_y spectra being azimuthally dependent (except for case d in Figure 4.2). Spectra for receivers placed at an azimuth of 45° , as they are shown in Figure 4.2, exhibit all the critical features that may affect a k_y sampling strategy. The following observations can be made for each of the cases:

(a) *Source direction in the x-z-plane, receiver component parallel to the source direction.*

The P -part of the solution exhibits an amplitude decreasing and an oscillation frequency increasing with increasing k_y ; at wavenumbers greater than k_P both real and imaginary parts are zero. The S -part of the solution exhibits an increasing amplitude towards k_S , where it ends in a pole; above k_S , the real part decays rapidly and the imaginary part is zero. The S -spectra are very similar to those for the acoustic case; k_S would correspond to k_P in Zhou and Greenhalgh (2006). The resulting total spectra have one pole at k_S and only a slight bend at k_P . Oscillations increase in frequency towards the pole. This behaviour becomes more pronounced with increasing d values. Above k_S , the imaginary part disappears and the real part representing the evanescent phase decays rapidly to zero.

For a receiver placed at an azimuth of 0° (not shown), the amplitude of the P -part of the spectra is maximal, resulting in a greater distortion of the total spectra around k_P , whereas for a receiver placed at an azimuth of 90° (not shown) the P -spectrum disappears and the total spectrum is equivalent to the S -part.

(b) *Source direction in the x-z-plane, receiver component in the x-z-plane but perpendicular to the source direction.*

Here, the P -part and the S -part both are of qualitatively the same shape as the P -part in case (a). The former decays to zero towards k_P , the latter towards k_S , such that the pattern of the total spectra changes somewhat at k_P . Again, the

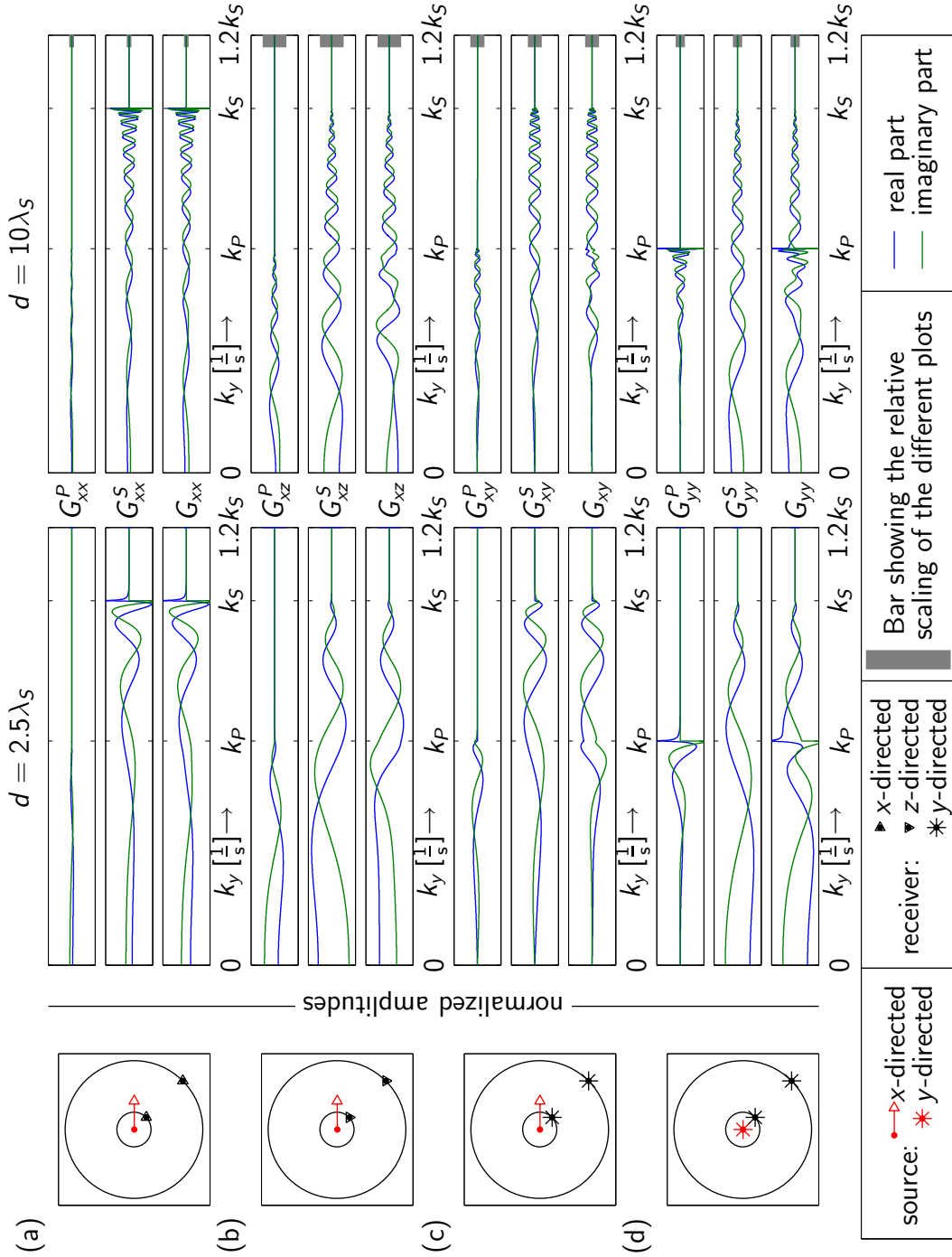


Figure 4.2: Solution amplitudes versus wavenumbers k_y for a homogeneous full space at source/receiver distances d of (a) $2.5\lambda_s$ and (b) $10\lambda_s$. For each source/receiver configuration, the P -wave contribution G_{ij}^P , the S -wave contribution G_{ij}^S and the total solution G_{ij} are shown separately ($i, j \in \{x, y, z\}$). The model is introduced in section 4.2.1. The receivers are located at an azimuth of 45° with respect to the source direction.

effect of increasing oscillation towards k_S is more pronounced at larger d values. By contrast to (a), the amplitudes decay rather than increase towards k_S and no evanescent phase is observed.

For receivers placed at an azimuth of 0° and 90° (not shown) the solution is zero.

- (c) *Source direction in the x-z-plane, receiver component perpendicular to the x-z-plane.*

In this case, the P - and the S -part of the spectra again are of the same form, this time first exhibiting an increasing amplitude, to decrease again towards the respective critical wavenumbers. There is no pole but a discontinuity at k_P or k_S and the real parts decay rapidly above these values, while the imaginary parts disappear. Compared with cases (a) and (b), the spectral patterns of the resulting sum for case (c) change more significantly at k_P . Again, the oscillations increase towards k_P and k_S , respectively.

For a receiver at an azimuth of 0° (not shown) the spectra retain the same shape but with higher amplitude; at an azimuth of 90° (not shown) they are zero.

- (d) *Source direction perpendicular to the x-z-plane, receiver component parallel to source direction.*

In this situation, the P part is of the same shape as the S -part in case (a) with a pole at k_P and evanescent behaviour above, while the S -part assumes the shape of the P -part of case (a), smoothly decaying to zero towards k_S . The resulting sum exhibits an increasing amplitude and increasing oscillation frequency towards the poles at k_P , whereas above k_P the amplitude decreases while the oscillation again increases towards k_S .

4.2.2 Efficient sampling strategy

Solution symmetries

Having computed the FEM approximation to the solution of the wave equations in the ω - x - k_y - z -domain (3.2), the last step is the inverse transform back to the ω - x - y - z -domain. For one component of the solution vector, denoted by $U_{i\zeta}$, the solution for field component $\zeta \in \{x, y, z\}$ at model node $i \in [1, n]$ (see section 3.1.4), this inverse transform is given by

$$U_{i\zeta}(\omega, y) = \frac{1}{\sqrt{2\pi}} \int_{-\infty}^{\infty} U_{i\zeta}(\omega, k_y) e^{ik_y y} dk_y. \quad (4.3)$$

A closer look at the global FEM matrix equation (3.47) reveals, that the solutions for configurations xx , zz , yy , xz and zx are symmetric in k_y , while those for configurations xy , yx , zy , yz are antisymmetric in k_y (see Appendix section A.3). Taking these

symmetries into account, equation (4.3) can be rewritten as

$$\mathfrak{G}_{\zeta v}(y) = \begin{cases} \sqrt{\frac{2}{\pi}} \int_0^{\infty} \mathfrak{G}_{\zeta v}(k_y) \cos(k_y y) dk_y & \text{for } \zeta v \in \{xx, zz, yy, xz, zx\} \\ \sqrt{\frac{-2}{\pi}} \int_0^{\infty} \mathfrak{G}_{\zeta v}(k_y) \sin(k_y y) dk_y & \text{for } \zeta v \in \{xy, yx, zy, yz\} \end{cases}, \quad (4.4)$$

where $\mathfrak{G}_{\zeta v}$ is one part of the FEM Green's tensor introduced in Appendix section A.3; note that I have abbreviated the functional dependencies. This means that only the positive half of the k_y -space needs to be sampled and thus half of the computation time can be saved.

In section 3.1.3 of the previous chapter I restricted the source to locations within the x - z -plane, implying $y_s \equiv 0$. Source/receiver distances perpendicular to the x - z -plane, due to sources and/or receivers placed at $y \neq 0$ can be accounted for during the inverse transform (4.4). Since the problem is by definition invariant with respect to translation in the y -direction, the variable y denoting the receiver position in equation (4.4), can be replaced by the out-of-the-plane source/receiver distance $\Delta y := y - y_s$.

If both source and receiver are placed inside the x - z -plane (i.e. $\Delta y \equiv 0$), the inverse transform reduces to

$$\mathfrak{G}_{\zeta v}(y) = \begin{cases} \sqrt{\frac{2}{\pi}} \int_0^{\infty} \mathfrak{G}_{\zeta v}(k_y) dk_y & \text{for } \zeta v \in \{xx, zz, yy, xz, zx\} \\ 0 & \text{for } \zeta v \in \{xy, yx, zy, yz\} \end{cases}. \quad (4.5)$$

Note that for configurations xy , yx , zy and yz the solution is not zero in the ω - x - k_y - z -domain. It vanishes in the case of $\Delta y \equiv 0$ only during the inverse transformation, due to its symmetry.

Gauss-Legendre sampling

Analyses of the analytic k_y -spectra have revealed the following important features that need to be considered when establishing a suitable sampling strategy:

- (i) All spectra contain significant contributions up to k_S . Above this point the signal vanishes or decays rapidly. No significant energy is observed beyond $1.2 k_S$.
- (ii) Receivers near the source are affected by a more pronounced evanescent phase beyond k_S than compared with the more distant receivers.
- (iii) Like in the acoustic case, the more oscillatory nature of the spectra at large distances d requires a denser sampling. The number of sample points should be set according to the value of the maximum distance d^{\max} .
- (iv) Cases (c) and (d) have discontinuities at k_P and k_S .

Following the system introduced by Zhou and Greenhalgh (2006), these points can be addressed by dividing the integration interval into sub-intervals of $[0 - k_P]$, $[k_P - k_S]$ and optionally $[k_S - 1.2k_S]$ with N_P , $N_S - N_P$ and $0.2 N_S$ sample points, respectively. The values of N_P and N_S are defined as

$$N_P = \max \left\{ 5, \frac{M \cdot d^{\max}}{\lambda_P} \right\} \quad \text{and} \quad N_S = \max \left\{ 10, \frac{M \cdot d^{\max}}{\lambda_S} \right\} \quad (4.6)$$

where for my examples $\lambda_P = 6.5$ m and $\lambda_S = 4$ m. Within each interval, the points are distributed according to Gauss-Legendre quadrature sample spacings (e.g. Press et al., 1992). The sampling inside the interval $[0, k_P]$ needs some special consideration if the symmetry of the solution should be taken into account. To achieve a suitable sampling density, I compute $2N_P - 1$ Gaussian quadrature weights and points for the interval $[-k_P, k_P]$ and use only the last N_P weights, corresponding to the sampling points inside the interval $[0, k_P]$; the first weight additionally has to be halved.

Once the $N_{GL} = 1.2N_S$ (taking the nearest integer value) points having abscissae $KY_{j_{GL}}$ and weights $W_{j_{GL}}$ are determined, the inverse transform (4.4) reduces to the sum

$$\mathfrak{G}_{\zeta v}(y) = \sum_{j_{GL}=1}^{N_{GL}} W_{j_{GL}} \tilde{\mathfrak{G}}_{j_{\zeta v}}(KY_{j_{GL}}), \quad (4.7)$$

where

$$\tilde{\mathfrak{G}}_{\zeta v}(KY_{j_{GL}}) := \begin{cases} \sqrt{\frac{2}{\pi}} \mathfrak{G}_{\zeta v}(KY_{j_{GL}}) \cos(KY_{j_{GL}} y) & \text{for } \zeta v \in \{xx, zz, yy, xz, zx\} \\ \sqrt{\frac{-2}{\pi}} \mathfrak{G}_{\zeta v}(KY_{j_{GL}}) \sin(KY_{j_{GL}} y) & \text{for } \zeta v \in \{xy, yx, zy, yz\} \end{cases}, \quad (4.8)$$

and restriction to $y \equiv 0$ simplifies this to

$$\tilde{\mathfrak{G}}_{\zeta v}(KY_{j_{GL}}) := \begin{cases} \sqrt{\frac{2}{\pi}} \mathfrak{G}_{\zeta v}(KY_{j_{GL}}) & \text{for } \zeta v \in \{xx, zz, yy, xz, zx\} \\ 0 & \text{for } \zeta v \in \{xy, yx, zy, yz\} \end{cases}, \quad (4.9)$$

Figure 4.3 shows the distribution of the Gauss-Legendre sampling points for different values of the sampling parameter M in equation (4.6) and Figure 4.4 illustrates how M can be determined for the example of case (a) of Figure 4.2, which proved to be

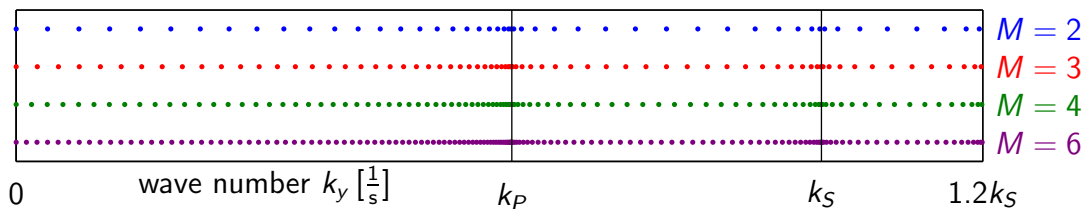


Figure 4.3: Gauss-Legendre sampling points along the k_y -axis for different values of sampling parameter M assuming a maximal source/receiver distance of $d_{\max} = 20\lambda_S$.

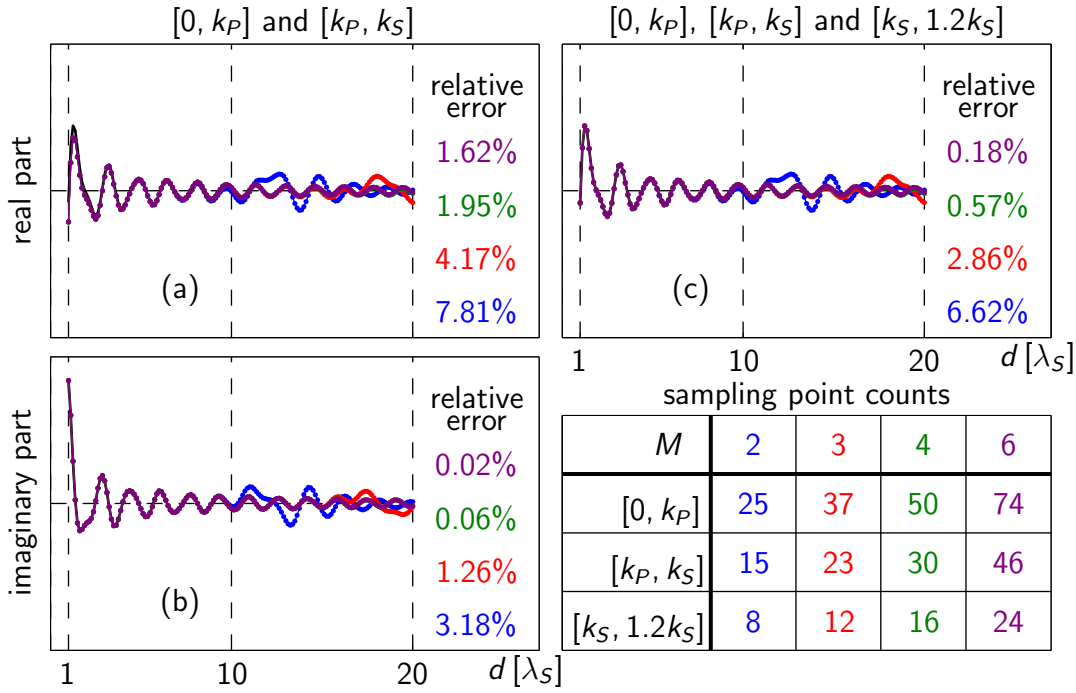


Figure 4.4: Error with respect to the analytic solution in the ω - x - y - z -domain for the Gauss-Legendre sampling on the analytic solution in the ω - x - k_y - z -domain. Shown is the solution versus source/receiver distance d in units of λ_S on an axis along the source direction for a x -directed source and a x -directed receiver. (This has been the worst case scenario for the FEM accuracy in the analysis of the 2D case.) The analytic solution for the full space model introduced in section 4.2.1 is represented by black lines. They are almost completely hidden behind the inversely transformed solutions shown in blue, red, green and purple for $M = 2, 3, 4$ and 6 , respectively. (a) and (b) show results for the real and imaginary parts of the solution when the sampling is restricted to $k_y < k_S$. (c) shows the improvement for the real part of the solution, if the sampling is extended to wavenumbers of up to $1.2k_S$.

the most difficult for obtaining accurate results. The real and imaginary parts of the Green's functions for x -directed sources and receiver components as a function of d are displayed in Figures 4.4a-4.4c. Black lines (only visible near the source in panel (a)) are waveforms representing the analytic full space solutions in the ω - x - k_y - z -domain (see Appendix section C.2.3), whereas the blue, red, green, and purple lines are waveforms obtained by inverse transformation of the analytic k_y -spectra given in equations (C.9) by means of Gauss-Legendre quadrature using different choices of M and a fixed value of $d^{\max} = 20 \lambda_S$. Results are only shown for $d > \lambda_S$ in Figure 4.4, because near-source effects prevent accurate results at shorter distances.

Deviations of the coloured lines from the black ones and the associated relative errors indicate that $M = 2$ and $M = 3$ lead to unsatisfactory results at large d values (Figure 4.4). There is a substantial increase in accuracy for $M = 4$. Results for $M = 6$ are visually indistinguishable from those for $M = 4$, but the relative errors are notably smaller. The influence of the sampling interval $[k_S - 1.2k_S]$ can be seen by comparing Figures 4.4a and 4.4c. Minor differences at short distances are the result of ignoring

the evanescent phase in the calculations for Figure 4.4a; extending the k_y sampling to $1.2 k_S$ results in lower relative errors. No improvements would result from extending the sampling interval in calculations of the imaginary part, because it vanishes above k_S .

4.2.3 FEM results

Homogeneous full-space model

As an example for 2.5D FEM simulation I used the same subsurface parameters, signal frequency and source/receiver configurations as for the analytic k_y -spectra presented in the previous section and shown in Figure 4.2. The $60 \text{ m} \times 60 \text{ m}$ model was surrounded by a Perfectly Matched Layer (PML) of 10 m thickness, corresponding to a PML width of $n_{\text{PML}} = 50$ elements. A mesh of quadratic finite elements with 0.2 m edge length provides 20 nodes per minimum wavelength. This results in 160,000 elements and 160,801 nodes. Such a parametrisation is expected to provide accurate results (see section 3.2.1). The parameter d^{max} was chosen to be the maximum distance from the source in the centre of the model to the boundary between model and PML, approximately 42 m. My preferred choice $M = 4$ yields $N_p = 30$, $N_S - N_p = 20$, and $0.2 N_S = 20$ (a total of 60 k_y sample points).

The relative errors of the FEM solution for $M = 4$ and sampling up to $1.2 k_S$ are 1.15% and 0.38% for the real and imaginary parts, respectively. Although these errors are higher than those based on the analytic solution using the same sampling strategy (i.e., 0.57% in Figure 4.4c and 0.06% in 4.4b), they are acceptably good. I conclude that numerical errors caused by my k_y sampling strategy are not a limiting factor in 2.5D frequency-domain FEM modelling of elastic waves.

Homogeneous full-space model with stochastic inhomogeneities

Now, I investigate the performance of my k_y sampling strategy using a moderately heterogeneous model, for which no analytic solution exists. As a reference, I compare sampling based on my strategy with a very fine uniform sampling. The average subsurface parameters, signal frequency, source/receiver configurations and FEM mesh of the now $80 \text{ m} \times 80 \text{ m}$ model remain the same as for previous calculations using the homogeneous full-space. Heterogeneities are added in form of stochastic fluctuations (standard deviation = 10%, correlation length = 6 m ($2.5 \lambda_S$), Hurst number = 0.2) to the velocities and density, from a distance of $2 \lambda_S$ to $20 \lambda_S$. For the dense uniform sampling computations, the interval between k_y values was set to 10^{-3} m^{-1} , yielding a total of 1886 wavenumbers. For sampling based on my adapted strategy, setting $M = 6$ results in a total of 144 wavenumbers. Figure 4.5 demonstrates that the two sampling strategies reproduce the k_y -spectra with comparable accuracy. In the regions with highly oscillatory behaviour around the critical wavenumber k_S , my sampling strategy chooses some sampling points not covered by the even sampling, visible in the spectra for $d = 2.5 \lambda_S$ in Figures 4.5b and c. The general shapes of the spectra in Figures 4.2 and 4.5 are similar in many respects, but those in Figure 4.5 are distinguished by generally higher frequency oscillations. For case (b) there is a lack of decay in amplitudes towards higher wavenumbers and there are nonzero values in the imaginary part above k_S . These features probably result from shear wave scattering at the inhomogeneities.

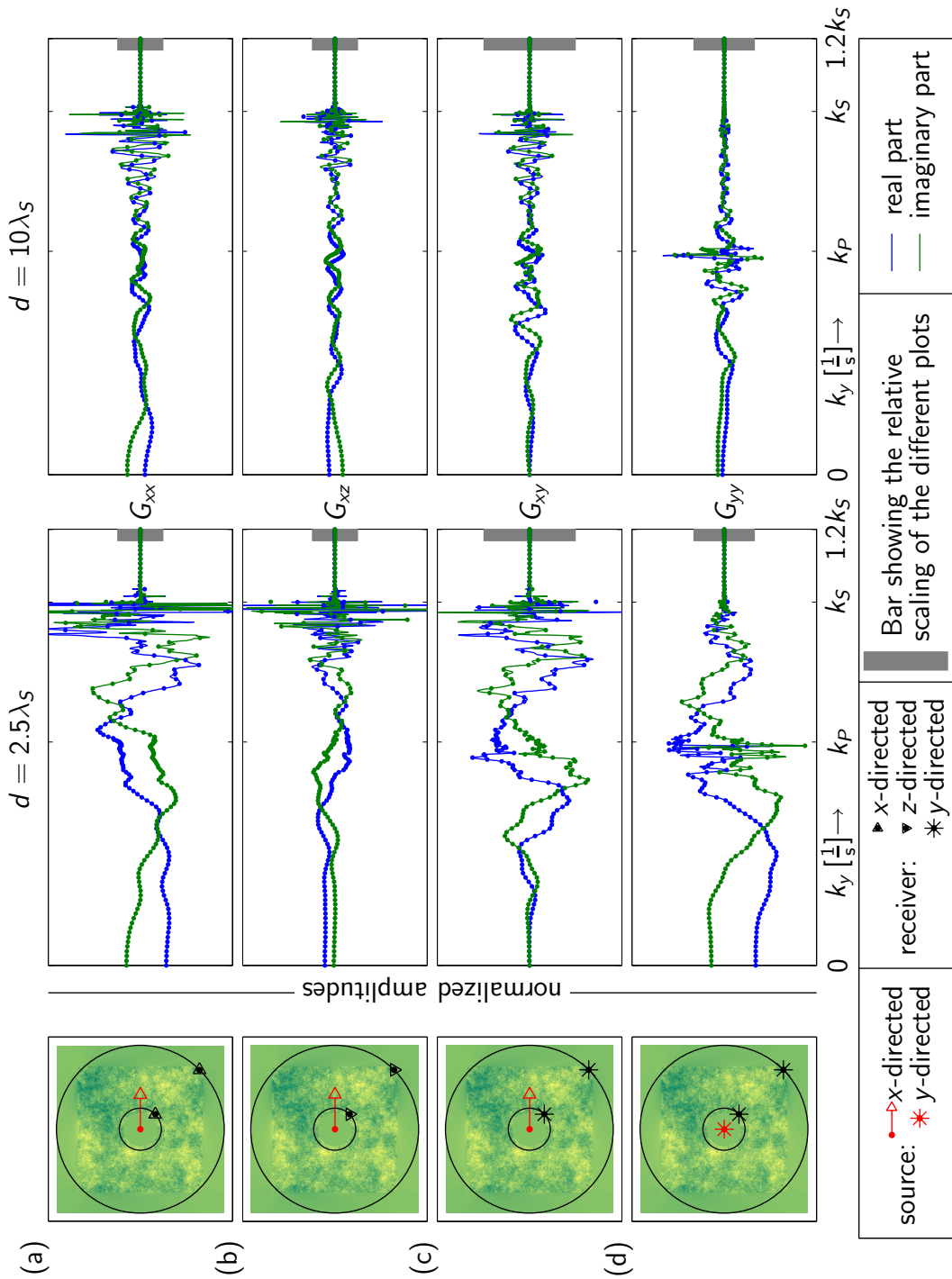


Figure 4.5: Solution amplitudes versus wavenumbers k_y for a slightly inhomogeneous full space model with stochastic parameter fluctuations around the mean parameter values of the homogeneous model introduced in section 4.2.1 at source/receiver distances d of (a) $2.5\lambda_s$ and (b) $10\lambda_s$. The receivers are located at an azimuth of 45° with respect to the source direction.

4.3 Homogeneous isotropic half space

Figures 4.6 and 4.7 show k_y -spectra computed for a homogeneous half space model with the same elastic parameters as for the full space model, the analytic k_y -spectra of which are shown in Figure 4.2. The spectra are computed for a FEM model of the size $82\text{ m} \times 41\text{ m}$ and a frequency of 300 Hz . The source is placed at the free surface, in the middle of the top edge of the model. The two receivers are placed at distances $2.5\lambda_S$ and $10\lambda_S$ to the right of the source. Due to the free surface, the phase exhibiting the smallest velocity is no longer the S -wave but the Rayleigh wave, propagating with a velocity of $v_R = 1092\text{ m/s}$ (see Nkemzi, 2008). Thus the smallest wavelength is not λ_S , but the Rayleigh wave wavelength $\lambda_R = 3.6\text{ m}$. I chose a FEM grid step of $dh = 10\text{ cm}$ to assure an accurate simulation with $N = 36$ nodes per minimal wavelength. Furthermore, the highest critical wavenumber is not k_S , but $k_R = 1.73\text{ m}^{-1}$ and hence the spectra have to be sampled up to $1.2k_R = 2.07\text{ m}^{-1}$. For Figures 4.6 and 4.7 I employed an even sampling using a spacing of $dk_y = 0.002\text{ m}^{-1}$ ($n_{k_y} = 1052$ sampling points).

By comparing Figures 4.6 and 4.7 to Figure 4.2 one observes that the half-space and full-space spectra exhibit similar characteristics. The only difference involves the additional critical wavenumber corresponding to the Rayleigh wave velocity. Only configurations xx and xy (see Figure 4.7a and c) exhibit a pole at k_S , the former one is more pronounced. At k_R , all configurations except for xx have a pronounced pole. At k_P , configurations zx (Figure 4.6b), zy (Figure 4.6c) and xy (Figure 4.7c) include a discontinuity, configuration yy exhibits a small pole there.

Since all three critical wavenumbers are known analytically and the structure of the spectra is qualitatively the same as the structure of those for the homogeneous full space, a modified version of the sampling strategy proposed in section 4.2.2 can be employed. That is, one can divide the k_y -axis into the intervals $[0 - k_P]$, $[k_P - k_S]$, $[k_S - k_R]$ and $[k_R - 1.2k_R]$ and use N_P , $N_S - N_P$, $N_R - N_S - N_P$ and $0.2 N_R$ sampling points, respectively. The values of N_P and N_S can be defined using equation (4.6) and N_R is suggested to be chosen as

$$N_R = \max \left\{ 15, \frac{M \cdot d^{\max}}{\lambda_R} \right\}. \quad (4.10)$$

4.4 Sampling problems for heterogeneous models

For highly heterogeneous full-space models, each subvolume corresponding to different values of v_P and v_S in the model, will give rise to corresponding critical wavenumbers. In the sampling strategies I presented in sections 4.2.2 and 4.3, this would lead to a very high number of integration intervals that would have to be taken into account, rendering the approach to be inefficient. Moreover, for heterogeneous half-space models and full-space models with internal boundaries, the critical wavenumbers corresponding to the surface-wave and Stoneley phases are not known. Since the sampling strategies I presented in sections 4.2.2 and 4.3 are based on the knowledge of these critical wavenumbers and the associated structure of the k_y -spectra, they are not suitable for strongly heterogeneous

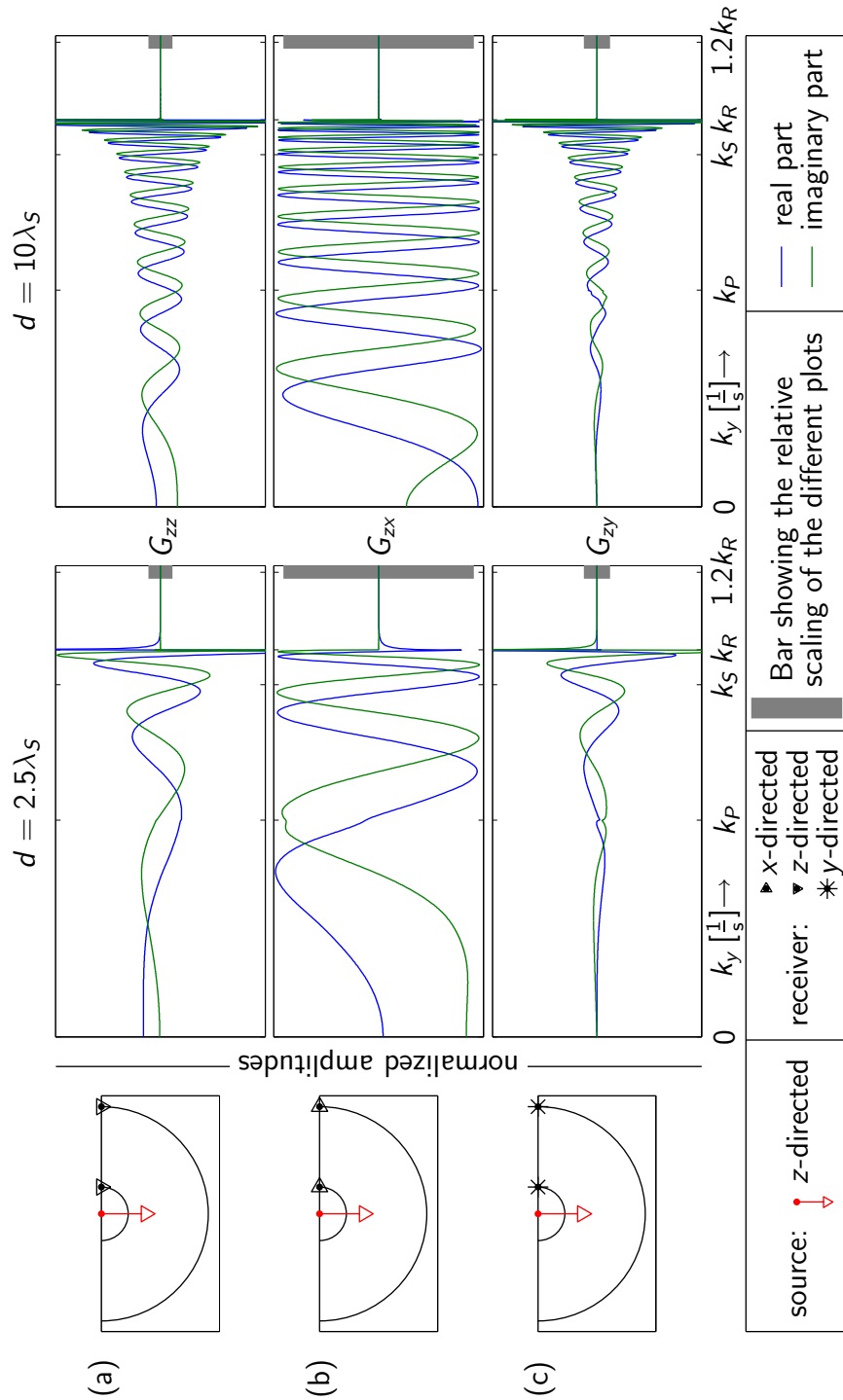


Figure 4.6: Solution amplitude versus wavenumber k_y for a homogeneous half space model with model parameters of the full-space model introduced in section 4.2.1 at source/receiver distances d of (a) $2.5\lambda_s$ and (b) $10\lambda_s$. The vertically directed source and the receivers are located on the free surface.

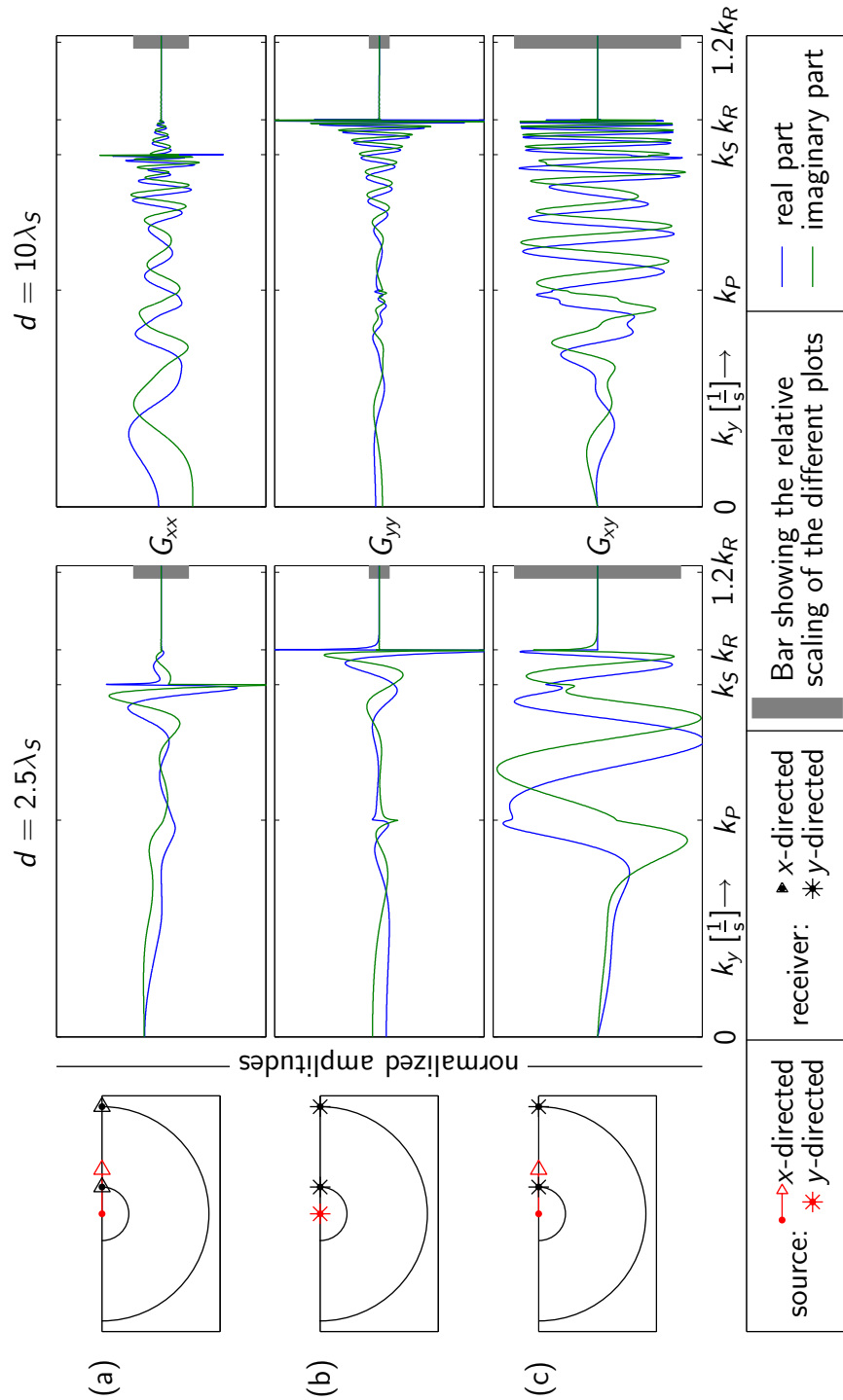


Figure 4.7: Solution amplitude versus wavenumber k_y for a homogeneous half space model with model parameters of the full-space model introduced in section 4.2.1 at source/receiver distances d of (a) $2.5\lambda_s$ and (b) $10\lambda_s$. The horizontally directed sources and the receivers are located on the free surface.

models with or without a free surface. The only feasible solution to this problem is to employ an even sampling along the k_y axis.

An even sampling may include a large number of wavenumbers, which will be computationally expensive. Therefore, it is critical to choose an appropriate sampling interval. In the following, I will first introduce an even sampling strategy and then investigate the trade-off between the sampling density in k_y -space and the density of the FEM grid. Finally, I will discuss a potential problem with even sampling that may occur, when one or more wavenumbers are too close to the poles of the k_y spectra.

4.4.1 Sampling strategy for even sampling

Since the symmetries of the solution, presented in section 4.2.2 are also preserved for heterogeneous models, the sampling still only has to be performed for positive k_y -values, starting at $k_y = 0^{1/m}$.

In a similar manner as for the Gauss-Legendre sampling strategy, the upper endpoint of the sampling interval is chosen to be

$$k_y^{\max} := 1.2 \frac{2\pi}{\lambda_{\min}}, \quad (4.11)$$

where $\lambda_{\min} := \frac{v_{\min}}{f}$ is the wavelength corresponding to the minimum velocity of the sub-surface model. For models without a free surface, v_{\min} is equal to the minimal S-wave velocity; for models including a free surface, it is usually the minimum velocity of the surface wave phases. Since the Rayleigh wave velocity is not known analytically for heterogeneous models, I compute it for a homogeneous half space with wave velocities equal to the minimum values of v_P and v_S in the heterogeneous model.

The sampling density Δk_y and the total number of sampling points n_{k_y} are chosen to be

$$n_{k_y} = \lceil 1.2M \frac{d^{\max}}{\lambda_{\min}} \rceil \quad \text{and} \quad \Delta k_y = \frac{2\pi}{Md^{\max}}, \quad (4.12)$$

where M is the sampling parameter already used in equations (4.6) and (4.10). In this way, the total number of sampling points is in accordance with the number chosen for the Gauss-Legendre sampling and the sampling density is independent of frequency and the model parameters. It depends only on the maximum source/receiver offset d^{\max} , which was found to be a good measure of the highest degree of oscillation in the k_y -spectra (see Figures 4.2, 4.5, 4.6 and 4.7).

The inverse transform to the ω - x - y - z -domain can still be performed using equation (4.7), where the sampling points KY are now evenly spaced and the Gauss-Legendre weights W are replaced by $\frac{1}{n_{k_y}}$.

4.4.2 Grid density dh versus sampling density Δk_y

To test the importance of the sampling parameter M on the accuracy of the solution for inhomogeneous models using an even sampling in k_y -domain, I performed a series of simulations for ten different values of M and six different grid steps dh for a gradient model and a layer-over-half-space model. The latter mimics a gravel pit with a water table at ten meters depth. I chose a signal frequency of $f = 150$ Hz. The model geometry

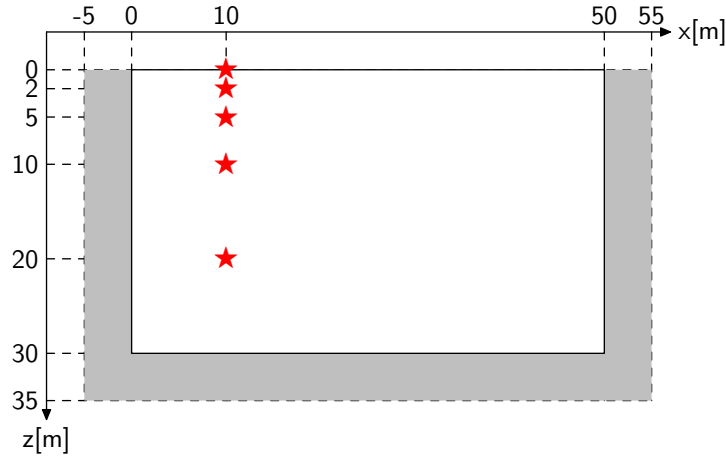


Figure 4.8: Model geometry and source locations (denoted by red stars) for the sampling test. Both models are of dimension 30 m \times 50 m with PMLs of 5 m width (shaded grey).

and source locations are shown in Figure 4.8, whereas the depth-dependent values of the elastic parameters are depicted in Figure 4.9. The values chosen for M and grid step dh , together with the resulting values for the number of k_y -sampling points n_{k_y} and the number of grid steps per minimum wavelength $N = \frac{\lambda_{\min}}{dh}$, are given in Tables 4.1 and 4.2.

As explained in section 4.4.1, I estimate the minimum propagation velocity from the Rayleigh velocity of a homogeneous half space, having seismic P - and S -wave velocities equivalent to the minimal values of v_P and v_S in the models. This velocity, denoted by v_R in Tables 4.1 and 4.2, and its corresponding wave length $\lambda_R = \lambda_{\min}$, determine the width of the sampling interval along the k_y -axis and the number of sampling points via equations (4.11) and (4.12). Note that the values chosen for the grid step dh are

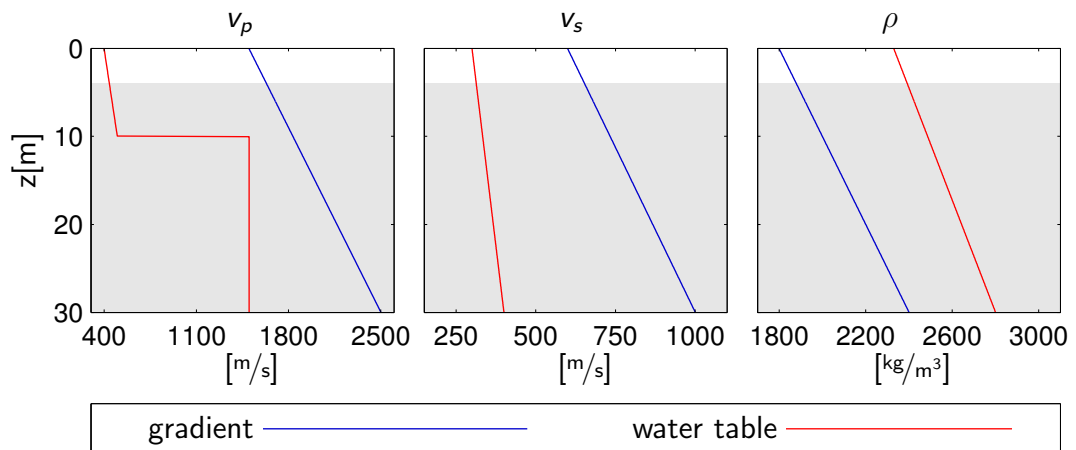


Figure 4.9: Elastic parameters of the two models employed for the sampling test. The gradient model has the same parameters as the one used throughout the thesis (see e.g. Figure 2.1). The water table model is supposed to simulate a gravel pit with a water table at a depth of 10 m.

dh [cm]	40	25	20	12.5	10	8	$v_P^{\min} = 1500 \text{ m/s}$		$v_R = 566 \text{ m/s}$	
N	9	15	19	30	38	47	$v_S^{\min} = 600 \text{ m/s}$		$\lambda_{\min} = 3.77 \text{ m}$	
M	5	10	15	20	25	30	35	40	45	50
n_{k_y}	81	161	241	321	401	481	561	641	721	802

Table 4.1: Sampling test parameters for the gradient model.

dh [cm]	40	25	20	12.5	10	8	$v_P^{\min} = 400 \text{ m/s}$		$v_R = 254 \text{ m/s}$	
N	4	7	9	14	17	21	$v_S^{\min} = 300 \text{ m/s}$		$\lambda_{\min} = 1.69 \text{ m}$	
M	5	10	15	20	25	30	35	40	45	50
n_{k_y}	185	369	553	737	921	1105	1289	1473	1657	1841

Table 4.2: Sampling test parameters for the water table model.

equivalent for both models and thus the resulting values for N differ in Tables 4.1 and 4.2 due to the different minimum velocities.

Since there are no analytic solutions available, I consider the solution computed for the finest FEM grid ($dh = 8 \text{ cm}$) and the densest k_y -sampling ($M = 50$) as the reference solution. The relative errors of all other solutions are computed with respect to this solution. For each solution, I calculate the difference from the reference solution. The median of the absolute value of this difference, divided by the maximum value of the reference solution, is then taken to be the relative error. I restrict the error computation to the area outside a radius of λ_R around the source to avoid near-field effects.

Figures 4.10 and 4.11 show overview plots of the relative error values for the water table model and the gradient model, respectively. The panel columns show, left to right, error values for the source/receiver configurations xx , zz , yy , xz and zx (the solutions for all other configurations vanish, see equation (4.5)). The panel rows show the results for the five different source depths z_s depicted in Figure 4.8. The colour scale is clipped at a value of 10%, the highest values exceeding 100%.

In most of the panels, the error plots are dominated by vertical stripes (the sporadically occurring deviations from the vertical stripe patterns will be discussed later). This indicates that the solution accuracy is governed primarily by the grid step dh and that the k_y sampling plays a less important role. The results further indicate that a value of $N = 20$ seems to be sufficient; higher values of N do not significantly improve the accuracy. This means that the deviation values shown in Figure 4.11 would not change significantly if a simulation for $N = 20$ and $M = 50$ would have been chosen as the reference solution, such that the absolute values in Figures 4.10 and 4.11 can be compared (the reference solution for Figure 4.10 is computed for $N = 21$ and $M = 50$). This comparison shows that the error values also are not too dependent on the subsurface model parameters. The error values for $N = 9, 14$ and 17 for the water table model (Figure 4.10) are about the same as those for $N = 9, 15$ and 19 for the gradient model (Figure 4.11).

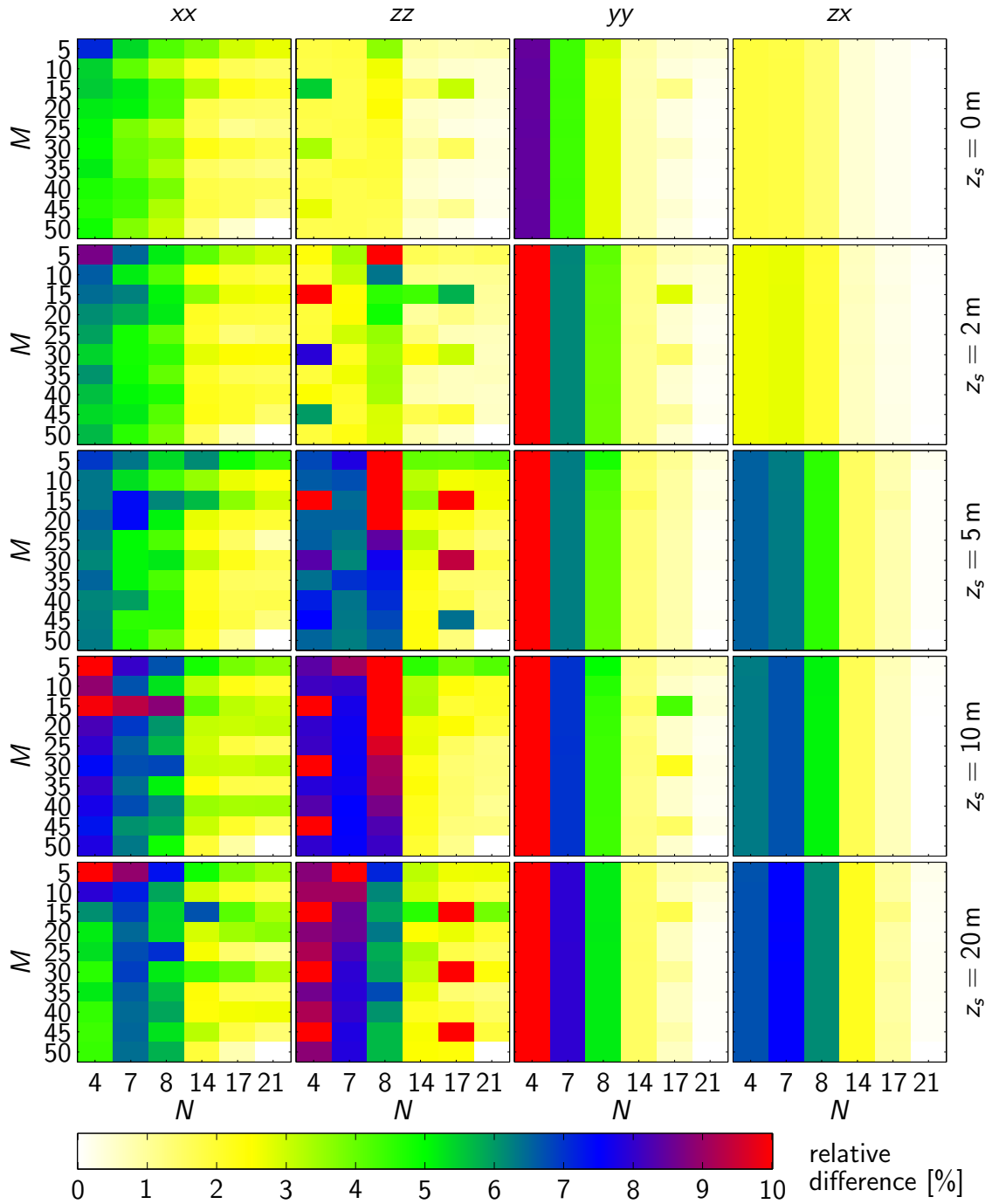


Figure 4.10: Relative median difference of solutions computed with different sampling densities in the k_y -space and different grid steps in spatial sampling for the water table model. M is the quantity governing the sampling density in the k_y -domain and N is the number of grid points per minimum wave length.

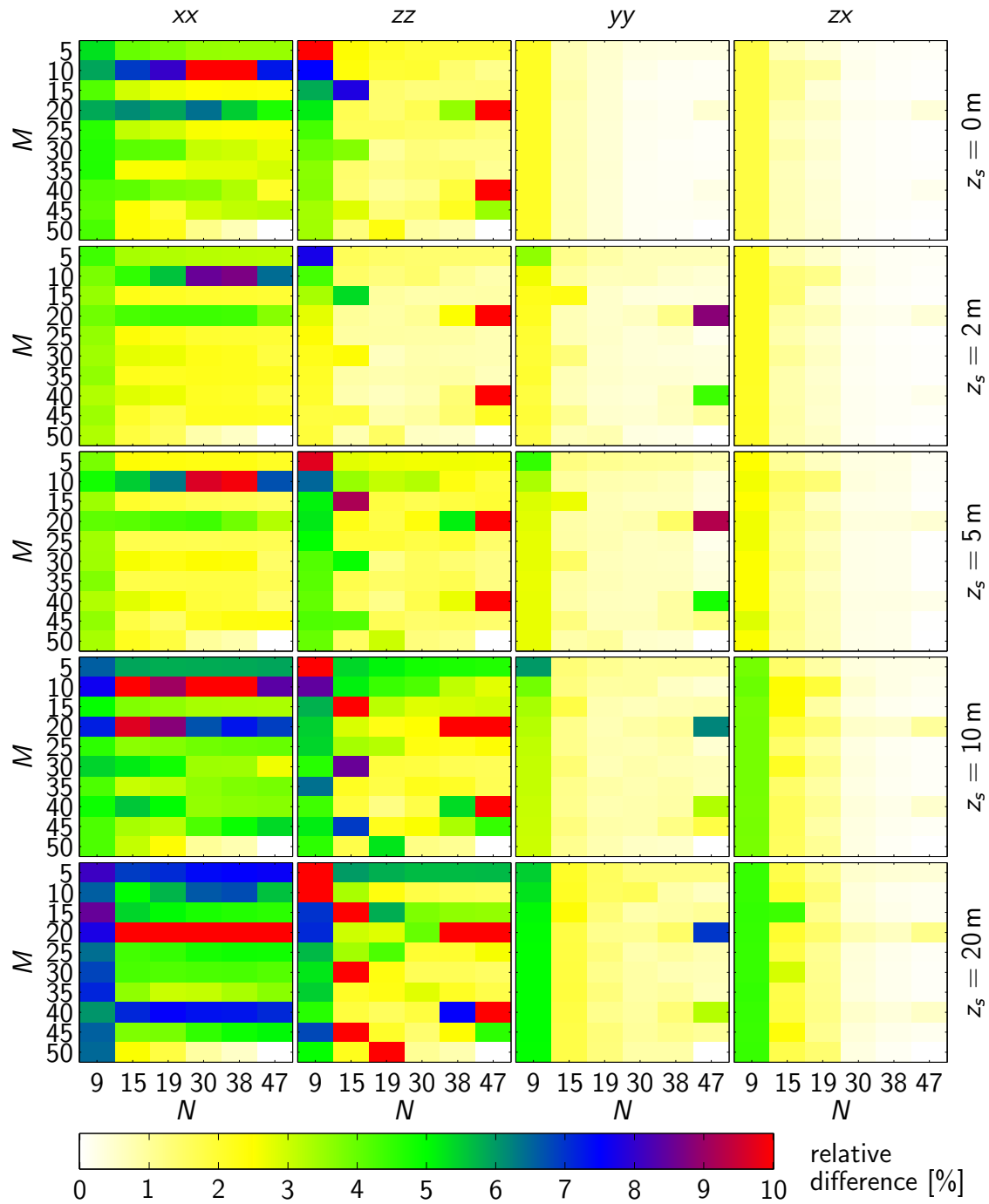


Figure 4.11: Relative median difference of solutions computed with different sampling densities in the k_y -space and different grid steps in spatial sampling for a gradient model. M is the quantity governing the sampling density in the k_y -domain and N is the number of grid points per minimum wave length.

4.4.3 The failure of the PML boundary conditions at the critical wavenumbers

Superimposed on the vertical stripe patterns in Figures 4.10 and 4.11 there are combinations of M and N for which large deviations from the reference solution are observed. This applies particularly to the zz and to some extent to the xx source-receiver combinations, but other configurations seem to be affected as well. There is no clear pattern of occurrence; the large errors seem to appear almost randomly.

To understand this problem, I have plotted in Figure 4.12 the actual frequency-domain wave fields for the zz configuration and a source depth of $z_s = 0$ m calculated

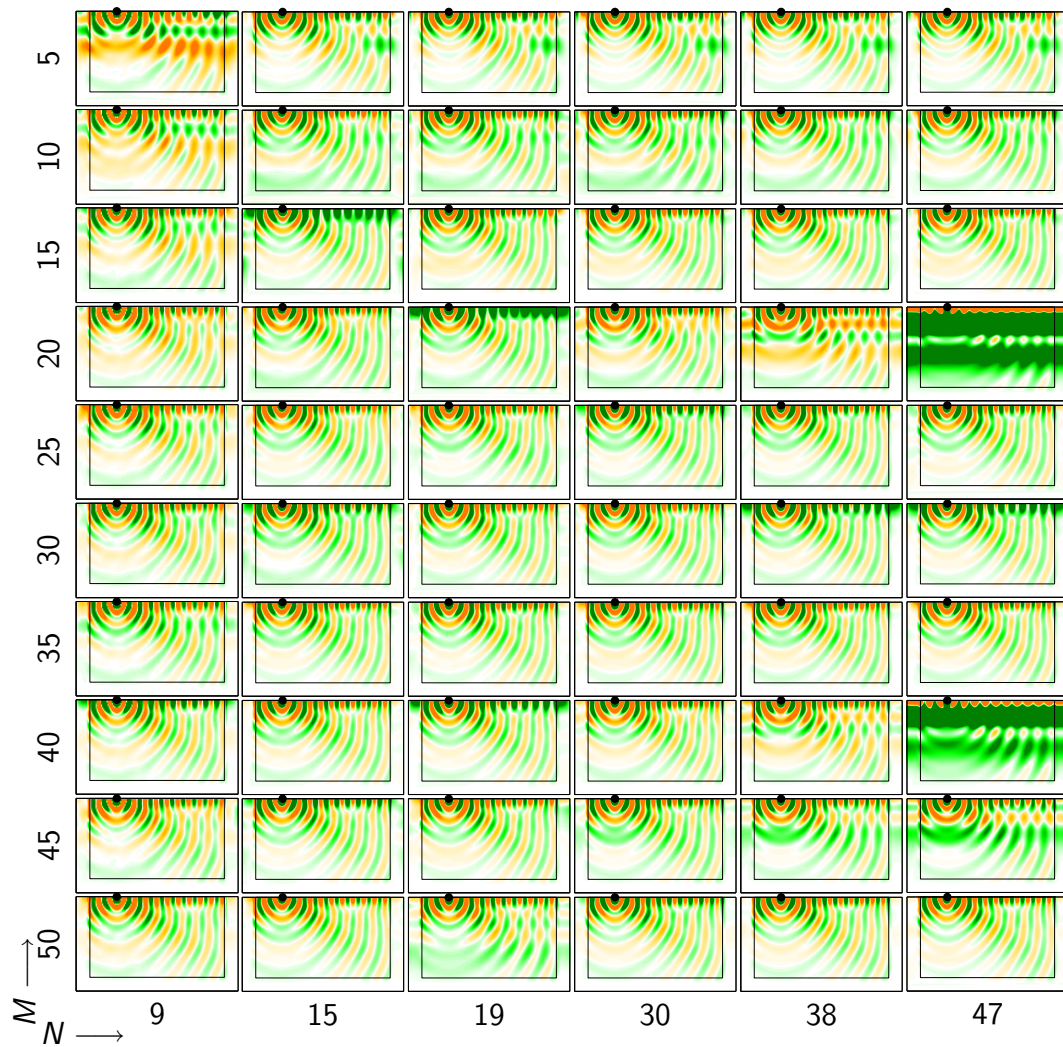


Figure 4.12: Thumbnail solution plots for configuration zz and source at the free surface for the gradient model. The boundaries to the PMLs are drawn as a black frame and the source location is designated by the black dots. The coordinate axes are omitted for better visibility; the model geometry is shown in Figure 4.8. M is the quantity governing the sampling density in the k_y -domain and N is the number of grid points per minimum wave length. See Figure 2.7b for the colour scale.

with the gradient model (see Figures 4.9 and 4.11 and Table 4.1). The wave fields associated with large errors exhibit bold horizontal bars of high amplitude values, which are not suppressed at all inside the PMLs.

The reason for the strange patterns observed for the problematic combinations of M and N in Figure 4.12 is the even sampling along the k_y -axis. Since an even sampling strategy chooses k_y values irrespective of any critical wavenumbers associated with the model (which are in this case unknown), it is possible that some sampling points fall close to a pole in the spectrum. As can be seen in the plots showing the k_y -spectra for homogeneous models (Figures 4.2, 4.6 and 4.7), the solution includes significant evanescent-phase energy in the direct vicinity of some of the critical wavenumbers. The configurations predominantly affected by this strange effect, xx , zz and yy , are indeed the configurations, for which the k_y -spectra for the homogeneous half space show an increase in amplitude towards the critical wavenumber (see Figures 4.7a, 4.6a and 4.7b), such that the amplitude of the evanescent phase is higher than that for the propagating phases at the ‘normal’ wavenumbers.

This leads to problems with the PML boundary conditions as described in section 3.1.2. They are designed primarily for propagating waves, and do not sufficiently attenuate the evanescent phases. This results in standing waves as observed in Figure 4.12.

The problem is illustrated in more detail in Figure 4.13, which shows the solution for $M = 20$, $N = 47$ and the summand $\mathfrak{G}_{zz}(KY_j)$ of the inverse transform sum (see equations (4.7) and (4.9)) for $j = 174$ and abscissae $KY_j = 1.08699 \text{ m}^{-1}$. The figure clearly shows a standing wave, where the shape of the wave field seems to be unrelated to the source location. Since this solution has a much higher amplitude (by a factor of about 20) than all the other solutions contained in the sum (4.7), the inversely transformed solution is heavily influenced (and contaminated) by this summand.

The (seemingly critical) wavenumber $k_y = 1.08699 \text{ m}^{-1}$ is contained in the set of sampling points for $M = 20$ and $M = 40$ for the gradient model, but not in those for any

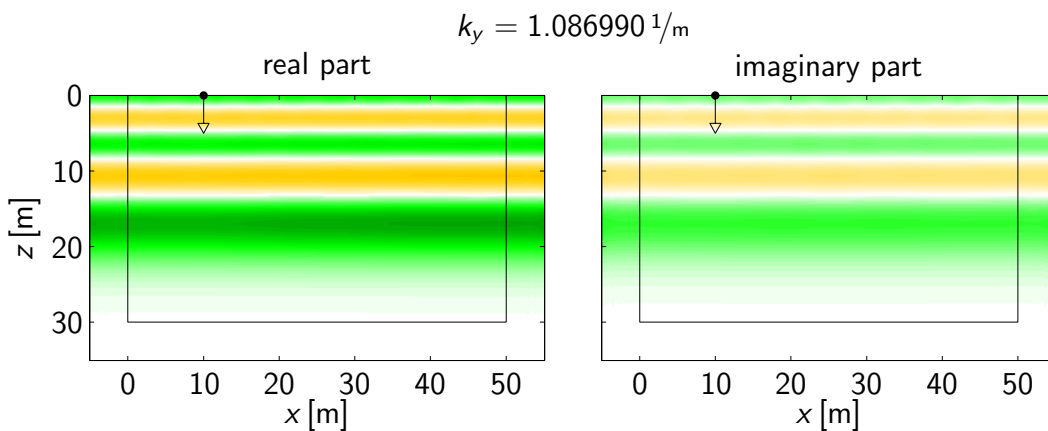


Figure 4.13: Example plot showing a solution for a critical wavenumber (k_y -index 174 for $M = 20$ and $N = 47$) for the gradient model. The wave field shows the behaviour of a standing wave rather than that of a propagating wave. The PMLs (boundaries shown as a black frame) do not have any effect and the solution is independent of the source position (shown as a black arrow). See Figure 2.7b for the colour scale.

other values of M . The finding, that the contaminated solutions are not observed for combinations of a certain value of M with all values of N hints to the conclusion that the critical wavenumbers for the continuous problem and those for the discretised problem are not equivalent. It rather seems, that their location along the k_y -axis depends on the choice of the grid step dh for the FEM grid.

Thus, even if the critical wavenumbers for the continuous problem involving heterogeneous models would be known analytically, their values would be modified by the discretisation for the FEM simulation, such that accidentally choosing them as a sampling point cannot be avoided.

4.5 Conclusions

This chapter showed that 2.5D forward modelling for elastic isotropic wave propagation, as a compromise between the physically inappropriate 2D forward modelling and the computationally very expensive full 3D forward modelling, can be problematic.

For homogeneous and nearly homogeneous full space models, I presented an efficient strategy for sampling the k_y -space that leads to solutions of acceptable accuracy (see section 4.2). The strategy can be extended to the case of homogeneous half space models (see section 4.3).

However, this sampling strategy cannot be employed for highly heterogeneous models. In the case of strongly heterogeneous full-space models, too many critical wavenumbers would lead to a very high number of integration intervals. In the case of a heterogeneous half space, which is the case my work is concentrated on, the critical wavenumbers corresponding to the dominant surface wave phases cannot be computed. Dense even sampling strategies along the k_y axis can lead to erroneous solutions (see section 4.4). The reason for the failure of the sampling strategy for heterogeneous models is the presence of critical wavenumbers which produce pole-like behaviour, contaminating the wavenumber spectra. It is highly likely that some of the sampling points lie on or close to a critical wavenumber and such coincidence cannot be avoided.

To overcome this problem, one could try to suitably modify the PML boundary conditions. An alternative option could be to avoid the poles of the k_y spectra. They are located on the real axis. By either shifting the k_y values or the poles away from the real axis the poles could be by-passed. This will be discussed in more detail in Chapter 5.

Chapter 5

Conclusions and Outlook

5.1 Main results

5.1.1 Sensitivities and data information content

The comparison of wave fields and waveform sensitivities in Chapter 2 indicated clearly that the acoustic approximation is inadequate for near-surface waveform inversion problems and that an elastic approach needs to be considered. The P -wave arrivals, which are the only phases modelled with an acoustic approximation, are concealed by surface-wave and guided-wave phases. These phases that are absent in wave fields calculated with an acoustic approximation show the highest sensitivities with respect to the elastic subsurface properties. Therefore, the acoustic approximation does not only produce incorrect wave fields, but also neglects important information that could be extracted from the data.

A 2D analysis of the information content of elastic multi-component data sets suggests that a vertically directed source and a horizontally directed receiver provide the highest subsurface information content. From the reciprocity principle, the same information content would be offered by a horizontally directed source and a vertical-component geophone. However, the former option can be implemented in the field with less effort. There is little additional benefit in recording the full tensorial wave fields (i.e., vertical and horizontal sources in combination with vertical and horizontal receiver components).

If complete seismograms (in the time domain) or corresponding complete spectra (in the frequency domain) would be considered during an inversion, the same amount of information would be obtained. Windowing the time domain data or selecting only a few frequencies obviously reduces the information content, but it is interesting to note that a few judiciously chosen frequencies allow the information content to be better exploited compared with time windowing approaches.

Sensitivity analyses and computations of data information content were performed for several subsurface models. Although sensitivities and the related measures show considerable variations between the individual models, the above conclusions seem to be model independent.

5.1.2 Elastic modelling

I have implemented an elastic frequency domain finite element (FEMFd) code suitable for computing seismic data in the absence or presence of a free surface. The algorithm has been validated by a comparison with an analytical full space solution. The results indicated that the solution accuracy depends on the choice of the source and receiver components that are modelled. For an in-line configuration, e.g. an x -directed source and an x -directed receiver, the accuracy is about four times higher compared with a configuration involving a z -directed source and an x -directed receiver. This needs to be considered when integrating my forward solver into a full waveform inversion programme.

To account for the artificial ground boundaries at the left, right and bottom of the computational domain, I have implemented perfectly matched layer boundary conditions to suppress artificial reflections. They proved to be very effective. In most cases, a boundary layer only 10 grid points wide was sufficient, and with a layer width of 30 grid points even all the troublesome cases (e.g. sources close to the boundary) could be handled adequately.

A comparison of modelling results with a well established time domain finite difference code showed a very good match. In the framework of this comparison I could also draw very important conclusions with regard to the general computational efficiency of time and frequency domain modelling algorithms. If the response for several sources is required, the frequency domain approach is much faster compared with the time domain computations. This conclusion also holds when all frequencies required to generate a complete seismogram are computed.

This advantage is a consequence of the direct matrix solver used in the frequency domain algorithm but comes at the expense of a higher computer memory consumption. This is currently the major limitation for large-scale (e.g. 3D) elastic frequency domain modelling and inversion tasks (see e.g. Virieux et al., 2009). A possible option could be to replace the direct matrix solver by an iterative solver (e.g. Plessix, 2009), which would reduce the memory requirements. However, this would sacrifice the advantages for multiple source computations.

5.1.3 Sampling strategies for elastic 2.5D forward modelling

Generally, 2.5D modelling of elastic wave propagation is a compromise between expensive 3D modelling and the crude approximation of 2D modelling in combination with data filtering (e.g. Williamson and Pratt, 1995). The solution is computed in the frequency-wavenumber domain, where the additional Fourier transform is taken along the coordinate axis along which the model parameters are constant, which is in my case the y -direction. Thus, the equations that have to be solved represent a 2D problem, which has to be solved repeatedly for a series of wavenumbers k_y . Finally, an inverse Fourier transform with respect to wavenumber k_y yields the frequency-domain solution. A critical aspect of this strategy is the choice of the wavenumbers k_y .

For homogeneous and mildly heterogeneous elastic isotropic models an efficient sampling strategy was introduced in Chapter 4 that is based on the *a priori* knowledge of the critical wavenumbers of the body waves in the medium. The number of sampling points along the k_y -axis is proportional to the maximal source/receiver distance and inversely proportional to the minimum wavelength occurring in the resulting wave fields.

For inhomogeneous models, this efficient strategy is not applicable since the number of critical wavenumbers is prohibitively high or, in presence of a free surface, the critical wavenumbers (associated with the surface waves) are unknown. Consequently, an even sampling has to be employed. Again, the number of forward solutions is proportional to the maximum source/receiver distance and inversely proportional to the minimum wavelength, but the total number of required wavenumbers is higher compared with the optimised non-equal sampling strategy for the homogeneous models.

I have investigated the influence of the sampling density along the k_y -axis on the solution accuracy, and compared this with the effects of different spatial sampling densities with the finite element grid. Generally, effects of the finite element spatial sampling density dominates over the k_y sampling. However, in the course of these investigations I discovered a fundamental problem of using even k_y sampling. It may happen that a sample lies on or close to an unknown critical wavenumber, which distorts the solution in a major way. This requires further modifications of the 2.5D algorithm. This is discussed in more detail in the next section.

5.2 Areas of future research

5.2.1 Sensitivities and data information content

Sensitivity calculation

Due to the lack of alternative options at the time, I computed waveform sensitivities using a brute force perturbation approach (Chapter 2). In the mean time, the explicit sensitivity expressions established for the acoustic case (Zhou and Greenhalgh, 1999), have been extended to the 3D and 2.5D elastic cases (Zhou and Greenhalgh, 2009, Zhou and Greenhalgh, 2010a). These expressions are currently implemented in the framework of another PhD project at ETH Zurich (Manukyan, 2010). This will allow elastic sensitivities for all nine components of the Green's tensor (i.e. all possible source/receiver direction combinations) to be computed.

These new developments will allow the 2.5D elastic sensitivities for source/receiver configurations to be directly compared to their 2D counterparts to investigate the influence of the geometrical spreading on the sensitivities. The additionally available sensitivities for the source/receiver configurations involving y -directed sources and/or y -directed receivers can be used to compare the amplitude of the sensitivities of Rayleigh-wave phases (already visible in the 2D case) to those of Love-wave phases.

Data information content

As discussed in Chapter 2, the sensitivities computed with the brute force approach exhibit a significant amount of numerical noise. This error is propagated and amplified during the computation of the approximate Hessian matrices, which are the basis of the information content analysis. This required a relatively high eigenvalue cutoff threshold $\theta = 10^{-5}$ to be chosen for computing the RER information criterion (see equation (2.18) and section 2.4.1). With the explicit sensitivity expressions the numerical errors are expected to be much lower, which would allow a lower threshold to be chosen, such

as in Maurer et al. (2009) This may enable more subtle features of the data information content offered by the individual source/receiver combinations to be analysed.

The availability of the configurations yy , yx (xy) and yz (zy) will further expand the scope of my experimental design analysis. In particular, it will be interesting to see how well the yy configuration performs, which is commonly employed for shear wave (SH) investigations.

Having more accurate sensitivities available would make it, in my view, also worthwhile to investigate other measures of information content. In Chapter 2, I used the criterion of the Relative Eigenvalue Range (RER, see equation (2.18)), which is a measure of the size of the null space. As already discussed in section 2.4.2, the RER criterion does not take into account the actual shape of the normalised eigenvalue curve. For this reason I proposed an alternative criterion to assess the information content, that is the Relative Eigenvalue Area criterion (REA, see equation (2.22)). Due to the numerical inaccuracies of the brute-force approach I discarded this option, but for more accurate eigenvalue spectra, the REA criteria should be further investigated. According to Curtis (2004), the REA is a direct measure of the expected post-survey model parameter uncertainties if Gaussian errors can be assumed, whereas the RER only measures the number of model parameters that can be resolved.

Besides considering alternative information content criteria, the experimental design analysis could be extended to an investigation of the information content with regard to restricted parts of the model that may be of particular interest. This can be achieved by using focusing criteria, which replace the eigenvalues λ_i in equations (2.18) and (2.22) by $\sum_{j=1}^{n_M} \lambda_i^2 (\mathbf{e}_i \cdot \mathbf{v}_j)$, where n_M is the number of model parameters. The \mathbf{e}_i are the eigenvectors of the approximate Hessian matrix, corresponding to the λ_i , and the \mathbf{v}_j are a basis of the subspace of interest (see Curtis, 2004).

In addition to only investigating the influence of data selection on the information content, one may also consider data weighting. This can be easily achieved using the operator $\hat{\mathbf{W}}_D$ in the equations (2.3) and (2.11) and in the approximate Hessian matrix whose eigenvalues are used in equation (2.18). Data weighting can be done, for example, by estimating the noise conditions and setting the diagonal elements of $\hat{\mathbf{W}}_D$ proportional to the expected signal-to-noise ratio.

Model resolution

Using the explicit sensitivity expressions, the approximate Hessian matrices should be accurate enough to be used for computing model resolution matrices \mathbf{R}^M via equation D.13 given in Appendix D. Thus, the investigation of the data information content can be supplemented by an analysis of the model resolution ability of different kinds of data sets. The diagonal elements of \mathbf{R}^M are a measure of how well the single model parameters can be resolved. For example, it would be interesting to see which parts of the model are well resolved for certain time window choices in the time domain or for certain frequencies in the frequency domain. I would expect that data windowing in the time domain would result in focused model resolution in those areas where the sensitivities are high at the selected times. For frequency domain data selection, I would rather expect a more even resolution of the model, with varying detail depending on the frequencies chosen.

5.2.2 Elastic modelling

Anisotropy and viscoelasticity

My FEMFd forward solver is currently being extended to include anisotropic media (Manukyan, 2010). A further useful extension would be to incorporate viscoelasticity, which should be straightforward. The only change necessary would be to replace the real-valued elastic parameters by complex-valued quantities (see e.g. Forbriger and Friederich, 2005). However, this may require the PML boundary conditions to be reformulated (Liu, 1998).

Minor topographic features may have a significant effect on the waveforms observed. As discussed in Robertsson et al. (1996), it is therefore necessary to account for topography of the free surface (and subsurface discontinuities) in obtaining reliable results. This can be implemented in my finite element algorithm by incorporating unstructured meshes. Additionally, this would allow grid refinement strategies to be implemented, which would not only facilitate complicated topographies to be considered, but it could also generally improve the accuracy and efficiency of the algorithm. (e.g. Blome et al., 2009).

5.2.3 Elastic 2.5D forward modelling

Further reduction of sampling points

The efficiency of the 2.5D elastic forward solver is closely related to the number of sampling points along the k_y -axis for which the solution has to be computed. This number is constrained by the largest wavenumber that may occur. In Chapter 4 the largest wavenumber was determined by the lowest velocity (either lowest v_S or Rayleigh wave velocity). Preliminary tests revealed that the largest wavenumber is governed primarily by the velocities at the source point, since the source-region properties determine which wavenumbers are excited. This should be further investigated. I propose the following test procedure, sketched in Figure 5.1:

- A full-space model comprising two homogeneous half spaces (parts), with two different values of the critical wavenumber k_S should be used (see Figure 5.1).
- The source should be placed in the model region having the lower critical wavenumber k_S (left side in Figure 5.1).
- For different distances d_b of the source to the boundary between the low- k_S medium and the high- k_S medium (Figure 5.1a to c), the maximal k_y can be determined, for which the solution at receivers in the high- k_S medium contains significant energy.
- I expect that for source positions far away from the internal boundary, only energy for wavenumbers up to the low- k_S threshold will be observed. For distances d_b smaller than some minimal distance d_{bmin} (to be determined), I suspect there will be energy contributions up to the high- k_S threshold, induced by near-field phases that reach into the high- k_S -medium.

An obvious extension would be to consider additional intermediate layers between source and receiver which may ‘filter’ out the higher wavenumbers.

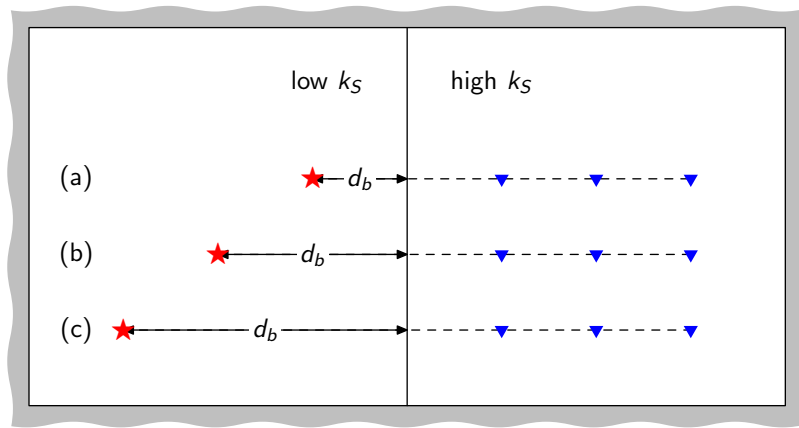


Figure 5.1: Sketch of a possible source/receiver geometry for finding the minimum upper limit of the k_y -sampling interval. The areas shaded in grey denote PML boundaries, the red stars and blue triangles denote the locations of sources and receivers, respectively. In (a), (b) and (c) the source is placed at increasing distance from the boundary between two homogeneous half spaces having different values of k_S .

Avoiding the poles in the k_y wavenumber spectra

To overcome the problems related with the poles of the wavenumber spectra, three different possible solutions could be tested:

- (i) When k_y is considered to be a complex-valued parameter, written as $k_y := k_y^R + ik_y^I$, the poles of the k_y -spectra are located on the real axis. Thus, one could sample the k_y -spectra along a contour that circumnavigates the poles by adding a small imaginary part k_y^I to the wavenumber in the solution process. For discrete wavenumber methods for 1D media, Phinney (1965) rejects this possibility since the additional exponential term $e^{k_y^I y}$ that is introduced in the inverse transform (4.3) would be prone to amplify singularities in the k_y spectra, negating the benefit of integration away from the poles on the real k_y -axis.
- (ii) A method of widespread use in discrete wavenumber summation techniques (e.g. Phinney, 1965; Bouchon, 1979; Müller, 1985; Mallick and Frazer, 1987; Bouchon, 2003) for synthetic seismogram computations is the complex-frequency method. Here, the spectra are computed for complex-valued frequency with a small imaginary part, which is determined by the length of the seismograms that are to be computed (Bouchon, 2003). Instead of moving the integration contour away from the poles, the poles are moved away from the real k_y -axis and the integration along the real axis can be easily performed. This method is well suited, for obtaining solutions in the time domain. The resulting waveforms are exponentially damped towards later times, which can be compensated by multiplying the time domain signals with $e^{\omega^I t}$, after the inverse temporal Fourier transform is taken, where ω^I is the imaginary part of the angular frequency that has been used in the solution process (note that ω^I is equal for all frequencies).
- (iii) In the case of viscoelastic models, the poles of the k_y -spectra along the real axis are likely to disappear, as in the case of the discrete wavenumber techniques (Forbriger,

2003). Thus, introducing viscoelasticity (i.e. complex elastic constants) into the FEMFd forward solver might be the most elegant way to overcome the problems of integration over the singular points of the spectrum.

Appendix A

Mathematical details

A.1 Fourier transform definition

Since there exists more than one valid definition of 'the' Fourier Transform it is necessary to explicitly state which definition is used in this thesis.

For the transformation pair interconnecting the vector field \mathbf{u} in the t - x - y - z -domain (denoted by \mathbf{u}) and in the ω - x - y - z -domain ($\bar{\mathbf{u}}$) I define

$$\begin{aligned}\bar{\mathbf{u}}(x, y, z, \omega) &= \frac{1}{\sqrt{2\pi}} \int_{-\infty}^{\infty} \mathbf{u}(x, y, z, t) e^{-i\omega t} dt \\ \mathbf{u}(x, y, z, t) &= \frac{1}{\sqrt{2\pi}} \int_{-\infty}^{\infty} \bar{\mathbf{u}}(x, y, z, \omega) e^{+i\omega t} d\omega.\end{aligned}\tag{A.1}$$

To undertake 2.5D frequency-domain modelling, another transformation pair needs to be introduced, which interconnects the ω - x - y - z -domain ($\bar{\mathbf{u}}$) and the ω - x - k_y - z -domain ($\bar{\bar{\mathbf{u}}}$)

$$\begin{aligned}\bar{\bar{\mathbf{u}}}(x, k_y, z, \omega) &= \frac{1}{\sqrt{2\pi}} \int_{-\infty}^{\infty} \bar{\mathbf{u}}(x, y, z, \omega) e^{-ik_y y} dy \\ \bar{\mathbf{u}}(x, y, z, \omega) &= \frac{1}{\sqrt{2\pi}} \int_{-\infty}^{\infty} \bar{\bar{\mathbf{u}}}(x, k_y, z, \omega) e^{+ik_y y} dk_y,\end{aligned}\tag{A.2}$$

where k_y denotes the wavenumber corresponding to the cross-plane or strike coordinate y . All other symbols are used according to their usual meaning (for details see the symbol index on page xi). Note that an overbar on the quantity denotes Fourier transformation.

A.2 Derivation of the elemental matrix entries for the medium with perfectly matched layers (PMLs)

The purpose of this section is to show the steps leading from equations (3.31), (3.32) and (3.33) to the final result for the elemental matrix entries as given in equations (3.35), (3.36) and (3.39).

The first step is to plug the definition of the ε_ζ (3.30) and the coordinate stretching functions (3.34) into the matrix elements in (3.31) and the integrals in (3.33). After restricting the integration area to that of one element, namely Ω_e , and using (3.10) to transform into local coordinates and inserting the shape functions (3.11), all that is left to do is the evaluation of integrals involving the shape functions and their derivatives, the local coordinates η and ξ and the coefficients given in Table 3.1.

For the elemental mass matrix entries, this leads to

$$\begin{aligned} \tilde{M}_{AB\zeta\zeta}^e = \mathcal{V}_\zeta \bigg\{ & [1 - A_x A_z - i(A_x + A_z)] \mathcal{I}^{AB} \\ & - iB_x(1 - iA_z) \mathcal{I}^{\xi AB} \\ & - iB_z(1 - iA_x) \mathcal{I}^{\eta AB} \\ & - B_x B_z \mathcal{I}^{\eta\xi AB} \bigg\} \end{aligned} \quad (\text{A.3})$$

and using the explicit results for the integrals

$$\mathcal{I}^{\xi AB} = \int_{\Omega_e} \xi N_A N_B d\Omega = \begin{bmatrix} -2 & -1 & 0 & 0 \\ -1 & -2 & 0 & 0 \\ 0 & 0 & +2 & +1 \\ 0 & 0 & +1 & +2 \end{bmatrix} \frac{\Delta x \Delta z}{36} \quad (\text{A.4a})$$

$$\mathcal{I}^{\eta AB} = \int_{\Omega_e} \eta N_A N_B d\Omega = \begin{bmatrix} -2 & 0 & -1 & 0 \\ 0 & +2 & 0 & +1 \\ -1 & 0 & -2 & 0 \\ 0 & +1 & 0 & +2 \end{bmatrix} \frac{\Delta x \Delta z}{36} \quad (\text{A.4b})$$

$$\mathcal{I}^{\eta\xi AB} = \int_{\Omega_e} \eta \xi N_A N_B d\Omega = \begin{bmatrix} +1 & 0 & 0 & 0 \\ 0 & -1 & 0 & 0 \\ 0 & 0 & -1 & 0 \\ 0 & 0 & 0 & +1 \end{bmatrix} \frac{\Delta x \Delta z}{36} \quad (\text{A.4c})$$

in (A.3) the final result given in (3.35) is achieved.

For the integrals (3.33a) and (3.33b) one finds

$$\begin{aligned} \tilde{\mathcal{I}}_{xx}^{AB} = & [1 + A_x A_z + i(A_x - A_z)] \mathcal{G}_{xx}^{AB} \\ & + iB_x(1 - iA_z) \mathcal{G}_{xx}^{\xi AB} \\ & - iB_z(1 + iA_x) \mathcal{G}_{xx}^{\eta AB} \\ & + B_x B_z \mathcal{G}_{xx}^{\eta\xi AB} \end{aligned} \quad (\text{A.5a})$$

$$\begin{aligned} \tilde{\mathcal{I}}_{zz}^{AB} = & [1 + A_x A_z + i(A_z - A_x)] \mathcal{G}_{zz}^{AB} \\ & - iB_x(1 + iA_z) \mathcal{G}_{zz}^{\xi AB} \\ & + iB_z(1 - iA_x) \mathcal{G}_{zz}^{\eta AB} \\ & + B_x B_z \mathcal{G}_{zz}^{\eta\xi AB}, \end{aligned} \quad (\text{A.5b})$$

where the abbreviations \mathcal{G} have different values in the different PML zones shown in Figure 3.2. Their general form is

$$\mathcal{G}_{xx}^{AB} = \int_{\Omega_e} \frac{1}{1 + A_x^2 + 2A_x B_x \xi + B_x^2 \xi^2} \partial_x N_A \partial_x N_B d\Omega \quad (\text{A.6a})$$

$$= \frac{1}{2} \mathcal{I}_{xx}^{AB} \mathcal{G}_1^x$$

$$\mathcal{G}_{xx}^{\xi AB} = \int_{\Omega_e} \frac{\xi}{1 + A_x^2 + 2A_x B_x \xi + B_x^2 \xi^2} \partial_x N_A \partial_x N_B d\Omega \quad (\text{A.6b})$$

$$= \frac{1}{2} \mathcal{I}_{xx}^{AB} \left(\mathcal{G}_2^x - \frac{A_x}{B_x} \mathcal{G}_1^x \right)$$

$$\mathcal{G}_{xx}^{\eta AB} = \int_{\Omega_e} \frac{\eta}{1 + A_x^2 + 2A_x B_x \xi + B_x^2 \xi^2} \partial_x N_A \partial_x N_B d\Omega \quad (\text{A.6c})$$

$$= \frac{1}{2} \mathcal{I}_{xx}^{\eta AB} \mathcal{G}_1^x$$

$$\mathcal{G}_{xx}^{\eta\xi AB} = \int_{\Omega_e} \frac{\eta\xi}{1 + A_x^2 + 2A_x B_x \xi + B_x^2 \xi^2} \partial_x N_A \partial_x N_B d\Omega \quad (\text{A.6d})$$

$$= \frac{1}{2} \mathcal{I}_{xx}^{\eta AB} \left(\mathcal{G}_2^x - \frac{A_x}{B_x} \mathcal{G}_1^x \right)$$

$$\mathcal{G}_{zz}^{AB} = \int_{\Omega_e} \frac{1}{1 + A_z^2 + 2A_z B_z \eta + B_z^2 \eta^2} \partial_z N_A \partial_z N_B d\Omega \quad (\text{A.6e})$$

$$= \frac{1}{2} \mathcal{I}_{zz}^{AB} \mathcal{G}_1^z$$

$$\mathcal{G}_{zz}^{\eta AB} = \int_{\Omega_e} \frac{\eta}{1 + A_z^2 + 2A_z B_z \eta + B_z^2 \eta^2} \partial_z N_A \partial_z N_B d\Omega \quad (\text{A.6f})$$

$$= \frac{1}{2} \mathcal{I}_{zz}^{AB} \left(\mathcal{G}_2^z - \frac{A_z}{B_z} \mathcal{G}_1^z \right)$$

$$\mathcal{G}_{zz}^{\xi AB} = \int_{\Omega_e} \frac{\xi}{1 + A_z^2 + 2A_z B_z \eta + B_z^2 \eta^2} \partial_z N_A \partial_z N_B d\Omega \quad (\text{A.6g})$$

$$= \frac{1}{2} \mathcal{I}_{zz}^{\xi AB} \mathcal{G}_1^z$$

$$\mathcal{G}_{zz}^{\eta\xi AB} = \int_{\Omega_e} \frac{\eta\xi}{1 + A_z^2 + 2A_z B_z \eta + B_z^2 \eta^2} \partial_z N_A \partial_z N_B d\Omega \quad (\text{A.6h})$$

$$= \mathcal{I}_{zz}^{\xi AB} \left(\mathcal{G}_2^z - \frac{A_z}{B_z} \mathcal{G}_1^z \right),$$

but in the zones T, D and B the equations involving A_x and A_z reduce to

$$\begin{aligned}\mathcal{G}_{xx}^{AB} &= \int_{\Omega_e} \frac{1}{1 + A_x^2 + 2A_x B_x \xi + B_x^2 \xi^2} \partial_x N_A \partial_x N_B d\Omega \\ &= \frac{1}{2} \mathcal{I}_{xx}^{AB}\end{aligned}\tag{A.7a}$$

$$\begin{aligned}\mathcal{G}_{xx}^{\xi AB} &= \int_{\Omega_e} \frac{\xi}{1 + A_x^2 + 2A_x B_x \xi + B_x^2 \xi^2} \partial_x N_A \partial_x N_B d\Omega \\ &= 0\end{aligned}\tag{A.7b}$$

$$\begin{aligned}\mathcal{G}_{xx}^{\eta AB} &= \int_{\Omega_e} \frac{\eta}{1 + A_x^2 + 2A_x B_x \xi + B_x^2 \xi^2} \partial_x N_A \partial_x N_B d\Omega \\ &= \frac{1}{2} \mathcal{I}_{xx}^{\eta AB}\end{aligned}\tag{A.7c}$$

$$\begin{aligned}\mathcal{G}_{xx}^{\eta \xi AB} &= \int_{\Omega_e} \frac{\eta \xi}{1 + A_x^2 + 2A_x B_x \xi + B_x^2 \xi^2} \partial_x N_A \partial_x N_B d\Omega \\ &= 0\end{aligned}\tag{A.7d}$$

whereas in the zones L, D and R the equations involving A_z and B_z become

$$\begin{aligned}\mathcal{G}_{zz}^{AB} &= \int_{\Omega_e} \frac{1}{1 + A_z^2 + 2A_z B_z \eta + B_z^2 \eta^2} \partial_z N_A \partial_z N_B d\Omega \\ &= \frac{1}{2} \mathcal{I}_{zz}^{AB}\end{aligned}\tag{A.8a}$$

$$\begin{aligned}\mathcal{G}_{zz}^{\eta AB} &= \int_{\Omega_e} \frac{\eta}{1 + A_z^2 + 2A_z B_z \eta + B_z^2 \eta^2} \partial_z N_A \partial_z N_B d\Omega \\ &= 0\end{aligned}\tag{A.8b}$$

$$\begin{aligned}\mathcal{G}_{zz}^{\xi AB} &= \int_{\Omega_e} \frac{\xi}{1 + A_z^2 + 2A_z B_z \eta + B_z^2 \eta^2} \partial_z N_A \partial_z N_B d\Omega \\ &= \frac{1}{2} \mathcal{I}_{zz}^{\xi AB}\end{aligned}\tag{A.8c}$$

$$\begin{aligned}\mathcal{G}_{zz}^{\eta \xi AB} &= \int_{\Omega_e} \frac{\eta \xi}{1 + A_z^2 + 2A_z B_z \eta + B_z^2 \eta^2} \partial_z N_A \partial_z N_B d\Omega \\ &= 0,\end{aligned}\tag{A.8d}$$

while all other terms remain as given in (A.6). The abbreviations introduced there are

$$\begin{aligned}\mathcal{G}_1^i &= \int_{-1}^1 \frac{d\zeta}{1 + A_i^2 + 2A_i B_i \zeta + B_i^2 \zeta^2} \\ \mathcal{G}_2^i &= \int_{-1}^1 \frac{\zeta}{1 + A_i^2 + 2A_i B_i \zeta + B_i^2 \zeta^2} d\zeta \\ &\quad + \frac{A_i}{B_i} \int_{-1}^1 \frac{d\zeta}{1 + A_i^2 + 2A_i B_i \zeta + B_i^2 \zeta^2}\end{aligned}\tag{A.9a}$$

and the result of these integrals can be found in equation (3.38). Inserting all this into equations (3.32a), (3.32b) and (3.32c) leads to the final result given in (3.36).

The remaining expressions for the elemental stiffness matrix entries are obtained by evaluating the integrals (3.33c) to (3.33f) which yields

$$\begin{aligned}\tilde{\mathcal{I}}_{xy}^{AB} &= (1 - iA_z)\mathcal{I}_{xy}^{AB} - iB_z\mathcal{I}_{xy}^{\eta AB} \\ \tilde{\mathcal{I}}_{yx}^{AB} &= (1 - iA_z)\mathcal{I}_{yx}^{AB} - iB_z\mathcal{I}_{yx}^{\eta AB} \\ \tilde{\mathcal{I}}_{yz}^{AB} &= (1 - iA_x)\mathcal{I}_{yz}^{AB} - iB_x\mathcal{I}_{yz}^{\xi AB} \\ \tilde{\mathcal{I}}_{zy}^{AB} &= (1 - iA_x)\mathcal{I}_{zy}^{AB} - iB_x\mathcal{I}_{zy}^{\xi AB};\end{aligned}\tag{A.10}$$

using (3.22) and

$$\mathcal{I}_{xy}^{\eta AB} = \int_{\Omega_e} \eta \partial_x N_A N_B d\Omega = \begin{bmatrix} +1 & 0 & +1 & 0 \\ 0 & -1 & 0 & -1 \\ -1 & 0 & -1 & 0 \\ 0 & +1 & 0 & +1 \end{bmatrix} \frac{\Delta z}{12}\tag{A.11a}$$

$$\mathcal{I}_{yx}^{\eta AB} = \int_{\Omega_e} \eta N_A \partial_x N_B d\Omega = \begin{bmatrix} +1 & 0 & -1 & 0 \\ 0 & -1 & 0 & +1 \\ +1 & 0 & -1 & 0 \\ 0 & -1 & 0 & +1 \end{bmatrix} \frac{\Delta z}{12}\tag{A.11b}$$

$$\mathcal{I}_{yz}^{\xi AB} = \int_{\Omega_e} \xi N_A \partial_z N_B d\Omega = \begin{bmatrix} +1 & -1 & 0 & 0 \\ +1 & -1 & 0 & 0 \\ 0 & 0 & -1 & +1 \\ 0 & 0 & -1 & +1 \end{bmatrix} \frac{\Delta x}{12}\tag{A.11c}$$

$$\mathcal{I}_{zy}^{\xi AB} = \int_{\Omega_e} \xi \partial_z N_A N_B d\Omega = \begin{bmatrix} +1 & +1 & 0 & 0 \\ -1 & -1 & 0 & 0 \\ 0 & 0 & -1 & -1 \\ 0 & 0 & +1 & +1 \end{bmatrix} \frac{\Delta x}{12}\tag{A.11d}$$

$$\mathcal{I}_{xx}^{\eta AB} = \int_{\Omega_e} \eta \partial_x N_A \partial_x N_B d\Omega = \begin{bmatrix} -1 & 0 & +1 & 0 \\ 0 & +1 & 0 & -1 \\ +1 & 0 & -1 & 0 \\ 0 & -1 & 0 & +1 \end{bmatrix} \frac{\Delta z}{6\Delta x}\tag{A.11e}$$

$$\mathcal{I}_{zz}^{\xi AB} = \int_{\Omega_e} \xi \partial_z N_A \partial_z N_B d\Omega = \begin{bmatrix} -1 & +1 & 0 & 0 \\ +1 & -1 & 0 & 0 \\ 0 & 0 & +1 & -1 \\ 0 & 0 & -1 & +1 \end{bmatrix} \frac{\Delta x}{6\Delta z}.\tag{A.11f}$$

and inserting these results in equations (3.32d) to (3.32i) leads to the final expressions for the elemental stiffness matrix entries as given in (3.39).

A.3 2.5D FEM solution symmetries with respect to k_y

The starting point for the investigation of the symmetry properties of the 2.5D FEM solution with respect to k_y is the FEM matrix equation

$$\mathbf{S}\mathfrak{U} + \mathfrak{F} = \mathbf{0}, \quad (3.47)$$

where \mathbf{S} is the complete system matrix as defined in equation (3.45), \mathfrak{U} and \mathfrak{F} is the source vector as introduced in Appendix B.

To examine the behaviour of the solution for all possible combinations of source direction and receiver component at once, I expand equation (3.47) to the matrix equation

$$\mathbf{S}\mathbf{G} + \mathbf{F} = \mathbf{0}, \quad (A.12)$$

where

$$\mathbf{G} := \begin{bmatrix} \mathfrak{G}_{xx} & \mathfrak{G}_{zx} & \mathfrak{G}_{yx} \\ \mathfrak{G}_{zx} & \mathfrak{G}_{zz} & \mathfrak{G}_{yz} \\ \mathfrak{G}_{yx} & \mathfrak{G}_{zy} & \mathfrak{G}_{yy} \end{bmatrix} \quad \text{and} \quad \mathbf{F} := \begin{bmatrix} \mathfrak{F}_x & \mathbf{0} & \mathbf{0} \\ \mathbf{0} & \mathfrak{F}_z & \mathbf{0} \\ \mathbf{0} & \mathbf{0} & \mathfrak{F}_y \end{bmatrix} \quad (A.13)$$

are the FEM Green's tensor and a matrix combining source vectors into the three coordinate directions. That is,

$$\mathfrak{U} = \begin{bmatrix} \mathfrak{G}_{xx} \\ \mathfrak{G}_{xz} \\ \mathfrak{G}_{xy} \end{bmatrix}, \quad \mathfrak{U} = \begin{bmatrix} \mathfrak{G}_{zx} \\ \mathfrak{G}_{zz} \\ \mathfrak{G}_{zy} \end{bmatrix} \quad \text{and} \quad \mathfrak{U} = \begin{bmatrix} \mathfrak{G}_{yx} \\ \mathfrak{G}_{yz} \\ \mathfrak{G}_{yy} \end{bmatrix} \quad (A.14)$$

are the solutions of (3.47) for the source vectors

$$\mathfrak{F} = \begin{bmatrix} \mathfrak{F}_x \\ \mathbf{0} \\ \mathbf{0} \end{bmatrix}, \quad \mathfrak{F} = \begin{bmatrix} \mathbf{0} \\ \mathfrak{F}_z \\ \mathbf{0} \end{bmatrix} \quad \text{and} \quad \mathfrak{F} = \begin{bmatrix} \mathbf{0} \\ \mathbf{0} \\ \mathfrak{F}_y \end{bmatrix}. \quad (A.15)$$

For a FEM grid consisting of n nodes, \mathbf{S} is of size $3n \times 3n$ and \mathbf{G} and \mathbf{F} are of size $3n \times 3$.

To examine the symmetry, I write equation (A.12) for $+k_y$ and $-k_y$,

$$\begin{aligned} \mathbf{S}^+ \mathbf{G}^+ + \mathbf{F} &= \mathbf{0} \\ \mathbf{S}^- \mathbf{G}^- + \mathbf{F} &= \mathbf{0}, \end{aligned} \quad (A.16)$$

defining $\mathbf{S}^+ := \mathbf{S}(+k_y)$ and $\mathbf{S}^- = \mathbf{S}(-k_y)$. Closer inspection of the equations for the matrix elements, (3.35) (3.36) and (3.39), reveals the relations

$$\begin{aligned} S_{ii}^+ &= S_{ii}^- \quad \text{for } i \in \{x, y, z\} \\ S_{ij}^+ &= S_{ij}^- \quad \text{for } ij \in \{xz, zx\} \\ S_{ij}^+ &= -S_{ij}^- \quad \text{for } ij \in \{xy, zy, yx, yz\}. \end{aligned} \quad (A.17)$$

The $3n \times 3n$ matrix

$$\mathbf{L} := \begin{bmatrix} \mathbf{I} & \mathbf{0} & \mathbf{0} \\ \mathbf{0} & \mathbf{I} & \mathbf{0} \\ \mathbf{0} & \mathbf{0} & -\mathbf{I} \end{bmatrix} \quad \text{with } \mathbf{L} = \mathbf{L}^{-1}, \quad (A.18)$$

where \mathbf{I} is the $n \times n$ unit or identity matrix, relates \mathbf{S}^+ and \mathbf{S}^- via $\mathbf{S}^- = \mathbf{L}\mathbf{S}^+\mathbf{L}$. Inserting this into the second equation of (A.16) leads to

$$\begin{aligned}
 & \mathbf{L}\mathbf{S}^+\mathbf{L}\mathbf{G}^- + \mathbf{F} = \mathbf{0} \\
 \Leftrightarrow & \mathbf{S}^+\mathbf{L}\mathbf{G}^- + \mathbf{L}\mathbf{F} = \mathbf{0} \\
 \Leftrightarrow & \mathbf{S}^+\mathbf{L}\mathbf{G}^-\mathbf{L} + \mathbf{L}\mathbf{F}\mathbf{L} = \mathbf{0} \\
 \Leftrightarrow & \mathbf{S}^+\mathbf{L}\mathbf{G}^-\mathbf{L} + \mathbf{F} = \mathbf{0},
 \end{aligned} \tag{A.19}$$

where I used $\mathbf{L}\mathbf{F}\mathbf{L} = \mathbf{F}$ for the last equivalence. This means $\mathbf{G}^+ = \mathbf{L}\mathbf{G}^-\mathbf{L}$, that is the solution components \mathfrak{G}_{xx} , \mathfrak{G}_{zz} , \mathfrak{G}_{yy} , \mathfrak{G}_{xz} and \mathfrak{G}_{zx} are symmetric in k_y while the components \mathfrak{G}_{xy} , \mathfrak{G}_{yx} , \mathfrak{G}_{zy} and \mathfrak{G}_{yz} are antisymmetric in k_y . Thus, once the particular combination of source and receiver is specified, only the spectra for the positive wavenumbers need to be computed. The spectra for negative wavenumber values are determined from the odd or even symmetry.

Appendix B

Assembly of the complete finite element system matrix - from local to global

With the matrix entries given in equations (3.35), (3.36) and (3.39), the 12×12 elemental matrices defined in (3.18a) and (3.19a) are completely known, such that all that is left to do is to assemble them into the complete system matrix \mathbf{S} , defined in equation (3.45), to establish the global matrix equation (3.47) viz.

$$\mathbf{S}\mathbf{u} + \mathbf{f} = \mathbf{o}, \quad (\text{B.1})$$

which is the global version of the elemental equation 3.15.

Each row and each column of the sub-matrices $\mathbf{S}_{\zeta v}$ with $\zeta, v \in \{x, y, z\}$ (see equation (3.45)) corresponds to one model node. To find out where in this matrix the elemental matrix entries have to be placed, the correspondence between the global shape functions, defined on the global grid, and the shape functions defined locally by (3.11) on the corner nodes of the individual elements have to be found. For the example grid, these correspondences are shown in Figure B.1. Three different types of nodes need to be differentiated. Corner nodes (N_1, N_4, N_{13} and N_{16} in Figure B.1) belong to only one element, edge nodes (nodes $N_2, N_3, N_5, N_8, N_9, N_{12}, N_{14}$ and N_{15} in Figure B.1) take part in two different elements and interior nodes (nodes N_6, N_7, N_{10} and N_{11} in Figure B.1) are shared by four different elements. The global shape functions for corner nodes thus each correspond to one local shape function of one element. The global shape functions associated with edge nodes each correspond to one local shape function of each of the two adjacent elements. The global shape functions of the interior nodes each correspond to one local shape function of each of the four elements adjacent to the node. These equalities between the local and global shape functions define a mapping between local and global node indices. Since only neighbouring nodes interact, the majority of elements inside the global matrix \mathbf{S} is zero.

Starting from a matrix of all zeros, \mathbf{S} is assembled by performing the following steps for all elements:

- (1) Find the global indices i, j, k , and l of the corner nodes I, J, K , and L .
- (2) Add each of the 16 matrix entries of each of the nine sub-matrices of the elemental matrix (see equations 3.18a, 3.19a and 3.46) to the corresponding entry of the

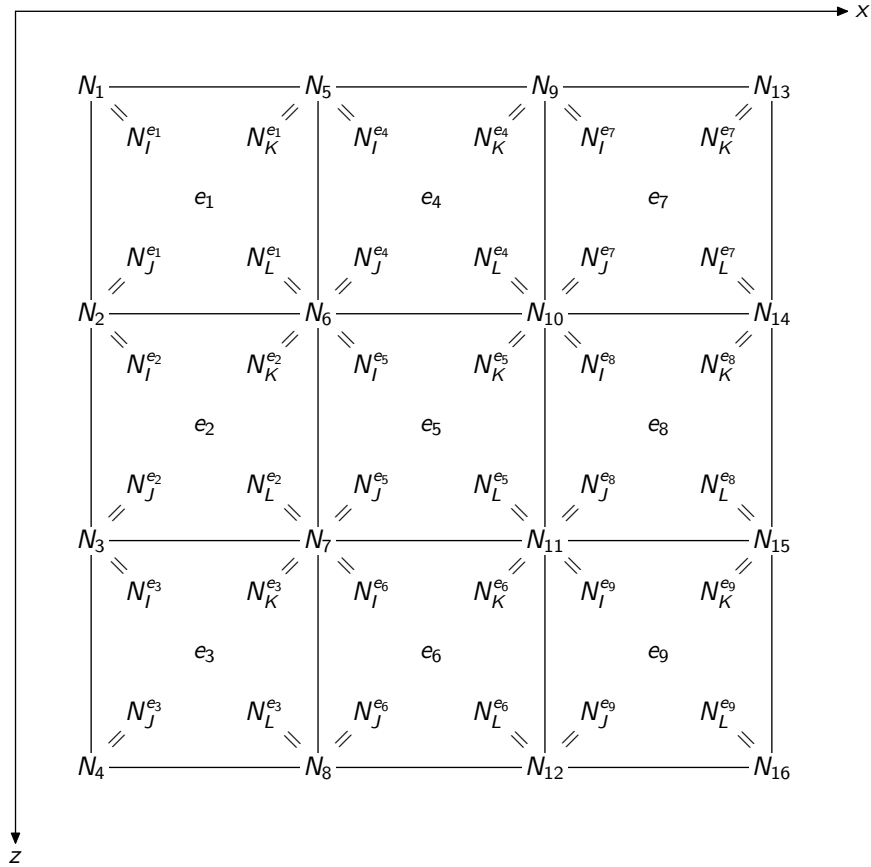


Figure B.1: Example of a FEM grid consisting of three by three elements and 16 nodes. The nodes are ordered in column major order and for each node the correspondence between the globally defined shape functions N_i and the local shape functions $N_A^{e_j}$ is shown, where $i \in [1, 16]$ is the global node index, $j \in [1, 9]$ is the element index and $A \in \{I, J, K, L\}$ is the local node index relative to the respective elements.

corresponding sub-matrix of the global matrix (see equation 3.45). The component S_{IJxz}^e of the elemental matrix for example has to be added to the entry S_{ijxz} of the global matrix.

To illustrate the structure of the resulting matrix, I zoom into a group of four adjacent elements, located in the interior of the FEM grid. The upper left corner of the top left element of this element group is located at global node i , as it is sketched in Figure B.2a. A snippet of one of the $n \times n$ sub-matrices, showing the rows and columns corresponding to the grid nodes shown in B.2a, can be found in Figure B.3. Using the colours introduced in Figure B.2, it shows which elemental matrix entries of the four elements contribute to which of the nonzero elements (depicted as black frames) of the global matrix. The entries in the main diagonal of the global matrix are the sum of four elemental matrix entries of four different elements. Two different elemental matrix entries contribute to the global matrix entries located in the diagonals $S_{i,i-n_z}$, $S_{i,i-1}$, $S_{i,i+1}$ and $S_{i,i+n_z}$. The entries in the four diagonals $S_{i,i-n_z-1}$, $S_{i,i-n_z+1}$, $S_{i,i+n_z-1}$ and $S_{i,i+n_z+1}$ consist of only one elemental matrix entry each, with the remaining elements of the sub-matrix being zero.

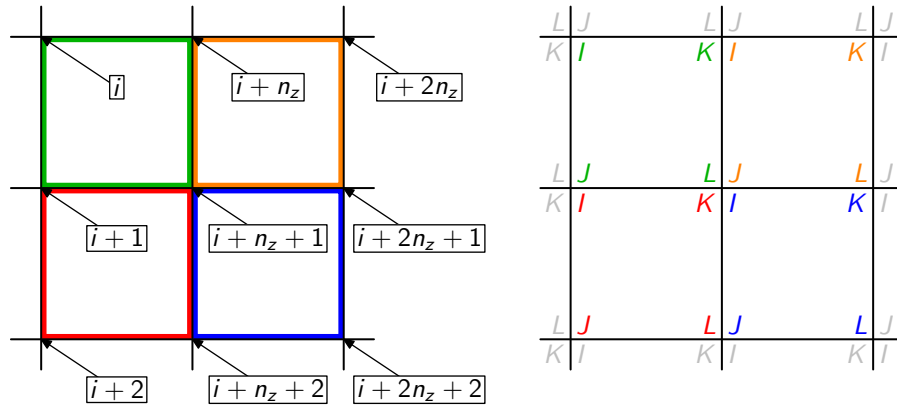


Figure B.2: Zoom into four elements of a FEM grid. The elements are colour coded to demonstrate the location of the corresponding elemental matrix entries in the global matrix in Figure B.3. (a) shows the global node indices of these elements in the FEM grid. The upper left corner of the element group is node i , the lower right corner lies at node $i + 2n_z + 2$. (b) depicts the local node indices I , J , K and L of the respective elements shown in (a).

As stated before, Figures B.2 and B.3 show the situation for four elements that belong to the interior of the FEM grid. Since nodes at the edges and corners of the grid have only three or two respective nearest neighbours the rows and columns of \mathbf{S} corresponding to such nodes have only six or four respective nonzero entries instead of nine.

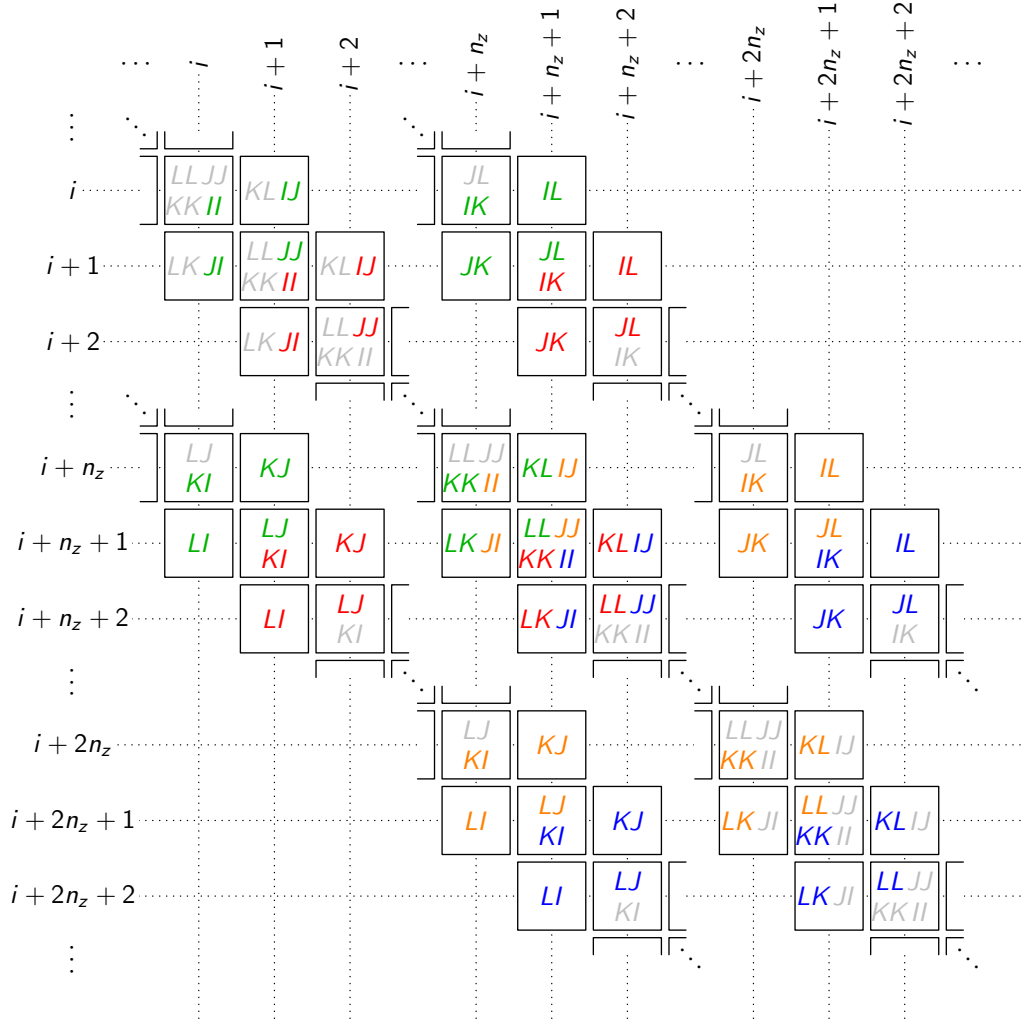


Figure B.3: Location of the elemental matrix entries in one of the $n \times n$ sub-matrices of the complete system matrix for the four elements shown in Figure B.2. The rows and columns of the matrix are indicated by dashed lines, each annotated with its corresponding global node index (see Figure B.2a). The nonzero elements of the matrix are shown as black frames, each containing the local node indices (see Figure B.2b) of the elemental matrix entries that contribute to the actual global entry. Coloured entries indicate which local node of which of the four elements shown in Figure B.2 corresponds to the given global matrix entry.

Appendix C

Time harmonic analytic Green's functions for a homogeneous isotropic unbounded domain

C.1 Acoustic approximation

The relevant equation of motion considered when solving under the acoustic approximation is the scalar Helmholtz equation

$$\nabla^2 G(\mathbf{x}; \mathbf{x}_s) + k_P^2 G(\mathbf{x}; \mathbf{x}_s) = -\delta(\mathbf{x} - \mathbf{x}_s), \quad (\text{C.1})$$

where $G(\mathbf{x}; \mathbf{x}_s)$ is the Green's function for a source at \mathbf{x}_s , $k_P = \omega/v_P$ is the wavenumber of a wave travelling with longitudinal wave velocity v_P . and $\omega = 2\pi f$ is the angular frequency.

C.1.1 Green's function for a homogeneous isotropic unbounded domain in the acoustic approximation in 2D

In 2D, the Green's function which solves (C.1) when restricting to waves travelling outward from the source position \mathbf{x}_s , is (see Achenbach, 1984, equation (3.155))

$$G(r) = \frac{i}{4} H_0^{(2)}(k_P r), \quad (\text{C.2})$$

where $H_0^{(2)}$ is the Hankel function of the second kind and zeroth order, $i = \sqrt{-1}$ is the imaginary unit and $r = |\mathbf{x} - \mathbf{x}_s|$ is the distance to the source point. (C.2) is also the solution for a line source in a 3D medium when r is taken to be the perpendicular distance to the infinite line sources (in y direction).

C.1.2 Green's function for a homogeneous isotropic unbounded domain in the acoustic approximation in 3D

In 3D, the Green's function which solves (C.1), also restricted to waves travelling outward from the source position \mathbf{x}_s is (see Achenbach, 1984, equation (3.147))

$$G(r) = \frac{1}{4\pi r} e^{-ik_P r}. \quad (\text{C.3})$$

with $i = \sqrt{-1}$ and r defined as in (C.2).

C.2 Elastic Green's tensor

To account for the vector character of the displacement field and the directivity of the source, in the elastic case the scalar Green's function is replaced by a second rank Green's tensor \mathbf{G} with components

$$G_{ij}(\mathbf{x}; \mathbf{x}_s), \quad (\text{C.4})$$

where i denotes the source direction, j the vector component of the displacement field and \mathbf{x}_s again denotes the source location.

C.2.1 Green's tensor for a homogeneous isotropic elastic unbounded domain in 2D

In the two-dimensional case, (C.4) is the solution for equations (3.2) with $k_y \equiv 0$, source vector $\mathbf{f} = \hat{\mathbf{e}}_i \delta(\mathbf{x} - \mathbf{x}_s)$ and $i, j \in \{x, z\}$. The expressions for the tensor components corresponding to a vertically directed source, i.e. those with z as the first subscript on G , are

$$\begin{aligned} G_{zx} &= \frac{\partial \phi^z}{\partial x} + \frac{\partial \psi^z}{\partial z} & \text{with} & & \phi^z &= -\frac{Q}{4\rho\omega^2} \frac{\partial}{\partial z} \left[-iH_0^{(2)}(k_P r) \right] \\ G_{zz} &= \frac{\partial \phi^z}{\partial z} + \frac{\partial \psi^z}{\partial x} & & & \psi^z &= \frac{Q}{4\rho\omega^2} \frac{\partial}{\partial x} \left[-iH_0^{(2)}(k_S r) \right] \end{aligned} \quad (\text{C.5})$$

as given by Båth (1968) in Chapter 12, equations [3] and [33]. Here, $k_P = \omega/v_P$ and $k_S = \omega/v_S$ are the wavenumbers corresponding to the P- and S-waves, ρ is the density, $r = |\mathbf{x} - \mathbf{x}_s|$ is the distance from the source, Q is a constant and $H_0^{(2)}$ is again the Hankel function of the second kind and zeroth order. For the tensor components corresponding to a horizontally directed source, i.e. those with x as the first subscript on G , one obtains

$$\begin{aligned} G_{xx} &= \frac{\partial \phi^x}{\partial x} + \frac{\partial \psi^x}{\partial z} & \text{with} & & \phi^x &= -\frac{Q}{4\rho\omega^2} \frac{\partial}{\partial x} \left[-iH_0^{(2)}(k_P r) \right] \\ G_{xz} &= \frac{\partial \phi^x}{\partial z} + \frac{\partial \psi^x}{\partial x} & & & \psi^x &= -\frac{Q}{4\rho\omega^2} \frac{\partial}{\partial z} \left[-iH_0^{(2)}(k_S r) \right] \end{aligned} \quad (\text{C.6})$$

following the derivation of (C.5) in Båth (1968), section 12.1.2.

Explicit expressions for the derivatives in equations (C.5) and (C.6) are

$$\frac{\partial \phi^x}{\partial x} = -i \frac{Q}{4\rho\omega^2} \frac{x^2}{r^2} \left\{ k_P^2 H_0^{(2)}(k_P r) - k_P r \left(\frac{2}{r^2} - \frac{1}{x^2} \right) H_1^{(2)}(k_P r) \right\} \quad (\text{C.7a})$$

$$\frac{\partial \phi^x}{\partial z} = -i \frac{Q}{4\rho\omega^2} \frac{xz}{r^2} \left\{ k_P^2 H_0^{(2)}(k_P r) - k_P \frac{2}{r} H_1^{(2)}(k_P r) \right\} \quad (\text{C.7b})$$

$$\frac{\partial \psi^x}{\partial x} = -i \frac{Q}{4\rho\omega^2} \frac{xz}{r^2} \left\{ k_S^2 H_0^{(2)}(k_S r) - k_S \frac{2}{r} H_1^{(2)}(k_S r) \right\} \quad (\text{C.7c})$$

$$\frac{\partial \psi^x}{\partial z} = -i \frac{Q}{4\rho\omega^2} \frac{x^2}{r^2} \left\{ k_S^2 H_0^{(2)}(k_S r) - k_S r \left(\frac{2}{r^2} - \frac{1}{z^2} \right) H_1^{(2)}(k_S r) \right\} \quad (\text{C.7d})$$

and

$$\frac{\partial \phi^x}{\partial x} = -i \frac{Q}{4\rho\omega^2} \frac{xz}{r^2} \left\{ k_P^2 H_0^{(2)}(k_P r) - k_P \frac{2}{r} H_1^{(2)}(k_P r) \right\} \quad (\text{C.7e})$$

$$\frac{\partial \phi^x}{\partial z} = -i \frac{Q}{4\rho\omega^2} \frac{z^2}{r^2} \left\{ k_P^2 H_0^{(2)}(k_P r) - k_P r \left(\frac{2}{r^2} - \frac{1}{z^2} \right) H_1^{(2)}(k_P r) \right\} \quad (\text{C.7f})$$

$$\frac{\partial \psi^x}{\partial x} = i \frac{Q}{4\rho\omega^2} \frac{z^2}{r^2} \left\{ k_S^2 H_0^{(2)}(k_S r) - k_S r \left(\frac{2}{r^2} - \frac{1}{z^2} \right) H_1^{(2)}(k_S r) \right\} \quad (\text{C.7g})$$

$$\frac{\partial \psi^x}{\partial z} = i \frac{Q}{4\rho\omega^2} \frac{xz}{r^2} \left\{ k_S^2 H_0^{(2)}(k_S r) - k_S \frac{2}{r} H_1^{(2)}(k_S r) \right\}. \quad (\text{C.7h})$$

Note that by introducing the dimensionless variables $\hat{r} := r/\lambda_S$, $\hat{x} := x/\lambda_S$ and $\hat{z} := z/\lambda_S$, where $\lambda_S = 2\pi/k_S$, the G_{ij} defined in equations (C.5) and (C.6) become frequency-independent (the frequency dependence is implicitly retained through the frequency dependent \hat{r} , \hat{x} and \hat{z}).

The terms in equation (C.7) are discontinuous at $r = 0$; their real parts go to infinity at this point but the discontinuity is removable in the case of the imaginary parts and one finds

$$\begin{aligned} \lim_{r \rightarrow 0} \Im \left(\frac{\partial \phi^x}{\partial x} \right) &= \frac{Q k_P^2}{4\rho\omega^2} \frac{k_P^2 x^2 - 4}{8} & \lim_{r \rightarrow 0} \Im \left(\frac{\partial \phi^x}{\partial x} \right) &= \frac{Q}{4\rho\omega^2} \frac{k_P^4 xz}{8} \\ \lim_{r \rightarrow 0} \Im \left(\frac{\partial \phi^x}{\partial z} \right) &= \frac{Q}{4\rho\omega^2} \frac{k_P^4 xz}{8} & \lim_{r \rightarrow 0} \Im \left(\frac{\partial \phi^x}{\partial z} \right) &= \frac{Q k_P^2}{4\rho\omega^2} \frac{k_P^2 z^2 - 4}{8} \\ \lim_{r \rightarrow 0} \Im \left(\frac{\partial \psi^x}{\partial x} \right) &= \frac{Q}{4\rho\omega^2} \frac{k_S^4 xz}{8} & \lim_{r \rightarrow 0} \Im \left(\frac{\partial \psi^x}{\partial x} \right) &= -\frac{Q k_S^2}{4\rho\omega^2} \frac{k_S^2 x^2 - 4}{8} \\ \lim_{r \rightarrow 0} \Im \left(\frac{\partial \psi^x}{\partial z} \right) &= \frac{Q k_S^2}{4\rho\omega^2} \frac{k_S^2 z^2 - 4}{8} & \lim_{r \rightarrow 0} \Im \left(\frac{\partial \psi^x}{\partial z} \right) &= -\frac{Q}{4\rho\omega^2} \frac{k_S^4 xz}{8}. \end{aligned} \quad \text{and} \quad (\text{C.8})$$

C.2.2 Green's tensor for a homogeneous isotropic elastic unbounded domain in 2.5D

The solutions for equations (3.2) for general k_y and source vectors of the form $\mathbf{f} = \frac{1}{\sqrt{2\pi}} f(\omega) \delta(x - x_s) \delta(z - z_s) e^{-ik_y y_s} \hat{\mathbf{e}}_i$ are the components of the Green's tensor in 2.5D. Explicit expressions are given by Tadeu and Kausel (2000). Adapting them to my situation, that is a Fourier transform with respect to y instead of z and using the definition given in (A.2), leads to

$$G_{xx} = -i \frac{\bar{Q}}{4\rho\omega^2} \left\{ k_S^2 H_0^{(2)}(k_\beta r) - \frac{1}{r} B_1 + \gamma_x^2 B_2 \right\} \quad (\text{C.9a})$$

$$G_{zz} = -i \frac{\bar{Q}}{4\rho\omega^2} \left\{ k_S^2 H_0^{(2)}(k_\beta r) - \frac{1}{r} B_1 + \gamma_z^2 B_2 \right\} \quad (\text{C.9b})$$

$$G_{yy} = -i \frac{\bar{Q}}{4\rho\omega^2} \left\{ k_S^2 H_0^{(2)}(k_\beta r) - k_y^2 B_0 \right\} \quad (\text{C.9c})$$

$$G_{xy} = G_{yx} = i \frac{\bar{Q}}{4\rho\omega^2} \{ i k_y \gamma_x B_1 \} \quad (\text{C.9d})$$

$$G_{zy} = G_{yz} = i \frac{\bar{Q}}{4\rho\omega^2} \{ i k_y \gamma_z B_1 \} \quad (\text{C.9e})$$

$$G_{xz} = G_{zx} = -i \frac{\bar{Q}}{4\rho\omega^2} \{ \gamma_x \gamma_z B_2 \}, \quad (\text{C.9f})$$

where

$$\gamma_x = \frac{x}{r} \quad \text{and} \quad \gamma_z = \frac{z}{r} \quad (\text{C.10})$$

are the direction cosines. I have introduced the definitions

$$B_n := k_\beta^n H_n^{(2)}(k_\beta r) - k_\alpha^n H_n^{(2)}(k_\alpha r), \quad n \in \{0, 1, 2\}. \quad (\text{C.11})$$

The modified wavenumbers k_α and k_β are defined as

$$k_\alpha := \sqrt{k_p^2 - k_y^2} \quad \text{and} \quad k_\beta := \sqrt{k_S^2 - k_y^2} \quad (\text{C.12})$$

using the branch $\Im m(k_{\alpha,\beta}) < 0$ with negative imaginary part. For $k_y \equiv 0$, the G_{xj} and G_{zj} for $j \in \{x, z\}$ in equations (C.9) reduce to the terms given in equations (C.6) and (C.5), respectively, with $\bar{Q} = Q/\sqrt{2\pi}$ to take account for the different source terms.

To aid the analysis of the behaviour with respect to k_y of the tensor components given in equations (C.9), I split them up into two parts. The first part, representing the P -wave, is given by

$$G_{xx}^P = -i \frac{\bar{Q}}{4\rho\omega^2} \left\{ \frac{k_\alpha}{r} H_1^{(2)}(k_\alpha r) - \gamma_x^2 k_\alpha^2 H_2^{(2)}(k_\alpha r) \right\} \quad (\text{C.13a})$$

$$G_{zz}^P = -i \frac{\bar{Q}}{4\rho\omega^2} \left\{ \frac{k_\alpha}{r} H_1^{(2)}(k_\alpha r) - \gamma_z^2 k_\alpha^2 H_2^{(2)}(k_\alpha r) \right\} \quad (\text{C.13b})$$

$$G_{yy}^P = -i \frac{\bar{Q}}{4\rho\omega^2} \left\{ k_y^2 H_0^{(2)}(k_\alpha r) \right\} \quad (\text{C.13c})$$

$$G_{xy}^P = G_{yx}^P = \frac{\bar{Q}}{4\rho\omega^2} k_y \gamma_x k_\alpha H_1^{(2)}(k_\alpha r) \quad (\text{C.13d})$$

$$G_{zy}^P = G_{yz}^P = \frac{\bar{Q}}{4\rho\omega^2} k_y \gamma_z k_\alpha H_1^{(2)}(k_\alpha r) \quad (\text{C.13e})$$

$$G_{xz}^P = G_{zx}^P = i \frac{\bar{Q}}{4\rho\omega^2} \gamma_x \gamma_z k_\alpha^2 H_2^{(2)}(k_\alpha r) \quad (\text{C.13f})$$

and the second part, representing the S -wave, is given by

$$G_{xx}^S = -i \frac{\bar{Q}}{4\rho\omega^2} \left\{ k_S^2 H_0^{(2)}(k_\beta r) - \frac{k_\beta}{r} H_1^{(2)}(k_\beta r) + \gamma_x^2 k_\beta^2 H_2^{(2)}(k_\beta r) \right\} \quad (\text{C.14a})$$

$$G_{zz}^S = -i \frac{\bar{Q}}{4\rho\omega^2} \left\{ k_S^2 H_0^{(2)}(k_\beta r) - \frac{k_\beta}{r} H_1^{(2)}(k_\beta r) + \gamma_z^2 k_\beta^2 H_2^{(2)}(k_\beta r) \right\} \quad (C.14b)$$

$$G_{yy}^S = -i \frac{\bar{Q}}{4\rho\omega^2} \left\{ k_S^2 H_0^{(2)}(k_\beta r) - k_y^2 H_0^{(2)}(k_\beta r) \right\} \quad (C.14c)$$

$$G_{xy}^S = G_{yx}^S = -\frac{\bar{Q}}{4\rho\omega^2} k_y \gamma_x k_\beta H_1^{(2)}(k_\beta r) \quad (C.14d)$$

$$G_{zy}^S = G_{yz}^S = -\frac{\bar{Q}}{4\rho\omega^2} k_y \gamma_z k_\beta H_1^{(2)}(k_\beta r) \quad (C.14e)$$

$$G_{xz}^S = G_{zx}^S = -i \frac{\bar{Q}}{4\rho\omega^2} \gamma_x \gamma_z k_\beta^2 H_2^{(2)}(k_\beta r) \quad (C.14f)$$

The tensor components in equations (C.9), (C.13) and (C.14) are related by $G_{ij} = G_{ij}^P + G_{ij}^S$ for $i, j \in \{x, y, z\}$.

C.2.3 Green's tensor for a homogeneous isotropic elastic unbounded domain in 3D

The Green's tensor in a three-dimensional medium can be written in the frequency domain as (e.g. Aki and Richards, 2009, equation (4.35))

$$G_{ij} = \frac{\bar{Q}}{4\pi\rho} \left\{ \underbrace{\frac{e^{-\frac{i\omega r}{v_P}}}{v_P^2 r} \left[\gamma_i \gamma_j + (3\gamma_i \gamma_j - \delta_{ij}) \left(\frac{v_P}{i\omega r} + \left(\frac{v_P}{i\omega r} \right)^2 \right) \right]}_{\text{P-wave}} - \underbrace{\frac{e^{-\frac{i\omega r}{v_S}}}{v_S^2 r} \left[\gamma_i \gamma_j + (3\gamma_i \gamma_j - \delta_{ij}) \left(\frac{v_S}{i\omega r} + \left(\frac{v_S}{i\omega r} \right)^2 \right) \right]}_{\text{S-wave}} \right\}, \quad (C.15)$$

with $i, j \in \{x, y, z\}$ and the γ_i defined as given in equation (C.10), which is the solution for (3.1) for the source term $\mathbf{f} = \hat{\mathbf{e}}_i \delta(\mathbf{x} - \mathbf{x}_s)$.

Appendix D

Gauss Newton type iterative local optimisation algorithms

Greenhalgh et al. (2006) give a very good overview of different local optimisation schemes used by the geophysical community and how these algorithms are related to each other; based on this overview and the ideas about model resolution presented in Ory and Pratt (1995), I will give a short summary of Gauss-Newton type local optimisation algorithms and how the corresponding model resolution capability can be assessed.

D.1 Norm definitions

Define the norm of the data space \mathcal{D} for $\mathfrak{d} \in \mathcal{D}$ as

$$\|\mathfrak{d}\|_D := \mathfrak{d}^T \underbrace{\mathbf{W}_D^T \mathbf{W}_D}_{\hat{\mathbf{W}}_D} \mathfrak{d} \quad (\text{D.1})$$

with data weighting operator $\hat{\mathbf{W}}_D$ and the norm of the model space \mathcal{M} for $\mathfrak{m} \in \mathcal{M}$ as

$$\|\mathfrak{m}\|_M := \mathfrak{m}^T \underbrace{\mathbf{W}_M^T \mathbf{W}_M}_{\hat{\mathbf{W}}_M} \mathfrak{m} \quad (\text{D.2})$$

with model parameter weighting operator $\hat{\mathbf{W}}_M$.

D.2 Different guises of the Gauss-Newton Algorithm

Our goal is to find a set of model parameters \mathfrak{m} that minimises

$$\|\mathfrak{d}_0 - \mathfrak{d}(\mathfrak{m})\|_D + \lambda \|\mathfrak{m} - \mathfrak{m}^0\|_M \quad (\text{D.3a})$$

or

$$\|\mathfrak{d}_0 - \mathfrak{d}(\mathfrak{m})\|_D + \lambda \|\mathfrak{m}\|_M. \quad (\text{D.3b})$$

Using the objective function (D.3a) tied to an apriori model \mathbf{m}^0 we find four possibilities for iteration schemes, which can be written as

$$\mathbf{m}^{k+1} = \mathbf{m}^0 + \left[\hat{\mathbf{W}}_M^{-1} \mathbf{J}^k \hat{\mathbf{W}}_D \mathbf{J}^k + \lambda \mathbf{1} \right]^{-1} \hat{\mathbf{W}}_M^{-1} \mathbf{J}^k \hat{\mathbf{W}}_D [\mathfrak{d}_0 - \mathfrak{d}(\mathbf{m}^k) + \mathbf{J}^k (\mathbf{m}^k - \mathbf{m}^0)] \quad (\text{D.4a})$$

$$\mathbf{m}^{k+1} = \mathbf{m}^0 + \left[\mathbf{J}^k \hat{\mathbf{W}}_D \mathbf{J}^k + \lambda \hat{\mathbf{W}}_M \right]^{-1} \mathbf{J}^k \hat{\mathbf{W}}_D [\mathfrak{d}_0 - \mathfrak{d}(\mathbf{m}^k) + \mathbf{J}^k (\mathbf{m}^k - \mathbf{m}^0)] \quad (\text{D.4b})$$

$$\mathbf{m}^{k+1} = \mathbf{m}^k + \left[\hat{\mathbf{W}}_M^{-1} \mathbf{J}^k \hat{\mathbf{W}}_D \mathbf{J}^k + \lambda \mathbf{1} \right]^{-1} \left\{ \hat{\mathbf{W}}_M^{-1} \mathbf{J}^k \hat{\mathbf{W}}_D [\mathfrak{d}_0 - \mathfrak{d}(\mathbf{m}^k)] + \lambda (\mathbf{m}^k - \mathbf{m}^0) \right\} \quad (\text{D.4c})$$

$$\mathbf{m}^{k+1} = \mathbf{m}^k + \left[\mathbf{J}^k \hat{\mathbf{W}}_D \mathbf{J}^k + \lambda \hat{\mathbf{W}}_M \right]^{-1} \left\{ \mathbf{J}^k \hat{\mathbf{W}}_D [\mathfrak{d}_0 - \mathfrak{d}(\mathbf{m}^k)] + \lambda \hat{\mathbf{W}}_M (\mathbf{m}^k - \mathbf{m}^0) \right\}. \quad (\text{D.4d})$$

If we do not require that the solution be close to an à priori model \mathbf{m}^0 then we use (D.3b) and find

$$\mathbf{m}^{k+1} = \left[\hat{\mathbf{W}}_M^{-1} \mathbf{J}^k \hat{\mathbf{W}}_D \mathbf{J}^k + \lambda \mathbf{1} \right]^{-1} \hat{\mathbf{W}}_M^{-1} \mathbf{J}^k \hat{\mathbf{W}}_D [\mathfrak{d}_0 - \mathfrak{d}(\mathbf{m}^k) + \mathbf{J}^k \mathbf{m}^k] \quad (\text{D.5a})$$

$$\mathbf{m}^{k+1} = \left[\mathbf{J}^k \hat{\mathbf{W}}_D \mathbf{J}^k + \lambda \hat{\mathbf{W}}_M \right]^{-1} \mathbf{J}^k \hat{\mathbf{W}}_D [\mathfrak{d}_0 - \mathfrak{d}(\mathbf{m}^k) + \mathbf{J}^k \mathbf{m}^k] \quad (\text{D.5b})$$

$$\mathbf{m}^{k+1} = \mathbf{m}^k + \left[\hat{\mathbf{W}}_M^{-1} \mathbf{J}^k \hat{\mathbf{W}}_D \mathbf{J}^k + \lambda \mathbf{1} \right]^{-1} \left\{ \hat{\mathbf{W}}_M^{-1} \mathbf{J}^k \hat{\mathbf{W}}_D [\mathfrak{d}_0 - \mathfrak{d}(\mathbf{m}^k)] + \lambda \mathbf{m}^k \right\} \quad (\text{D.5c})$$

$$\mathbf{m}^{k+1} = \mathbf{m}^k + \left[\mathbf{J}^k \hat{\mathbf{W}}_D \mathbf{J}^k + \lambda \hat{\mathbf{W}}_M \right]^{-1} \left\{ \mathbf{J}^k \hat{\mathbf{W}}_D [\mathfrak{d}_0 - \mathfrak{d}(\mathbf{m}^k)] + \lambda \hat{\mathbf{W}}_M \mathbf{m}^k \right\}. \quad (\text{D.5d})$$

D.3 Model resolution

If we assume there is a true model \mathbf{m}^{true} such that $\mathfrak{d}_0 = \mathfrak{d}(\mathbf{m}^{\text{true}})$ and set $\mathbf{m}^k = \mathbf{m}^{\text{true}}$ in (D.4) we find for the model \mathbf{m}^{est} estimated by the algorithm

$$\delta \mathbf{m}^{\text{est}} = \left[\hat{\mathbf{W}}_M^{-1} \mathbf{J}^k \hat{\mathbf{W}}_D \mathbf{J}^k + \lambda \mathbf{1} \right]^{-1} \hat{\mathbf{W}}_M^{-1} \mathbf{J}^k \hat{\mathbf{W}}_D \mathbf{J}^k \delta \mathbf{m}^{\text{true}} \quad (\text{D.6a})$$

$$\delta \mathbf{m}^{\text{est}} = \left[\mathbf{J}^k \hat{\mathbf{W}}_D \mathbf{J}^k + \lambda \hat{\mathbf{W}}_M \right]^{-1} \mathbf{J}^k \hat{\mathbf{W}}_D \mathbf{J}^k \delta \mathbf{m}^{\text{true}}, \quad (\text{D.6b})$$

where we define $\delta \mathbf{m}^{\text{est}} = \mathbf{m}^{\text{est}} - \mathbf{m}^0$ and $\delta \mathbf{m}^{\text{true}} = \mathbf{m}^{\text{true}} - \mathbf{m}^0$. If instead we use (D.5), we get

$$\mathbf{m}^{\text{est}} = \left[\hat{\mathbf{W}}_M^{-1} \mathbf{J}^k \hat{\mathbf{W}}_D \mathbf{J}^k + \lambda \mathbf{1} \right]^{-1} \hat{\mathbf{W}}_M^{-1} \mathbf{J}^k \hat{\mathbf{W}}_D \mathbf{J}^k \mathbf{m}^{\text{true}} \quad (\text{D.7a})$$

$$\mathbf{m}^{\text{est}} = \left[\mathbf{J}^k \hat{\mathbf{W}}_D \mathbf{J}^k + \lambda \hat{\mathbf{W}}_M \right]^{-1} \mathbf{J}^k \hat{\mathbf{W}}_D \mathbf{J}^k \mathbf{m}^{\text{true}} \quad (\text{D.7b})$$

for the model estimated from the true model.

Equations (D.6) and (D.7) can be abbreviated as

$$\begin{aligned} \delta \mathbf{m}^{\text{est}} &= \mathbf{R}^M \delta \mathbf{m}^{\text{true}} \\ \mathbf{m}^{\text{est}} &= \mathbf{R}^M \mathbf{m}^{\text{true}}, \end{aligned} \quad (\text{D.8})$$

which defines the model resolution matrix \mathbf{R}^M . It relates the true model and the estimated model that our algorithm would return given the true model as an input.

From equations (D.6a) and (D.7a) we find

$$\mathbf{R}^M = \left[\hat{\mathbf{W}}_M^{-1} \mathbf{J}^k \hat{\mathbf{W}}_D \mathbf{J}^k + \lambda \mathbf{1} \right]^{-1} \hat{\mathbf{W}}_M^{-1} \mathbf{J}^k \hat{\mathbf{W}}_D \mathbf{J}^k. \quad (\text{D.9})$$

Alternatively, from equations (D.6b) and (D.7b) we find

$$\mathbf{R}^M = \left[\mathbf{J}^k \hat{\mathbf{W}}_D \mathbf{J}^k + \lambda \hat{\mathbf{W}}_M \right]^{-1} \mathbf{J}^k \hat{\mathbf{W}}_D \mathbf{J}^k. \quad (\text{D.10})$$

Using a matrix formula called the Sherman-Morrison-Woodbury formula (see Golub and van Loan, 1996, page 50 formula (2.1.4)), we have

$$(\mathbf{U} \mathbf{V}^T + \mathbf{A})^{-1} = \mathbf{A}^{-1} - \left[\mathbf{A}^{-1} \mathbf{U} (\mathbf{1} + \mathbf{V}^T \mathbf{A}^{-1} \mathbf{U})^{-1} \mathbf{V}^T \mathbf{A}^{-1} \right] \quad (\text{D.11})$$

we can reconcile this issue. Since (D.9) and (D.10) match in the last three factors $\mathbf{J}^k \hat{\mathbf{W}}_D \mathbf{J}^k$, we only have to prove the equality of the first parts. We find

$$\begin{aligned} & \left(\mathbf{J}^k \hat{\mathbf{W}}_D \mathbf{J}^k + \lambda \hat{\mathbf{W}}_M \right)^{-1} \\ &= \frac{1}{\lambda} \left(\underbrace{\frac{1}{\lambda} \mathbf{J}^k \hat{\mathbf{W}}_D \mathbf{J}^k}_{\mathbf{U}} + \underbrace{\hat{\mathbf{W}}_M}_{\mathbf{A}} \right)^{-1} \\ &\stackrel{(\text{D.11})}{=} \frac{1}{\lambda} \left\{ \hat{\mathbf{W}}_M^{-1} - \left[\hat{\mathbf{W}}_M^{-1} \frac{1}{\lambda} \mathbf{J}^k \hat{\mathbf{W}}_D \mathbf{J}^k \hat{\mathbf{W}}_M^{-1} \frac{1}{\lambda} \mathbf{J}^k \hat{\mathbf{W}}_D \mathbf{J}^k \hat{\mathbf{W}}_M^{-1} \right] \right\} \\ &= \frac{1}{\lambda} \left\{ \mathbf{1} - \left[\hat{\mathbf{W}}_M^{-1} \frac{1}{\lambda} \mathbf{J}^k \hat{\mathbf{W}}_D \mathbf{J}^k \hat{\mathbf{W}}_M^{-1} \frac{1}{\lambda} \mathbf{J}^k \hat{\mathbf{W}}_D \mathbf{J}^k \right] \right\} \hat{\mathbf{W}}_M^{-1} \\ &= \left\{ \underbrace{(\lambda \mathbf{1})^{-1}}_{\mathbf{A}^{-1}} - \left[\underbrace{(\lambda \mathbf{1})^{-1} \hat{\mathbf{W}}_M^{-1} \mathbf{J}^k \hat{\mathbf{W}}_D \mathbf{J}^k}_{\mathbf{U}} \left(\mathbf{1} + \hat{\mathbf{W}}_D \mathbf{J}^k (\lambda \mathbf{1})^{-1} \hat{\mathbf{W}}_M^{-1} \mathbf{J}^k \right)^{-1} \underbrace{\hat{\mathbf{W}}_D \mathbf{J}^k}_{\mathbf{V}^T} \right] \right\} \hat{\mathbf{W}}_M^{-1} \\ &\stackrel{(\text{D.11})}{=} \left(\hat{\mathbf{W}}_M^{-1} \mathbf{J}^k \hat{\mathbf{W}}_D \mathbf{J}^k + \lambda \mathbf{1} \right)^{-1} \hat{\mathbf{W}}_M^{-1}. \end{aligned} \quad (\text{D.12})$$

Having established the equivalence, we will use

$$\mathbf{R}^M = \left[\mathbf{J}^k{}^T \hat{\mathbf{W}}_D \mathbf{J}^k + \lambda \hat{\mathbf{W}}_M \right]^{-1} \mathbf{J}^k{}^T \hat{\mathbf{W}}_D \mathbf{J}^k. \quad (\text{D.13})$$

since it is the more compact form.

Appendix E

Relation between sensitivities for different sets of parameters

E.1 Parameter sets in the elastic case

Some examples for parameter sets that are used in seismic waveform inversion are

SET 1 (v_P, v_S, ρ) ,

SET 2 (λ, μ, ρ) or

SET 3 (μ, κ, ρ) ,

or in words

SET 1 P-wave-velocity, S-wave velocity and density,

SET 2 Lamé parameters and density,

SET 3 Second Lamé parameter, compressibility modulus and density.

These parameter sets are linked by the relations (e.g. Smidt, 2009)

	SET 1 (v_P, v_S, ρ)	SET 2 (λ, μ, ρ)	SET 3 (μ, κ, ρ)
v_P	•	$\sqrt{\frac{\lambda+2\mu}{\rho}}$	$\sqrt{\frac{\kappa+\frac{4}{3}\mu}{\rho}}$
v_S	•	$\sqrt{\frac{\mu}{\rho}}$	$\sqrt{\frac{\mu}{\rho}}$
λ	$\rho(v_P^2 - 2v_S^2)$	•	$\kappa - \frac{2}{3}\mu$
μ	ρv_S^2	•	•
κ	$\rho(v_P^2 - \frac{4}{3}v_S^2)$	$\lambda + \frac{2}{3}\mu$	•

(E.1)

E.2 Partial derivatives

E.2.1 SET 1 with respect to SET 2

$$\frac{\partial v_P}{\partial \lambda} = \frac{1}{2} \frac{1}{\sqrt{\rho(\lambda + 2\mu)}} = \frac{1}{2\rho v_P} \quad (\text{E.2a})$$

$$\frac{\partial v_P}{\partial \mu} = \frac{1}{\sqrt{\rho(\lambda + 2\mu)}} = \frac{1}{\rho v_P} \quad (\text{E.2b})$$

$$\frac{\partial v_P}{\partial \rho} = \frac{1}{2\rho} \sqrt{\frac{\lambda + 2\mu}{\rho}} = \frac{v_P}{2\rho} \quad (\text{E.2c})$$

$$\frac{\partial v_S}{\partial \lambda} = 0 \quad (\text{E.2d})$$

$$\frac{\partial v_S}{\partial \mu} = \frac{1}{2} \frac{1}{\sqrt{\rho\mu}} = \frac{1}{2\rho v_S} \quad (\text{E.2e})$$

$$\frac{\partial v_S}{\partial \rho} = \frac{1}{2\rho} \sqrt{\frac{\mu}{\rho}} = \frac{v_S}{2\rho} \quad (\text{E.2f})$$

E.2.2 SET 2 with respect to SET 1

$$\frac{\partial \lambda}{\partial v_P} = 2\rho v_P = 2\sqrt{\rho(\lambda + 2\mu)} \quad (\text{E.3a})$$

$$\frac{\partial \lambda}{\partial v_S} = -4\rho v_S = -4\sqrt{\rho\mu} \quad (\text{E.3b})$$

$$\frac{\partial \lambda}{\partial \rho} = v_P^2 - 2v_S^2 = \frac{\lambda}{\rho} \quad (\text{E.3c})$$

$$\frac{\partial \mu}{\partial v_P} = 0 \quad (\text{E.3d})$$

$$\frac{\partial \mu}{\partial v_S} = 2\rho v_S = 2\sqrt{\rho\mu} \quad (\text{E.3e})$$

$$\frac{\partial \mu}{\partial \rho} = v_S^2 = \frac{\mu}{\rho} \quad (\text{E.3f})$$

E.2.3 SET 1 with respect to SET 3

$$\frac{\partial v_P}{\partial \kappa} = \frac{1}{2} \frac{1}{\sqrt{\rho(\kappa + \frac{4}{3}\mu)}} = \frac{1}{2\rho v_P} \quad (\text{E.4a})$$

$$\frac{\partial v_P}{\partial \mu} = \frac{2}{3} \frac{1}{\sqrt{\rho(\kappa + \frac{4}{3}\mu)}} = \frac{2}{3\rho v_P} \quad (\text{E.4b})$$

$$\frac{\partial v_P}{\partial \rho} = \frac{1}{2\rho} \sqrt{\frac{\kappa + \frac{4}{3}\mu}{\rho}} = \frac{v_P}{2\rho} \quad (\text{E.4c})$$

$$\frac{\partial v_S}{\partial \kappa} = 0 \quad (\text{E.4d})$$

$$\frac{\partial v_S}{\partial \mu} = \frac{1}{2} \frac{1}{\sqrt{\rho\mu}} = \frac{1}{2\rho v_S} \quad (\text{E.4e})$$

$$\frac{\partial v_S}{\partial \rho} = \frac{1}{2\rho} \sqrt{\frac{\mu}{\rho}} = \frac{v_S}{2\rho} \quad (\text{E.4f})$$

E.2.4 SET 3 with respect to SET 1

$$\frac{\partial \kappa}{\partial v_P} = 2\rho v_P = 2\sqrt{\rho(\kappa + \frac{4}{3}\mu)} \quad (\text{E.5a})$$

$$\frac{\partial \kappa}{\partial v_S} = -\frac{8}{3}\rho v_S = -\frac{8}{3}\sqrt{\rho\mu} \quad (\text{E.5b})$$

$$\frac{\partial \kappa}{\partial \rho} = v_P^2 - \frac{4}{3}v_S^2 = \frac{\kappa}{\rho} \quad (\text{E.5c})$$

$$\frac{\partial \mu}{\partial v_P} = 0 \quad (\text{E.5d})$$

$$\frac{\partial \mu}{\partial v_S} = 2\rho v_S = 2\sqrt{\rho\mu} \quad (\text{E.5e})$$

$$\frac{\partial \mu}{\partial \rho} = v_S^2 = \frac{\mu}{\rho} \quad (\text{E.5f})$$

E.2.5 Interrelating SET 2 with SET 3

$$\frac{\partial \lambda}{\partial \kappa} = 1 \quad \frac{\partial \lambda}{\partial \mu} = -\frac{2}{3} \quad \frac{\partial \lambda}{\partial \rho} = 0 \quad (\text{E.6})$$

$$\frac{\partial \kappa}{\partial \lambda} = 1 \quad \frac{\partial \kappa}{\partial \mu} = \frac{2}{3} \quad \frac{\partial \kappa}{\partial \rho} = 0 \quad (\text{E.7})$$

E.3 Relations between small perturbations

Considering small perturbations of the medium parameters, i.e. $(\delta v_P, \delta v_S, \delta \rho)$, $(\delta \lambda, \delta \mu, \delta \rho)$ and $(\delta \mu, \delta \kappa, \delta \rho)$ respectively, and remembering the interrelations of the different parameter sets given in (E.1), one can see how the parameters in the other sets change due

to perturbation of one certain parameter in another set. If terms of second and higher order in the perturbations are neglected, the perturbations are related via the following equations.

$$\left. \begin{aligned} \delta v_P &= \frac{\partial v_P}{\partial \lambda} \delta \lambda + \frac{\partial v_P}{\partial \mu} \delta \mu + \frac{\partial v_P}{\partial \rho} \delta \rho \\ \delta v_S &= \frac{\partial v_S}{\partial \mu} \delta \mu + \frac{\partial v_S}{\partial \rho} \delta \rho \end{aligned} \right\} \quad \text{SET 2} \rightarrow \text{SET 1} \quad (\text{E.8a})$$

$$\left. \begin{aligned} \delta v_P &= \frac{\partial v_P}{\partial \mu} \delta \mu + \frac{\partial v_P}{\partial \kappa} \delta \kappa + \frac{\partial v_P}{\partial \rho} \delta \rho \\ \delta v_S &= \frac{\partial v_S}{\partial \mu} \delta \mu + \frac{\partial v_S}{\partial \rho} \delta \rho \end{aligned} \right\} \quad \text{SET 3} \rightarrow \text{SET 1} \quad (\text{E.8b})$$

$$\left. \begin{aligned} \delta \kappa &= \frac{\partial \kappa}{\partial v_P} \delta v_P + \frac{\partial \kappa}{\partial v_S} \delta v_S + \frac{\partial \kappa}{\partial \rho} \delta \rho \\ \delta \mu &= \frac{\partial \mu}{\partial v_S} \delta v_S + \frac{\partial \mu}{\partial \rho} \delta \rho. \end{aligned} \right\} \quad \text{SET 1} \rightarrow \text{SET 3} \quad (\text{E.8c})$$

$$\left. \begin{aligned} \delta \lambda &= \frac{\partial \lambda}{\partial v_P} \delta v_P + \frac{\partial \lambda}{\partial v_S} \delta v_S + \frac{\partial \lambda}{\partial \rho} \delta \rho \\ \delta \mu &= \frac{\partial \mu}{\partial v_S} \delta v_S + \frac{\partial \mu}{\partial \rho} \delta \rho. \end{aligned} \right\} \quad \text{SET 1} \rightarrow \text{SET 2} \quad (\text{E.8d})$$

$$\left. \begin{aligned} \delta \kappa &= \frac{\partial \kappa}{\partial \mu} \delta \mu + \frac{\partial \kappa}{\partial \lambda} \delta \lambda + \frac{\partial \kappa}{\partial \rho} \delta \rho \\ \delta \lambda &= \frac{\partial \lambda}{\partial \mu} \delta \mu + \frac{\partial \lambda}{\partial \kappa} \delta \kappa + \frac{\partial \lambda}{\partial \rho} \delta \rho \end{aligned} \right\} \quad \text{SET 2} \leftrightarrow \text{SET 3} \quad (\text{E.8e})$$

E.4 Relations between sensitivities

After defining

$$D_{\mathbf{I}}^{\xi} \doteq \frac{\partial u}{\partial \xi} \quad \mathbf{I} \in \{1, 2, 3\} \quad (\text{E.9})$$

as a shorthand notation for the sensitivity of wave field component u with respect to parameter ξ belonging to **SET I**, the sensitivities with respect to parameters of the three sets have to fulfil the conditions

$$D_1^{v_P} \delta v_P + D_1^{v_S} \delta v_S + D_1^{\rho} \delta \rho \stackrel{!}{=} D_2^{\lambda} \delta \lambda + D_2^{\mu} \delta \mu + D_2^{\rho} \delta \rho \quad (\text{E.10a})$$

$$D_1^{v_P} \delta v_P + D_1^{v_S} \delta v_S + D_1^{\rho} \delta \rho \stackrel{!}{=} D_3^{\kappa} \delta \kappa + D_3^{\mu} \delta \mu + D_3^{\rho} \delta \rho \quad (\text{E.10b})$$

$$D_2^{\lambda} \delta \lambda + D_2^{\mu} \delta \mu + D_2^{\rho} \delta \rho \stackrel{!}{=} D_3^{\kappa} \delta \kappa + D_3^{\mu} \delta \mu + D_3^{\rho} \delta \rho. \quad (\text{E.10c})$$

Inserting (E.8) in (E.10) leads to

$$\begin{aligned}
 D_1^{vp} &= \frac{\partial \lambda}{\partial v_P} D_2^\lambda \\
 D_1^{vs} &= \frac{\partial \lambda}{\partial v_S} D_2^\lambda + \frac{\partial \mu}{\partial v_S} D_2^\mu \\
 D_1^\rho &= \frac{\partial \lambda}{\partial \rho} D_2^\lambda + \frac{\partial \mu}{\partial \rho} D_2^\mu + D_2^\rho
 \end{aligned} \tag{E.11}$$

$$\begin{aligned}
 D_2^\lambda &= \frac{\partial v_P}{\partial \lambda} D_1^{vp} \\
 D_2^\mu &= \frac{\partial v_P}{\partial \mu} D_1^{vp} + \frac{\partial v_S}{\partial \mu} D_1^\mu \\
 D_2^\rho &= \frac{\partial v_P}{\partial \rho} D_1^{vp} + \frac{\partial v_S}{\partial \rho} D_1^\mu + D_1^\rho
 \end{aligned} \tag{E.12}$$

$$\begin{aligned}
 D_1^{vp} &= \frac{\partial \kappa}{\partial v_P} D_3^\kappa \\
 D_1^{vs} &= \frac{\partial \kappa}{\partial v_S} D_3^\kappa + \frac{\partial \mu}{\partial v_S} D_3^\mu \\
 D_1^\rho &= \frac{\partial \kappa}{\partial \rho} D_3^\kappa + \frac{\partial \mu}{\partial \rho} D_3^\mu + D_3^\rho
 \end{aligned} \tag{E.13}$$

$$\begin{aligned}
 D_3^\kappa &= \frac{\partial v_P}{\partial \kappa} D_1^{vp} \\
 D_3^\mu &= \frac{\partial v_P}{\partial \mu} D_1^{vp} + \frac{\partial v_S}{\partial \mu} D_1^\mu \\
 D_3^\rho &= \frac{\partial v_P}{\partial \rho} D_1^{vp} + \frac{\partial v_S}{\partial \rho} D_1^\mu + D_1^\rho
 \end{aligned} \tag{E.14}$$

and

$$\begin{aligned}
 D_3^\kappa &= D_2^\lambda \\
 D_3^\mu &= D_2^\mu - \frac{2}{3} D_2^\lambda \\
 D_3^\rho &= D_2^\rho.
 \end{aligned} \tag{E.15}$$

Appendix F

Frequency and spatial sampling strategies for crosshole seismic waveform spectral inversion experiments

Hansruedi Maurer, Stewart Greenhalgh, Sabine Latzel

GEOPHYSICS, VOL. 74, NO. 6 NOVEMBER-DECEMBER 2009; P.WCC11WCC21

Abstract

Analyses of synthetic frequency-domain acoustic waveform data provide new insights into the design and imaging capability of crosshole surveys. We show that the full complex Fourier spectral data offer significantly more information than other data representations such as the amplitude, phase or Hartley spectrum. By means of extensive eigenvalue

analyses we further inspect the information content offered by the seismic data. The goodness of different experimental configurations is investigated by varying the choice of (i) the frequencies, (ii) the source and receiver spacings along the boreholes, and (iii) the borehole separation. It is demonstrated that with only a few carefully chosen frequencies a similar amount of information can be extracted from the seismic data as with a much larger suite of equally spaced frequencies. Optimized data sets should include at least one very low frequency component. The remaining frequencies should be chosen from the upper end of the spectrum available. This strategy proved to be applicable to a simple homogeneous and a very complex velocity model. Further tests are required, but it appears on the available evidence to be model-independent. Source and receiver spacings also have an effect on the goodness of an experimental setup, but we show that there are only minor benefits to denser sampling when the increment is much smaller than the shortest wavelength included in a data set. If the borehole separation becomes unfavorably large, the information content of the data is degraded, even when many frequencies and small source and receiver spacings are considered. Our findings are based on eigenvalue analyses using the true velocity models. Since under realistic conditions the true model is not known, we demonstrate that the optimized data sets are sufficiently robust, such that they allow the iterative inversion schemes to converge to the global minimum. This is demonstrated by means of tomographic inversions of several optimized data sets.

Introduction

Seismic tomography is a powerful and versatile tool for a wide range of imaging applications in the earth sciences. Crosshole techniques are of particular interest for shallow and intermediate target depths. So far, the vast majority of applications reported in the literature have considered ray-based methods, in which arrival times and possibly amplitudes have been inverted for subsurface velocity and attenuation parameters (e.g. Lehmann, 2007, and references therein).

In the middle 1980s, full waveform inversion schemes that exploit the full information content offered by the seismic data were devised (e.g. Tarantola, 1984; Mora, 1987). Unfortunately, the computing resources at that time did not allow these time-domain schemes to be applied to realistic problems. To ease the computational burden, a number of frequency-domain inversion schemes were proposed (e.g. Pratt, 1999; Zhou and Greenhalgh, 2003; Greenhalgh and Zhou, 2004). They considered only a few frequencies during the inversions. This approach provided tomographic images that were comparable to their time-domain counterparts, but at substantially lower computational costs. The success of frequency-domain inversions is primarily based on the fact that most seismic data are band-limited, such that only a limited number of frequencies are required for characterizing the entire waveforms.

During the course of the seemingly continuously increasing computing power, particularly through the availability of affordable computer clusters, both time- and frequency-domain waveform inversion schemes experienced a rapid increase in popularity over the past few years. The recent literature includes a plethora of synthetic studies (e.g. Plessix,

2008, and references therein), and it is expected that the number of publications on applications to field data will increase in the near future.

The numerous synthetic studies have demonstrated quite impressively the general superiority of waveform inversions over ray-based traveltimes inversions, but less attention has been paid so far to optimized survey designs of waveform inversion experiments. Critical parameters to be determined for frequency-domain waveform inversion surveys include

- selection of frequencies,
- source and receiver spacings, and
- borehole separations for crosshole surveys.

The spacings of the sensor elements and the borehole separations can usually be freely chosen for a particular survey in the light of target dimensions and available recording channels, but the choice of frequencies can be limited by the subsurface conditions and/or may be constrained by the source and instrument characteristics. It is therefore particularly important to know upfront the useful portions of the frequency spectrum before the final decision for conducting an experiment is made or the costs for buying/leasing specialized equipment are incurred. An approach for selecting frequencies has been proposed by Sirgue and Pratt (2004) for surface-based surveys and by Yokota and Matsushima (2003) for crosshole experiments. They devised strategies for selecting frequencies on the basis of the maximum spatial wavenumbers connected with a particular survey design. The influence of spatial sampling has been investigated by Brenders and Pratt (2007), but to the best of our knowledge, no quantitative survey design studies have been performed that consider source and receiver spacing and borehole separation in the context of frequency-domain waveform inversions of crosshole data.

In this paper we investigate options for optimizing frequency-domain crosshole seismic experiments using statistical experimental design. These techniques were introduced to geophysics by Curtis and Snieder (1997), Maurer and Boerner (1998a), Curtis (1999) and Maurer et al. (2000), who formulated survey design as an optimization problem using measures from linear inversion theory. This provided a general framework for analyzing a wide range of survey types and data acquisition parameters, and is thus also amenable for our present purposes.

In the first part of the paper, we briefly describe our waveform inversion approach, followed by an introduction to the particular objective function used, by which the goodness of a particular survey design can be quantified. Then, we investigate model dependencies and the suitability of different representations of frequency-domain data. Subsequently, we present different strategies for selecting frequencies and source and receiver spacings. Finally, our findings are tested by means of synthetic data inversions.

Frequency-domain waveform inversions

As with many linearized least-squares inversion schemes, our algorithm includes a forward solver F that predicts (computes) the complex-valued frequency-domain data $\mathfrak{d}^{\text{pred}}$ for a particular subsurface model \mathfrak{m}

$$\mathfrak{d}^{\text{pred}} = F(\mathfrak{m}) \quad (\text{F.1})$$

and a corresponding inverse operator

$$\mathbf{m}^{\text{est}} = F^{-1} (\mathfrak{d}^{\text{obs}} - \mathfrak{d}^{\text{pred}}), \quad (\text{F.2})$$

which estimates the subsurface medium parameters \mathbf{m}^{est} from the observed data $\mathfrak{d}^{\text{obs}}$. Here, we make several simplifying assumptions to ease the calculations and to gain more direct insight. For the forward operator, we employ an acoustic approximation to the elastic wave equation and assume constant density throughout the medium, such that the model parameter vector \mathbf{m} includes only the P-wave velocities. Furthermore, only 2D wave propagation (line source) is considered. Point source (2.5D or 3D modeling) would add to the computational effort considerably. Finally, we assume the source functions to be known. It is, however, important to note that these assumptions are only applied for the reasons given above, and in no way invalidate the generality of the approach; the concepts presented in this paper can be readily extended to the 2.5D or 3D elastic problems or to the visco-elastic case including anisotropy, and to simultaneous inversions of subsurface parameters and source functions.

Our forward operator F solves the 2D acoustic problem using a simple frequency-domain structured grid finite-element approximation. For further details see Zhou and Greenhalgh (1998a). The subsurface is discretized with a regular grid of linear rectangular elements. Perfectly matched layer boundary conditions are implemented (Heikkola et al., 2003) and the system matrix is solved using the direct matrix solver PARDISO (Schenk et al., 2002). This allows efficient computations of the pressure spectral wavefields for a large number of sources.

As noted by Pratt et al. (1998) and others, a Gauss-Newton approximation of the inverse operator F^{-1} allows often faster convergence of the iterative inversion procedure than the more traditional conjugate-gradient back-propagation approaches. Our Gauss-Newton type inverse operator F^{-1} can be written as

$$\mathbf{m}_{i+1}^{\text{est}} = (\mathbf{J}^T \mathbf{J} + \mathbf{C}_M^{-1})^{-1} \mathbf{J}^T [(\mathfrak{d}^{\text{obs}} - \mathfrak{d}^{\text{pred}}) + \mathbf{J} \mathbf{m}_i^{\text{est}}], \quad (\text{F.3})$$

where \mathbf{J} is the Jacobian matrix the elements of which are the sensitivities or Fréchet derivatives, i is the iteration number ($\mathbf{m}_0^{\text{est}}$ is the initial model); and \mathbf{C}_M^{-1} is the à priori model covariance matrix, which allows regularization constraints, such as damping and smoothing, to be supplied (e.g. Maurer et al., 1998). An L2 norm misfit objective function is implicit in equation (F.3).

It has been argued (e.g. Tarantola, 2005) that conjugate gradient methods are computationally more efficient than Gauss-Newton algorithms, because they do not require the Jacobian matrix to be computed explicitly. However, the sensitivities in \mathbf{J} can be computed swiftly using the explicit expressions published by Zhou and Greenhalgh (1999). Furthermore, the matrix $\mathbf{J}^T \mathbf{J}$ and the vector $\mathbf{J}^T [(\mathfrak{d}^{\text{obs}} - \mathfrak{d}^{\text{pred}}) + \mathbf{J} \mathbf{m}_i^{\text{est}}]$ in equation (F.3) can be accumulated sequentially (e.g. Sheen et al., 2006), such that the only limiting factor in terms of computer memory is the number of model parameters in \mathbf{m} , which determines the dimension of $\mathbf{J}^T \mathbf{J}$. For 3D problems \mathbf{m} can be very large, which may require other inversion schemes to be considered. The inversion runs shown in the last part of this paper typically converged after 10 to 20 iterations.

Experimental design

Over the past few decades, major efforts have been made to improve the efficiency of numerical forward modeling and inversion algorithms for geophysical data. In contrast, surprisingly few studies on optimized design of geophysical experiments have been published (Maurer and Boerner, 1998b). This is unfortunate, since the information content offered by a geophysical data set is inherently limited by the reliability of the inversion models.

It is our goal to identify survey layouts with optimized benefit/cost ratios. Costs are typically associated with the number of source and receiver positions. In seismic waveform tomography there are additional costs to consider, which may be related to the frequency bandwidth of the seismic sources and the receiver instrumentation.

Since waveform tomography algorithms are based on linearized inversion theory, we consider corresponding measures for quantifying the benefits of a particular survey (e.g. Menke, 1989). The choice of a survey layout governs the structure of the Jacobian matrix \mathbf{J} , and close inspection of equation (F.3) indicates that the reliability of the parameter estimates \mathbf{m}^{est} depends primarily on our ability to invert the matrix $(\mathbf{J}^T \mathbf{J} + \mathbf{C}_M^{-1})$. Without the regularization constraints in \mathbf{C}_M^{-1} , this matrix would likely be singular, such that its determinant would be zero and its condition number (i.e., ratio of the largest to the smallest eigenvalues) would be infinite. Since the sensitivities in \mathbf{J} represent the information content offered by a particular survey design, and \mathbf{C}_M^{-1} indicates our preconceived ideas on the subsurface structure (e.g., closeness to initial model or smooth variation of the seismic velocities), it is certainly advisable to maximize the contribution of $\mathbf{J}^T \mathbf{J}$ and to minimize the influence of \mathbf{C}_M^{-1} .

Figure F.1 shows two typical eigenvalue spectra of $\mathbf{J}^T \mathbf{J}$ as they may arise from two frequency-domain waveform tomography crosshole experiments involving different recording geometries. The vertical axis is logarithmically scaled and normalized with respect to the largest eigenvalue of the corresponding spectra, and the horizontal axis is normalized by the total number of eigenvalues (number of model parameters). Due to the finite precision of numerical computations, eigenvalues are rarely identical to zero, even when the matrix is singular. Therefore, a threshold has to be introduced below which the eigenvalues have to be considered to be insignificant (dashed line in Figure F.1). The intersections of the eigenvalue spectra with the threshold line indicate the portions of the resolved model space and the unresolved null space. We define the portion to the left of the intersection points as the Relative Eigenvalue Range (RER), which provides a simple and intuitive means for quantifying the goodness of a particular survey design. Although both matrices related to the eigenvalue spectra shown in Figure F.1 are singular, the RER indicates that survey design 2 is superior to design 1, because its null space is smaller. Note that the concepts and terminology introduced in Figure F.1 are the basis for diagrams in many of the other Figures.

The choice of threshold level is problem-dependent, but extensive tests indicated that this is not a critical parameter for our experimental design approach, since it just scales the individual RER values. Any threshold choices we make between 10^{-8} and 10^{-12} yield similar results. All the eigenvalue spectra shown in the following Figures are plotted down to a value of 10^{-10} , such that the RER value can be easily recognized as the intersection

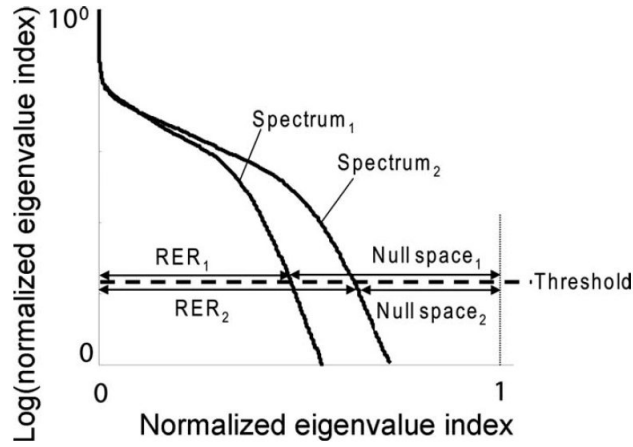


Figure F.1: Schematic representation of two normalized eigenvalue spectra of the Hessian matrix $\mathbf{J}^T \mathbf{J}$ (equation (F.3)). The horizontal axis is normalized with respect to the total number of model parameters and the vertical axis is normalized with respect to the largest eigenvalues. RER_{1,2} indicate the measures of goodness employed in this paper.

with the horizontal axis. Here, we consider noise-free data. In the presence of noise it would be necessary to raise the threshold to an appropriate level.

For the computations of the RER, a subsurface model has to be specified. Ideally, one would choose the true subsurface model, but this is generally unknown. Therefore, an educated guess of the subsurface structure may be required at a design stage. This problem was investigated by Stummer et al. (2004) in the framework of geoelectrical survey design. They concluded that although sensitivities may vary substantially between different Earth models, this has a surprisingly small effect on the optimal choice of electrode configurations. In this study, we will examine whether similar conclusions can also be drawn for frequency-domain waveform tomography experiments.

The non-linear effects introduced by the model dependency also affect the convergence behavior of waveform inversions. The existence of local minima may preclude convergence of the algorithms to the global minimum of the data misfit function. This makes the choice of an appropriate initial model critical (e.g. Plessix and Mulder, 2008). It has been observed by several researchers (e.g. Brenders and Pratt, 2007) that convergence of the inversion algorithm may improve significantly when initially only low frequency data are inverted and higher frequencies are added later.

Experimental setup

The simple experimental setup employed in this study involves two 30 m long, parallel boreholes. Our data space comprises 30 frequencies equally spaced between 100 and 1500 Hz. The band-limited nature of seismic data is approximated with a Ricker wavelet having a center frequency of 700 Hz. Its amplitude spectrum is shown in Figure F.2. Furthermore, we consider various source (left borehole) and receiver (right borehole) spacings of 0.25 m, 0.5 m, 1 m, 2 m and 4 m, and borehole separations of 10 m, 20 m, 30 m, 40 m and 50 m. Such geometries are typical of civil engineering crosshole experi-

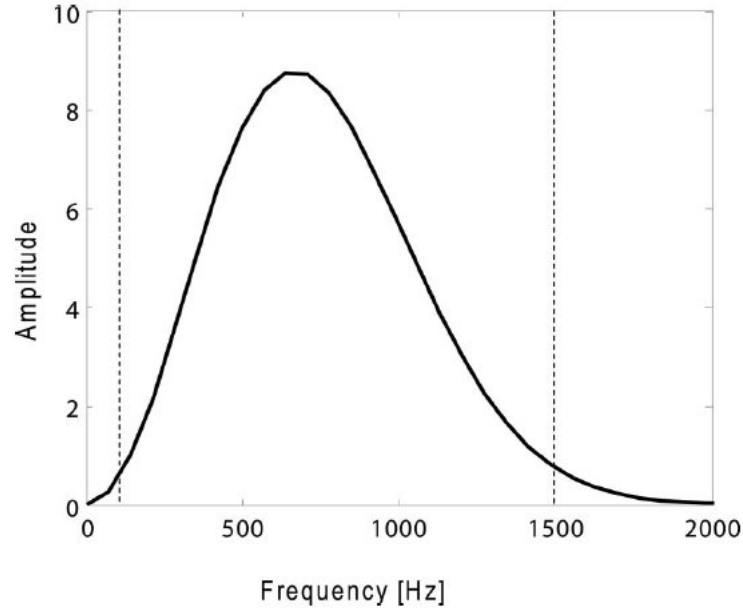


Figure F.2: Amplitude spectrum of a Ricker source wavelet with 700 Hz center frequency. The dashed vertical lines indicate the lower and upper frequency limits considered.

ments. Oilfield surveys would scale up by a factor of 10 to 20, but the frequencies do typically not scale down by a similar factor, and the aspect ratio (hole length/hole separation) would be rarely smaller than 2. Our investigations indicate that it is worthwhile making an effort to extend the frequency spectrum as much as possible towards lower frequencies.

For the solution of the forward problem the model space is discretized with square cells of 0.15 m side length. Our inversion grid comprises square cells of side length 0.6 m. The size of the forward cells is dictated by the stability criterion of the finite element solver, and the size of the inversion cells should represent a good compromise between the spatial and formal resolution (e.g. Menke, 1989). We have repeated some of the computations described later in the paper with inversion cell sizes of 0.3 m and 1.2 m and came essentially to the same results.

Two different velocity distributions are considered – a homogenous model with $v_P = 2000 \text{ m/s}$ and a stochastic model with a mean velocity of $v_P = 2000 \text{ m/s}$, a standard deviation of 100 m/s , a correlation length of 8 m, and a fractal dimension of 0.5 (e.g. Goff and Jordan, 1988). Additionally, we added a positive and a negative square-shaped velocity anomaly with dimensions $2 \times 2 \text{ m}^2$ to the stochastic model. Figure F.3 shows the stochastic model for a borehole separation of 30 m (most computations performed in this study consider 30 m borehole separation). Note, that the wavelengths (λ) for the homogeneous model vary from 20 m (100 Hz) to 1.33 m (1500 Hz). Therefore, for the lowest frequency employed, the borehole separation varies from $\lambda/2$ to 2.5λ , and the source/receiver spacings vary from approximately $\lambda/100$ to $\lambda/5$.

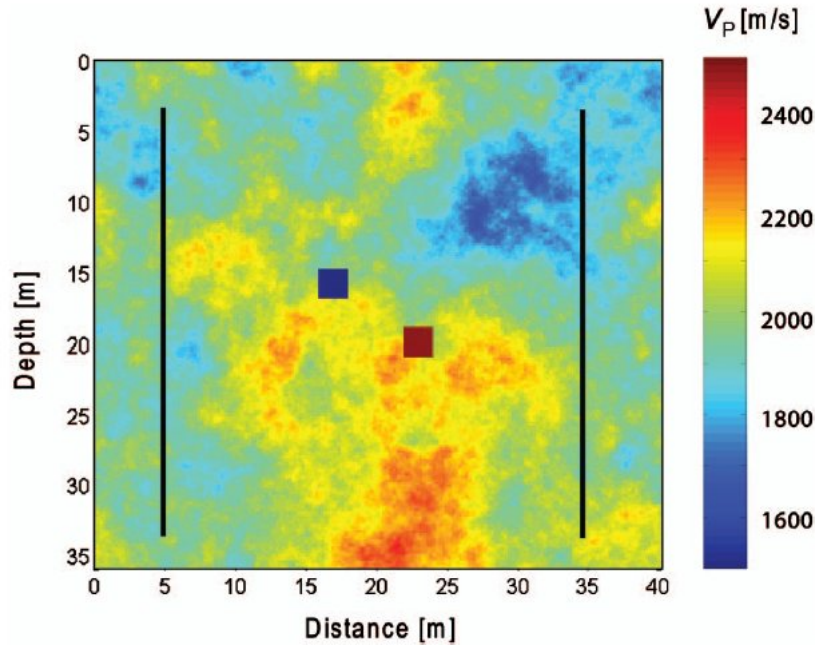


Figure F.3: Example stochastic model employed in this study for a borehole separation of 30 m. Boreholes are indicated by black vertical lines.

Model dependency

Since seismic waveform data and the corresponding model parameters are related to each other in a non-linear fashion (equations (F.1) and (F.2)), the sensitivities required for the solution of equation (F.3) are model dependent. This is illustrated in Figure F.4, which shows sensitivity patterns for a source at 3 m depth, a receiver at 33 m depth, and a hole separation of 30 m. Panels F.4a to F.4c are based on the homogenous model and panels F.4d to F.4f are computed using the stochastic model in Figure F.3. Only the real parts of the complex sensitivities for low (100 Hz, Figure F.4a and F.4d), intermediate (750 Hz, Figure F.4b and F.4e) and high (1500 Hz, Figure F.4c and F.4f) frequencies are displayed; the corresponding imaginary parts show comparable features. It is obvious that the velocity model influences the sensitivity patterns substantially at all frequencies, and it is particularly noteworthy that the velocity fluctuations distort the symmetries of the sensitivity patterns in Figure F.4d to F.4f.

Figure F.4g to F.4i show the eigenvalue spectra for the homogeneous (red curves) and stochastic (blue curves) models based on source and receiver spacings of 1 m. As expected intuitively, the low frequency 100 Hz data provide only minor information on both velocity models, i.e. their RER values (intersections with the horizontal axis) are quite small (≈ 0.1). The 750 Hz (Figure F.4h) and 1500 Hz (Figure F.4i) data show higher RERs between 0.2 and 0.5. Interestingly, the spectra for the homogeneous and stochastic models differ significantly for the 750 Hz data, thereby indicating that the stochastic model is better constrained by the seismic data than the homogenous model. This observation can be understood by considering seismic wave propagation in media with different model complexities. In a homogenous medium, there is only a direct

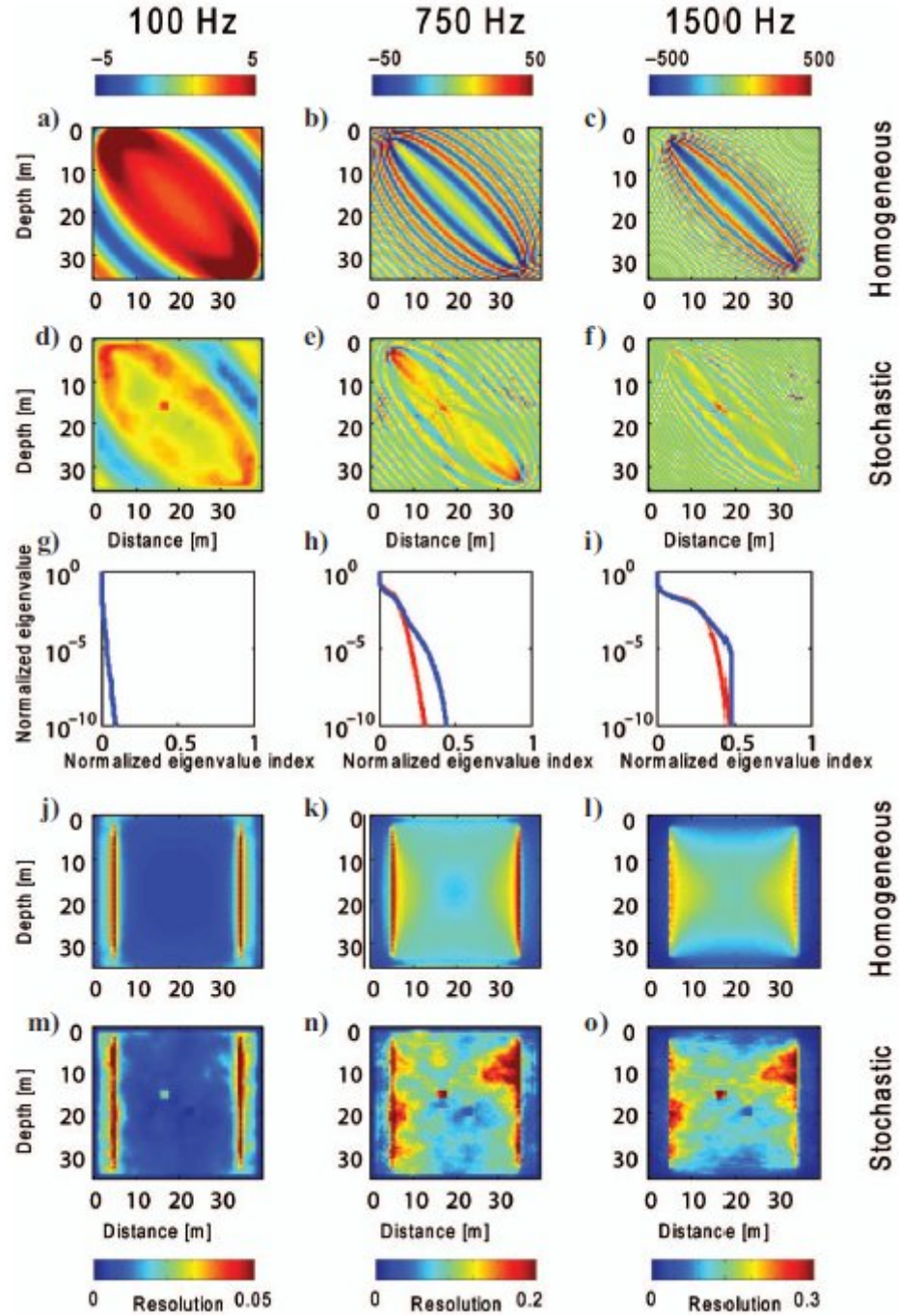


Figure F.4: Model dependency of sensitivities, eigenvalues and model resolution. Panels a) to c) show the real parts of the waveform sensitivities for a homogeneous model using frequencies 100, 750, and 1500 Hz respectively. Sources are placed at 5 m distance and 3 m depth and the receivers are positioned at 35 m distance and 33 m depth. Panels d) to f) show the corresponding plots for the stochastic model shown in Figure F.3. Panels g) to i) show the eigenvalue spectra of the Hessian matrix $\mathbf{J}^T \mathbf{J}$ (equation (F.3)) for the homogeneous (red curves) and the stochastic (blue curves) models using frequencies of 100, 750 and 1500 Hz. Borehole separation is 30 m and source and receiver spacing is 1 m. Panels j) to o) depict the spatial distribution of the diagonal elements of the model resolution matrices for the simulations associated with the curves shown in g) to i).

wave traveling through the medium, whereas in a more complicated medium, multiple scattering at the heterogeneities occur. This causes the individual parts of the model to be “illuminated” from many different directions, increasing the wavenumber coverage and thus enhancing the model resolution. At the high frequency end (1500 Hz) the RERs of the homogeneous and stochastic model are again comparable. Apparently, multiple scattering of a single high-frequency spectral component is not beneficial in terms of model resolution because the imaging wavelength is now similar to the wavelength of model variations. In contrast, we will demonstrate that combinations of high and low frequencies result in a significant improvement of the stochastic model compared with the homogeneous case.

The model resolution can be formally expressed by the model resolution matrix \mathbf{R} , defined as

$$\mathbf{R} = (\mathbf{J}^T \mathbf{J} + \mathbf{C}_M^{-1})^{-1} \mathbf{J}^T \mathbf{J} \quad (\text{F.4})$$

(e.g. Menke, 1989). It relates the estimated model parameters \mathbf{m}^{est} with the true model parameters \mathbf{m}^{true} ($\mathbf{m}^{\text{est}} \approx \mathbf{R} \mathbf{m}^{\text{true}}$). Of particular interest are the diagonal elements of \mathbf{R} . Values close to zero indicate poorly resolved model parameters, and values close to one indicate well resolved model parameters.

Figure F.4j to F.4o show the spatial distributions of the diagonal elements of \mathbf{R} for the different models and frequencies. With only one low frequency, acceptable model resolution is restricted to the areas near the boreholes, whereas better resolution is observed at higher frequencies over larger parts of the model space. Again, there are substantial differences between the homogenous and the stochastic models. Figure F.4m to F.4o also demonstrate the relationship between the seismic velocities and the model resolution. Generally, there is increased resolution in areas of decreased velocities. This can be explained by the shorter wavelengths that result in these regions.

Two main conclusions can be drawn from the results in Figure F.4. First, there are significant differences in the sensitivities, eigenvalue spectra and model resolution for different types of velocity model. Second, heterogeneous models may be generally better constrained by seismic waveform data, because of the occurrence of multiple scattering at heterogeneities. In the following, all analyses are performed for both velocity models in order to explore whether different experimental design strategies have to be chosen for different types of velocity model.

Data representation

Frequency-domain seismic data are generally complex-valued quantities, but it has been proposed to use only the amplitude spectrum, only the phase spectrum or only the Hartley spectrum. The latter is defined as the difference between the real and imaginary parts of the spectrum (e.g. Bracewell, 1984). The advantage of such real valued data representations is that they reduce the size of the Jacobian matrix by a factor of two. Zhou and Greenhalgh (1998b) showed that inversion of the Hartley spectrum could lead to similar results as provided by the full complex spectrum. It has been also shown that (normalized) amplitude inversions can be formulated such that the influence of the source wavelet is removed (Zhou and Greenhalgh, 2003; Xu et al., 2006). In contrast,

Bleibinhaus et al. (2007) inverted only phase data to avoid artifacts caused by anelastic effects.

By means of an eigenvalue spectrum analysis, we have inspected the information content of the different data representations. Figure F.5 shows normalized eigenvalue spectra for 100 Hz (Figs F.5a and F.5d), 750 Hz (Figs. F.5b and F.5e) and 1500 Hz (Figs. F.5c and F.5f) data using the homogeneous and the stochastic models, and a source/receiver spacing of 1 m. At low frequencies (Figs F.5a and F.5d), the different spectra are very similar, but at higher frequencies the individual curves diverge. In particular, the 1500 Hz data demonstrate clearly that the full complex frequency spectral data lead to a much better constrained inversion problem than all other data representations. Results for the Hartley spectra, only real parts and only imaginary parts are virtually identical in all panels of Figure F.5. The Hartley spectrum seems to be slightly superior to the Amplitude data, and phase data are somewhat inferior to the other data representations. This latter observation changes, if the eigenvalue threshold rises up to 0.1, which may be required in the presence of a very high noise level. In such a situation, the phase data are superior to any other data representation. This may imply that when the data are too noisy to rely on scattered wave observations, first break travel time tomography should be applied.

From our analysis it can be concluded that, whenever possible, the full complex

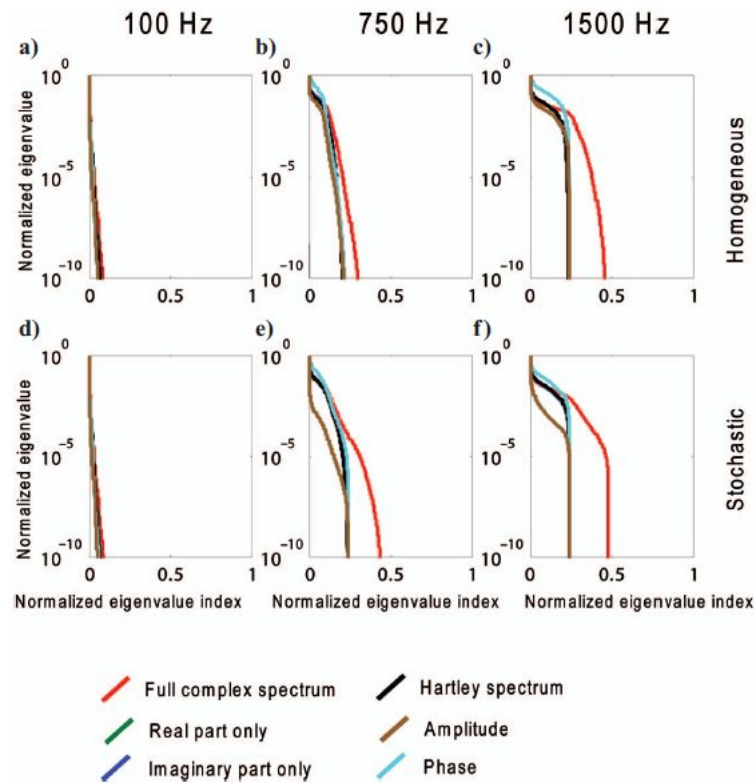


Figure F.5: Effects of different data representations. Eigenvalue spectra of the Hessian matrix $\mathbf{J}^T \mathbf{J}$ (equation (F.3)) for frequencies 100, 750, and 1500 Hz and the homogeneous and the stochastic model. Borehole separation is 30 m, and source and receiver spacings are 1 m.

spectrum should be considered. The larger size of the Jacobian matrix is not critical, because the normal equations (F.1) can be accumulated sequentially. All subsequent computations described in this contribution are based on the full complex spectrum.

Selection of frequencies

We consider three different types of data sets: (i) single frequencies, (ii) cumulative frequencies and (iii) optimized frequencies. The single frequency data sets only include a single frequency at a time. For the cumulative frequencies (e.g., Figure F.6c and F.6d), the lowest frequency (100 Hz) forms the first data set. The second data set includes the lowest and next higher frequency data. For the following data sets, higher frequency data are successively added, and the last data set includes all frequencies.

Optimized data sets also start with the lowest frequency. The next frequency is selected such that it complements the preceding data set in an optimal fashion. This is achieved by adding (one at a time) all other frequency data sets to the Jacobian matrix and testing to see, which frequency provides the highest RER value for the resulting Hessian matrix. This frequency is then chosen.

Choosing the lowest frequency for initializing the optimization process is governed by the results of Brenders and Pratt (2007) and others, who demonstrated that low frequency data are essential to avoid local minima during the iterative inversion procedure. In fact, an inversion with only the lowest frequency was sufficient for determining an appropriate initial model.

Eigenvalue spectra are computed for single, cumulative and optimized frequency data sets and all combinations of source and receiver spacings, borehole separations and velocity models. A selection of results is displayed in Figures F.6 to F.8. They show the results for a borehole spacing of 30 m and shot/receiver spacings of 1, 2 and 4 m respectively. The left panels (a, c, e, g, i) in each figure display the results for the homogeneous model and the right panels (b, d, f, h, and j) depict the curves for the stochastic model.

Results for the single frequency data are shown in panels a and b of Figures F.6 to F.8. The lowest frequency data provide the lowest RER values. With increasing frequencies the RER values increase. As expected, the RERs decrease with increasing source and receiver spacings. Likewise, the RERs decrease with increasing borehole separations (not shown).

Similar observations can be made for the cumulative frequencies in panels c and d of Figures F.6 to F.8, but there are some important differences. Compared to the single frequency data, the RER values for the cumulative frequencies are generally much higher. For the stochastic model and the largest source and receiver spacings (Figure F.8), the differences between the single and cumulative frequencies are substantial. The highest frequency leads to a RER of less than 0.05 (Figure F.8b) and the data set including all the frequencies (Figure F.8d) shows a RER of almost 0.9, such that the null space is very small. Again, the stochastic model is generally much better constrained than the homogeneous model. As for the single frequencies, the RER values for the cumulative frequency data sets generally decrease with increasing source and receiver spacings and with decreasing borehole separations (not shown).

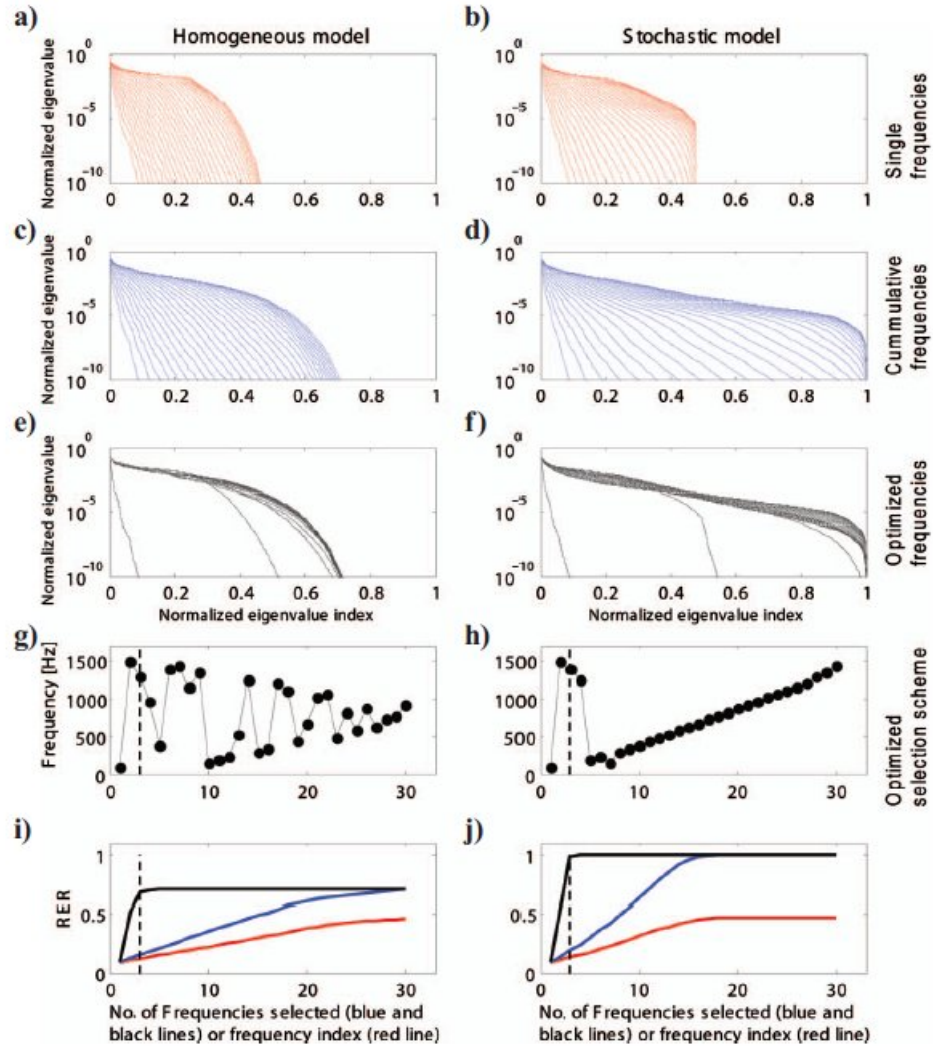


Figure F.6: Selection of frequencies for a borehole separation of 30 m and source and receiver spacings of 1 m. Left panels show the results for the homogeneous model, and right panels show the results for the stochastic model. a) and b) show the eigenvalue spectra for single frequencies. The lowest frequency (100 Hz) results in the lowest RER (intersection with the horizontal axis), and the highest frequency provides the largest RER (intersection with horizontal axis). c) and d) include the results for the cumulative frequency distributions, and e) and f) depict the eigenvalues for the optimized frequency selection scheme. In panels g) and h) the sequences of selected frequencies are shown for the optimized selection scheme (panels e) and f)). Panels i) and j) sketch the development of the RER for single (red curves), cumulative (blue curves) and optimized (black curves) selection schemes. The dashed vertical lines in panels g) to j) indicate the number of selected frequencies, where the RERs for the optimized scheme exceed 95% of the maximum level achievable (plateau of the black curves in i) and j)).

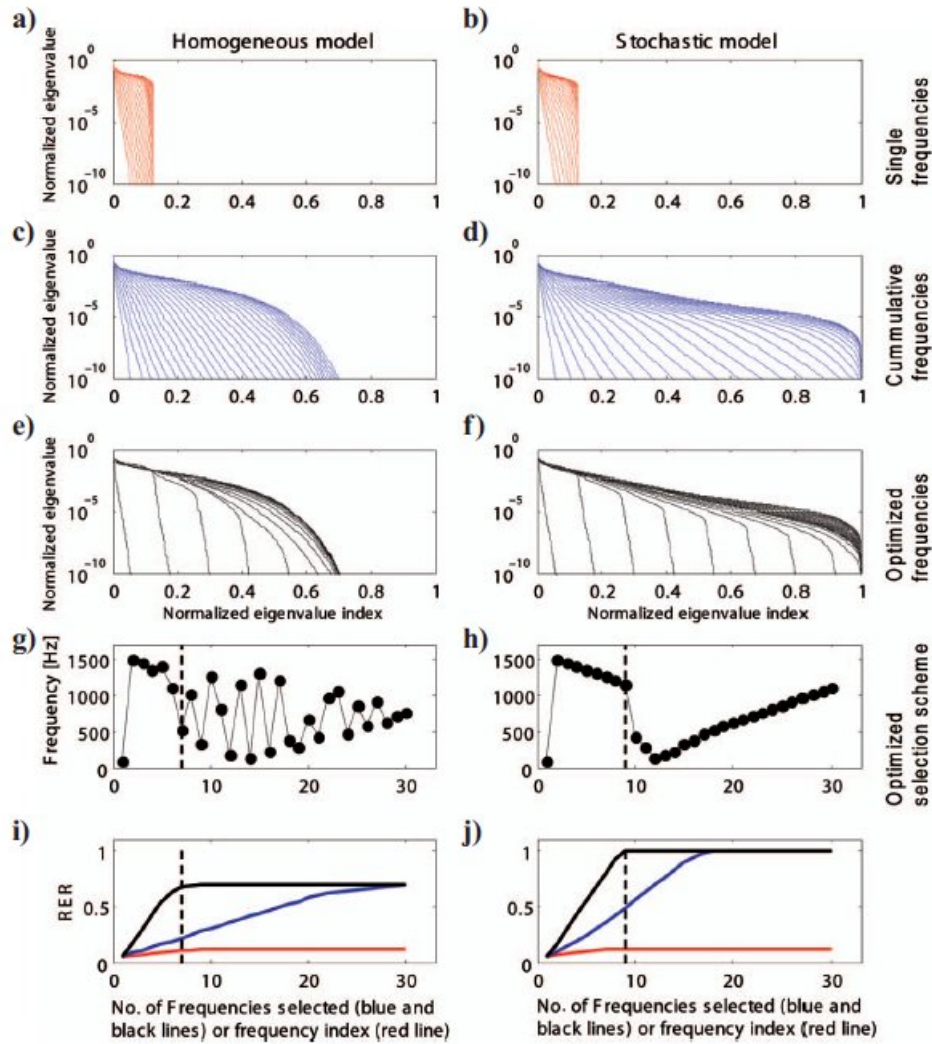


Figure F.7: Selection of frequencies for a borehole separation of 30 m and source and receiver spacings of 2 m. Left panels show the results for the homogeneous model, and right panels show the results for the stochastic model. a) and b) show the eigenvalue spectra for single frequencies. The lowest frequency (100 Hz) results in the lowest RER (intersection with the horizontal axis), and the highest frequency provides the largest RER (intersection with horizontal axis). c) and d) include the results for the cumulative frequency distributions, and e) and f) depict the eigenvalues for the optimized frequency selection scheme. In panels g) and h) the sequences of selected frequencies are shown for the optimized selection scheme (panels e) and f)). Panels i) and j) sketch the development of the RER for single (red curves), cumulative (blue curves) and optimized (black curves) selection schemes. The dashed vertical lines in panels g) to j) indicate the number of selected frequencies, where the RERs for the optimized scheme exceed 95% of the maximum level achievable (plateau of the black curves in i) and j)).

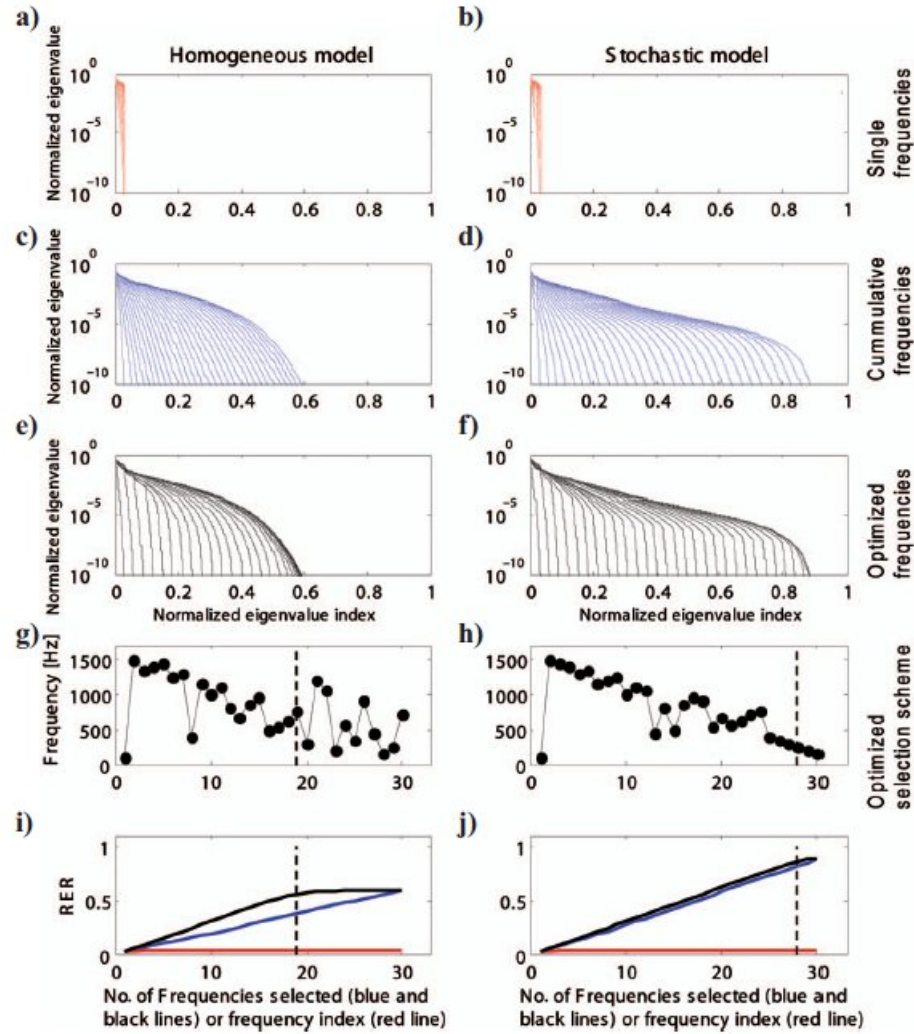


Figure F.8: Selection of frequencies for a borehole separation of 30 m and source and receiver spacings of 4 m. Left panels show the results for the homogeneous model, and right panels show the results for the stochastic model. a) and b) show the eigenvalue spectra for single frequencies. The lowest frequency (100 Hz) results in the lowest RER (intersection with the horizontal axis), and the highest frequency provides the largest RER (intersection with horizontal axis). c) and d) include the results for the cumulative frequency distributions, and e) and f) depict the eigenvalues for the optimized frequency selection scheme. In panels g) and h) the sequences of selected frequencies are shown for the optimized selection scheme (panels e) and f)). Panels i) and j) sketch the development of the RER for single (red curves), cumulative (blue curves) and optimized (black curves) selection schemes. The dashed vertical lines in panels g) to j) indicate the number of selected frequencies, where the RERs for the optimized scheme exceed 95% of the maximum level achievable (plateau of the black curves in i) and j)).

Eigenvalue spectra for the optimized data sets are depicted in panels e and f in Figures F.6 to F.8. For source and receiver spacings of 1 m (Figure F.6) a large increase in the value of RER is achieved by adding only one additional frequency, and with 3 frequencies the RER is already very close to its maximum value. Figure F.6g and F.6h indicate the sequence in which the frequencies are selected. For both the homogeneous and the stochastic model, the second frequency selected is 1500 Hz, which is the highest possible frequency. The next few frequencies are also quite high, but it is noteworthy that the third and fourth choices are not the highest frequencies possible. Again, this applies to the selection procedures for both velocity models.

Figures F.6i and F.6j display the development of the RER for the single, cumulative and optimized selection schemes. The curves for the optimized selection scheme exhibit a sharp kink after the 3rd frequency selected and then plateau. This indicates that the remaining frequencies added to the data sets contribute virtually no additional information. Consequently, the sequence of the remaining frequencies is insignificant. To help compare Figures F.6 to F.8, a dashed vertical reference line is added to the panels g to j, which indicates the number of frequencies needed for the RER to exceed 95% of its maximum value for the optimized selection scheme.

The RER developments of the single and cumulative selection schemes (red and blue curves in Figures F.6i and F.6j) are more gradual. They require all the frequencies for the homogenous model and 16 frequencies for the stochastic model in order to reach 95% of the maximum RER. As already indicated in Figures F.6a and F.6b, the single frequencies never achieve the maximum RER for multiple frequency data sets.

Results for source and receiver spacings of 2 and 4 m (Figures F.7 and F.8) indicate that maximum RERs similar to those of the 1 m spacing can be achieved. However, as illustrated in Figures F.7g, F.7h, F.8g and F.8h, more frequencies are required to attain the maximum RER. An interesting observation is made in Figure F.8j. Here, the RER curves for the cumulative and optimized data sets nearly coincide. The selection sequence, shown in Figure F.8h is almost the opposite to that of the cumulative selection strategy. This could indicate that it does not really matter which frequencies are selected when the data sets are excessively sparse, although selection of the first frequency to be low is still important. Similar observations are also made for larger borehole separations (not shown).

Figure F.9 summarizes the key results of this section. Panels F.9a and F.9b show the maximum RER achievable as a function of the source and receiver spacings and the borehole separation (corresponds to the plateau level of the black lines in panels i and j of Figures F.6 to F.8). For the homogenous model, it is only possible to obtain an RER close to 1.0, when the borehole separation is small. In contrast, for the stochastic model, almost all combinations of spacings and hole separations result in an RER close to 1.0, when a sufficiently high number of frequencies are used. The vertical stripe pattern in Figure F.9a also illustrates that the goodness of an experimental layout is predominantly governed by the borehole separation and not by the source and receiver spacings.

In Figures F.9c and F.9d, the development of the RER is imaged as a function of the source and receiver spacings and the number of (optimized) frequencies considered (for a fixed borehole separation of 30 m). This result clearly demonstrates that the most useful information content offered by the seismic data can be obtained with surprisingly few frequencies. For spacings of 0.25, 0.5, 1.0 and 2.0 m only 2, 2, 3 and 9 frequencies

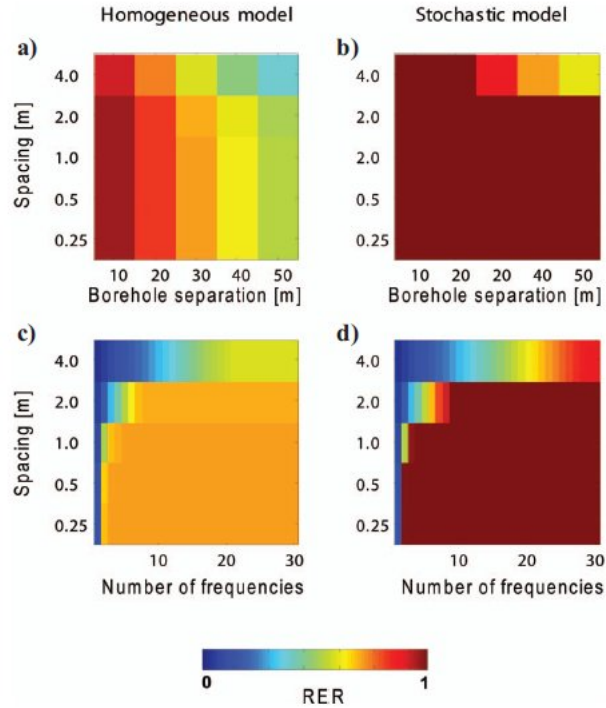


Figure F.9: Summary plots for the optimized frequency selection schemes. Panels a) and b) show the maximum RER level achievable for the homogeneous and the stochastic model as a function of borehole separation and source and receiver spacings. c) and d) show the development of the RER as a function of the number of frequencies and the source and receiver spacings. Borehole separation for c) and d) is 30 m.

are required, respectively, to reach 95% of the maximum RER achievable. For the largest spacing of 4 m, the complete suite of frequencies is insufficient to achieve such a high RER.

Inversion results

With the eigenvalue analyses given in the previous sections it was possible to identify the theoretical information content offered by the seismic data. However, due to the non-linearity of the waveform inversion problem, it is necessary to check if this information can actually be exploited in practice, or, if the iterative inversion process gets trapped in local minima. This not only depends on the information content of the data set, but also relies on (i) the inversion algorithm chosen (conjugate gradient, Gauss-Newton, full Newton, etc.), (ii) the complexity of the true model, (iii) the regularization constraints applied, (iv) the level of data noise contamination and, most importantly, (v) the choice of the initial model.

It is beyond the scope of this paper to explore all the above issues in detail (see Bren- ders and Pratt, 2007, and references therein for a more extensive discussion). Instead, we choose a robust approach that requires neither an educated guess of the initial model nor involves a sophisticated regularization operator. As an initial model we choose a

homogenous medium with average velocity equal to that of the true model (2000 m/s). Regularization constraints are supplied in the form of an equal amount of damping and smoothing (Maurer et al., 1998). Initially, we only invert the lowest frequency (100 Hz) for obtaining the long wavelength variations of the model. This initial inversion result is then employed as a starting model for a second inversion run, where all the selected frequencies are inverted simultaneously.

Computing time is dominated by the solution of the forward problem and the associated sensitivities. Predicting the data and computing the sensitivities for a single frequency required roughly 2 minutes on a standard workstation, such that a full inversion run with, for example, 5 frequencies and 10 iterations could be completed in about 100 minutes.

Key results of this study are illustrated in Figures F.9b and F.9c, which demonstrate that only a very limited number of frequencies are required for fully exploiting the information content offered by the seismic data. To test this conjecture, synthetic data are generated for the stochastic model of Figure F.3 and a borehole separation of 30 m. Figure F.10a shows again the true model, but resampled down to the inversion block size (0.6 m). The best inversion results are obviously expected for a “comprehensive” data set involving the densest source and receiver spacings (0.25 m) and all 30 frequencies (~ 900000 data points). The corresponding tomogram is shown in Figure F.10b. It recovers all the important features reliably.

Figures F.10c to F.10e show the inversion results for a spacing of 0.5 m and two frequencies (roughly 15000 data points), a spacing of 1.0 m and three frequencies (~ 5000 data points), and a spacing of 2 m and 9 frequencies (~ 5000 data points). For the 0.5 m spacing, the lowest (100 Hz) and the highest (1500 Hz) frequencies were selected. The other frequency selections are shown in Figures F.6h and F.7h (using the frequencies identified for the homogeneous model (Figures F.6g and F.7g) would lead to very similar results). According to Figure F.9d, these data sets should provide tomograms of comparable quality to those in Figure F.10b. This is indeed the case, although the “comprehensive” tomogram is slightly superior to the other inversion results. In particular, the high velocity zone at the bottom part of the model is better imaged. The high and low velocity anomalous blocks are similarly well resolved in all tomograms, and also the reconstructions of the other stochastic features are of comparable quality.

Discussion

Our investigations have revealed several important features of frequency-domain full waveform crosshole seismic tomography. In the following, an attempt is made to generalize the results obtained with our specific choices of data and model spaces, such that recommendations for a wider range of problems can be made.

Results displayed in Figure F.4 indicate clearly the non-linearity (model dependency) of seismic waveform inversions. It is found that the resolution capabilities of seismic waveform data sets increase with the degree of heterogeneity. The homogeneous and stochastic models considered in this study represent the end members in terms of model complexity. It is expected that resolution capabilities for a wide range of models are bracketed by the results presented here.

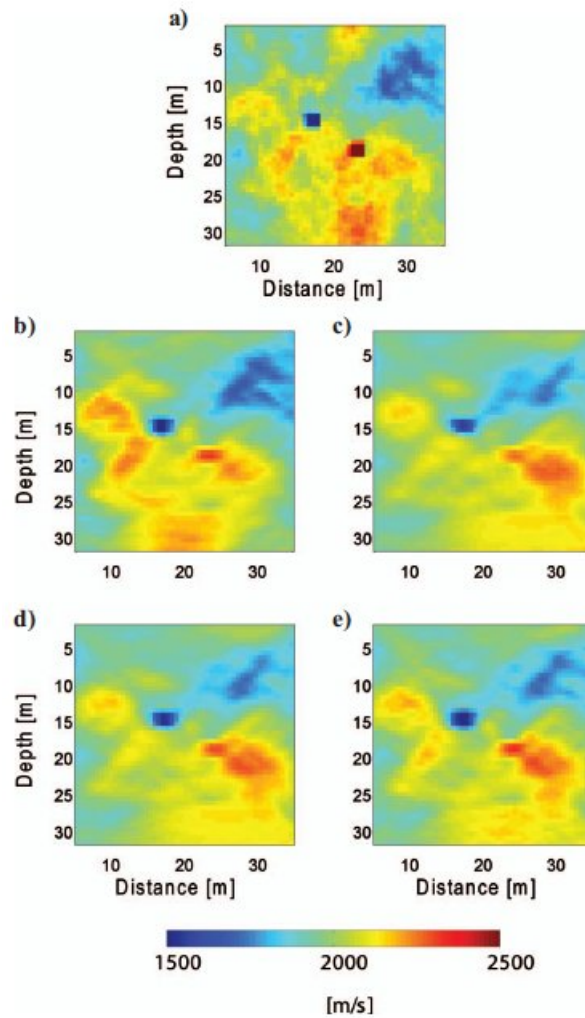


Figure F.10: Tomographic inversion results using a borehole separation of 30 m. a) The true model (Figure F.3) resampled with the size of the inversion blocks (0.6 m). b) The inversion result for a source and receiver spacing of 0.25 m and all 30 frequencies ("comprehensive" data set). c) to e) Tomograms for a spacing of 0.5 m and two frequencies, 1 m and three frequencies, and 2 m and 9 frequencies respectively.

Benefits of multiple frequency inversions have been demonstrated in a variety of papers (e.g. Plessix and Mulder, 2008). With our eigenvalue analysis, we have established a simple means for identifying optimized selections of frequencies. It was found that a few (optimal) frequencies suffice for obtaining results that are comparable to those using comprehensive data sets that include all frequencies and employ a dense sampling along the boreholes. Panels g and h in Figures F.6 to F.8 show the optimal sequences for particular geometries and velocity models. From a comparison of all sequences (also including those for source and receiver spacings and borehole separations not shown in the paper), a general rule of thumb can be derived. At least one low frequency is required for obtaining a reliable initial model, and to ensure a certain bandwidth, one high frequency is needed. Additional frequencies should then be chosen from the upper end of the spectrum. Another important conclusion from our simulations is that this rule of thumb applies to both the homogeneous model and the stochastic model, such that the frequency selection procedure does not seem to be model-dependent.

To some extent, this is a surprising result, because most of the frequencies selected lie in the low-amplitude range of the employed Ricker wavelet spectrum (Figure F.2). Intuitively, one would expect that the high amplitude data around the center frequency should be selected, which is apparently not the case. In reality, one would not ignore the mid-frequency range, where the signal-to-noise-ratio is usually best. In fact, our recommendation to practitioners is to incorporate such information, but also to utilize the relatively high frequency data, even when their relative amplitudes may be low. The signal-to-noise bandwidth will change from one situation to another and this imposes practical limits on the imaging frequencies. Noise suppression techniques can be helpful in extending this bandwidth, but one must accept the available frequencies offered by nature (attenuation) and the source/receiver characteristics. The critical point is to utilize the relatively high frequency end of the available spectrum. This is much more beneficial than selecting many frequencies around the center frequency.

The summary plots in Figure F.9 show that there exist trade-offs between the selection of frequencies and the spatial sampling along boreholes. Sparse spatial sampling can be, to some extent, compensated by considering additional frequencies. However, if the spatial sampling is sufficiently small, the trade-off disappears. That is, there are only small imaging benefits to be obtained by using an overly dense spatial sampling (smaller than the minimum wavelength) along the boreholes. Dense spatial sampling results in a large number of traces to be analyzed during the inversion. Thus the computational cost is vastly reduced by working with a significantly reduced amount of data without sacrificing image quality. Of course, there are other benefits to be gained from using dense arrays to combat noise, but that lies outside the scope of this paper. The conclusions from our noise-free experiments are nevertheless valid to some extent in the presence of noise, provided that the frequency selection is within the band where the signal lies sufficiently above the noise floor. One effect of white noise (and other frequency-dependent factors like absorption) is to simply narrow the available spectrum (Figure F.2). Systematic noise, such as tube waves, will undoubtedly distort the inversion results. Therefore, careful pre-processing of the data is required prior to the inversion.

Conclusions

We have undertaken an analysis of frequency-domain crosswell acoustic waveform inversion using both homogeneous and stochastic models incorporating embedded targets, with a view to optimal selection of frequencies and source/receiver spacings along the boreholes. The information content of the data for each candidate recording configuration and suite of frequencies (single, cumulative, etc) was determined by examining the eigenvalue spectrum of the Hessian matrix. The relative eigenvalue range was found to be a key determinant of imaging capability.

Comparisons of different types of data representations demonstrate that, whenever possible, the full complex Fourier spectrum should be used. At lower frequencies pure amplitude or pure phase data alone yield comparable results to the full complex spectral data, but at higher frequencies there is a substantial loss of information content for these restricted data representations. This conclusion does not seem to be model-dependent.

We found, rather surprisingly, that only a few carefully chosen frequencies are sufficient to extract from the seismic data the same amount of subsurface information as with a more extensive suite of equally spaced frequencies. The optimized data set should include at least one very low frequency component and the remaining frequencies should be chosen from the upper end of the available spectrum. Source and receiver spacings are of less importance than frequency selection, in the sense that much denser spatial sampling leads to only minor improvement, with the proviso that the increment is smaller than the minimum wavelength in the model. Borehole separation should also not be much larger than the depth, otherwise even with many frequencies and small source/receiver spacings image quality is seriously degraded.

Future research should address a number of complications that were not yet considered in this contribution. In particular, it needs to be investigated, how source radiation patterns, receiver coupling, elastic and viscoelastic effects and anisotropy affect experimental design of waveform inversion projects.

Acknowledgments

We thank Alan Green for a thorough in-house review of the manuscript. Furthermore, we thank Josep de la Puente and an anonymous reviewer for useful comments that improved the clarity of the paper. This study was partially financed by the SNF grant 200021-111846.

Bibliography

- Abraham, O. and Dérobert, X. (2003). Non-destructive testing of fired tunnel walls: the Mont-Blanc Tunnel case study. *Independent Nondestructive Testing and Evaluation*, 36(6):411 – 418.
- Achenbach, J. D. (1984). *Wave Propagation in Elastic Solids*, volume 16 of *Applied Mathematics and Mechanics*. North-Holland.
- Aki, K. and Richards, P. G. (2009). *Quantitative Seismology*. University Science Books, second edition.
- Amundsen, L. and Reitan, A. (1994). Transformation from 2-D to 3-D wave propagation for horizontally layered media. *Geophysics*, 59(12):1920–1926.
- Banerjee, P. K., Ahmad, S., and Manolis, G. D. (1986). Transient elastodynamic analysis of three-dimensional problems by boundary element method. *Earthquake Engineering & Structural Dynamics*, 14(6):933–949.
- Basu, U. and Chopra, A. K. (2003). Perfectly matched layers for time-harmonic elastodynamics of unbounded domains: theory and finite-element implementation. *Computer Methods in Applied Mechanics and Engineering*, 192(11-12):1337–1375.
- Båth, M. (1968). *Mathematical Aspects of Seismology*, volume 4 of *Developments in Solid Earth Geophysics*. Elsevier.
- Ben-Hadj-Ali, H., Operto, S., and Virieux, J. (2008). Velocity model building by 3D frequency-domain, full-waveform inversion of wide-aperture seismic data. *Geophysics*, 73(5):VE101–VE117.
- Berenger, J.-P. (1994). A perfectly matched layer for the absorption of electromagnetic waves. *Journal of Computational Physics*, 114(2):185–200.
- Bleibinhaus, F., Hole, J., Ryberg, T., and Fuis, G. (2007). Structure of the californian coast ranges and san andreas fault at safod from seismic waveform inversion and reflection imaging. *Journal of Geophysical Research*, 112(B6):B06315.
- Bleistein, N. (1986). Two-and-one-half dimensional in-plane wave propagation. *Geophysical Prospecting*, 34(5):686–703.
- Blome, M., Maurer, H., and Schmidt, K. (2009). Advances in three-dimensional geoelectric forward solver techniques. *Geophysical Journal International*, 176(3):740–752.

- Bohlen, T. (2002). Parallel 3-D viscoelastic finite difference seismic modelling. *Computers & Geosciences*, 28(8):887 – 899.
- Bohlen, T. and Saenger, E. H. (2006). Accuracy of heterogeneous staggered-grid finite-difference modeling of Rayleigh waves. *Geophysics*, 71(4):T109–T115.
- Bouchon, M. (1979). Discrete wave number representation of elastic wave fields in 3-space dimensions. *Journal of Geophysical Research*, 84(NB7):3609–3614.
- Bouchon, M. (2003). A review of the discrete wavenumber method. *Pure and Applied Geophysics*, 160(3-4):445–465.
- Bracewell, A. N. (1984). The Fast Hartley Transformation. In *Proceedings of the IEEE*, pages 1010–1018.
- Brenders, A. J. and Pratt, R. G. (2007). Efficient waveform tomography for lithospheric imaging: Implications for realistic, two-dimensional acquisition geometries and low-frequency data. *Geophysical Journal International*, 168:152–170.
- Brenner, S. C. and Scott, L. R. (2008). *The Mathematical Theory of Finite Element Methods*. Number 15 in Texts in Applied Mathematics. Springer, New York, third edition.
- Brossier, R., Operto, S., and Virieux, J. (2009). Seismic imaging of complex on-shore structures by 2d elastic frequency-domain full-waveform inversion. *Geophysics*, 74(6):WCC105–WCC118.
- Buchanan, D. J. and Jackson, L. J., editors (1986). *Coal Geophysics*, volume 6 of *SEG reprint series*. Soc. of Expl. Geophys.
- Buske, S., Lecomte, I., Nemeth, T., Operto, S., and Sallares, V. (2009). Imaging and inversion — introduction. *Geophysics*, 74(6):WCA1–WCA4.
- Butler, D. K., editor (2005). *Near-surface geophysics*. Number 13 in Investigations in Geophysics. Society of Exploration Geophysics, Tulsa.
- Cao, S. and Greenhalgh, S. (1997). 2.5-D acoustic wave modelling in the frequency-wavenumber domain. *Exploration Geophysics*, 28(2):11–15.
- Cao, S. and Greenhalgh, S. (1998). 2.5-D modeling of seismic wave propagation: Boundary condition, stability criterion, and efficiency. *Geophysics*, 63(6):2082–2090.
- Cerjan, C., Kosloff, D., Kosloff, R., and Reshef, M. (1985). A nonreflecting boundary condition for discrete acoustic and elastic wave equations. *Geophysics*, 50(4):705–708.
- Claerbout, J. F. (1985). *Imaging the Earth's Interior*. Blackwell Science Inc.
- Curtis, A. (1999). Optimal experiment design: Cross-borehole tomographic examples. *Geophysical Journal International*, 136:637–650.
- Curtis, A. (2004). Tutorial—theory of model-based geophysical survey and experimental design. *The Leading Edge*, 23(10):997–1004.

- Curtis, A. and Snieder, R. (1997). Reconditioning inverse problems using the genetic algorithm and revised parameterization. *Geophysics*, 62:1524–1532.
- Danecek, P. and Seriani, G. (2008). An efficient parallel Chebyshev pseudospectral method for large-scale 3D seismic forward modelling. In *70th Conference & Technical Exhibition*, number 70, Rome. EAGE.
- de Hoop, A. T., Remis, R. F., and van den Berg, P. M. (2007). The 3D wave equation and its cartesian coordinate stretched perfectly matched embedding - a time-domain green's function performance analysis. *Journal of Computational Physics*, 221:88–105.
- Dorn, C., Carpentier, S., Kaiser, A., Green, A. G., Horstmeyer, H., Campbell, F., Campbell, J., Jongens, R., Finnemore, M., and Nobes, D. (2009). First seismic imaging results of tectonically complex structures at shallow depths beneath the northwest canterbury plains, new zealand. *Journal of Applied Geophysics*, In Press, Corrected Proof:–.
- Eaton, D. W., Milkereit, B., and Salisbury, M. H., editors (2003). *Hardrock Seismic Exploration*. Soc. of Expl. Geophys., Tulsa.
- Forbriger, T. (2003). Notizen zur Berechnung synthetischer Seismogramme mit der Reflektivitätsmethode. <http://www-gpi.physik.uni-karlsruhe.de/pub/forbriger/download/paperware/>. Course “Berechnung von synthetischen Seismogrammen und seismischen Strahlen mit praktischen Übungen”.
- Forbriger, T. and Friederich, W. (2005). A proposal for a consistent parametrization of earth models. *Geophysical Journal International*, 162(2):425–430.
- Fornberg, B. (1998). *A Practicle Guide to Pseudospectral Methods*. Cambridge Monographs on Applied and Computational Mathematics. Cambridge University Press, Cambridge.
- Fujiwara, H. (1997). Windowed f-k spectra of a three-dimensional wavefield excited by a point source in a two-dimensional multilayered elastic medium. *Geophysical Journal International*, 128(3):571–584.
- Furumura, T. and Takenaka, H. (1996). 2.5-D modelling of elastic waves using the pseudospectral method. *Geophysical Journal International*, 124(3):820–832.
- Gélis, C., Virieux, J., and Grandjean, G. (2007). Two-dimensional elastic full waveform inversion using born and rytov formulations in the frequency domain. *Geophysical Journal International*, 168(2):605–633.
- Givoli, D. (1991). Non-reflecting boundary conditions. *Journal of Computational Physics*, 94(1):1–29.
- Goff, J. A. and Jordan, T. (1988). Stochastic modeling of seafloor morphology: Inversion of sea beam data for second-order statistics. *Journal of Geophysical Research*, 93:13589–13608.

- Golub, G. H. and van Loan, C. F. (1996). *Matrix Computations*. Johns Hopkins Studies in the Mathematical Sciences. Johns Hopkins University Press, Baltimore, third edition.
- Greenhalgh, S. and Zhou, B. (2004). Surface seismic imaging by multi-frequency amplitude inversion. *Exploration Geophysics*, 34:214–224.
- Greenhalgh, S., Zhou, B., and Green, A. G. (2006). Solutions, algorithms and inter-relations for local minimization search geophysical inversion. *Journal of Geophysics and Engineering*, 3(2):101–113.
- Guterch, A., Grad, M., Špičák, A., Brückl, E., Hegedüs, E., Keller, G. R., and Thybo, H. (2003). Special contribution: An overview of recent seismic refraction experiments in central europe. *Studia Geophysica et Geodaetica*, 47(3):651–657.
- Heikkola, E., Rossi, T., and Toivanen, J. (2003). Fast direct solution of the Helmholtz equation with a perfectly matched layer or an absorbing boundary condition. *International Journal for Numerical Methods in Engineering*, 57(14):2007–2025.
- Heincke, B., Maurer, H., Green, A. G., Willenberg, H., Tom, S., and Burlini, L. (2006). Characterizing an unstable mountain slope using shallow 2d and 3d seismic tomography. *Geophysics*, 71(6):B241–B256.
- Hosken, J. W. J. (1988). Ricker wavelets in their various guises. *First Break*, 6(1):24–33.
- Igel, H., Mora, P., and Rioulet, B. (1995). Anisotropic wave propagation through finite-difference grids. *Geophysics*, 60(4):1203–1216.
- Johnson, L. R. (1974). Green's function for Lamb's problem. *Geophysical Journal of the Royal Astronomical Society*, 37(1):99–131.
- Kennett, B. L. N. (1985). *Seismic Wave Propagation in Stratified Media*. Cambridge Monographs on Mechanics. Cambridge University Press.
- Kennett, B. L. N. and Bunge, H.-P. (2008). *Geophysical Continua*. Cambridge University Press.
- Kirsch, R., editor (2008). *Groundwater Geophysics*. Springer, second edition.
- Knödel, K., Lange, G., and Voigt, H.-J. (2007). *Environmental Geology*. Springer.
- Komatitsch, D. and Tromp, J. (1999). Introduction to the spectral element method for three-dimensional seismic wave propagation. *Geophysical Journal International*, 139:806–822.
- Komatitsch, D. and Tromp, J. (2002a). Spectral-element simulations of global seismic wave propagation: I. validation. *Geophysical Journal International*, 149(2):390–412.
- Komatitsch, D. and Tromp, J. (2002b). Spectral-element simulations of global seismic wave propagation: II. three-dimensional models, oceans, rotation and self-gravitation. *Geophysical Journal International*, 150(1):303–318.

- Lamb, H. (1904). On the propagation of tremors over the surface of an elastic solid. *Philosophical Transactions of the Royal Society of London. Series A*, 203:1–42.
- Lanz, E., Maurer, H., and Green, A. G. (1998). Refraction tomography over a buried waste disposal site. *Geophysics*, 63(4):1414–1433.
- Lehmann, B. (2007). *Seismic Traveltime Tomography for Engineering and Exploration Applications*. EAGE Publications BV.
- Levander, A. R. (1988). Fourth-order finite-difference p-sv seismograms. *Geophysics*, 53(11):1425–1436.
- Levenberg, K. (1944). A method for the solution of certain non-linear problems in least squares. *Quarterly of Applied Mathematics*, 2:164–168.
- Liberty, L. M., Clement, W. P., and Knoll, M. D. (1999). Surface and borehole seismic characterization of the boise hydrogeophysical research site. *Symposium on the Application of Geophysics to Engineering and Environmental Problems*, 12(1):723–732.
- Liner, C. L. (1991). Theory of a 2.5-D acoustic wave equation for constant density media. *Geophysics*, 56(12):2114–2117.
- Liner, C. L. (1995). Some analytic aspects of a 2.5-D wave equation. *Geophysics*, 60(5):1536–1540.
- Liu, L. and Guo, T. (2005). Seismic non-destructive testing on a reinforced concrete bridge column using tomographic imaging techniques. *Journal of Geophysics and Engineering*, 2(1):23–31.
- Liu, Q. H. (1998). The pseudospectral time-domain (pstd) algorithm for acoustic waves in absorptive media. *Ultrasonics, Ferroelectrics and Frequency Control, IEEE Transactions on*, 45(4):1044–1055.
- Mallick, K. and Frazer, N. L. (1987). Practical aspects of reflectivity modeling. *Geophysics*, 52(10):1355–1364.
- Manukyan, E. (2010). *Anisotropic waveform inversions for non-intrusive monitoring of radioactive waste*. PhD thesis, ETH Zurich. in preparation.
- Marfurt, K. J. (1984). Accuracy of finite-difference and finite-element modeling of the scalar and elastic wave equations. *Geophysics*, 49(5):533–549.
- Marquardt, D. W. (1963). An algorithm for least-squares estimation of nonlinear parameters. *SIAM Journal on Applied Mathematics*, 11(2):431–441.
- Marquering, H., Dahlen, F. A., and Nolet, G. (1999). Three-dimensional sensitivity kernels for finite-frequency traveltimes: the banana-doughnut paradox. *Geophysical Journal International*, 137(3):805–815.
- Maurer, H. and Boerner, D. E. (1998a). Optimized and robust experimental design. *Geophysical Journal International*, 132:458–468.

- Maurer, H. and Boerner, D. E. (1998b). Optimized design of geophysical experiments. *The Leading Edge*, 17:1119–1125.
- Maurer, H., Boerner, D. E., and Curtis, A. (2000). Design strategies for electromagnetic geophysical surveys. *Inverse Problems*, 16(5):1–21.
- Maurer, H., Greenhalgh, S., and Latzel, S. (2009). Frequency and spatial sampling strategies for crosshole seismic waveform spectral inversion experiments. *Geophysics*, 74(6):WCC11–WCC21.
- Maurer, H., Holliger, K., and Boerner, D. E. (1998). Stochastic regularization: Smoothing or similarity? *Geophysical Research Letters*, 25(15):2889–2892.
- Menke, W. (1989). *Geophysical Data Analysis: Discrete Inverse Theory*, volume 45 of *International Geophysics Series*. Academic Press, revised edition.
- Min, D.-J., Shin, C., Pratt, R. G., and Yoo, H. S. (2003). Weighted-averaging finite-element method for 2D elastic wave equations in the frequency domain. *Bulletin of the Seismological Society of America*, 93(2):904–921.
- Mora, P. (1987). Nonlinear two-dimensional elastic inversion of multioffset seismic data. *Geophysics*, 52(9):1211–1228.
- Müller, G. (1985). The reflectivity method: a tutorial. *Journal of Geophysics*, 58:153–174.
- Nkemzi, D. W. (2008). A simple and explicit algebraic expression for the Rayleigh wave velocity. *Mechanics Research Communications*, 35(3):201 – 205.
- Operto, S., Virieux, J., Amestoy, P., L'Excellent, J.-Y., Giraud, L., and Ali, H. B. H. (2007). 3d finite-difference frequency-domain modeling of visco-acoustic wave propagation using a massively parallel direct solver: A feasibility study. *Geophysics*, 72(5):SM195–SM211.
- Ory, J. and Pratt, R. G. (1995). Are our parameter estimators biased? the significance of finite-difference regularization operators. *Inverse Problems*, 11(2):397–424.
- Phinney, R. A. (1965). Theoretical calculation of the spectrum of first arrivals in layered elastic mediums. *Journal of Geophysical Research*, 70(20):5107–5123.
- Plessix, R.-E. (2008). Introduction: Towards a full waveform inversion. *Geophysical Prospecting*, 56(6):761–763.
- Plessix, R.-E. (2009). Three-dimensional frequency-domain full-waveform inversion with an iterative solver. *Geophysics*, 74(6):WCC149–WCC157.
- Plessix, R.-E. and Mulder, W. A. (2008). Exploring some issues in acoustic full waveform inversion. *Geophysical Prospecting*, 56(6):827–841.
- Pratt, R. G. (1990). Frequency-domain elastic wave modeling by finite differences: A tool for crosshole seismic imaging. *Geophysics*, 55(5):626–632.

- Pratt, R. G. (1999). Seismic waveform inversion in the frequency domain, part 1: Theory and verification in a physical scale model. *Geophysics*, 64(3):888–901.
- Pratt, R. G., Shin, C., and Hicks, G. (1998). Gauss-Newton and full Newton methods in frequency-space seismic waveform inversion. *Geophysical Journal International*, 133(2):341–362.
- Press, W., Teukolsky, S., Vetterling, W., and Flannery, B. (1992). *Numerical Recipes in C*. Cambridge University Press, Cambridge, UK, second edition.
- Robertsson, J. O. A., Blanch, J. O., and Symes, W. W. (1994). Viscoelastic finite-difference modeling. *Geophysics*, 59(9):1444–1456.
- Robertsson, J. O. A., Holliger, K., and Green, A. G. (1996). Source-generated noise in shallow seismic data. *Journal of Environmental & Engineering Geophysics*, 1:107–124.
- Romanowicz, B. (2003). Global mantle tomography: Progress status in the past 10 years. *Annual Review of Earth and Planetary Sciences*, 31(1):303–328.
- Rose, J. L. (2004). *Ultrasonic Waves in Solid Media*. Cambridge University Press, Cambridge.
- Roten, D. (2007). *Site effects in the Rhône valley analysed by ambient noise, weak motion records and numerical simulations*. PhD thesis, ETH Zürich. Diss. ETH No. 17471.
- Roth, M. and Holliger, K. (1999). Inversion of source-generated noise in high-resolution seismic data. *The Leading Edge*, 18(12):1402–1406.
- Rubin, Y. and Hubbard, S. S., editors (2006). *Hydrogeophysics*. Springer, first edition.
- Sarma, G. S., Mallick, K., and Gadhinglajkar, V. R. (1998). Nonreflecting boundary condition in finite-element formulation for an elastic wave equation. *Geophysics*, 63(3):1006–1016.
- Schenk, O. and Gärtner, K. (2004). Solving unsymmetric sparse systems of linear equations with pardiso. *Future Generation Computer Systems*, 20(3):475 – 487. Selected numerical algorithms.
- Schenk, O. and Gärtner, K. (2006). On fast factorization pivoting methods for symmetric indefinite systems. *Electronic Transactions on Numerical Analysis*, 23:158–179.
- Schenk, O., Röllin, S., and Hagemann, M. (2002). Recent advances in sparse linear solver technology for semiconductor device simulation matrices. In *Proceedings of the 2003 International Conference on Simulation of Semiconductor Processes and Devices*. IEEE.
- Sen, M. and Stoffa, P. L. (1995). *Global Optimization Methods in Geophysical Inversion*, volume 4 of *Advances in Exploration Geophysics*. Elsevier, Amsterdam.

- Shearer, P. M. (2009). *Introduction to Seismology*. Cambridge University Press, Cambridge, second edition.
- Sheen, D. H., Tuncay, K., Baag, C. E., and Ortoleva, P. J. (2006). Time domain gaussian newton seismic waveform inversion in elastic media. *Geophysical Journal International*, 167:1373–1384.
- Sheriff, R. E. and Geldart, L. P. (1985). *Exploration Seismology*. Cambridge University Press, Cambridge, second edition.
- Sinclair, C., Greenhalgh, S., and Zhou, B. (2007). 2.5D modelling of elastic waves in transversely isotropic media using the spectral element method. *Exploration Geophysics*, 38(4):225–234.
- Sirgue, L. and Pratt, R. G. (2004). Efficient waveform inversion and imaging: A strategy for selecting temporal frequencies. *Geophysics*, 69(1):231–248.
- Smidt, J. M. (2009). Table of elastic constants for isotropic media. *The Leading Edge*, 28(1):116–117.
- Socco, L. V., Boiero, D., Foti, S., and Wisén, R. (2009). Laterally constrained inversion of ground roll from seismic reflection records. *Geophysics*, 74(6):G35–G45.
- Socco, L. V. and Strobbia, C. (2004). Surface-wave method for near-surface characterization: a tutorial. *Near Surface Geophysics*, 2(4, Sp. Iss. SI):165–185.
- Song, Z.-M. and Williamson, P. R. (1995). Frequency-domain acoustic-wave modeling and inversion of crosshole data: Part I—2.5-D modeling method. *Geophysics*, 60(3):784–795.
- Stokoe, K. H. I. (2007). *Field Seismic Testing in Geotechnical Earthquake Engineering*, volume 6 of *Geotechnical, Geological, and Earthquake Engineering*, chapter 7, pages 151–157. Springer.
- Stummer, P., Maurer, H., and Green, A. G. (2004). Experimental design: Electrical resistivity data sets that provide optimum subsurface information. *Geophysics*, 69:120–139.
- Tadeu, A. J. B. and Kausel, E. (2000). Green's functions for two-and-a-half-dimensional elastodynamic problems. *Journal of Engineering Mechanics*, 126(10):1093–1097.
- Takenaka, H., Kennett, B. L. N., and Fujiwara, H. (1996). Effect of 2-D topography on the 3-D seismic wavefield using a 2.5-D discrete wavenumber-boundary integral equation method. *Geophysical Journal International*, 124(3):741–755.
- Takeuchi, H. and Saito, M. (1972). Seismic surface waves. In Bolt, B. A., editor, *Methods in Computational Physics*, volume 11 (Seismology: Surface waves and earth oscillations). Academic Press, New York and London.
- Tarantola, A. (1984). Inversion of seismic reflection data in the acoustic approximation. *Geophysics*, 49(8):1259–1266.

- Tarantola, A. (2005). *Inverse problem theory and methods for model parameter estimation*. SIAM: Society for Industrial and Applied Mathematics.
- Thomsen, L. (1986). Weak elastic anisotropy. *Geophysics*, 51(10):1954–1966.
- Trefethen, L. N. and Bau, D. (1997). *Numerical Linear Algebra*. Society for Industrial and Applied Mathematics, Philadelphia.
- Virieux, J. (1986). P-sv wave propagation in heterogeneous media: Velocity-stress finite-difference method. *Geophysics*, 51(4):889–901.
- Virieux, J. and Operto, S. (2009). An overview of full-waveform inversion in exploration geophysics. *Geophysics*, 74(6):WCC1–WCC26.
- Virieux, J., Operto, S., Ben-Hadj-Ali, H., Brossier, R., Etienne, V., Sourbier, F., Giraud, L., and Haidar, A. (2009). Seismic wave modeling for seismic imaging. *The Leading Edge*, 28(5):538–544.
- Wang, R. (1999). A simple orthonormalization method for stable and efficient computation of Green's functions. *Bulletin of The Seismological Society of America*, 89(3):733–741.
- Wapenaar, K., Draganov, D., and Robertsson, J. O. A., editors (2008). *Seismic Interferometry: History and Present Status*. Number 26 in Geophysics Reprint Series. Society of Exploration Geophysics, Tulsa, Oklahoma, U.S.A.
- Williamson, P. R. and Pratt, R. G. (1995). A critical review of acoustic wave modeling procedures in 2.5 dimensions. *Geophysics*, 60(2):591–595.
- Williamson, P. R. and Worthington, M. H. (1993). Resolution limits in ray tomography due to wave behavior: Numerical experiments. *Geophysics*, 58(5):727–735.
- Xu, K., Greenhalgh, S., and Wang, M. Y. (2006). Comparison of source-independent methods of elastic waveform inversion. *Geophysics*, 71(6):R91–R100.
- Yang, Y.-B. and Hung, H.-H. (2001). A 2.5D finite/infinite element approach for modelling visco-elastic bodies subjected to moving loads. *International Journal for Numerical Methods in Engineering*, 51(11):1317–1336.
- Yilmaz, O. (2000). *Seismic Data Analysis*. Soc. of Expl. Geophys., Tulsa, first edition.
- Yokota, T. and Matsushima, J. (2003). Seismic waveform inversion in frequency-space domain: Strategy for the optimal inversion step selection. In Saito, M. and Murata, S., editors, *Environmental rock engineering*, pages 299–304. Swets and Zeitlinger.
- Zhang, J. and Verschuur, D. J. (2002). Elastic wave propagation in heterogeneous anisotropic media using the lumped finite-element method. *Geophysics*, 67(2):625–638.
- Zheng, Y. and Huang, X. (2002). Anisotropic perfectly matched layers for elastic waves in cartesian and curvilinear coordinates. Earth resources laboratory consortium report, Massachusetts Institute of Technology, Cambridge.

- Zhou, B. and Greenhalgh, S. (1998a). Composite boundary-valued solution of the 2.5-D Green's function for arbitrary acoustic media. *Geophysics*, 63(5):1813–1823.
- Zhou, B. and Greenhalgh, S. (1998b). Crosswell acoustic velocity imaging with full waveform spectral data: 2.5D numerical simulations. *Exploration Geophysics*, 29:680–684.
- Zhou, B. and Greenhalgh, S. (1998c). A damping method for the computation of the 2.5-D Green's function for arbitrary acoustic media. *Geophysical Journal International*, 133(1):111–120.
- Zhou, B. and Greenhalgh, S. (1999). Explicit expressions and numerical calculations for the Fréchet and second derivatives in 2.5D Helmholtz equation inversion. *Geophysical Prospecting*, 47(4):443–468.
- Zhou, B. and Greenhalgh, S. (2003). Crosshole seismic inversion with normalized full-waveform amplitude data. *Geophysics*, 68(4):1320–1330.
- Zhou, B. and Greenhalgh, S. (2006). An adaptive wavenumber sampling strategy for 2.5D seismic-wave modeling in the frequency domain. *Pure and Applied Geophysics*, 163(7):1399–1416.
- Zhou, B. and Greenhalgh, S. (2009). On the computation of the Fréchet derivatives for seismic waveform inversion in 3D general anisotropic, heterogeneous media. *Geophysics*, 74(5):WB153–WB163.
- Zhou, B. and Greenhalgh, S. (2010a). Computing the sensitivity kernels for 2.5-d seismic waveform inversion in heterogeneous, anisotropic media. submitted to *Pure and Applied Geophysics*.
- Zhou, B. and Greenhalgh, S. (2010b). Wavenumber sampling strategies for 2.5-D frequency-domain seismic wave modelling in general anisotropic media. submitted to *Geophysical Prospecting*, under revision.
- Zienkiewicz, O. C., Taylor, R. L., and Zhu, J. Z. (2005). *The Finite Element Method Set*. Butterworth-Heinemann, sixth edition.

Curriculum Vitae

Personal

Sabine Latzel

Date of Birth: 19 / 12 / 1979

Place of Birth: Mutlangen, Germany

Citizen of: Germany

Education

2005 - 2010 Doctoral student at the Institute of Geophysics,
Swiss Federal Institute Technology (ETH) Zürich (Switzerland)

1999 - 2004 Diploma student at the University of Stuttgart (Germany)
Degree (Dipl.-Physik) received: 13 / 12 / 2004
Pre-Diploma (physics) received: 18 / 10 / 2001

1990 - 1999 Student at Limes-Gymnasium in Welzheim (Germany)
Abitur received: 29 / 06 / 1999
